

Architecture
of a nanocrystalline biomineralised shell
by

Riyad Mahmud-Mistry Mucadam

A thesis
submitted to the Victoria University of Wellington
in fulfilment of the requirements for the degree of
Doctor of Philosophy
Applied Physics

Victoria University of Wellington /
MacDiarmid Institute of Advanced Materials and Nanotechnology

2014

Except where otherwise indicated, this thesis is my original work.

© Riyad M M Mucadam, 2014

Bismillah ar rahman ir raheem

“Nature is not concerned with categorization but with producing effective results.”

J. D. Currey

Acknowledgements

I am *lucky* to have entered this science wonderland and use it to explore a topic, made of subtopics. When I started this thesis, I knew literally nothing about this topic, of its vocabulary, its past, that scholar.google or that its contents existed, or that tools used in this thesis exist. I just “saw” and I have enjoyed stretching beyond any comfort zone to learn about how to apply tools to investigate what I saw. Thanks are due to many, some for their contributions before and some for after that “seeing”.

Late Dad> for buying science books as birthday gifts until I was 16 years old and for supporting unconditionally my education; Mom> for her constant support, for travelling far to visit me in colder New Zealand; Nelling> for compelling me to say yes when I had hesitated to accept the scholarship; for her devotion and support everyday, everywhere; Misbah my teen (other PhD)> thanks for being your self-assembling self... aarrgh ? for sacrificing and switching schools so often. Faizan and Sana... far away but close.

Assoc. Prof. John Collen> for doing generously what he did in 2008 and for allowing what he allowed in 2009. Prof. Vijay Naidu> for helping sort out the admissions process to VUW, at a time when I had virtually no access to the internet; for being part of the Oceania Development Network in which I was awarded an Emerging Researcher grant award in 2010...to do research in the islands unrelated to this work; New Zealand Ministry of Foreign Affairs and Trade>the NZAID advisors at Victoria International- Bridget, Ingrid and Julia> thanks for the financial support and the huge bureaucratic network that they managed patiently, with concern and attention. Wellington> the coolest capital in the world; Lyall Bay>coolest city-beach town in New Zealand; Vic Library> responsive Inter-loans staff and the awesome movies section.

Sele Lowe, Dr. Noshir Gowadia, Tuk Masao, Mohammed Farah, the Ahulelei brothers, Raj Patkar, Keith Imai, Keith Kenya, Nazir Haider, Younis Obad, the Mexicans> for companionship, silence, chess, humour, volleyball, shampoo, sharing the “Economist” and spare meals in tough conditions in Hawaii until a week before I travelled to NZ; Sherry Rone> for facilitating money transfers when I was in hard cells, for taking Misbah in as a daughter and encouragement at the tough-end. Dr. Manoj Nair > for making the phone call that informed me of the charter flight from Majuro to Kiribati on Feb 14, 2008, of the Japanese girl who fell sick and vacated her seat. Florence Botou and Titeem – in Tarawa and Wellington- for warmly, coolly being there.

John Carter in SGEES for saying “go the MacDiarmid Institute...blue skies research should be encouraged.” Prof. David Bibby, Dean of SEAD at VUW and Prof. John Spencer Head of School, SCPS, for hearing me out as I presented my concept of a thesis and for saying: “ you have a framework; very risky doing it this way... but go to Kate McGrath”. Kate McGrath> for saying yes at first and all through; for allowing me to continue down all paths without raising *both* eyebrows (i.e. superwising *not* supervising, did she have a choice?); for organising the attachment at the Division of Applied Mathematics at the Australian National University; for entertaining a zig-zag approaches to things, and being a solid supporter; for usually enjoyable one-on-one meetings; for supporting my win at the 3-minute thesis, NanoArt, for reading my submitted abstracts to international conferences; for patience; for being Kate, appropriately short of being a mate. Prof. John Overton and Assoc. Prof. Ralph Chapman who allowed me to sit in to any and all classes in the first year as I vetted myself and sharpened my island-life dulled pencil against the new internet world wide webbed

developed world university environment. Assoc. Prof. Michael Hannah> for being there. Shona deSain and Patricia Stein> you made the admin hoops easy when these could have strangled me.

UNI people> Ashishika Sharma at USP who guided me to a sampling site in Fiji. Early days with Faisal Nabi, Gayna Vetter, Ahmad Shukri, Abu Conteh, Shabana Khan of SGEES, Catherine Davis, Conrad Lendrum, Benjamin Matthewson, Agathe Fournier the MGM group members; Adella Campbell, Lala Sharma, Sanjay Samuel, Omar al-Sager, Alice Doughty, Elf Eldridge (yes-Transit of Venus in Gisborne!), Annette Bolton, and Katie Collins > for talking and for helping in some way as I stumbled around university or being mates or being excited about my research as much as theirs. David Flynn> a quarter of this work is directly related to your help with the SEM and with laughing with you; Stewart Bush> for help with thin-sections. Juliana Ungaro for a *lot*, and Baraa Al-yamani for a little.

Applied Maths at ANU> A set of crackerjack set of people I had the privilege of sipping espressos with, asking for their feedback on my little project...and receiving their encouragement. Prof. Tim Senden: for being excited by my ideas and for pushing me on and through all doors; Prof. Stephen Hyde: for being interested and answering every question with a question or with an amazing book to look at- really, how many PhD candidates get a chance to work with someone who was their supervisor's PhD supervisor? Dr. Mahyar Mahdadi and Dr. Ajay Limaye-> two soft spoken low-key wizards in their computing fields. Dr. John Fitzgerald of Microscopy in ANU's Earth Sciences> an expert who made successful my TEM adventure. Dr. Michael Turner and Jill Middleton> for their technical tweaking. Dr. Osamu Sasaki of Tohoku University Museum and, Carmen Norris of Fonterra Innovation> for first sharing with me X-ray MCT's capabilities.

The Pacifika Leadership Cluster> Pine Southon for emails with Maori inspirational quotes and anecdotes; Prof. Kabini for inviting me to write a chapter in the book, now published by USP "Harvesting Ideas...", the Pacifika symposia and conferences in which I could present my research and learn with Leadership Pacifika- the heart remained warm despite the Wellington gales. UNITEC Pasifika Leadership program> late Dr. Fraser McDonald and the sumptuously catered training workshop retreats; for the comraderie of the Pasifika group of NZAID scholars who will remain a solid node in my Pacifika network; The MAiki Poneke Maori Doctoral Students group, Dr. Pauline Harris, Dennis, Mike and Dr. Ewan Pohe> for including and accommodating my participation in their activities- the retreats and the Doctoral conferences-an unbelievable experience of Maori scholardom in NZ; Dr. Ocean Mercier> for inviting me to Running Hot- *the* most fun NZ science get-together ever; The MacDiarmid Institute> for its doctoral and post-doctoral symposia 4 years in a row- so many diverse subjects and eager minds, and science periphery-related training and discussions. Hon. Matt Zachras, H.E. J.B. Kabua in Tokyo, H.E. Amatlain K. in NYC and H.E. Fred Muller in Suva> for your sure-fire help during the 4 years in which I managed daily from NZ the rural solar refrigeration pilot project in the outer atolls of the Marshalls while doing this research. Dare I say, *that* was difficult real-world *work*; *this* work was mostly fun! Zaheda & Chris Davies> simply friends-like-family. Shakil Kumar & Vinay Kumar> for the house in Lyall Bay. And others who are definitely in my mindspace but may not be mentioned here. Kom emmol, thanks, kia ora, bros.

--- Riyad M. M. Mucadam, Wellington, December 2013.

Abstract

Marginopora sp. is an eukaryotic large benthic foraminifera that biomineralises a high magnesium calcitic test (shell) in which dinoflagellate symbionts are stored. The discoidal test has a complex architecture; a very large cellular organism expends considerable energy to assemble and maintain a complex shell. What does the organism realise from this architecture? What are the *elemental* features of the architecture? Researchers have studied the test's microstructures and chemical composition; its functional value has been suggested but an endeavour to pinpoint any particular value can be extremely complicated in a biological structure, i.e. an intractable problem is presented. Form is related to and often determines the adaptive functional value of biological structures; an enhanced understanding of form precedes and informs an understanding of function. This work increases an understanding of the form and functional value of the complex architecture of the test. Particularly, it adds to existing knowledge by: extending to a nanoscale a detailed characterization of the microstructures of the test, revealing calcium carbonate nanostructures and their associations to form crystals; conceptualising and applying a hierarchical arrangement of the microstructures across nano-macro dimensions of scale; visualising in three dimensions (3D) the microstructures of the test through ontogeny to reveal anisotropy and symmetry in the morphology of microstructures and in the test; and discovering and interpreting structural patterns that were previously not visible. Based upon these findings, the architecture and microstructures of the test; properties of biomineralised structures such as bone and echinoderm skeletons; structural arrangement of adequate models; and predominantly the mechanical adaptive value of the test are correlated. This thesis advances ideas and suggestions for research, design and practical applications of the structural principles abstracted from these findings and interpretations towards a biomimetic design of structures and processes.

A combination of advanced microscopy techniques at higher resolutions and magnifications than previously used in the research of the test were used to evaluate pristine specimens of the test of *Marginopora sp.* Data and images obtained by the use of high resolution and cryo-scanning electron microscopy, transmission electron microscopy, polarising microscopy and, X-ray micro computed tomography (X-ray MCT) of several specimens representing different ontogenic stages were analysed. Especially, the applicability of X-ray MCT as a technique was tested for the quantitative and qualitative analysis of 3D features of the test. Visualisation and statistical techniques used in network analysis were applied to the data obtained by X-ray MCT. A materials sciences approach was adopted towards interpreting the nano-macro scale structural features of the test. In lieu of a protracted and difficult experimental approach a method used in the field of artificial intelligence was adopted to find models that could adequately point to the adaptive value of the architecture of the test. Results obtained using this approach indicated that the adaptive values are self-assembly in a phyllotactic pattern that allows an effective mechanical flexural response using a minimum of materials; close-packing of a particular pore volume; and that enables large surface areas and transmission of light through a 3D biconcave disc.

Contents

Acknowledgements	i
Abstract	iii
Contents	iv
Figures	x
Note.....	xiv
CHAPTER 1: Introduction	16
1.1 Overview	16
1.2 Foraminifera	17
1.3 Relevance of the Research	21
1.4 Research Objectives	23
1.5 Structure of this Thesis	24
CHAPTER 2: Materials and Methods	26
2.1 Field work and Specimens	26
2.2 Instrumental techniques used in the characterization of the test of <i>Marginopora sp.</i>	27
2.2.1 Standard Techniques	27
2.2.1.1 Thin Sections	27
2.2.1.2 Scanning Electron Microscopy	28
2.2.1.3 Transmission Electron Microscopy	28
2.2.1.4 Cryo-Scanning Electron Microscopy (Cryo-SEM)	28
2.2.1.5 Energy Dispersive Spectrometry (EDS)	29
2.2.1.6 Mercury Porosimetry	29
2.3 Characterization using X-ray Micro Computed Tomography	29
2.3.1 Introduction	29
2.3.2 Principles of X-ray Tomography	30
2.3.3 X-ray MCT Equipment	33
2.3.3.1 Source	33
2.3.3.2 Scanners	34
2.3.3.3 Detectors	35
2.3.3.4 Sample Preparation	36
2.3.3.5 Calibration	36
2.3.3.6 Data Collection and Reconstruction	36

2.3.3.7 Artefacts	37
2.3.3.8 Size and Resolution	38
2.3.4 X-ray MCT Application in Research.....	38
2.3.5 X-ray MCT and Foraminifera Research	41
2.3.6 Procedure and Experiments: X-ray MCT	43
2.3.6.1 Low Resolution Scanning.....	43
2.3.6.2 High Resolution Scanning.....	44
2.3.6.2.1 A.N.U.....	44
2.3.6.2.2 Xradia	45
2.3.6.3 Calibration.....	47
2.3.6.4 Image Processing	48
2.3.6.5 NCView and Mango.....	50
2.3.6.6 Drishti.....	50
2.3.6.7 ImageJ and BoneJ	51
2.3.7 Rapid Prototyping.....	52
CHAPTER 3: Results	54
3.1 Optical Microscopy Thin sections of <i>Marginopora sp.</i>	54
3.1.1 Introduction.....	54
3.1.2 Observations.....	55
3.1.2 Discussion	64
3.2 Polarized Light Microscopy of ultra-thin sections of <i>Marginopora sp.</i> : Chamber walls, orientation of walls and polarization of incident light	65
3.2.1 Introduction.....	65
3.2.2 Observations.....	68
3.2.2 Discussion	70
3.3 High resolution electron microscopy of surface wall structure.....	71
3.3.1 Introduction.....	71
3.3.2 Observations.....	72
3.3.3 Discussion	73
3.4 Electron Microscopy of <i>Marginopora sp.</i> : 2D visualization of calcite crystal morphology, dimensions and orientation in the region surrounding a chamberlet	75
3.4.1 Introduction.....	75
3.4.2 Observations- SEM	76
3.4.3 Cryo-SEM and TEM Observations of Selected Microstructures	83

3.4.4 Results in Summary	93
3.4.5 Discussion	94
3.4.4.1 Colloidal crystallite nanostructures (CCN)	94
3.4.4.2 Biomineralisation	96
3.4.4.3 Euhedral crystals	98
3.4.4.4 Synthetic minerals	99
3.4.4.5 Directed orientation of clusters of euhedral crystals	100
3.4.4.6 Organic-inorganic composite	100
3.4.5 Conclusion	102
3.5 Results: Scanning Electron Microscopy 2D high resolution visualization of internal microstructures of <i>Marginopora sp.</i> assembled in a hierarchical structure	102
3.5.1 Introduction	102
3.5.2 Hierarchical level 1: CCN	105
3.5.3 Hierarchical Level 2: Organic	107
3.5.4 Hierarchical level 3: Bundles, Ensembles, Lamellae	109
3.5.5 Hierarchical Level 4: Curvilinear, Meshed Microstructures	113
3.5.6 Hierarchical level 5.1: Crystalline solid and chamber void periodic structure	115
3.5.7 Hierarchical Level 5.2: Chamber or void microstructures packed with organic fluid and amorphous solids	117
3.5.8 Hierarchical Level 6: Tubular and Flange structures	119
3.5.9 Hierarchical level 7: 3D Porous Biconcave Disc Shape	121
3.5.10 Discussion	122
3.5.10.1 Hierarchical levels	122
3.5.10.2 CCN and crystals	122
3.5.10.3 Organic lining	123
3.5.10.4 Crystalline arrangements	124
3.5.10.5 Meshed curvilinear structures	125
3.5.9.6 3D cellular solid with fluid or foam filled void	125
3.5.9.7 Tubular and peripheral holes	126
3.5.9.8 3D biconcave disc	126
3.5.9.9 Levels of hierarchy	127
3.5.9.10 Future research	128
3.6 Results of X-ray MCT: Qualitative Analysis of Ontogeny of the test	129
3.6.1. Introduction	129

3.6.2 Results.....	130
3.6.2.1 Specimen M111.....	130
3.6.2.2 Specimen M112.....	132
3.6.2.3 Specimen M331.....	132
3.6.2.4 Specimen M332.....	134
3.6.2.5 Specimen441.....	134
3.6.2.6 Specimen M_smallest.....	135
3.6.2.7 Specimen M_smaller	137
3.6.2.8 Specimen small.....	137
3.6.2.9 Specimen M_551	139
3.6.2.10 Specimen Middle	141
3.6.2.11 Specimen Largest.....	143
3.6.2.12 Specimen M_young: High resolution	144
3.6.2.13 Specimen M_old- High resolution.....	144
3.6.3 Qualitative Results: High resolution X-ray MCT data based volumetric renderings for 3D visualization of architecture.....	145
3.6.3.1 Introduction.....	145
3.6.3.2 Results.....	147
Specimen M 110: Ultra High Resolution (submicrometre) phase contrast 3D visualization	151
3.6.4 Results in Summary	154
3.6.4.1 Shapes of the test changes during ontogeny.....	154
3.6.4.2 Grid structure.....	154
3.6.4.3 Distribution density of calcite.....	154
3.6.4.4 X-ray MCT resolution of viewable structural features.....	155
3.6.4.5 Microstructure characterization.....	155
3.6.5 Discussion	156
3.6.5.1 Mineralisation and architecture.....	156
3.6.5.2 Visualization	158
3.7 X-Ray MCT Quantitative Results: Porosity, Surface area, volume of the test.....	161
3.7.1 Introduction.....	161
3.7.2 Results.....	162
3.7.3 Discussion	164
3.8 Networks in the test.....	167

3.8.1 Introduction.....	167
3.8.1 Quantitative analysis of the distribution of void space (pore).....	169
3.8.1.1 Results	171
3.8.2 Visualization of a network: the void space in the test of <i>Marginopora sp.</i>	175
3.8.3 Summary of Results	179
3.8.4 Discussion	179
3.8.4.1 Network Statistics.....	179
3.8.4.2 Pore and Throat sizes.....	181
3.8.4.3 Visualization of pore-throat and solid fraction and adaptive value of network of the test.....	182
3.9 Analysis of the 2D and 3D spatial structure of <i>Marginopora sp.</i> using polygons.....	184
3.9.1 Introduction.....	184
3.9.2 Results.....	187
3.9.2 Discussion	191
3.10 Models for and of the test	196
3.10.1 Introduction.....	196
3.10.1 Results.....	200
3.10.1.1 Model 1	201
3.10.1.2 Model 2	202
3.10.1.3 Model 3	203
3.10.2 Discussion.....	203
CHAPTER 4: Conclusions and Outlook	206
4.1 Summary of Results	206
4.1.1 Role of Visualization.....	207
4.2 Future research	209
4.2.1 Biomineralisation.....	209
4.2.2 Role of microtubules	209
4.2.3 Role of the proloculus.....	209
4.2.4 <i>Marginopora sp.</i> and Homology.....	210
4.2.5 Structure and X-ray MCT	210
4.2.6 Mechanical Studies.....	210
4.2.7 Microfluidics	210
4.2.8 Optical studies	211
4.3 Outlook: Biomimetic Applications.....	211

4.3.1 Overall architecture.....	211
4.3.2 Arches.....	212
4.3.3 Assembly and Delivery process	212
4.3.4 Functional structures	212
4.3.5 Ceramic Materials and Shells.....	213
Bibliography	215
Appendix A.....	230
X-ray MCT – Thresholding procedure and parameters used	230
Appendix B- Supplementary SEM images	232

Figures

Figure 1: <i>Marginopora</i> sp. in its shallow coastal habitat attached to sea-grass (A) and coralline rock (B) substrates.	18
Figure 2: Salient morphological features of a test of <i>Marginopora</i> sp.	19
Figure 3: Similarities and differences in foraminiferal calcification pathways.	20
Figure 4 Discoidal test- with translucent surface and crystals of surface walls.	21
Figure 5 Hottinger cast of test of <i>Marginopora</i> sp. viewed with SEM.	23
Figure 6 Sampling Locations.	26
Figure 7 Sampling and fixing in the field.	27
Table 1 X-ray Tomography systems categorised by scale.	30
Figure 8 Intensity and attenuation coefficient of X-rays.	31
Figure 9 Attenuation of X-rays in the shadow zone of the object.	32
Figure 10 Shadow definition of object points.	32
Figure 11 Sample tomogram.	33
Figure 12 Reconstructed tomogram.	33
Figure 13 Commonly used X-ray MCT scanner or beam and detector configurations.	34
Figure 14 Differences in scans of planar configurations: (a) single beam; (b) fan beam; (c) cone beam; (d) cone beam with an offset.	35
Figure 15 Ring artefact: concentric rings centred at the approximate centre of the cross-section.	37
Figure 16 Beam hardening artefact.	38
Figure 17 Schematics of generic configuration for lab or desktop X-ray MCT.	43
Table 2 Low resolution X-ray MCT conditions.	44
Table 3 High resolution X-ray MCT conditions CTLab.	45
Figure 18 Sample in clear plastic cone held on sample stage.	46
Table 4 High resolution X-ray MCT conditions Xradia.	46
Table 5: Isotropic voxel sizes of X-ray MCT data sets.	47
Figure 19 Use of NCView for thresholding.	49
Figure 20 Bioimaging software's usability criteria.	52
Figure 21 Z-640 3D printer.	53
Figure 22 Test of an adult <i>Marginopora</i> sp. viewed with optical microscope x100; circularity for comparison of form.	55
Figure 23 Equatorial thin-section of an adult <i>Marginopora</i> sp.	56
Figure 24 Microstructures of <i>Marginopora</i> sp.	57
Figure 25 Chamberlet and Chambers- patterns visible in 2D equatorial thin-section.	57
Figure 26 Transverse thin-section of partial disc of <i>Marginopora</i> sp.	58
Figure 27 Microstructures of <i>Marginopora</i> sp. in transverse thin-section.	59
Figure 28 Axial thin-sections of <i>Marginopora</i> sp.	60
Figure 29 Transverse thin-section of <i>Marginopora</i> sp.: view from centre to margin. Region marked by white boxes are B1, B2.	61

Figure 30 Transverse view thin-section of <i>Marginopora sp.</i> : view towards embryonic apparatus.	62
Figure 31 Partial equatorial angular transverse thin-section of test of <i>Marginopora sp.</i>	63
Figure 32 Equatorial surficial thin-section of test of <i>Marginopora sp.</i>	64
Figure 33 Low magnification images of thin sections of <i>Marginopora sp.</i> viewed with polarising microscope.....	67
Figure 34 A: Parallel section 1.25x; B: 5x mag; C: 20x magnification; D: Crossed polars rotated 45; E: 40x crossed polars rotated 45 black white contrast.....	69
Figure 35 Focused ion beam milled surface of <i>Marginopora sp.</i>	72
Figure 36 Colloidal crystallites and crystal morphology during biomineralisation. ...	77
Figure 37 Crystal formation in vesicles, transport and construction of walls.	81
Figure 38 Cryo-SEM image of organic structure of early ontogenic stage of <i>Marginopora sp.</i>	83
Figure 39 TEM image of crystal orientation and porosity in <i>Marginopora sp.</i>	85
Figure 40 Variable size density and morphology of crystals.....	87
Figure 41 High resolution images of Crystal organic interface.	91
Figure 42 Single calcitic crystals.	105
Figure 43 Organic lining of varying thickness and density with adhered crystals or covering packed crystals.	107
Figure 44 Meshed assemblies of calcite crystals of varying density or packing, orientation, overlap and flow patterns.....	109
Figure 45 Circular port-hole openings and branched multicrystalline beams forming a mesh and margin.....	113
Figure 46 3-Dimensional alternating solid and void periodic structure of the test..	115
Figure 47 Amorphous and foam structure inside the void space.....	117
Figure 48 Dense flanged openings on the margin and dense smooth walled tubes connected to the interior of the test.	119
Figure 49 Anisotropic biconcave composite discoid with periodic internal void space and central soft region.....	121
Figure 50 X-ray MCT images: A: Grey-scale, B: thermal colour. C and D: 3D volume renderings. Bar: 100µm.....	130
Figure 51 Early ontogenic sequence of <i>Marginopora sp.</i> - revealing chamber formation, mineralization and change in shape.	134
Figure 52 X-ray MCT pre-adult specimen.	135
Figure 53 X-ray MCT mineral or density distribution in adult test.	138
Figure 54 X-ray MCT density variation in intercameral walls and in adult test.	139
Figure 55 X-ray MCT Change in morphology of test at pre reproductive stage: curved margins.....	141
Figure 56 X-ray MCT of reproductive stage of test: unresolved details of chambers; variable density of test annuli.	143
Figure 57 Reproductive test morphology and density of internal walls.....	144
Figure 58 Specimen M_young: 3D renderings in different orientations of the test.	147
Figure 59 Specimen M Young: A reconstructed tomogram.....	148

Figure 60 Specimen Foram Small and Foram 2.....	149
Figure 61 Specimen Foram Transverse section: very high resolution reconstruction and volume renderings.....	150
Figure 62 Nanotomography of the surface wall of the surface chamberlet.....	151
Figure 63 3D volumetric rendering of an isolated microstructural feature and quantification-surface chamberlet.	152
Figure 64 Rapid prototype 3D-print of internal structure of the test using X-ray MCT data: chambers, chamberlets.	153
Table 6 Threshold values for Figure 65 Porosity of tests of growth stages.	162
Figure 65 Trends in porosity with test size assessed with X-ray MCT data and ImageJ BoneJ.	163
Table 7 Mean values of density and porosity for five tests (dia. 4-5 mm) using mercury porosimetry.....	163
Figure 66 Basic descriptors of network topologies.	170
Figure 67 Skeletonisation: 3D medial axis of an object.	171
Table 9 Mean values of selected network statistics of test of Specimen M_young.	172
Figure 68 Frequency vs. Coordination number of pores.	172
Figure 69 Frequency vs. pore radius.....	173
Figure 70 Throat statistics.....	173
Figure 71 Pore volume and number of pores vs. number of neighbours.....	174
Figure 72 Pore space 3D visualization by network analysis of X-ray MCT data 9.	175
Figure 73 Ball-stick model of pore space in transverse section.....	176
Figure 74 Pore network using ball-stick model of network visualization.....	177
Figure 75 Visualization of (A & B) solid fraction skeletal topology and (C) combination of skeletonisation of pore network and grain.....	178
Figure 76 Clustering co-efficient of the pore network XY plane.....	181
Figure 77 Types of phyllotactic patterns- circles represent elements distributed on annular nodes.	185
Figure 78 X-ray MCT (A) reconstructed tomogram view in equatorial plane and (C) rendered volume view of the discoidal adult test.	187
Figure 79 A: Pairs of spirals in the test of <i>Marginopora sp.</i> ; B: Intersection of spirals; C: Changes in spirals.	187
Figure 80 Sketch of concepts.....	189
Figure 81 Tesellation of region of the test: Voronoi cells shown by blue lines; Delaunay by red lines.....	189
Figure 82 Plane symmetry group p3m1: the basic pattern observed at nano and macroscales of the test of <i>Marginopora sp.</i>	191
Figure 83 X-ray MCT transverse section of test showing spiral-like connectivity of chambers.	193
Figure 84 Schematic of concepts and relationships in adequate models.	199
Table 10 General reported parameters of the physical system of the test.	200
Figure 85 Structure of vertebrate disc.	201
Figure 86 Fovea and fovea centralis of the human eye.....	202

Figure 87 Heliostat layout (A) of polyhedral mirrors and (B) schematic of one type of simulated layout.	203
--	-----

Note

During the last two weeks of the writing of this dissertation, I became aware that Prof. J.J. Lee, of City University of New York, was preparing a paper that described a new species of *Marginopora* sp. found last year near Lizard Island in Australia's Great Barrier Reef. The specimens described in this work appear to be similar in their "extremely complex" structure to the new species described by Prof. Lee et al. in a draft version of their paper which is being prepared for publication. At this time, DNA analyses, a description of the structure and morphology of the new species -to be named *Marginopora rossi* - are being undertaken. Specimens studied in this work have been submitted recently to Prof. J.J. Lee for further examination. Preliminary reports by Prof. J.J. Lee indicate that the specimens studied in this work are "very different from the populations of *Marginopora vertebralis* found at Lizard Island" and are somewhat different from but could be related to the new species *Marginopora rossi*.

The specimens that are the subject of this work are referred to in this thesis as *Marginopora* sp. until further investigations are completed.

CHAPTER 1: Introduction

1.1 Overview and motivation for this research

The first detailed exploration of the forms found in nature their evolution and their possible functions was described in the classic book *On Growth and Form* (Thompson, D.W., 1942). The treatise showed that forms of shells, horns, trees, fish, and skeletal structures described by spirals, helixes, and unduloids show a mathematical character. Skeletonised forms found in nature have evolved over 550 million years, starting with the appearance and explosion of mineralised forms in the Cambrian period (Röttger, R., Irwan, A., Schmaljohann, R., & Franzisket, L., 1980).. Nature's designs, materials and structures survive the harsh tests of practicality and durability in a range of environmental and survival conditions. Nature's experiments with the principles of biology, physics, chemistry, materials science, structural mechanics and energy are visible through the course of evolution (Weiner, S.A.L., 1997). By studying the form and functions of various natural structures we can adapt many of nature's superior designs to improve our technology (Bar-Cohen, Y., 2006). Honeycomb, wool, and feathers have been studied at a range of scales for the design and utility of their microstructures (Rao, P., 2003). The forms of several biomineralised structures, that is, hard mineralised structures formed under the control of biological processes, such as bones, teeth, tusks, spines, fish scales, shells, cuticles, nacre, and exoskeletons, have been investigated. Research has shed light on the relationships between complex microstructures, scales, hierarchies, structural properties, and their functional roles (Aizenberg, J. et al., 2005; Boltovskoy, E., Scott, D., & Medioli, F., 1991; Currey, J.D., 1982; Currey, J.D., Brear, K., & Zioupos, P., 1994; Hildebrand, M., 2008; Ikoma, T., Kobayashi, H., Tanaka, J., Walsh, D., & Mann, S., 2003; Schmahl, W.W. et al., 2008; Sumper, M. & Brunner, E., 2006; Tarsitano, S.F., Lavalli, K.L., Horne, F., & Spanier, E., 2006).

The research presented here examines the form of the biomineralised outer protective layer or shell, known as the test, of a single celled organism that has undifferentiated tissues - a protist belonging to the order Foraminiferida (Loeblich, A.R. & Tappan, H., 1984). Most protists are less than 1 mm in diameter but the tests of the larger foraminifera can be as large as 10 cm. There are approximately 40,000 species of fossilised, and 10,000 species of extant, foraminifera ("forams") representing the most diverse group of shelled micro-organisms in the marine environment (Sen Gupta, B., 2003). They are among the earliest of biomineralised organisms and are characterised by foramina, or openings between voids or chambers enclosed in the test, and by granular, reticulated pseudopodia that extrude and anastomose from the test. The extant forms of large foraminifera represent the designs of very successful biomineralised protists (Hallock, P., 1985). The investigation of their structure and microstructures has the potential to offer insights into the efficient and successful design of porous structures, interconnected structures and into the evolution of biomineralised skeletal structures in higher evolved organisms.

A study of the microstructures of the brittlestar *Ophiocoma* sp. revealed that its calcitic lens microstructures with light sensitive nerve bundles located at estimated focal lengths were not present in species that were insensitive to light (Aizenberg, J., Tkachenko, A., Weiner, S., Addadi, L., & Hendler, G., 2001). In another study of the microstructures of a marine organism, the silica spicules of the glass sponge *Euplectella* sp. were shown to have optical properties that could allow the spicules to function in ways similar to commercial optical fibres (Aizenberg, J., Sundar, V.C., Yablon, A.D., Weaver, J.C., & Chen, G., 2004). These key studies strongly indicated that the position, scale and morphology of microstructures in these biomineralised structures were reconciled with mechanical and optical adaptive values. Researchers have sought to increase the efficiency of light trapping, harvesting and conversion in photovoltaic cells. Such efficiencies have been found to improve when the surfaces of crystalline and thin-film photovoltaic cells are provided with compound and textured microstructures (Dewan, R. et al., 2009). The position, scale and morphology of the 3D microstructures of these textured surfaces are strongly correlated to the changes in the optical and electrical performance of the cells (Sánchez-Illescas, P.J. et al., 2008). The convergence in the discovery of the correlation of microstructural characteristics and functional value in bio-optic structures and in optical technological artefacts is remarkable.

The crystalline tests of large symbiotic foraminifera are significant components of sand in atolls. My observation of the tests of these foraminifera, my work experience with photovoltaic modules and with the aquaculture of giant clams led to an investigation of a possible association between the structure of the tests and their biomimetic value. Despite being the subject of research efforts for over 150 years, very few experimental studies have been performed on the biomineralised tests of foraminifera (Hottinger, L., 2006). To the best of my knowledge not a single study has examined the test of a large extant foraminifera to investigate its potential structural hierarchy or experimentally characterise its 3-dimensional architecture and physical properties, and associate these with analogous patterns or structures found in biological systems and technological artefacts. It is with such a perspective that in this study the structure of the test of a foraminifera, *Marginopora* sp. was researched. The test has been found in the fossil record as early as 300 million years ago and *Marginopora* sp. is extant; thus, its test represents a very successful design. It is a large, marine, shallow water, and bottom-dwelling (benthic) foram which is symbiotic with algae, and has a test of complex architecture made of biomineralised calcite (Ross, C.A., 1972). This research sought to investigate and reconcile the characteristics of the microstructures of this test, its potential optical and mechanical adaptive value and the microstructural features of passive or photovoltaic solar structures or the structural and functional characteristics of photobioreactors for growing algae.

1.2 Foraminifera

Foraminifera are mentioned in Herodotus (fifth century BC) where he describes the presence of the large benthic foraminifer *Nummulites* in the limestone of the great pyramids. These forams' fossil record dates back to the Early Cambrian period (542 million years ago). Single-chambered foraminifera are among the earliest forams (Culver, S.J., 1991). Fossilised foraminifera are found in virtually all sedimentary deposits and extant foraminifera are found in aqueous environments,

including marine, brackish, coastal, deep, freshwater, tropical, and polar regions (Lee, J., McEnery, M.E., Kahn, E.G., & Schuster, F.L., 1979). A study of foraminifera DNA suggests that they are derived from a heterokaryotic marine protist of the late Proterozoic era, when the earliest forms of single celled, eukaryotic and multicellular life evolved as oxygen built up in the Earth's atmosphere (Wray, C.G., Langer, M.R., DeSalle, R., Lee, J.J., & Lipps, J.H., 1995). In 1872 the *Challenger* expedition was the first scientific oceanographic research to sample the ocean floor. It provided samples for scientists to work on for several decades (Murray, S.J., Renard, A.F., & Gibson, J., 1891). In the early 20th century, over several decades, Cushman made a notable contribution with establishing the use of foraminifera in biostratigraphy (Cushman, J.A., 1959). Later in the 20th century Loeblich and Tappan and Bolli pioneered the systematic classification of foraminifera (Loeblich, A.R. & Tappan, H., 1984).

Foraminiferal research is multi-disciplinary as a consequence of the ubiquity of foraminifera in fossilised and recent forms and serves varied roles. It is used in the fields of petroleum geology, biology, geology and chemical oceanography, palaeontology, stratigraphy, ecology of reefs, atoll and island sediments. In climate change research, foraminifera tests serve as indicators for a variety of information related to age determination of sediments, temperature, chemical composition of water masses and indicators of ecological processes or environmental conditions (Bostock, H.C., Hayward, B.W., Neil, H.L., Currie, K.I., & Dunbar, G.B., 2011; Collen, J.D. & Garton, D.W., 2004; Hallock, P., 2005; Martin, R.E., 2000; Saraswati, P.K., Seto, K., & Nomura, R., 2004). Foraminifera are also studied to understand cellular processes, crystallography of biological crystals, the chemistry of biomineralisation, and in the use of computational algorithms for constructing biological forms (Bentov, S., Brownlee, C., & Erez, J., 2009; Erez, J., 2003; Łabaj, P., Topa, P., Tyska, J., & Alda, W., 2003; Towe, K.M. & Cifelli, R., 1967).

Benthic and planktonic forams actively feed on other forams, algae, eggs, and fecal matter (Lee, J., 1974). The network of pseudopodia are used to catch prey (Lipps, J.H., 1982, 1983). Pseudopods are also used by planktonic forams to move in the water column and by benthic species e.g. *Marginopora* sp. to attach to substrates (Figure 1) such as rocks, gravel, or seaweed or to move along such surfaces (Murray, J.W., 1991). Foram habitats span the abyssal depths of the Challenger Trench, the entire oceanic water column, reefs, sea-grasses and the exposed air intertidal flats (Murray, J.W., 1991; Smith, R., 1968).

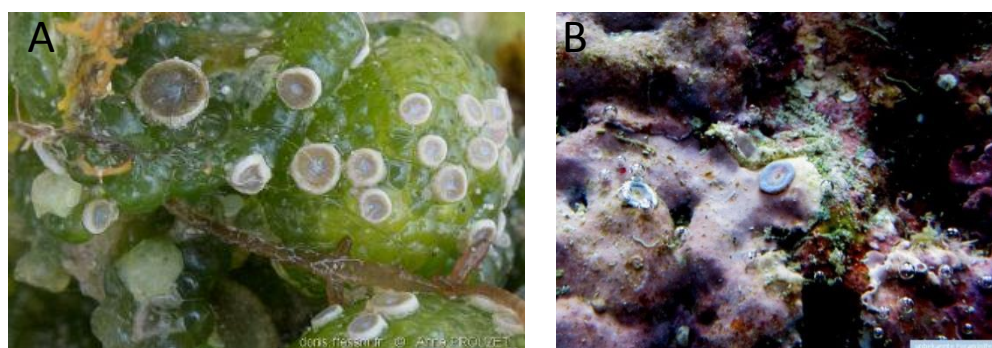


Figure 1: *Marginopora* sp. in its shallow coastal habitat attached to sea-grass (A) and coralline rock (B) substrates.

(Source: doris.ffessm.fr and www.reflex.net)

A very interesting aspect of the biology of foraminifera is the construction of the tests. The tests of foraminifera have varying complex shapes and structures of the walls, patterns, and ornamentation of spaces, canals, plates, pores, piles, beads, papillae etc. (Figure 1). The morphology, form, composition and wall structure of the test is the primary means by which foraminifera are identified and classified (Hemleben, C., 1990; Loeblich, A.R. & Tappan, H., 1984; Reiss, Z., 1958; Tappan, H.N. & Lipps, J.H., 1966; Wood, A., 1949). Foraminifera chambers are modular and are added sequentially during ontogeny (Hansen, H.J., 2002). A type of cyst is constructed by the pseudopodia and cytoplasm is extruded into the cavity organised into an array to determine the shape of the chamber (Be, A.W., Hemleben, C., Anderson, O.R., & Spindler, M., 1979; Hottinger, L., 1978). The biomineralised production of calcium carbonate tests by reef foraminifera has been estimated to contribute 43 million tons of calcium carbonate per year; large symbiotic foraminifera contribute 80% of this production (Langer, M.R., Silk, M.T., & Lipps, J.H., 1997). Many benthic forams greater than 1 mm. and planktonic forams are symbiotic with algae that are hosted in the test (Hallock, P., 2003). In Figure 2 are shown the main morphological features of an adult test of *Marginopora sp.* These features are referred to in the figures presented in the other sections of this thesis.

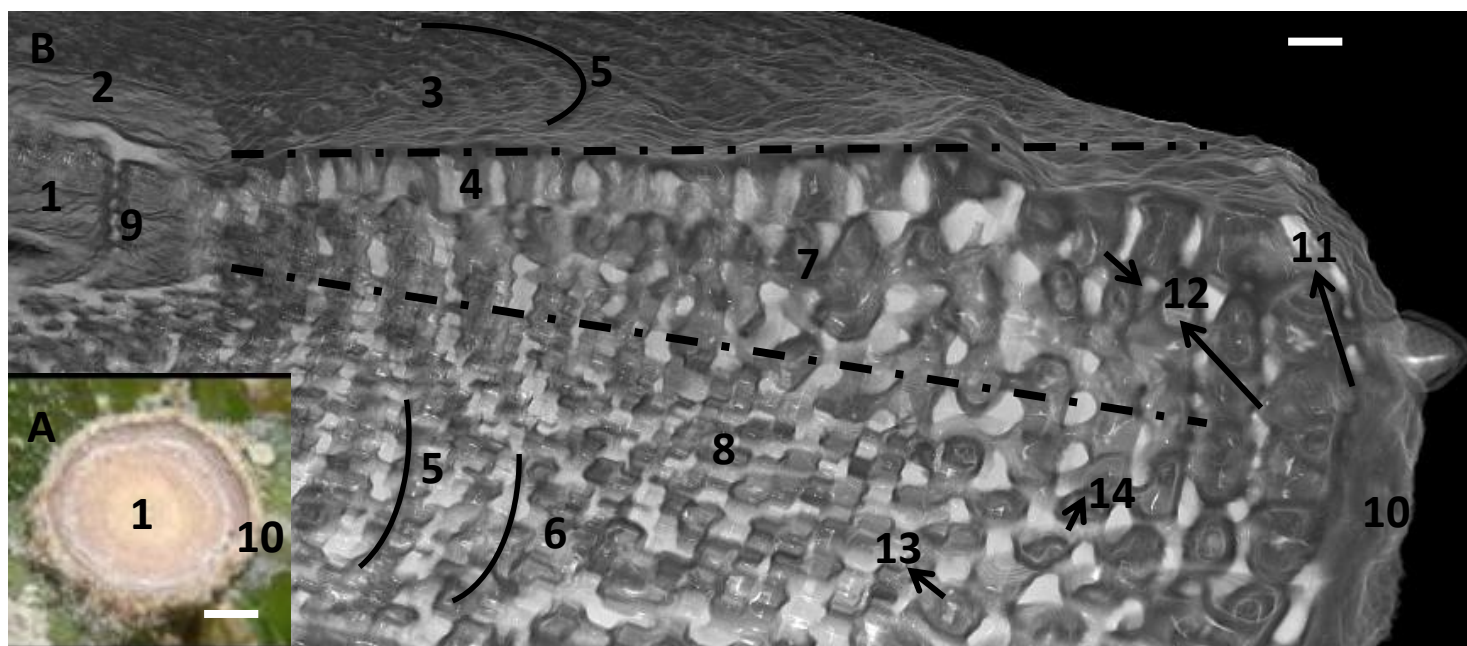


Figure 2: Salient morphological features of a test of *Marginopora sp.*

A: Plan view of the test of *Marginopora sp.* in its habitat. Scale bar 1.5mm. Note that the brownish red colour is of the symbiotic dinoflagellate algae that are hosted by *Marginopora sp.* Also visible are the circularly arranged larger microstructures of the test.
B: A rendering of the discoidal test with sections in the xy and yz plane revealing features of the interior of the test. Scale bar 50µm.

As shown in Figure 2, (1) at the centre of the discoidal test is found the embryonic apparatus consisting of the proloculus and deuteroconch - a cavity separated into two sections by a curved vertical wall (9). The protoplasm of the cell occupies this region. Biomineralised surfaces(2) are

found on both sides of this region. The equatorial surface (3) is covered with polygonal chamberlets (4) that occur in annular (5) rings of chambers that are separated by annular chamber or intercameral walls (6). The chambers (darker) and chamber walls (lighter) are structures that occur alternately and are visible in the transverse section (7) and equatorial section (8) of the discoidal test. The periphery of the test is a wall known as the marginal chord (10) which has marginal pores (11). These holes connect the interior of the test to the external environment. The interior of the test has tubular passages (12) that interconnect chamberlets (13) which are separated by chamberlet walls or septa (14).

Foram tests may be organic and flexible (Hedley, R.H., 1964). Agglutinated tests may be constructed of hard particles such as silica spicules or grains of sediment cemented together (Loeblich, A.R., Tappan H., 1974). Calcareous tests are built of mineralised calcium carbonate. These are classified by the appearance and crystalline structure of the test: porcellaneous, hyaline and microgranular (Hansen, H.J., 2002; Loeblich, A.R., Tappan H., 1974; Wood, A., 1963). Mechanisms of calcification for the two main types of tests, hyaline and porcellaneous or Miliolid, have been described as shown in Figure 3

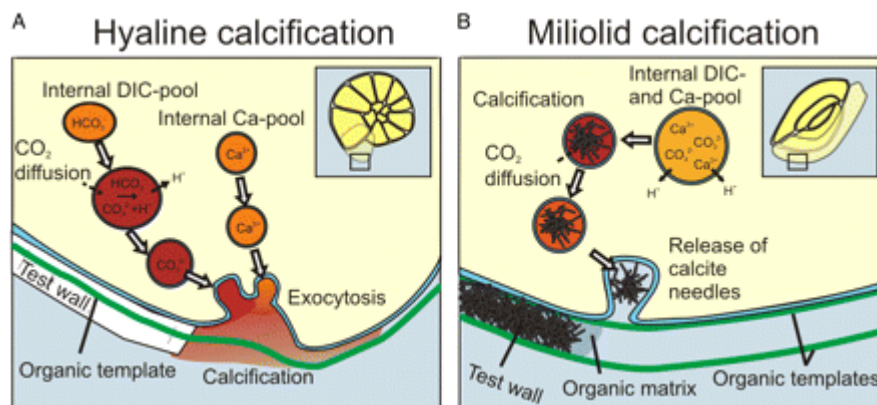


Figure 3: Similarities and differences in foraminiferal calcification pathways.

A: Increased pH in the carbonate pool and possible diffusion of metabolic CO_2 during chamber formation in a generalized hyaline foraminifer. Basic scheme modified from (16). B: Elevation of the pH during calcite precipitation and subsequent decrease during chamber formation in the Miliolid foraminifers.

Reprinted with permission from PNAS (de Nooijer, L.J., Toyofuku, T., & Kitazato, H., 2009).

1.3 Relevance of the Research

The milioline foram studied in this work, *Marginopora sp.*, builds an architecturally-complex discoidal porcellaneous test (Figure 4) of nano-crystalline calcite, organic membranes, cytoplasm, and reticulated microtubules.

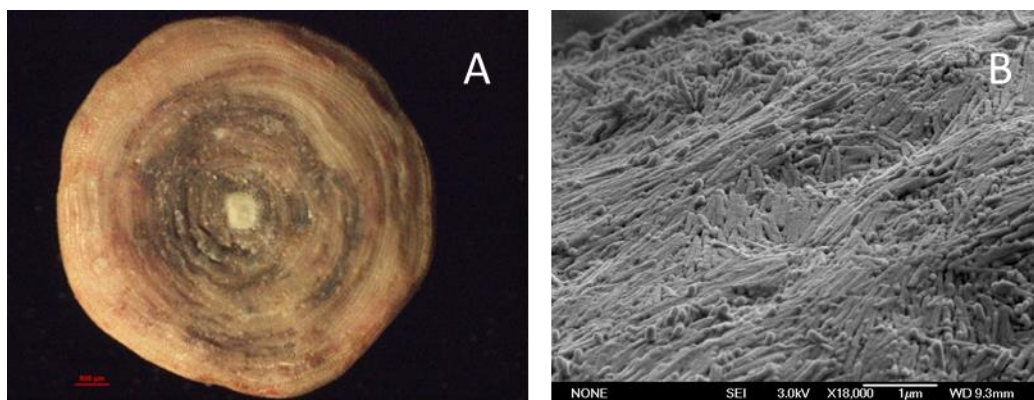


Figure 4 Discoidal test- with translucent surface and crystals of surface walls.

A: Optical image of *Marginopora sp.* showing circular sequential chambers, surface chamberlets (dark areas) packed with symbiont algae; B: SEM micrograph of the surface of *Marginopora sp.*

The protist develops this test through a process of biomineralisation of nanocrystals using ions in seawater. Symbiotic algae and cytoplasm occupy and move within the chambers and chamberlets of the test. Research has contributed towards an understanding of the symbiotic relation, the ecology, the evolution, the taxonomy, the composition, and the construction of the test. However, the functions of the complex architecture of the test have been proposed but not investigated through experiments or models. There are several propositions as to the function of the test structure that include but are not limited to:

- interaction of light in the environment with symbionts and the test (Hallock, P., 1979; Haynes, J., 1965; Hottinger, L., 2006);
- spatial-volume relationships where the void is used for food storage or symbionts (Hallock, P. & Anonymous, 1986; Hottinger, L., 1986);
- mechanical performance in its hydrodynamic environment (Briguglio, A. & Hohenegger, J., 2011b; Hohenegger, J., 2009);
- protection against predation and the physical or chemical environment (Marszalek, D.S., Wright, R.C., & Hay, W.W., 1969a).
- orientation in undisturbed sediments and surface area for respiration (Severin, K.P., 1987)

The structure of the test is composed of many anisotropic elements; this, combined with the complexity of the protist's natural marine environment, pose limitations on the scope of research. The small size of the test and its anisotropy exclude the use of several established experimental techniques. This makes a deeper or holistic analysis very difficult. Ellipsometric

techniques used in measurements of optical properties have been applied recently to thin surfaces of biological structures for the determination of optical properties of organic layers (Arwin, H., 2000). However an ellipsometric determination of optical properties require a planar smooth surface; *Marginopora*'s crystalline test is neither flat nor smooth (Figure 4).

Microprobe-based techniques used in a laboratory setting to determine the optical or mechanical properties of the internal microstructures require that the test is broken or fractured to allow the penetration of microprobes. Such breakages destroy the integrity of the microstructures and the overall architecture and measurements would not be representative. The environment outside the test of *Marginopora sp.* in an aquarium was studied in a laboratory based experimental study to observe the response of the symbionts to a change in the chemical environment (Kohler-Rink, S. & Kuhl, M., 2000). The benthic tropical intertidal environment is a challenging environment to deploy microprobe sensors for continuously measuring optical properties in the microenvironment surrounding the test. The measurement of mechanical properties using materials testing instrumentation, such as universal testing machines, requires the fabrication of small, specialised, expensive jigs. A study of the mechanical properties of an agglutinated foram test, which has completely different structural arrangements to the test of *Marginopora sp.*, was performed using such equipment (Kinoshita, R.K., 2001). *Marginopora*'s test is porous, biconcave, and anisotropic. In another study modelling techniques such as finite element analysis (FEA) using expensive specialised software were limited to the use of a simplified model of the shape of the test, i.e. a solid biconcave isotropic disk (Song, Y., Black, R.G., & Lipps, J.H., 1994). The effects of the internal architecture of the test were not considered in that study. Researchers of foraminifera have not usually been trained in the material sciences or biophysics, and material scientists have not studied the test structure and properties of foraminifera. Such constraints have so far limited the experimental investigation of propositions regarding the functions of the test and its microstructures.

Another important element in understanding the optical, mechanical, hydrodynamic, and diffusion performance of the test is a complete understanding of the three dimensional (3D) architecture of the test and the 3D morphology of the microstructures. The possible functions of the test and its microstructures can be better understood with a complete 3D characterisation of the test. Models and experimental methods can be applied with greater precision to understand the optical, mechanical, hydrodynamic, diffusion, and other functional properties of the materials, microstructure, and architecture of the test. The absence of 3D data, images, and analytical tools creates a significant gap in a fundamental aspect in advancing the understanding of the structure and function of the tests of foraminifera.

An innovative technique was developed by Hottinger to create a cast of the internal microstructure of foram tests (Hottinger, L., 1979). Resin (araldite) is vacuum-injected into the porous microstructure, allowed to harden and the calcitic test is dissolved. The remaining cast provided a precise solid representation of the void spatial structure within the porous test. Despite the creation of a 3D cast or representation, the small sizes of the casts meant that advanced microscopic techniques had to be used to image the casts (Figure 5).

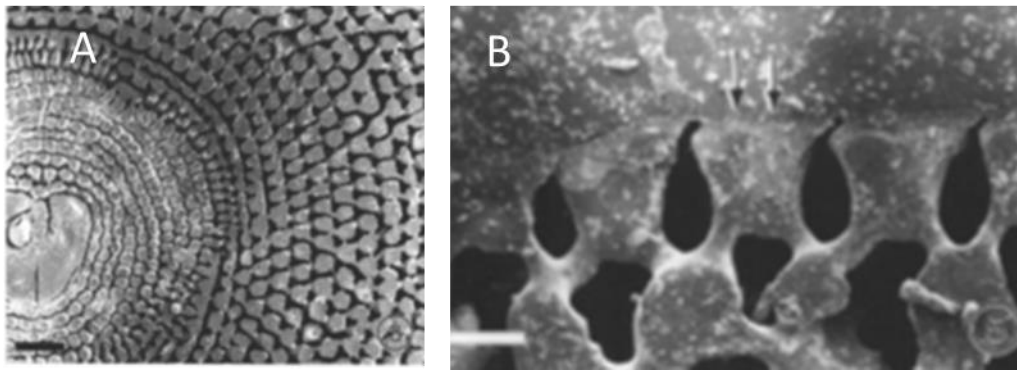


Figure 5 Hottinger cast of test of *Marginopora sp.* viewed with SEM.

Scale bar A: 500 μm . B: 50 μm . Reproduced with permission from ([Lee, J. et al., 1997](#)).

In order to obtain detailed, high resolution images of the interior microstructure, thin sections of the cast or of the test and scanning electron microscopy are used. Optical microscopy can resolve microstructures as small as 2 μm while scanning and transmission electron microscopes resolve up to 2 nm structures. However both of these techniques produce 2D images; morphology is revealed by the imaging of casts but details of crystalline and organic structures are not. This results in an incomplete visualisation and understanding of the microstructure's morphology. Importantly, the spatial and volumetric characteristics of the architecture of the test or its microstructures cannot be adequately obtained only by the analysis of 2D images. A complete understanding of the architecture and microstructures requires a quantitative and qualitative 3D characterisation of the test.

1.4 Research Objectives

The work presented here contributes to the understanding of the 3D architecture of the test through a variety of microscopic techniques coupled with improved 3D imaging. Optical microscopy, electron microscopy, X-ray microcomputed tomography, and 3D image processing and analysis techniques are applied to image the test. By combining coarser and detailed studies using complementary techniques this research aims at determining the internal and external morphology on all scales- from centimetre to nanometre. Rather than examining in great depth one aspect or proposed function, this research aims at creating a complete 3D version of the structure of the test to provide an enhanced basis by which the function(s) of the test can be investigated along several lines of inquiry. Models and virtual experimental methods, i.e. using software and 3D computing environments, can be used with the outputs of this research to investigate the hypotheses of the functions of the microstructures and the test.

The general hypothesis this research addresses is: if the architecture of the test is analysed at multiple scales and dimensions then its structural adaptive value can be inferred through appropriate models.

The objectives of the research were:

- to apply a non-invasive method, X-Ray microcomputed tomography (X-ray MCT), for characterising in 3D the architecture and the microstructures of the test of an extant, large benthic biomineralised foraminifera - *Marginopora sp.*;
- to complement it with 2D electron microscopy to fully characterise the hierarchy of the architecture at different scales of measurement particularly at the nanoscale;
- to analyse the 2D and 3D data sets to create novel holistic visualisations of the structural patterns and architecture of the test through ontogeny; and
- to identify potential applications based upon the patterns and the architecture of the test.

1.5 Structure of this Thesis

Following this introduction, in the second chapter are described the sampling sites for fieldwork, the methods of sampling of *Marginopora sp.* and sample preparation for optical and electron microscopy. The dominant method and equipment used in this research, X-ray MCT, is described in detail. The choice of the software used in the processing of 3D images is explained. Rapid prototyping and 3D printing, a technique used widely in industrial design, is introduced.

The experimental data obtained using X-ray MCT, microscopy observations and analyses are presented in the third chapter in several sections. Each of the sections in the third chapter may be read as stand-alone material; however the common theme is that of the analysis of high resolution electron microscopy and X-ray MCT data to find new information, visualizations and insights about a test that has been well-researched for over the past 50 years.

The sections in the third chapter describe evaluations of the thin-sections of the test by optical microscopy; of the pristine samples by high resolution electron microscopy and by low and high-resolution X-ray microcomputed tomography. An unprecedented observation of the nanocrystalline units is described. 2D images are synthesized in a new model of the structural hierarchy of the test of *Marginopora sp.* but may also be applicable with variations to other orders of foraminifera. The development of the 3D shape and the mineralization of the test is visualized using X-ray MCT data of a series of tests of different ontogenic stages of *Marginopora sp.* The value of 3D visualizations and quantification of morphological features is demonstrated using X-ray MCT data. Statistical analyses are presented to help understand the distribution of porosity in the test. The application of network analysis tools is explored for the first time with foraminifera to evaluate the connected internal voids of chamberlets and intercameral passages. The void space is illustrated in its entirety and visualized in 3D as a network within the test. The X-ray MCT data of the solid crystalline structure are rendered in 3D and analysed to identify a growth and structural pattern which has been shown to have a spatial and mechanical basis in the plant kingdom. The pattern has been observed as an emergent property of self-assembling systems but until now has not been identified in an extant organism belonging to the animal kingdom. Adequate models, a method used in the field of artificial intelligence is used as a framework to propose an explanation of the 2D and 3D architecture and to suggest an integrated

adaptive/function bauplan. These evaluations offer original ways of understanding the architecture and adaptive value of the test of *Marginopora sp.*

In the concluding chapter, the results are summarised. A perspective is created for the potential biomimetic value of the interpretations of the 2D and 3D architecture. Hypotheses and possible lines of investigation for various industrial or design applications are suggested for further research.

CHAPTER 2: Materials and Methods

2.1 Field work and Specimens

Live adult specimens of *Marginopora sp.* were collected by snorkelling and hand picking carefully at low tide from sandy flats (location: Nucumbucco) on the barrier reefs in Laucala Bay, Fiji, in November, 2009 (Figure 6). These specimens were transported in plastic containers to the Laucala campus of the University of the South Pacific. The specimens were placed in an outdoors aquarium filled with aerated seawater. The seawater was retrieved in plastic containers, along with sandy-gravelly sediments that had seagrass attached so as to resemble the conditions at the collection site (Figure 7A). Seawater in the aquarium was partially exchanged daily with filtered seawater from Laucala Bay. After three days a large number of gametes and post embryonic stages of *Marginopora sp.* were able to be seen attached to blades of seagrass. The blades of seagrass were picked carefully. About seven days later several specimens of *Marginopora sp.* ranging from 250 μm to 2.5 cm in diameter were sampled from the aquarium (Figure 7B). In order to retain and preserve the fine organic structures, the blades of seagrass and all of the selected live (Figure 7C) specimens were chemically fixed at Laucala Bay laboratory using 0.4 M gluteraldehyde prepared in a cacodylate buffer pH = 8.0 and 1 μm filtered seawater, according to the procedure (Figure 7D) developed by Anderson et al. (Anderson, O., Allan R., Be W.H., 1978). Samples were stored at 4° C in vials and centrifuge tubes and transported by air to New Zealand.

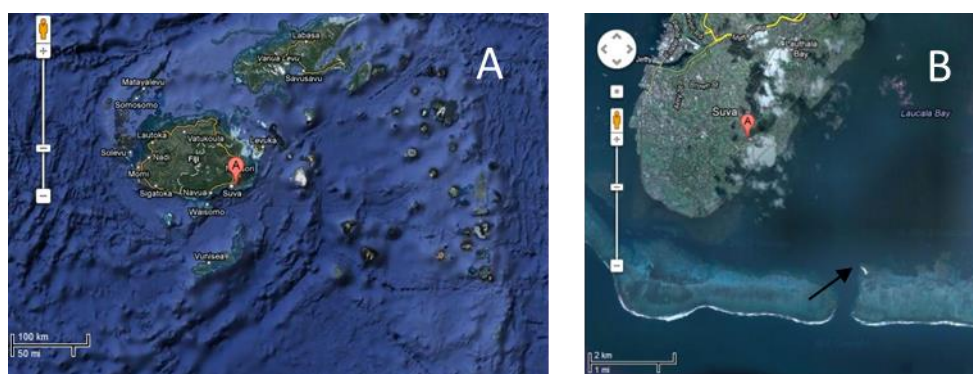


Figure 6 Sampling Locations.

A: Sampling location in the South Pacific ocean, Suva, Viti Levu, Fiji; B: Sampling site (arrow) at sandy formation off the barrier reef (arrow), Laucala Bay, Suva. (Source: Google Maps 2012).

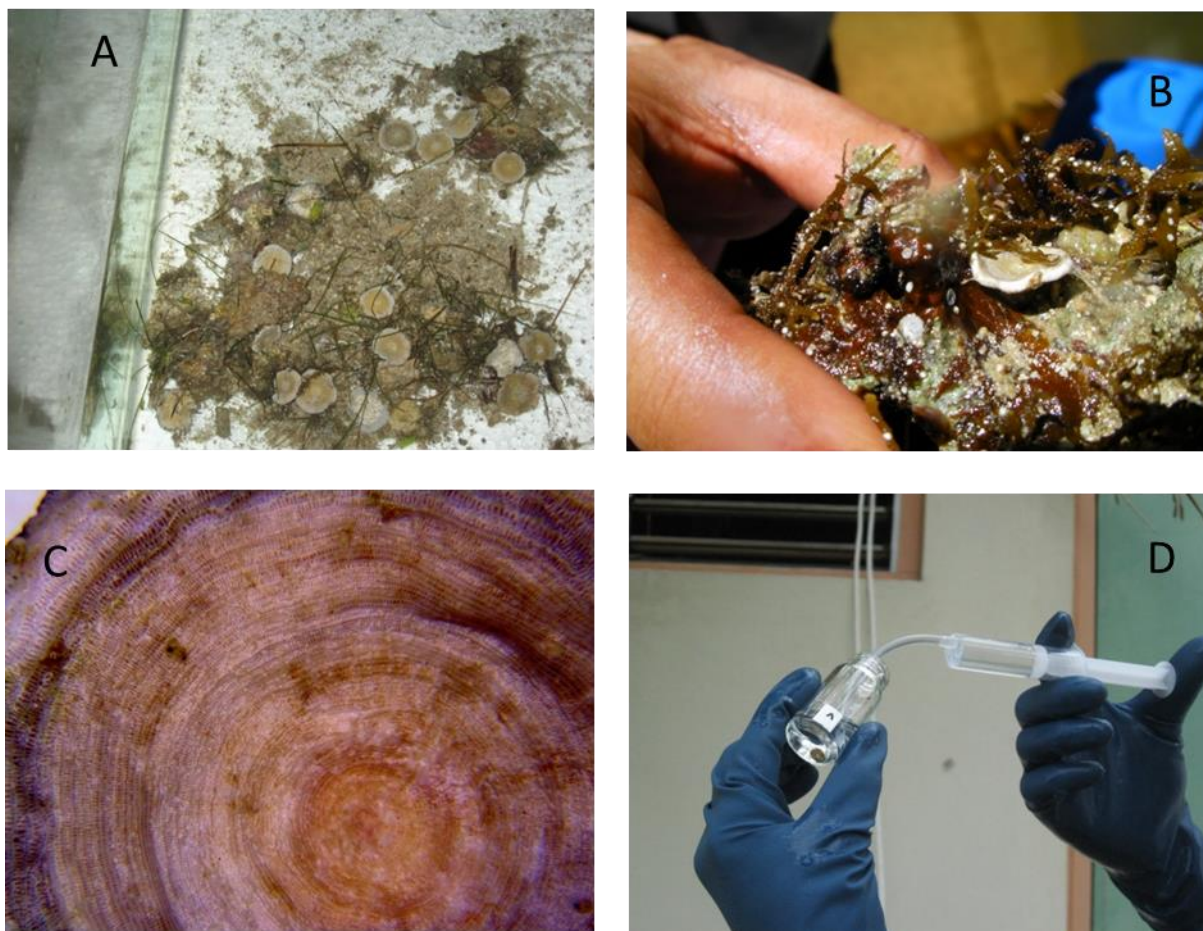


Figure 7 Sampling and fixing in the field.

A: Adult specimens transferred in an aquarium; B: Juvenile and adult specimens of *Marginopora sp.* after 5 days in the aquarium; C: Test of a living adult specimen with cytoplasm (grey) on the surface and endosymbionts (brown-yellow) inside the test as viewed in an optical microscope; D: Rapid injection of the fixative solution; gluteraldehyde around a specimen.

2.2 Instrumental techniques used in the characterization of the test of *Marginopora sp.*

2.2.1 Standard Techniques

2.2.1.1 Thin Sections

Selected specimens of *Marginopora sp.* were dried in a laboratory oven at 50°C for a minimum of six hours. The specimens were then embedded at random orientations in Epotek 301 epoxy using a plastic mould (24.5 mm). Standard petrographic-type thin sections were then prepared by cutting the epoxy blocks with a diamond embedded circular saw, gluing to a glass side and grinding the epoxy block encasing the specimens on a diamond cup-wheel to a thickness of ~80 µm. The glass slides were then lapped on a Logitech LP50 lapping/polishing machine using 9 µm aluminium oxide slurry to a thickness of 40 µm. They were then polished on an ATMRT sapphire 560 polishing machine using diamond suspension (3 & 1 µm), and finally on

colloidal silica, while periodically checking using an optical microscope for thickness, flatness, microstructures, scratches, smoothness and other defects to a practicable final polish.

2.2.1.2 Scanning Electron Microscopy

Selected complete specimens of *Marginopora sp.* ranging in diameter 0.5 mm to 15 mm were post-fixed with osmium tetra-oxide and dehydrated through an ascending graded series of laboratory grade ethanol. After dehydration of one specimen (diameter 10 mm) of *Marginopora sp.*, a sharp tipped punch tool was used to fracture it at its centre. The fracture produced a wedge-shaped section of the specimen. This section, and several of the whole dehydrated specimens, were critical-point dried, mounted with carbon tape on aluminium stubs, and sputter coated with carbon (10 nm-20 nm film thickness) and platinum (10 nm film thickness) in a Quorum Q150T E (U.K.) sputter coater. A Field Emission Scanning Electron Microscope (FESEM) (JEOL-JSM 6500 hot Strosky filament at Victoria University's School of Chemical Physical Sciences) was then used to investigate the samples at 11 keV and 9 μ A in backscatter and SEI modes. Sample preparation and handling for SEM imaging led to the destruction of several specimens.

A FESEM equipped with a Focussed Ion Beam (FIB) milling system (FEI Helios 600 NanoLab Focused Ion Beam system, Nanofabrication laboratory, Australian National University) was used at 3 kV to investigate a single specimen 4 mm in diameter. The non-conducting test was sputter coated with platinum (approximate thickness 10 nm). The FIB allowed precise ultra-milling of the surface of the specimen *in situ* within the chamber of the FESEM in order to reveal and to image at high resolution the cross-sectional surfaces. This method allowed a directional and systematic investigation of the upper surface wall of the discoidal specimen.

2.2.1.3 Transmission Electron Microscopy

Two pristine specimens of *Marginopora sp.* were used to prepare ultra-thin sections by ion beam milling using a Gatan Model 691 precision ion polishing system (Jaeger Research School of Earth Sciences, Australian National University). The thin sections (5 μ m) were epoxy glued on copper grids, the epoxy melted at 120°C and the grids were isolated. The grids were cleaned with laboratory grade acetone and were investigated by transmission electron microscopy (Phillips CM300 at 300 kV). Specimens were also investigated using a JEOL JEM2010-2011 transmission electron microscope operated at 200 kV (School of Chemical Physical Sciences (SCPS), Victoria University of Wellington).

2.2.1.4 Cryo-Scanning Electron Microscopy (Cryo-SEM)

Cryo-SEM is a standard electron microscopy technique that allows for samples to be imaged at high resolution in a hydrated state. Specimens need not be preserved if they are available in their “natural” or pristine state. The stage-wise dehydration of the sample used for high-resolution SEM is not required here. The changes in the fine structure of the specimen induced as a consequence of preservation and dehydration are avoided. A significant advantage of cryo-SEM imaging is that specimens can be fractured in a hydrated state to reveal the internal microstructures.

Juvenile specimens of *Marginopora sp.* were viewed under an optical compound microscope and extracted with plastic tweezers from the surface of a fixed adult specimen that had reproduced. A cryo-SEM Gatan Alto-2500 (Gatan, Inc., Warrendale, PA, USA) unit attached to the JEOL

JSM 6500 FE SEM was used to freeze the specimen as quickly as possible in liquid nitrogen that is under a partial vacuum at -196°C to maintain the morphology of the hydrated specimen; the sample was then vacuum transferred to prevent contamination; the sample was cold fractured at -130°C to expose internal microstructure then followed by sublimation at -100°C for 10 minutes to highlight or identify the solid rather than aqueous structures; the temperature was stabilised to -130°C and then the sample was sputter-coated to allow high resolution surface imaging. Specimens were imaged at an accelerating voltage of 11 kV with a probe current of 10 μA .

2.2.1.5 Energy Dispersive Spectrometry (EDS)

The Jeol EX-23000BU Energy Dispersive X-ray Spectrometry Analyser –EDS– (Thermo-Scientific Co. USA) an add-on to the JEOL JSM 6500 FE SEM operating at an accelerating voltage of 11 keV and a current of 9 μA was used to analyse the percent elemental content of selected specimens. EDS was also performed with transmission electron microscopy (EX-23003BU JED 23000T).

2.2.1.6 Mercury Porosimetry

Mercury porosimetry is a technique for analysing the porosity of small structures. It is widely used in the ceramics, concrete and metallics industries and in materials science laboratories. This method is based on the intrusion of high pressure mercury into the void spaces of the structure. The pressure required to enter the pores is related inversely to the size of the pores. The measurement process destroys the specimens (in this case, the tests). The tests were prepared for porosimetry by immersing the tests in NaOCl for 24 hours to digest the organic fraction and warming the immersed tests to evacuate the pore space. Tests were dried at 60°C for 4 hours, then dried overnight and the dry weights recorded. A Micrometrics Autopore IV instrument, Department of Applied Mathematics, Australian National University, was used to evaluate the porosity of five specimens ranging in size between 3-4 mm in diameter. The instrument is automated and provides a report of several quantitative characteristics associated with the void space of the sample. It provides quantitative data on pore diameter, void surface area and the bulk density of the material. The results obtained with this technique were compared with the results obtained from the X-ray MCT experiments of the evaluation of the porosity of the test of *Marginopora sp.*

2.3 Characterization using X-ray Micro Computed Tomography

2.3.1 Introduction

X-ray Micro Computed Tomography is a non-destructive radiological digital imaging technique based on the use of X-rays and their attenuation as they pass through different materials. The technique does not require special preparation of samples. It provides data that can be processed to image and quantify 3D properties of the material. It is particularly suited to characterizing and quantifying materials with two phases (e.g. solid-void) because of the different attenuating properties of the two phases. The term “micro” is included in the description of this technique because the smallest image (pixel) is in the micrometre range. There are other types of X-ray computed tomography systems (Table 1).

Table 1 X-ray Tomography systems categorised by scale.

CT Scanner type	Scale of observation	Scale of resolution
Conventional	m	mm
High-resolution	dm	100 μm
Ultra-high-resolution	cm	10 μm
Microtomography	mm	μm
Nanotomography	μm	nm

During the past decade X-ray MCT has gained usage in the materials industry- in the study of concrete, ceramics and metallic foams; in geology; in the wood and the foodstuffs industry; and in tissue engineering. It has also been used in research to characterize and analyse biomineralised structures such as teeth and bones. This technique was used to characterize in 3D the crystalline porous test of *Marginopora sp.*, quantify the void spaces of the test, enhance understanding of the organism's ontogeny, determine the inter-relationships of the microstructures of the test, seek new perspectives on the test architecture and to test the applicability of the technique to calcitic biological materials.

The following sections provide:

- an introduction to the principles of X-ray MCT, the components of an X-ray MCT system, artefacts, sample preparation etc.;
- an overview of X-ray MCT in research;
- a description of the equipment used and specific experimental conditions used in this study;
- an outline of image processing methods applied in this study;
- a summary of the rapid prototyping technique - 3D printing used in this study.

Further specifications of equipment or examples of the specific applications of the methods in this study are included in the appendices.

2.3.2 Principles of X-ray Tomography

Tomography (tomos = section, graphein = write (Greek)) is a technique used to image an object section by section and develop a 3D image of the object by applying mathematical algorithms to combine or reconstruct the sections into a whole. This creates a reconstructed view of the internal structure of the object and thereby opens up the possibility of exploring complex 3D structures. Tomograms generally refer to the images of the 2D sections or slices which are comprised of pixels. Volume imaging, comprised of voxels, is produced when tomograms are reconstructed into a 3D image. There are several sources of energy or physical phenomena e.g.

X-rays, seismic waves, radio frequency waves, electrical resistivity, ultrasound waves, sound waves, nuclear magnetic resonance, etc. that can be used to create tomograms.

In X-ray MCT, X-rays are directed at the object of study. A detector captures the attenuated X-rays that pass through the object. X-rays are attenuated or scattered in relation to the atomic number, the density of the material and the length of the path of the X-ray through the material. The actual quantity measured in the recorded pixels is the value of the linear attenuation coefficient which is proportional to the greyness detected in the pixel-image. The linear attenuation coefficient for a homogeneous material and monochromatic source is related to the intensity of absorption of the X-rays by Lambert-Beer's Law:

$$I = I_0 e^{-\mu x}$$

where, I is absorption intensity, I_0 is initial X-ray intensity, μ is linear attenuation coefficient, x is length of the X-ray path through the material or unit thickness (Figure 8). For several units of thickness, the intensity is the sum of the product of the attenuation coefficients and the thickness of each of the units.

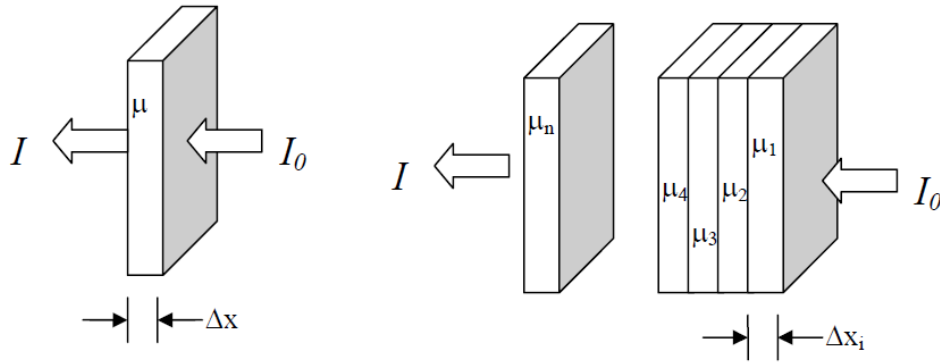


Figure 8 Intensity and attenuation coefficient of X-rays.

Δx is the unit thickness of the material, μ is the attenuation coefficient.

Thus, a distribution curve, histogram or map of the absorption of X-rays by a cross-section of the object can be obtained. This histogram of values of the absorption coefficient is converted to pixels which form an image. A continuous set of distributions of a sequence of a large number of 2D consecutive parallel cross-sections is assembled to create a set of images that represent the absorption of X-rays by the whole 3D object.

The attenuation of the X-rays by the materials of the object casts a shadow of absorption that decreases in intensity in the volume behind the object (Figure 9). The X-rays are directed in a specified pattern, usually rotational, sequentially from many directions as the object is being imaged. A shadow line consisting of attenuated X-rays striking an array of pixels is recorded at each direction.

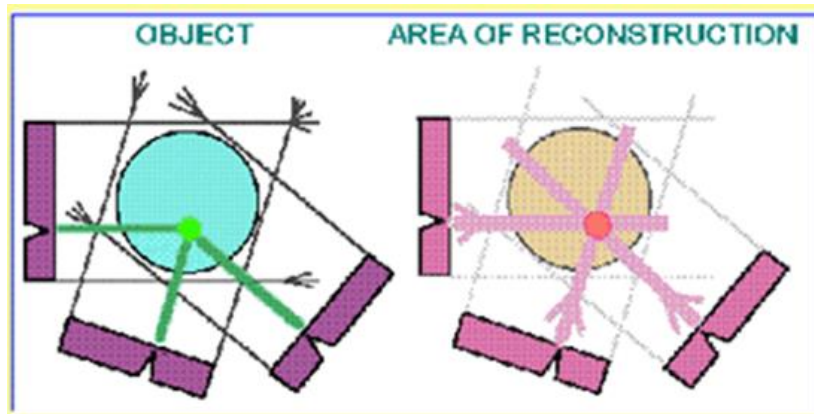


Figure 9 Attenuation of X-rays in the shadow zone of the object.

The detectors (purple) register attenuated X-rays each time, sequentially in different directions as the object (green circle) is rotated so that the shadow lines are formed and define a shadow of the object (red circle). This creates several sequentially produced shadow or absorption lines with a shadow point or absorption point becoming more defined gradually at the intersection as the number of shadow lines increase (Figure 10).

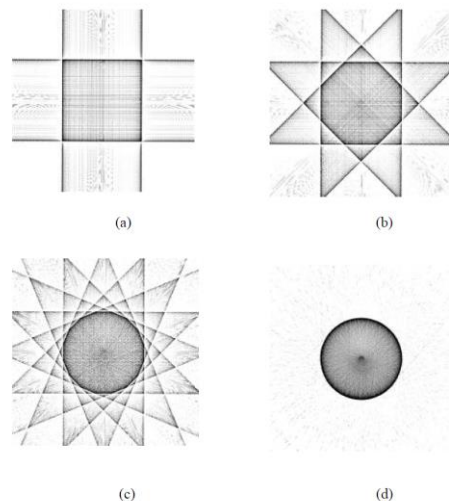


Figure 10 Shadow definition of object points.

As the number of shadow lines increases (Figure 10 (a)(b)(c): number of lines are 4, 6, 16, etc.) in different directions the shadow point becomes sharply defined (d).

Several mathematical methods are used to filter and “backproject” the linear data across the pixel field at the same angle as it was obtained. Essentially, by superimposing the shadow lines the absorption point is defined as the image of one point in one 2D section of the object. By obtaining images of a very large number of points in that section, the cross-sectional image of the object is created (Figure 11).

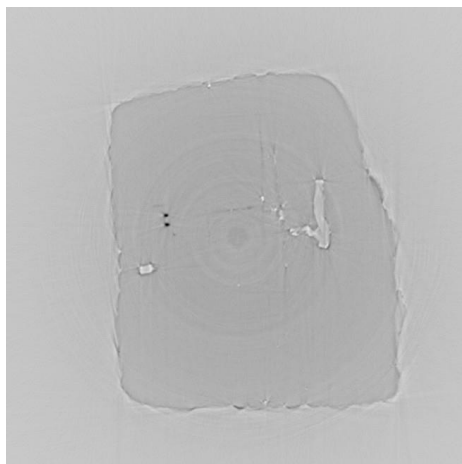


Figure 11 Sample tomogram.

A cross-sectional image or tomogram consists of many absorption points in a cross-section, e.g. tomogram of diamond crystal after backprojection and filtering (source: <http://www.mcs.anl.gov/research/projects/X-ray-cmt/rivers>).

Many sequential cross-sectional images of the entire object are similarly obtained. These are then reconstructed into a 3D image (Figure 12).

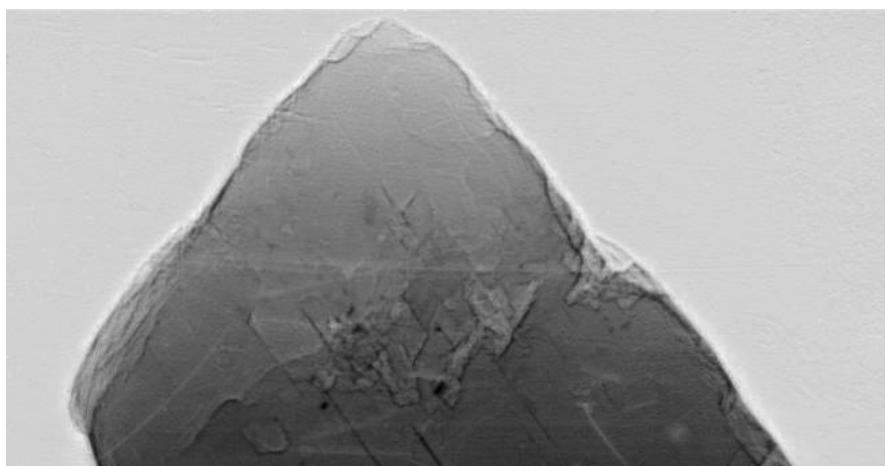


Figure 12 Reconstructed tomogram.

Hundreds of cross sections (tomograms) are reconstructed to form a 3D image of a diamond crystal (source: <http://www.mcs.anl.gov/research/projects/X-ray-cmt/rivers/diamonds.html>).

2.3.3 X-ray MCT Equipment

2.3.3.1 Source

X-ray MCT uses X-ray tubes as the source of the scanning X-rays. There are several characteristics of X-ray tube sources that affect the scanning process. The voltage and the current, the focal spot size, the target material and the energy spectrum or peak energy are important characteristics. The current affects the X-ray intensity which relates to signal-noise ratios and hence the sharpness of the image. The focal spot size is determined by the source to object distance and primarily affects the spatial resolution, although intensity and focal spot size can be manipulated to affect sharpness. Spatial resolution can also be affected by the detector's size and other characteristics. The energy spectrum of the X-rays affects the penetration or

relative attenuation of the X-rays through materials of different density and hence the sensitivity to differentiate materials. Lower energies result in greater sensitivity or contrast but may have more noise as the X-rays are relatively more scattered and vice versa for higher energy X-rays. A range of voltages, currents and spot sizes, source and object (or object and detector) distances are used; selections are primarily based upon the material that is to be scanned, the desired contrast between phases and the desired spatial resolution. The parameters used in this research are shown Tables 2-5.

2.3.3.2 Scanners

The source, an object and the detector are the main elements of the scanning configuration. A view of the object is formed when a set of X-ray attenuation or intensity measurements have been made at the detector for any single position or geometry of the object, source and detector. By changing the angular orientation of the source and detector in subsequent views, many views are obtained. This adds a dimension to the data set. In X-ray MCT usually the sample or object is rotated, whereas in medical CT generally the source and detector is rotated. Several scanning or beam configurations have been developed over the past decade. The main types are: planar fan beam, cone beam and parallel beam configuration (Figure 13).

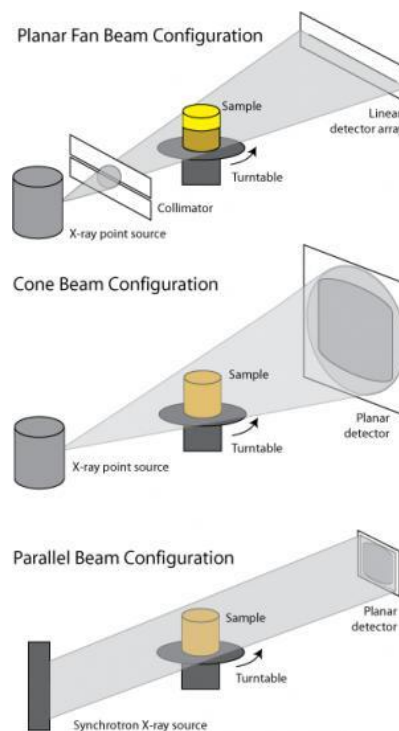


Figure 13 Commonly used X-ray MCT scanner or beam and detector configurations.

(Source: <http://www.sec.carleton.edu>).

Planar configurations result in the object being scanned in one plane only (Figure 14). The source and the detector usually move in one plane at a time across the object and rotate to change the angular orientation. These configurations can be single line or pencil beam with a single detector, and a fan beam with a series of detectors. Line or fan beam configurations which provide single slice views at each rotational position usually result in better quality images. A cone beam configuration uses a thick beam that can encompass the whole or almost the entire

object and uses a single planar detector. Cone beam configurations are able to scan the object faster because multiple views can be obtained in any one rotational position. These require higher computational processing capacities. Some distortion is also likely in the regions away from the central section or slice of the cone. But the fast acquisition rate means that more data can be acquired at each rotational position; thus the signal to noise ratio is higher.

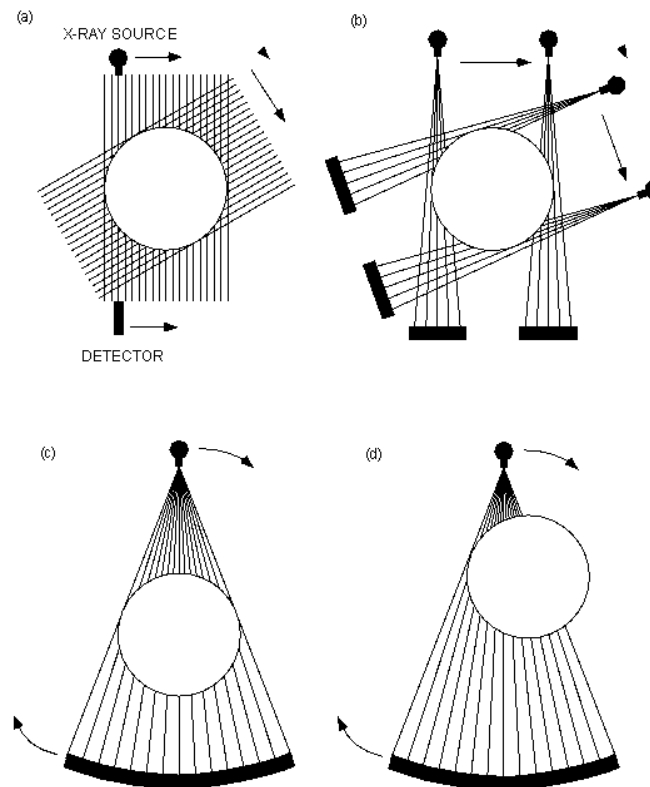


Figure 14 Differences in scans of planar configurations: (a) single beam; (b) fan beam; (c) cone beam; (d) cone beam with an offset.

(Source: <http://www.ctlab.geo.utexas.edu>).

Parallel beam configurations are not used in X-ray MCT but are most often used in synchrotron-based tomography. Spiral or heliacal configurations are gaining usage in X-ray MCT. The sample table is simultaneously rotated and its elevation is increased. This configuration reduces the distortions that are often seen in cone beam based configurations.

For each configuration a separate algorithm is used for processing and reconstructing the data. For cone beam configuration an algorithm that is derived from the equations that are the mathematical basis for the algorithm used in the fan beam configuration are used. In this research the reconstruction was performed using modified parallel Feldkamp algorithms (Sakellariou, Arthur et al., 2004).

2.3.3.3 Detectors

An X-ray MCT system uses detectors that count the scintillations or flashes of light emitted when X-rays enter the detector material. Detector resolution depends upon the type of materials, the number (how much data are gathered i.e. the rate of collection and the resolution) or size of the elements in the detector (how much of the object is viewed in one reading of intensity), and the efficiency in detecting the X-ray energy spectrum (high energy X-rays will

penetrate material more than low energy X-rays; how the detector responds to each energy level aids in the interpretation of how the material of the object scanned has attenuated the X-rays at a particular energy level).

The scintillator array is connected to a photodiode array often using fibre optic tapers. The photodiode array may be connected to a phosphor screen to produce an X-ray image. This image is converted by a CCD video camera (e.g. 1024×1024) to digital data, i.e. scan lines converted to 1024×1024 pixels.

2.3.3.4 Sample Preparation

Sample preparation in X-ray MCT is limited to assembling a cylindrical sample, e.g. a core of a rock or metallic foam, or packing the sample in a cylindrical shaped container filled with a material that does not attenuate X-rays. The field of view is cylindrical, i.e. a stack of circular slices, so this geometry best fits the scanning configuration. The sample is limited in size to the field of view and should not move (vibrate, displace) during the scan independently of the rotating sample table. Contrast between solid and void phases is increased, if necessary, by wetting fluids. In this research sample preparation was varied with different instruments; it is described in Section 2.3.6.

2.3.3.5 Calibration

Several steps are required for calibration of the X-ray MCT equipment prior to scanning an object. Calibrations that relate to exposure calibrations based on variations in the X-ray detector are known as offset and gain. The offset correction relates to the signal received at the detector with the X-ray source switched off (also known as dark current); the gain is the signal or flat field image received with the X-rays on and no object impairs the field of view. These calibrations and other corrections are necessary to avoid ring artefacts or intensity artefacts, which are described below. During a scan, i.e. during the acquisition of several projections, variations in the X-ray source output occur. Exposure corrections are applied to rectify these variations.

Another calibration is sometimes applied by obtaining signals of X-rays passing through a pin or wedge of material with similar attenuation characteristics, i.e. the same material composition, as the specimen. This is used again to minimize artefacts present in the collected data.

2.3.3.6 Data Collection and Reconstruction

The X-ray projections are collected by rotating the object continuously through 360° at incremental angles. Each angular increment provides one projection view. The number of projections can range from 180 to 3600 or more. The resultant raw data are called a sinogram. The raw data are reconstructed using a mathematical procedure known as the filtered backprojection algorithm. There are several types of backprojection algorithms- Feldkamp, Laks, Shepp-Logan etc. used in industrial and medical CT. Reconstruction results in changing the raw data to a CT numerical value or a grey scale value that is exported in a file by the computer system, usually in a 16 bit system. Different scales can be used in the assignment of numerical values to a range of grey scale values. Air is -1000 and water is 0 in the Hounsfield Units (HU) scale. In industrial X-ray MCT air has a value of 0 and water 1000 and aluminium 2700. The use of the scales depends upon the application, i.e. the material of interest, so as to allow positive values to much denser materials such as bone, rock or metals compared to air, water or tissue.

Practical considerations such as the variations in the experimental conditions (the X-ray spectrum, voltage, etc.), the variations in density or composition within specimens and the wide range of densities and compositions of materials call for the use of calibration scales that are peculiar to the experiment rather than predefined scales based upon arbitrary high and low values of greyness. Often, the highest attenuation value and the lowest value can be used as the high and low values of the scale and the edge of a phase such as the solid boundary of the specimen and air is assigned an average of the two values.

2.3.3.7 Artefacts

Variations in X-rays at the source and variations in the detector can produce different artefacts in X-ray MCT images. Beam hardening is an effect of an increase in the average energy of the X-rays passing through a material by the attenuation of lower energy X-rays. Ring artefacts are caused by variations in the response of detector elements to the X-rays owing to changes in temperature or other experimental conditions (Figure 15). The former artefact is visible as a bright circle around or brightening of the peripheral regions of the image (Figure 16). This latter artefact manifests itself as concentric rings centred on the specimen. Other artefacts such as blurring or streaks can be introduced by the specimen's movement during scanning, by beam hardening, and by partial volume effects. A volume may consist of materials of different densities, e.g. part of the volume (a voxel or a set of voxels) may be comprised of the attenuation coefficients that represents the density of bone and in part of cartilage, or of mineral and in part of pore. The software tends to average the densities and the image is blurred. Although beam hardening is more difficult to resolve these artefacts are generally tackled by the use of filters or wedges or by software based corrections applied before reconstruction of the sinograms (raw data lines).

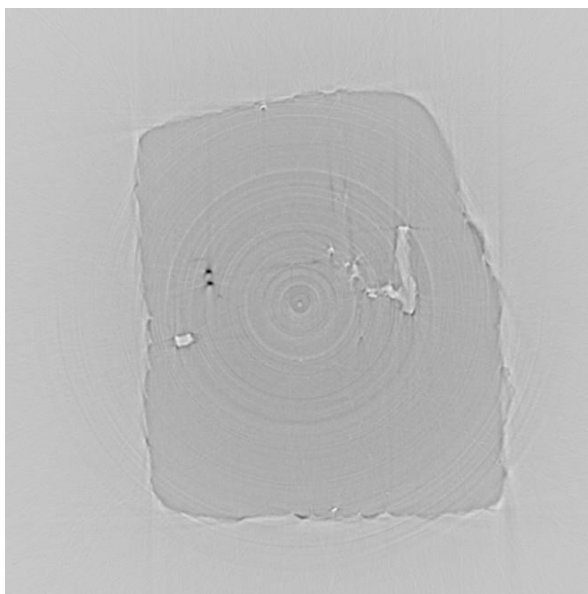


Figure 15 Ring artefact: concentric rings centred at the approximate centre of the cross-section.

(source: <http://www.mcs.anl.gov/research/projects/X-ray-cmt/rivers/diamonds.html>).

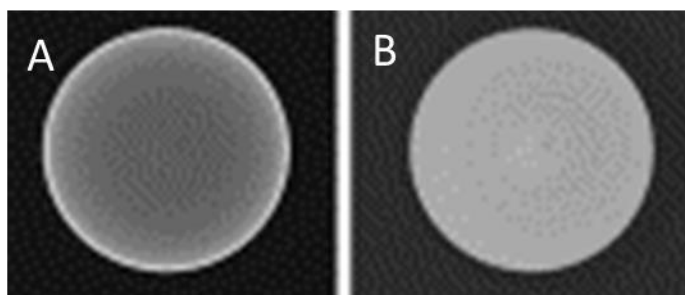


Figure 16 Beam hardening artefact.

X-ray MCT scan of a copper cylinder showing (A) beam hardening and streak artefact and after the artefact has been removed (B) by the application of an inverse algorithm (Source: Roche, R.C. et. al. 2010).

2.3.3.8 Size and Resolution

X-ray MCT systems provide spatial resolution in tens of micrometres but the size of the sample imaged is generally limited to between a millimetre and 30 centimetres. The size of the sample is usually limited by the size of the sample table, the thickness of the specimen and the source to object-detector distances. When the source and detector are at a fixed distance, the magnification is a function of the source to object distance; minimizing the distance leads to a higher magnification. The source and the detector can both contribute to noise; X-ray scattering and attenuation and the detector's electronics add noise to the signal. These can be minimized by increasing the intensity of the X-rays. The most important resolution of features or differentiating of phases and features is based on the attenuation of the X-rays by different densities of materials. The larger the difference in densities between phases or materials the higher is the possible contrast. Thus, resolution can generally be optimized by manipulating a set of scanning conditions based on the specimen's material composition, size and the features of interest.

2.3.4 X-ray MCT Application in Research

CT's earliest applications were in 1972 in medical clinical practice as an innovative technique that used mathematics to convert X-ray images into digital images. However the first X-ray *microcomputed* tomography setup was introduced in 1982 to visualize the shell of the snail *Biomphalaria glabrata* (Elliott, J.C. & Dover, S.D., 1982). Biophysical and bioengineering researchers at the Mayo Clinic, U.S.A., led the use and adaptation of this “multi-scientific principles” based technique in science X-ray MCT (Robb, R.A., 1982). Technology was improved significantly with the introduction of the cone beam algorithm and its successful demonstration subsequently as a method that can be used *in vitro* to assess the architecture of bone (Feldkamp, L., Davis, L., & Kress, J., 1984; Feldkamp, L.A., Goldstein, S.A., Parfitt, M.A., Jesion, G., & Kleerekoper, M., 1989). The technique allowed investigations of the internal structures of developments in micro-electronics such as transistors and semiconductors (Su, X. et al., 2002). An early interesting non-medical but cross-disciplinary use of MCT was the study of earthworm burrow networks. The effort was motivated by the need to visualize the internal morphology of the burrows without destroying the soil sample and provide the capacity to reconstruct the network at a larger scale (Joschko, M. et al., 1991). In a more recent study the 3D burrow networks of two species of earthworms were compared and contrasted using X-ray MCT to differentiate the size, distribution and sinuosity in artificial cores of soil (Capowiez, Y., Pierret,

A., & Moran, C., 2003). This research developed specific algorithms based on granulometry to differentiate between burrows made by different species of earthworms introduced together or separately into the soil cores.

X-ray tomography was rapidly adopted by researchers investigating the microstructures of bone and teeth. The concentration of mineral, an important indicator of bone quality in cortical bone, the porous structure of cancellous or trabecular bone, and the changes in mineral in enamel of teeth during demineralisation and remineralisation were studied most frequently with X-ray MCT (Li, H., Xu, Z.H., & Li, X., 2013). A very large body of literature associated with X-ray MCT developed in this field of biophysics and medical imaging. The increase in research studies and the advancement of the use of this technique in biomedical research are described in several reviews of the literature, of trends and developments (Addadi, L. & Weiner, S., 1997; Bassett, G.A., Menter, J.W., & Pashley, D.W., 1958; Folk, R.L. & Leo Lynch, F., 2001; Lee, S.W. et al., 2011). Muller's review particularly noted the role of X-ray MCT in understanding in 3D the hierarchical structure of bone at different scales of measurement and in relating these to bone failure at different hierarchies. X-ray MCT's 3D scaled imaging has allowed biomechanical studies of bone and tooth to advance rapidly; mechanical fracture, displacement, elasticity, and stress induced growth or failure has been modelled using finite element modelling and visualized *in vitro* experiments while imaging with X-ray MCT (Sandino, C., Planell, J.A., & Lacroix, D., 2008; Tajima, K. et al., 2009; Ulrich, D., Hildebrand, T., Van Rietbergen, B., Muller, R., & Rueggsegger, P., 1997). The application of these software based modelling techniques have been combined with solid models to create visualizations which provide new insights of the architecture of bone (Borah, B., Gross, G. J., Dufresne T. E., Smith T. S., Cockman M. D., Chmielewski P.A., Sod E. W., 2001).

Studies of scaffolds, which are templates that allow bone cells to attach and guide new growth, to bone tissue require precise 3D measurements of scaffold architecture. X-ray MCT based image analysis has facilitated the accurate measurement of properties particularly 3D measures such as pore size, distribution, thickness of struts, that are important in the evaluation of bone growth into and onto the surface of the scaffold (van Lenthe, G.H. et al., 2007). Jones et al. used the X-ray MCT technique and 3D measures in their research to present an important finding: scaffold pore sizes and topology were correlated to the in-growth of bone but that different designs of scaffolds were not important (Jones, A.C. et al., 2007). While a large body of literature has accumulated that describes studies of scaffold-bone interaction and the use of X-ray MCT, it is noteworthy that the quantitative results of properties obtained by the image analysis of bone and scaffold structures are well-matched with the results obtained by the use of other techniques such as electron microscopy, physical measurements and experimental tests (Alberich-Bayarri, A. et al., 2009; Ho, S.T. & Hutmacher, D.W., 2006).

The internal structure of other biological crystalline porous materials such as coral, particularly its homogeneity and porosity, has also been visualized and quantified using X-ray MCT to evaluate its suitability and use as clinical implant material in bone reconstruction. The visualizations and the quantitative measurements of porosity and pore size distribution allowed an understanding of different (homogeneous vs. disordered) internal structures of two corals, *Porites sp.* and *Goniopora sp.*, and showed uni vs. bimodal pore size distributions in these coral (Knackstedt, M.A., Arns, C.H., Senden, T.J., & Gross, K., 2006). In the study of coralline internal structure Roche et al.

noted in their study of *Acropora p.* at the Great Barrier Reef's King Reef that the X-ray MCT based technique offered the advantages of non-invasiveness, non-destructiveness, "a more thorough assessment of biomaterial properties" and the capacity to process a varied sample morphology over traditional techniques and offered comparable results (Nürnberg, D., Bijma, J., & Hemleben, C., 1996). These and numerous other studies of the structure and properties of biological materials report the use of X-ray MCT data and visualizations in the analyses of primarily two-phases of materials i.e. crystalline (usually calcium or calcium carbonate based material) and void space, or scaffold and void space.

Invertebrates such as corals, molluscs, echinoderms that biomineralise their skeletal structures have two dominant phases of materials- mineral and organic. X-ray MCT's major advantages as a technique for undertaking studies of the changes in biomineralised form and internal microstructures can be applied to such studies of the ontogenic stages of invertebrates- extant and fossil.

The growth and change in 3D in form and internal structure of biomineralised organisms is an area of research in which X-ray MCT has also been used to investigate the microstructure of biological materials that have mineral phases which are not calcium carbonate based. X-ray MCT has been used to study the structural and compositional properties in 3D of the spines and plates of the armour of field-caught marine *G. aculeatus*, a three-spine stickleback fish. In their study Song et al. used the 3D images of the microstructures and their chemical compositions to assess the mechanical function of the microstructures and their contribution to the survival of the species (Song, J. et al., 2010). During the decade 1998 to 2007 as catalogued by Medline and Compendex, the number of published studies of the use of X-ray MCT increased eightfold (Stock, S.R., 2009). Approximately one-third of the publications were non-biological while the remainder were largely medical topics-bone, implants, scaffolds, craniofacial and oral, heart, vessels, lung, and techniques- in descending frequency. In 2008, more than 400 publications reportedly used this technique. This increased use has continued during the past few years as the number of equipment manufacturers, resolution achieved by improved technology, applications in diverse research fields and laboratories has risen rapidly.

Geological studies especially of sedimentary rocks also report the use of X-ray MCT to better define fractures and fine interbeds in sediment cores. Applications of X-ray MCT in studies of sediment cores particularly in petrology and palaeontology and in rock materials research are found in detailed reviews of literature, especially of research conducted at the CT centre in Austin, Texas (Carlson, W.D., Rowe, T., Ketcham, R.A., & Colbert, M.W., 2003; Cnudde, V. et al., 2006; Debenay, J.P., Guillou, J.J., & Lesourd, M., 1996). Recently, petrographic studies of sandstone, the limitations of sample size, its relationship to spatial resolution sufficient to resolve the internal structure of rock and new software developed to analyse in 3D the images were reported by (Cnudde, V. et al.) Such analyses, based on X-ray MCT data of rock and strata, and their widespread use by the petroleum exploration industry have led to the development of a technology of commercial value in the petroleum exploration industry – a rapid analysis system for classifying sedimentary rocks (Wood, R., Curtis Andrew, Kayser Andreas, 2009).

The determination or analysis of rock porosity using X-ray MCT data is performed using an image processing technique called segmentation. Segmentation follows a process called

thresholding (see section 2.3.6.4). Because different results can emerge when the techniques of thresholding and segmentation may be applied to the same data by different users, uncertainties associated with the repeatability of the results of segmentation are often minimized by comparing the results with conventional methods of measuring porosity. Different data processing methods are also being developed to minimize such uncertainties. A “grey level method” considers the CT image as a surface and integrates it with the image histogram using algorithmic operations to obtain an estimated value of the porosity. Then a porosity distribution is developed which can reflect the properties of the rock. The results obtained by using this method have compared closely with a conventional method for measuring porosity (Taud, H., Martinez-Angeles, R., Parrot, J.F., & Hernandez-Escobedo, L., 2005).

2.3.5 X-ray MCT and Foraminifera Research

Foraminifera, along with corals, molluscs and gastropods, are important in the study of biomineralisation- the biological formation of crystals and structures- and much research has been done on understanding the biochemical processes involved. Research has been conducted using electron microscopy to aid in understanding the crystalline ultrastructure of some foraminifers because the use of different crystalline ultrastructures of the walls of the tests was used as an important basis for the identification and classification of foraminifera. The use of X-rays to understand the architecture of the tests of foraminifera has been fairly limited. An intensive study of 100,000 biometric characteristics of a large symbiotic foraminifer *Operculina ammonoides* was carried out by using computers and digitized X-rays to view in axial and equatorial planes separately and quantify the internal morphology. This study made an effort to link the revealed morphology with growth processes and the construction of the test-chamber formation, photosynthesis and calcification (Pechoux, M.J., 1995).

The Hottinger technique by which a cast of the test is made by injecting and hardening resin, followed by dissolving the calcitic test, sectioning the cast and imaging by electron microscopy has been the standard practice for over 25 years in the study of the architecture of the foraminiferal test. The electron micrographs permit 2D high resolution visualization of the internal morphology of the test. However X-ray MCT allows visualization in 3D, unlimited instant virtual sectioning, visualization of microstructures from any perspective, and detailed computerized quantification of many geometric properties including volumetric properties. Additionally, once the specimen has been scanned and the image reconstructed, it allows the user many advantages that digital data offer: storage, cataloguing, transmission, manipulation, comparison, rapid computation, animation, internal flythrough and numerous analyses using different software tools.

The development of a high resolution X-ray MCT at the University of Ghent allowed features as small as 1-5 μm to be resolved. The first application of this technique to view the internal structure of foraminiferal tests was the study of *Pseudonvigerina* sp. a fossilized foraminifera (Speijer, R.P. et al., 2008). Test chamber growth – using equivalent radius and volumes was quantified based upon X-ray MCT data. The authors suggested that the technique would prove useful and “open up a new era” in evolutionary research, morphometrics and paleoceanographic reconstructions.

Leading palaeontologists and ecomorphologists in Europe adopted the leading researchers' suggestions in a X-ray MCT study that compared the volumetric relationships of tests of two large nummulitic foraminifera (Briguglio, A., Metscher, B., & Hohenegger, J., 2011). *Operculina ammoinides*, the species earlier studied extensively by Pecheux with the use of X-rays was also studied in this research. This research advanced the application of the technique to foraminiferal test measurements by correlating linear measures that were traditionally used in palaeontology, paleogeography and ecology to estimate 3D values with actual 3D measurements based upon volumetric data. Microstructural quantities such as chamber area, chamber volume and septal (wall) distance were correlated with the 3D measurements; the chamber area in an equatorial section was shown to correlate with chamber volume. These microstructures are influenced by environmental conditions such as light, depth etc. and are important in understanding the phylogeny and distribution of foraminifera.

Briguglio et al. employed commercially available X-ray MCT equipment (X-Radia) and software tools that are also used in this research, while Speijer et al. used equipment developed at the University of Ghent. Both studies showed that chamber volume increased exponentially with growth of the test. Briguglio et al. also showed that chamber area and volume both grew at similar rates for most of the whorls (i.e. a growth cycle) in a test. They assert that the equatorial chamber area is a characteristic that should be used for studying growth or ontogeny in large foraminifera. Also the research suggests that the dimension (1D) of the proloculus or central embryonic area- a traditional feature used in recognising phylogenetic trends- is representative of sphericity (3D) for the 2 specimens. Importantly, this study showed that the measurements of thin-sections (2D) would lead to concluding that the chamber size of the test of one species is larger than the other, but the volumetric measurements (3D) showed that they were very similar. The differences in 3D shape and differences in sequentially added chamber sizes were not accounted for in 2D measurements. Although the authors note that the procedures are time consuming and laborious, the 3D data were used to calculate porosity, microporosity, and wall thickness to estimate the density of the test. These quantities are important in estimating sediment transport and in paleoceanographic reconstructions.

These very recent studies tested and demonstrated the applicability of the X-ray MCT technique to the identification, interpretation and quantification of morphometric features of the foraminiferal test- fossilized and recent. The studies did not validate the quantitative results for porosity, density, total surface area etc. by using other analytical experimental techniques nor did they compare the details of the microstructures with the results obtained with other high resolution microscopic techniques. Neither of the studies employed more than one type of X-Ray MCT hardware nor used the same X-ray MCT experimental conditions. Both studies stated the limitation imposed by the availability of X-Ray MCT equipment or the required scan-time on performing experiments with sample sizes that are larger than one or two specimens and the large computational resources necessary for the subsequent image processing. In both, the raw data were reconstructed using the same algorithm. Paleobiological and biometric themes dominate in the applications of X-ray MCT in the research of foraminifera. Nevertheless, these studies paved the way for using X-ray MCT as a new imaging technique to investigate further the architecture of a large foraminiferal test. As researchers refine the application of X-ray MCT to the tests of foraminifera new 3D structural information is revealed: e.g. two layers of equatorial

chambers rather than the known single layer were found in the test of *Cyclochypus carpenteri*, a large deep-water benthic foraminifera (Fabienke, W., Briguglio, A., & Hohenegger, J., 2012).

2.3.6 Procedure and Experiments: X-ray MCT

In this section is described the procedure, equipment and conditions used in the experiments with X-ray MCT for characterising in 3D the test of *Marginopora sp.*

The size of the specimen, the size of the microstructures that need to be resolved, the magnification, the desired spatial resolution, the type of geometry used for scanning, the time required for imaging-scans, the size of the resulting data set, and the related costs etc. are all factors and possible constraints in the use of X-Ray-MCT for imaging (Stock, S.R., 2008). In this study, a lower resolution and high resolution X-ray MCT scanner were used to facilitate the processing of several specimens of different sizes of the foraminifera *Marginopora sp.* The data sets obtained could be processed with a relative economy of equipment, hardware, software, computing power and scanning machine time. Except for the specimens labelled M_young, M_old, and Foram1, 2, specimens were scanned using a low resolution scanner. Scans were conducted at room temperature.

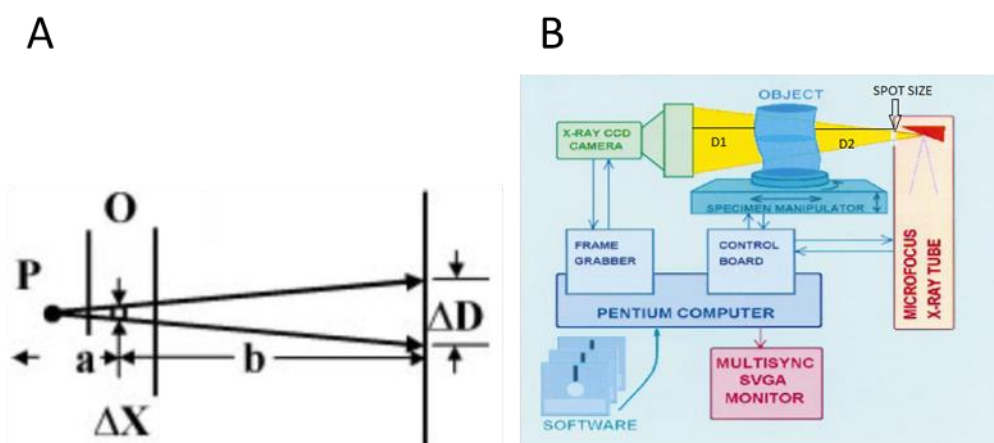


Figure 17 Schematics of generic configuration for lab or desktop X-ray MCT.

(Adapted from Sasov et al., 1998 and Stock, S.R., 1999).

In Figure 17A, the magnification of object O of width ΔX at distance a from source P and distance b from detector D is the number of pixels represented by ΔD . The general schematic of the equipment used is presented in Figure 17B; D1 is distance of specimen from source a, and D2 is the distance of specimen from detector corresponding with a and b respectively of Figure 17A.

2.3.6.1 Low Resolution Scanning

Comscan ScanXmate L080, a low resolution X-Ray MCT was used to scan the specimens at the Tohoku Museum, Japan. The L080 employs direct-projection and cone beam configurations. Spatial resolution depends on the X-ray spot size ($5\ \mu\text{m}$), the signal sampling pitch, which depends on the detector interval size ($100\ \mu\text{m}$) and the geometric magnification factor, which depends on the distance, D2, of the specimen from the detector (Figure 16A). Specimens were fixed using tragacant gum on the sample turntable and scanned in a dry state. Specimens were

placed close to the X-ray tube source to enable higher resolution scanning. D1 which is the distance of the specimen from the source, was less than 2 mm to achieve maximum resolution. The scanning of each specimen required approximately 40 minutes. Hence several different specimen sizes were scanned using this lower resolution scanner. The magnification factor was changed for each specimen by varying D1 because the specimen size changed. The scanning experimental conditions are presented in Table 2.

Table 2 Low resolution X-ray MCT conditions

Manufacturer	Comscan Techno
	ScanxmateL080
Configuration	Direct projection cone beam
Image size	1032 × 1012
Source	80 kV 100 μ A
Source Distance	2 mm
Detector distance	Variable
Rotation	360°
Voxel size	Range 3.097 - 35.85 μ m
Optical magnification	Range 2.84 × - 27 ×
Specimens	Msmall, smallest, medium, large, M_Mlargest

The set of 2D images of cross-sections of the specimen were obtained and reconstructed with the Feldkamp-type algorithm using "ConeCTexpress" software (Feldkamp, L. et al., 1984). "ConeCTexpress" is a customized software package developed for use with ComscanTechno X-ray MCT equipment. Four types of data files were produced with different file extensions: .brt file with brightness data or gain calibration, .drk file with darkness data or offset calibration, .row file with the transmission or attenuation image file, .sxm file that states the scanning conditions. The "ConeCTexpress" software reads the four output files to reconstruct cross-section images and was used to export cross-section image-sets in 16bit tiff, 8bit tiff and DICOM format. These files were processed further using the software and image processing techniques described in Section 2.3.6.4 "Image Processing".

2.3.6.2 High Resolution Scanning

2.3.6.2.1 A.N.U.

A X-ray MCT instrument that was developed and built at the Australian National University was used to scan and image at high resolution selected specimens of *Marginopora sp.* It operates with a cone beam geometry (Sakellariou, A., Sawkins, T., Senden, T., & Limaye, A., 2004). Samples were placed in an alumina foil cylinder packed with spherical carbon filler material that is X-ray

transparent and imaged using the X-ray source operating at 80 kV and with a beam current of 100 μ A. In order to minimize the beam hardening artefacts that can occur during scanning, a 1 mm aluminium filter was positioned in front of the sample cylinder (Sakellariou, A. et al., 2004). A set of 2048 two-dimensional (2D) radiograph projections were acquired at different rotation angles covering the complete 360° rotation to produce the resulting 2048³ voxel tomograms. Each tomogram slice was approximately 3 μ m thick. The 2D radiographs were first pre-processed to minimise and then reconstructed with a modified parallel Feldkamp algorithm to generate a tomogram consisting of voxels (Feldkamp, L. et al., 1984). The experimental conditions are presented in Table 3. One sample was scanned in approximately 24 hours.

Table 3 High resolution X-ray MCT conditions CTLab

Manufacturer	CTLab
Configuration	Cone beam
Image size	2048 × 2048
Source	80 kV 100 μ A
Rotation	360°
Voxel size	3.11 μ m
Optical magnification	20 ×
Specimen	Marg_young

2.3.6.2.2 Xradia

X-radia's MicroCT200 (www.xradia.com) provides high resolution (1 μ m) scanning. It was used to scan samples identified as M_wedge and Foram small1 and 2 at the Microscopy Lab at Fonterra Innovation and Research, New Zealand. Specimens were placed firmly in a cylindrical conical shaped clear plastic holder with thin wood dowel that was attached to the sample table Figure 17. Scanning required approximately 20 hours.



Figure 18 Sample in clear plastic cone held on sample stage.

The scanning experimental conditions are presented in Table 4.

Table 4 High resolution X-ray MCT conditions Xradia

Manufacturer/machine	Xradia Microfocus MCT200
Configuration	Cone beam with phase enhanced detector
Image size	1024×1024
Source	40 kV 200 μ A
Source Distance	19.4 mm
Detector distance	8.0 mm
Rotation	360°
Voxel size	$1.9 \mu\text{m}$ / $0.961 \mu\text{m}$
Optical magnification	$10.1 \times$
Specimen	Foram wedge / foram 1, foram 2

Specifications for each machine are provided in Appendix A. The isotropic voxel sizes for each specimen scanned and its reconstructed images are presented in Table 5.

Table 5: Isotropic voxel sizes of X-ray MCT data sets

Specimen label	$\mu\text{m}^3/\text{voxel}$ (isotropic)
foram wedge 10x (Xradia)	1.9
foram 1	0.961
foram 2	0.961
M111 (ScanXmate)	2.792
M112	2.792
M221	2.792
M222	2.792
M331	3.071
M332	3.071
M441	3.071
M551	6.742
M largest	40.92
M large	35.856
M middle	24.464
M small	8.08
M smaller	4.97
M smallest	3.704
Marg 2 young/ old (ANU-CTLAB)	3.11
	3.11

The isotropic voxel size for the images of samples- M large, M largest and M middle (with specimen diameters greater than 5 mm) were several tens of micrometres. This resolution was insufficient to allow certain image processing steps for quantitative evaluation of geometric or volumetric parameters because the dimensions of the microstructures (e.g. chamberlets) or the distances between consecutive chambers was smaller than this resolution.

2.3.6.3 Calibration

Specimens were scanned without referencing to a material of the same bulk composition (calcite) as the specimen e.g. a calcite pin, to calibrate reconstructed values to calcite CT values. In

studies in which the differences in densities between materials or specimens that are scanned are quantitatively evaluated, the difference in image values among specimens can be significant; in such a case each target specimen would need to be scanned with a reference target. In such a study of specimens composed of primarily of biological calcite, such as *Marginopora sp.*, a calcite pin may be used as a reference sample, and calibration would be required of the image values to the X-ray MCT value referenced to calcite, where air is -1000 and calcite is 0. These values reflect a scale of units (Hounsfield scale) used in many medical studies of biomineralised calcium carbonate or hydroxyapatite and their crystalline forms (Hounsfield, G.N., 1973).

The density of the mineral or solid content of specific structures of different specimens was not quantified per se using X-ray MCT nor were the variations in densities of the solid phases of different specimens quantitatively compared in this study; only in single specimens the relative distribution of density was observed. Because the structure of *Marginopora sp.* is cellular, i.e. it has two dominant phases- solid or mineral and pore or void, the differences in density between the two phases are the relevant parameters that are identified and quantified by the algorithms during image processing. The differences in density are represented by the differences in the intensity of the X-rays or the values of the attenuation coefficient. During the thresholding operation the user visually identifies and notes, based on knowledge of the structure and of grey-scale ranges, the lower and upper thresholds of these values for the solid (mineral) phase and the void (pore) phase. The algorithms used to quantify the two phases use these lower and upper threshold values as delineating values to distinguish the two phases. Thus the variation in density in the calcitic solid phase between several specimens was not directly relevant to the quantification of parameters such as porosity which was researched in this study.

Artefacts such as the ring artefacts, when present in the data, were corrected by applying algorithms to the data during processing. These artefact removal algorithms were available in the form of correction modules of the software packages that were used in this research.

2.3.6.4 Image Processing

Each manufacturer of equipment used in this study, i.e. Comscan Techno, ANU and XRadia, has its own proprietary or institutionally developed software for generating, viewing and converting the first set of images from the raw projections. In this research several software packages were used to pre-process and process the raw data sets. Two types or sets of images are generated by the scan process. These are the raw projections or X-ray negative images in which the denser material is lighter (“whiter”) and subsequently, the X-ray positive images in which the denser material is darker or coloured.

A region of interest (ROI) is selected from the raw data set by selecting a subset of the raw data set to define the volume of the object or specimen that will be processed. This demarcated image set is output in the form of a stack of, usually, grey-scale .TIFF files, .NC files or DICOM files.

The stack is then converted to the second set of binary images. These images are thresholded grey-scale images. Thresholding is a process or an operation by which the user assigns a lower grey-scale (brightness) value and an upper grey-scale value (Lower Upper Threshold -LUT) to the feature of interest so that the feature is identifiable as the foreground in the image. Different

grey-scale or colour values are assigned to different features to distinguish each from others. Crystalline (solid) phases are assigned different LUTs to differentiate them from the pore (void) phase. Thresholding depends to a considerable extent on the sensitivity of the user in the visual identification of the features, i.e. the user/viewer's knowledge of the features in the images. Thresholding of the tomograms was done using the software NCVIEW (Scripps Institute of Oceanography, USA, http://meteora.ucsd.edu/~pierce/ncview_home_page.html).

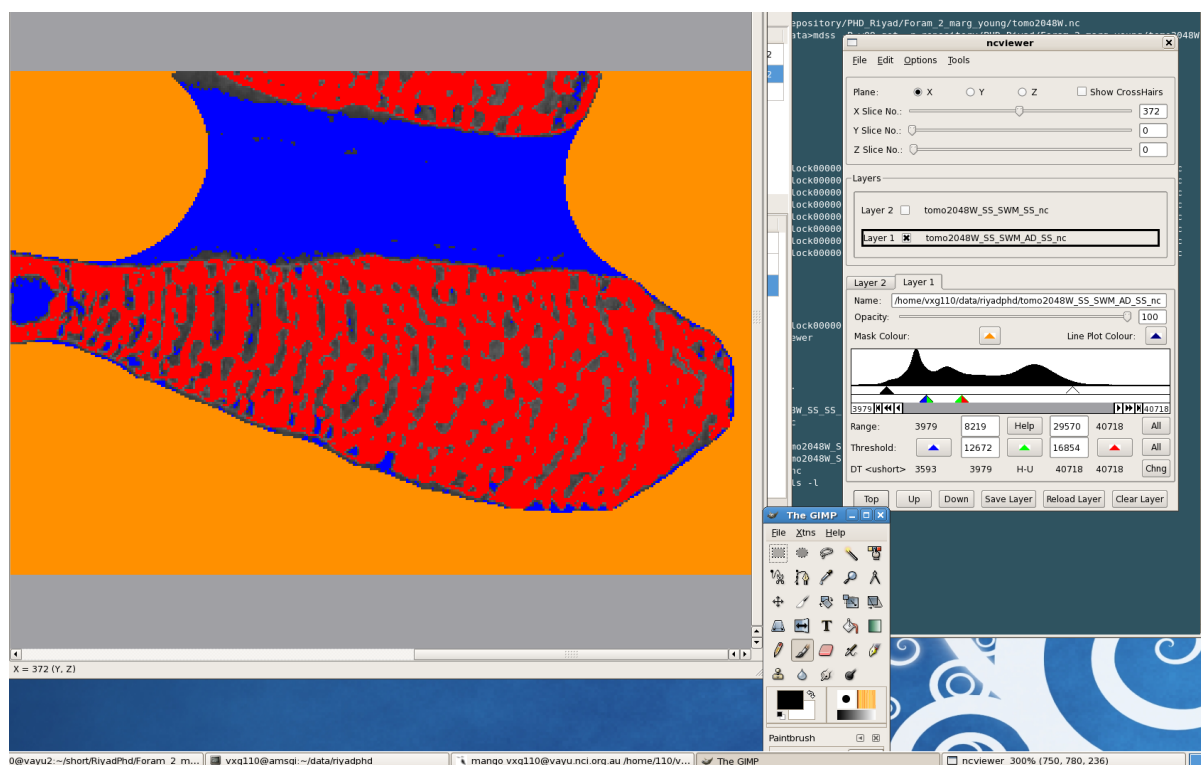


Figure 19 Use of NCVIEW for thresholding.

In Figure 19, using the grey-scale tomogram of the test of *Marginopora sp.*, pixels mapped red are solid. Pixels mapped blue (within the red structure) are void. Yellow is also a void phase but it is outside the structure. Thresholding, based on the histogram (right box Figure 19), is performed by identifying peaks in the histogram with pixelated structures in the tomogram, sliding the coloured triangles along the histogram's x-axis to populate as fully as possible a pixelated structure with one colour while not populating another type of structure or phase. The threshold quantitative values (lower and upper) are noted. The process is repeated for each phase or structure-feature. The slices in the stack of tomogram files can be viewed in x, y, or z-axis orientations collectively during the thresholding operation.

The image is said to be segmented into separate features of interest. Once a feature is thresholded and segmented, the segmentation applies to the entire stack of .TIFF or .NC files that represent the volume of the segmented feature. Segmentation is an apparently simple, but detail-oriented and a very important procedural step. The division of images into features or objects of interest which often coincide with structural units of interest converts the images into information. The analysis of the features, i.e. computation of various 2D and 3D geometric parameters is performed using the segmented files. Further visualizations in 3D are also performed using the segmented files.

2.3.6.5 NCView and Mango

Mango a proprietary software package developed by the Department of Applied Mathematics, Australian National University (<http://xct.anu.edu.au/mango/>) was used to process the reconstructed data obtained from scans at the ANU CTLab. Mango's capabilities include processing 2048^3 voxel data sets by using the ANU supercomputing facility. It is written in C++ and uses the Unix OS. Each step, such as noise filtering or segmentation requires a manual entry and selection of parameters but the entire sequence of steps is processed sequentially and outputted using the supercomputer. This allows huge datasets to be processed, and uses between 10-45 minutes of processor time at allocations of 60 GB - 90 GB of RAM. Mango was used for image enhancement using filters to remove noise and artefacts from the data and segmentation. The segmented file is then used as an input to Mango's image analysis modules for porosity computation, surface area and volume calculations and network analysis.

In this study, Mango was used to analyse the scan reconstructed data obtained with the ANU CTLab equipment for specimen Marg_young and for a series of specimens scanned with the ScanXmate L080.

2.3.6.6 Drishti

Drishti is a volume exploration and visualization open-source software package developed at the ANU Supercomputing Facility, Canberra (Limaye, A., 2006). Drishti has been mainly used for the visualization of the internal structures and networks of geological samples; recently it has been used for visualizing the scaffolding structure of horse femurs and fly-through visualization of fossil fish eyeballs. Drishti uses the X-ray MCT scan reconstructed data set in the form of a .nc file. The data sets are volumetric datasets because density is known at some 3D point in every volume (voxel). Volume visualization algorithms allow one to explore the internal structure by mapping or assigning the density in each volume to a colour and transparency. Drishti uses these algorithms to create visualizations. This technology allows an understanding of structures and microstructures in a way otherwise not possible.

A file import module, Drishti Importer, was used to import the .NC file. A subset of the stack of tomogram files was selected and converted to pvl.nc files, which are read by Drishti. The data set for the specimen labelled Marg_young was viewed as a histogram of intensities vs. frequency. This was used to identify the two phases- solid and void, i.e. crystalline and pore. Drishti does not use analytical modules based upon algorithms to compute geometries or undertake other analyses. However, each voxel in either phase was assigned a phase related colour and transparency (or opacity). This differentiation was used to count the voxels in a particular phase; this provided a method of arriving at sums of voxels (of phases) which are measures of porosity, crystallinity, total volume etc.

Volumetric renditions also permit visualization of the interior of the structure from different directions or perspectives by virtual sectioning in any plane or in multiple planes at the same time. This tool provides a major advantage in observing or visualization of small interior structures as compared to optical or electron microscopy techniques. Drishti was used to create different views of the test of *Marginopora sp.* X-ray MCT data obtained with the ScanXmate

L080A for a series of specimens representing the growth stages of *Marginopora sp.* were imported to Drishti. Data for specimen Marg_young, scanned at the ANU CT LAB was also rendered in cross-sections to compare and contrast with the results obtained from SEM. 3D volumetric rendering was used to produce a series of internal views of the test through ontogeny from embryonic to reproductive stages.

2.3.6.7 ImageJ and BoneJ

Quantitative analysis of porosity was done using ImageJ, an open source software package developed at the National Institutes of Health, Bethesda, MD, USA. ImageJ is an established sophisticated software tool used in the analyses of 2D images for biological and materials applications, e.g. for surface area, cell counts, particle analysis etc. It is also used with 3D or volumetric plug-ins to view and analyse tomographic data; the JAVA based plug-in BoneJ is widely used by medical researchers for the analysis of X-ray MCT data in studies of mammalian bone and teeth (Doubé, M., Klosowski M., Arganda-Carreras I., Cordelières F., Dougherty R., Jackson J., Schmid B., Hutchinson J., Shefelbine S., 2010). In this research, ImageJ was used with Bone-J, which is specifically written to analyse images of calcium carbonate based materials. Further, ImageJ and BoneJ address many of the “software usability criteria” (Figure 20) discussed in the imaging bioinformatics literature (Carpenter, A.E. et al., 2006); Mango and Drishti are less compliant with these criteria. ImageJ and Drishti support volume visualizations but ImageJ’s open architecture has allowed the development of an enormous number of open-source sophisticated analytical plug-ins for specialised applications such as biomedical imaging (MRI), mathematical morphology, surface assessment, confocal microscopy, TEM, fractals, optical flow estimation etc. A number of microscope manufacturers, e.g. Zeiss, Nikon, Hamamatsu, have developed specialised plug-ins for their products. ImageJ’s analytical plug-ins based on algorithms include numerous geometric operations, filters, segmentation, graphics, colour tools, selection tools, stack tools, utilities etc. A large online community, including commercial developers, contribute to ImageJ’s evolution and sophistication.

ImageJ can run on personal computers and is available for use with most operating systems; it is limited by the computing processor power of the operating machine but can be used with parallel or multi-CPU hardware. Mango and ImageJ may be used for similar analyses because both tools use sophisticated algorithms to analyse similar structural problems, possess a large set of algorithmic tools, and provide quantitative and visual reports. They differ in functionality in that Mango uses supercomputing power and processors for handling quickly very large data sets. A larger suite of quantitative results can be obtained with analyses using Mango.

In this research, ImageJ and BoneJ were used extensively on the data sets obtained from scans using the ScanXmate L080 and on specimen Marg_young scanned at ANU. Thus, the same data sets were analysed using two software packages- Mango and ImageJ; this allows for some comparison and validation of the application of software based methods to the test of *Marginopora sp.* Since reproducibility is an important element of research, the versions, configurations and specific settings of the software used in this research are presented in Appendix A.

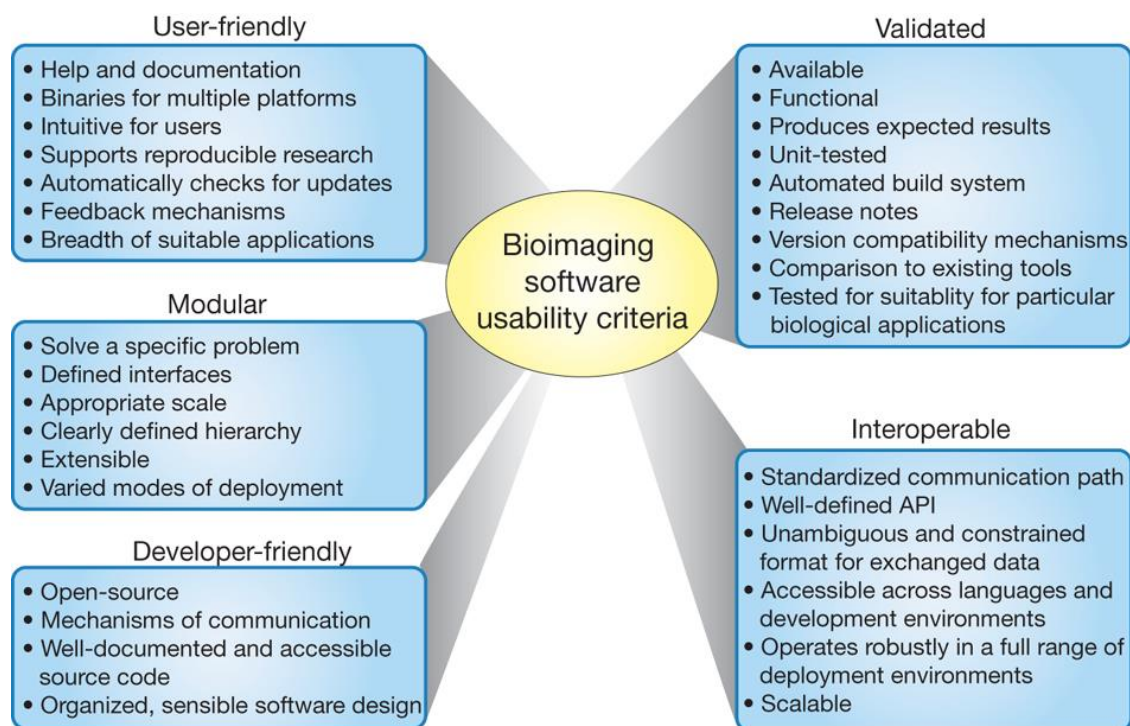


Figure 20 Bioimaging software's usability criteria.

(Source: adapted from Carpenter et al. 2006).

2.3.7 Rapid Prototyping

Rapid prototyping (RP) is a term used to describe a set of technologies that use hardware to create, print or fabricate a 3D scaled physical model that is derived from 3D digital data. 3D digital data may be obtained from computer aided design software, tomography, magnetic resonance imaging and X-ray MCT. RP methods provide aids to visualization of topologies and geometries, test models for parts or product design and manufacturing, mechanical or flow characteristics testing of components or structures, fitting models for nested components in structures and recently, final products. 3D printing is a RP technology. The salient difference between RP technology vs. computer aided engineering, which is virtual prototyping, is that the latter technique allows simulations on a computer based model rather than on a physical model (Chua, C., Teh, S., & Gay, R., 1999). 3D printing techniques allow powders and resins to be combined to create the organic structures of scaffolds for bone tissue growth. Bone tissue has a complex connected network of pores that is important in the creation of the scaffold and can be created by 3D printing. Both conventional X-ray MCT and synchrotron CT have been compared in their efficacy for the reconstruction of and non-destructive analysis of the 3D printed scaffolds (Buzug, T.M. et al., 2007).

In this study the data obtained with X-ray MCT were used with 3D printing technology. The 3D X-ray MCT data set consisting of a set or stack of .TIFF files (images) of an adult specimen of *Marginopora sp.* scanned using the ANU X-ray MCT equipment was converted to a .STL file using MeshLab. This format was used to construct a solid high performance composite representation of a 3D cross-section of the test of *Marginopora sp.* This was built with a model Z-Printer 650

(Z-Corp/3DSystems, USA). The printer (Figure 21) has a resolution of 600×540 dpi, allows the building of a minimum feature size of $50 \mu\text{m}$ with a maximum build size of $254 \times 381 \times 203$ mm. A printer head lays out the cross-section of the image-data on the powder bed or tray. A piston feeds powder with high accuracy over the cross-section and raises the bed an additional step or layer while a roller spreads the powder on the bed. The inkjet print heads print the cross-section and bind the powder. The bed is raised by 0.1 mm and the process is repeated for the next layer of the cross-section in an automated layer-by-layer print or build of the 3D section. The 3D build created was $110 \text{ mm} \times 70 \text{ mm} \times 70 \text{ mm}$ with a wall thickness of 0.025 mm at a build speed of 25 mm/hr. The build was removed from the printer bed after it had cooled. A compressed air-nozzle was used to remove the excess unbound powder to reveal the complete morphology of the built-structure. Thus the imaging data were used to provide a tangible larger scale representation of the microstructures of the test of *Marginopora sp.* This model was used to gain additional insights of the architecture and patterns of construction of the test.

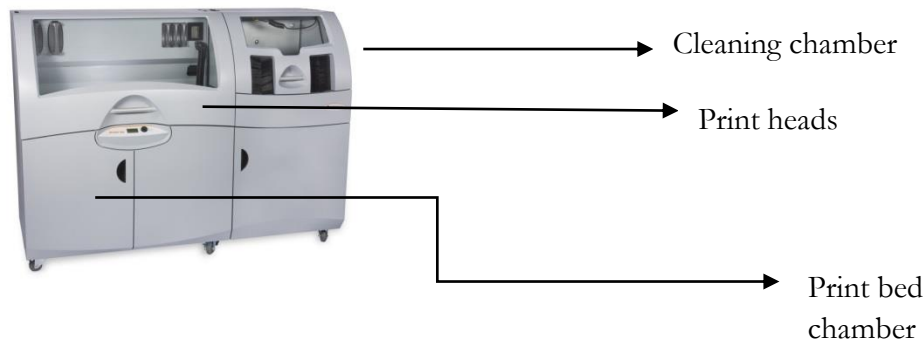


Figure 21 Z-640 3D printer.

(Source: www.zcorp.com).

CHAPTER 3: Results

3.1 Optical Microscopy Thin sections of *Marginopora sp.*

3.1.1 Introduction

Thin sections and optical microscopy have been used to understand foraminiferal test structure, particularly the structure of the wall, in numerous studies over the past 70 years (Hay, W.W., Towe, K.M., & Wright, R.C., 1963; Reiss, Z., 1958; Wood, A., 1949, 1963). Thin-sectioning is the earliest and simplest microscopy-based technique that can be used towards understanding the architecture of the foraminiferal test. Optical microscopy was also used with other microscopy techniques to understand the process of chamber formation and crystallisation in planktonic and benthic foraminifera (Be, A.W. et al., 1979; Deutsch, S.J., Green, H.W., & Lipps, J.H., 1973). Similarly the technique was used extensively in the study of coralline structures (Stolarski, J., Meibom, A., Przeniosło, R., & Mazur, M., 2007) and it is an established technique used in examining the optical mineralogy of petrographic samples. Although numerous studies exist describing the wall structure, ecology, symbiotic relationship, chemical composition of *Marginopora sp.*, (Hohenegger, J., 2009; Hottinger, L., 1982; Lee, J., Hallock, P., 1987; Raja, R. & Saraswati, P.K., 2007; Ross, C.A., 1972; Towe, K.M. & Cifelli, R., 1967) the literature is sparse in terms of images of thin-sections of its test. Most optical microscope detailed images and SEM images of thin-sections of the complete test are images of the casts produced using Hottinger's epoxy technique. Such images of the sectioned test were presented in a detailed study of the endosymbionts of *Marginopora sp.* (Lee, J. et al., 1997) and in a study by Ross of the ultrastructure of the test (Ross, C.A., 1976). The epoxy casts provide morphologic detail in two planes and are easier to prepare than thin-sections of the crystalline test. The discoidal shape, calcitic composition and the dimensions of *Marginopora sp.* test present difficulties in the process of making useful thin-sections. Insufficient penetration of the epoxy into the pore spaces and the complex morphology of the test may cause fractures of the structure during the thin-sectioning process. A large number of specimens are necessary for sectioning so that the images produced from randomly oriented sections reveal the test's structure in various planes (oblique, equatorial, transverse etc.) in 2 dimensions. Hottinger casts and replicas, when prepared adequately, allow detailed study of a single surface. Neither technique allows for a study of individual crystals. However, thin-sections of the test provide information which is not available from a view of sections of Hottinger casts: of the density of the walls, of variations of organic materials and, when viewed with polarized light, of the crystalline fibre orientations. In this section we present observations using transmitted light to outline, identify and extract information about the layout, walls, and microstructures of the test of *Marginopora sp.*, and to demonstrate the advantages and limitations of high quality thin-sections.

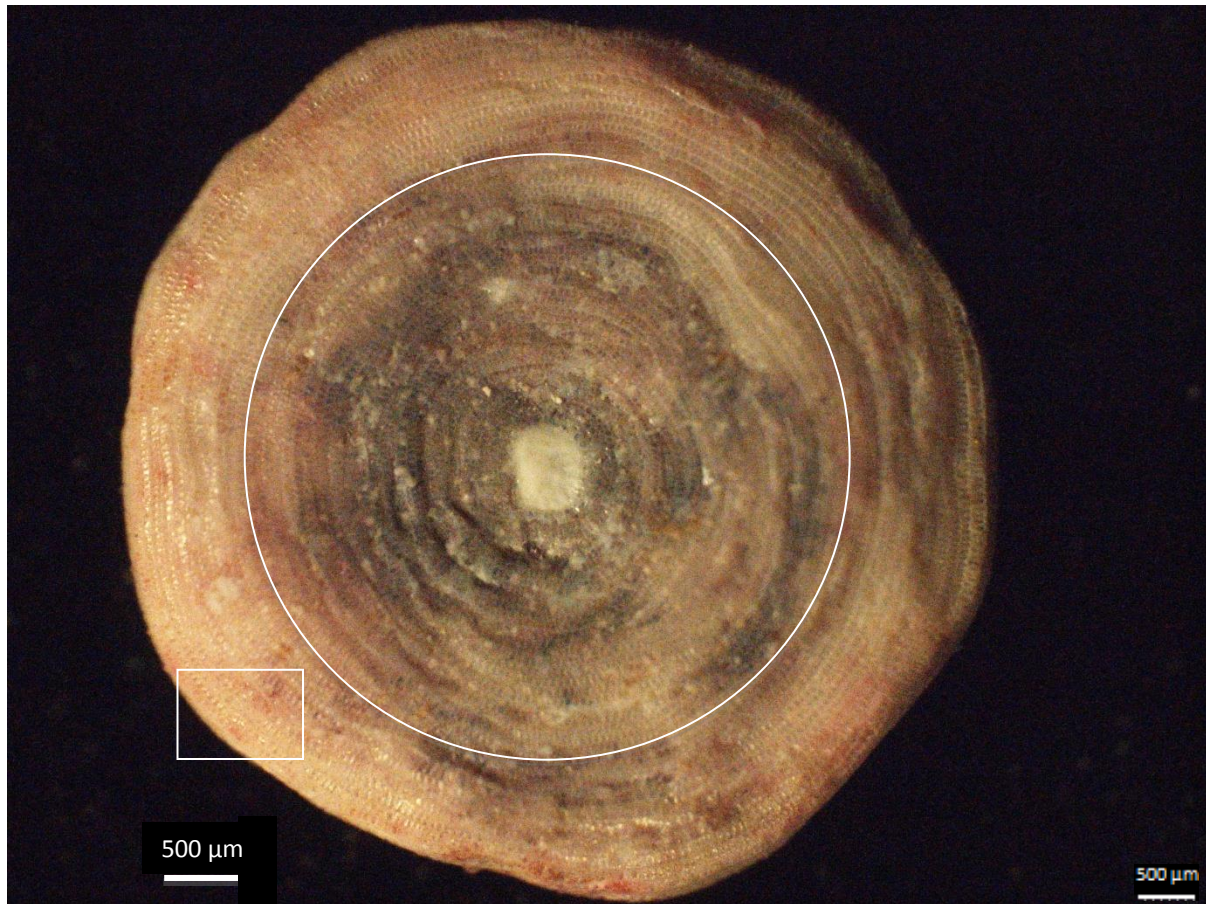


Figure 22 Test of an adult *Marginopora sp.* viewed with optical microscope x100; circularity for comparison of form.

Source: (Pochon, X., Pawlowski, J., Zaninetti, L., & Rowan, R., 2001). The pink colouration is the result of Rose Bengal dye that stained the cytoplasm and was used to identify live specimens using an established field technique (Arnold, Z.M., 1974).

3.1.2 Observations

The surface of the test appears glassy. The discoidal shape is roughly circular. There are regions of defects and deviations from circularity. In Figure 22, about 1500 μm outwards from the centre a significant change in elevation or thickness can be discerned. The concentric chambers are divided into window or tile shaped chamberlets packed closely (as visible in the box in Figure 22). The central regions are darker coloured. In these areas symbionts occupy the chambers. Symbionts in *Marginopora sp.* are primarily dinoflagellates of the *Symbiodinium sp.* (Pochon, X. et al., 2001).

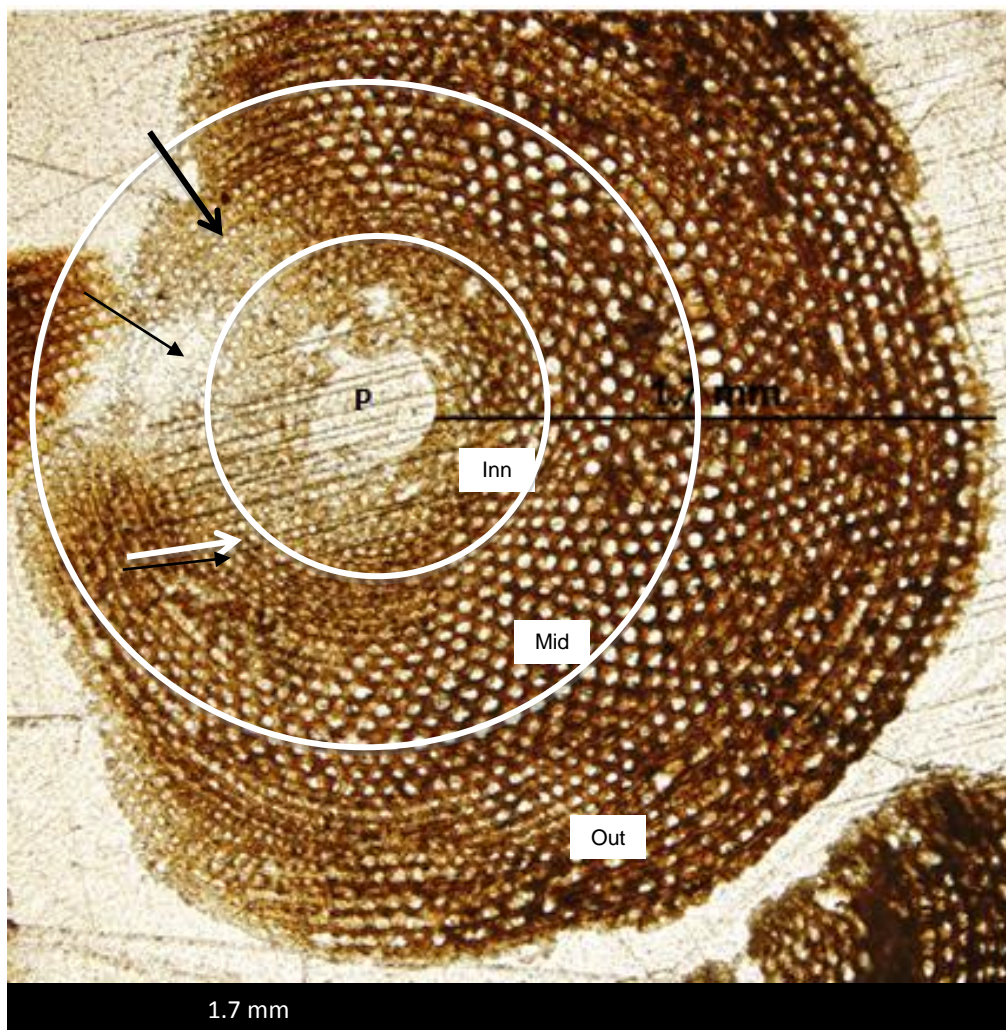


Figure 23 Equatorial thin-section of an adult *Marginopora sp.*

In Figure 23, the central region, consisting of the proloculus (P) or embryonic apparatus has been eroded by thin sectioning. The sectioned disc can be divided into three zones: an inner ringed zone (Inn) of circular chambers consists of chamberlets (lighter voids). These are followed by a middle (Mid) zone of regular spaced larger chambers. An outer zone (Out) is visible in which chambers are spaced closer. The chamberlets in this zone appear to be smaller than in the middle zone. There are regions (marked by arrows in Figure 23) in which the chamberlets appear to be significantly smaller. These surface chamberlets are packed closely and patterned at a higher frequency than the other chamberlets. Symbionts are not visible at this scale in this section.

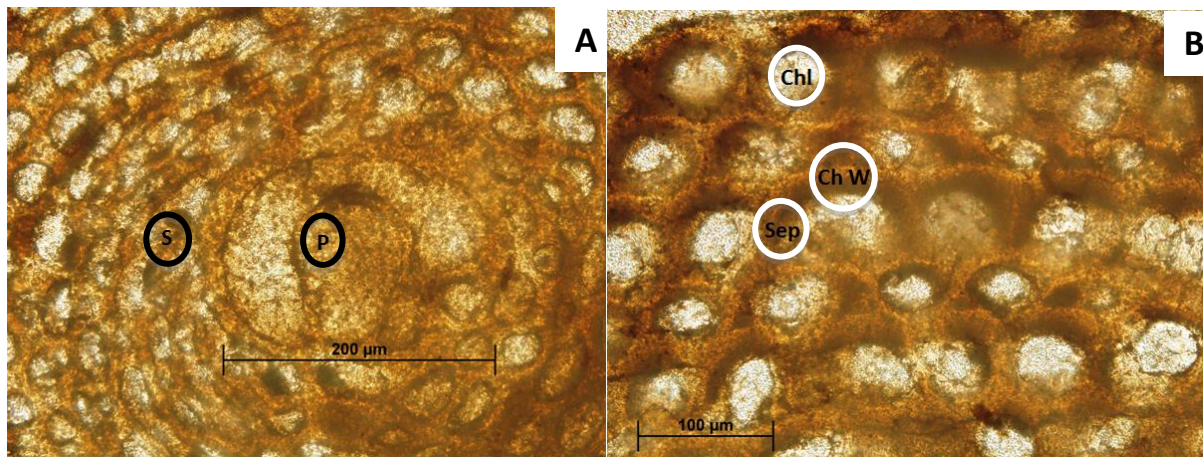


Figure 24 Microstructures of *Marginopora sp.*

A: Prolocular (P) or embryonic region of *Marginopora sp.* in thin section. B: A circumferential chamber wall (ChW), septal wall dividing chamber (Sep), subdivided chamber comprised of chamberlet (Chl). Circles in images highlight the text labels.

The large divided chambered central region (proloculus and deuteroconch) is approximately 200 µm along the longer elliptical axis (Figure 24A). It forms the first ontogenic stage and the crystalline chamber wall of the embryonic *Marginopora sp.* Subsequent chambers are added in concentric growth rings or annuli (Ross, C.A., 1972). In the middle zone- the chamberlets in each chamber appear to be similarly sized (approx. 50 µm) in cross-sectional diameter. The septal walls appear to be continuous and are generally curvilinear (Figure 24B).

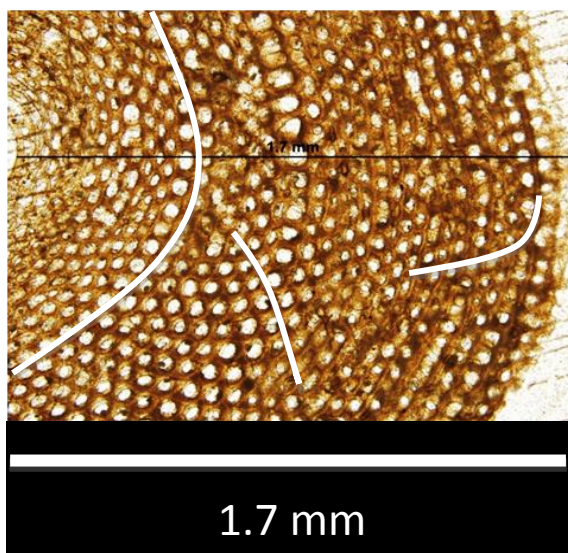


Figure 25 Chamberlet and Chambers- patterns visible in 2D equatorial thin-section.

The white lines indicate annular and radial wall directions.

Three curvilinear patterns are visible in the equatorial thin-section (Figure 25). Interlocking pairs of curves commence at the outer area of the inner zone. These are continuously visible through to the inner region of the outer zone in some areas. A circular or annular growth pattern of the chambers is visible. While the sizes of the chamberlets appear different there is an equidistant

periodicity to their distribution in each chamber. Although variations in relief or elevation across the section may be inferred by noting the lower density or thickness of the crystalline material in the innermost region of the inner zone, the surface chamberlets identifiable by their smaller size and higher frequency of patterning do not appear to be visible in this thin-section. In Figure 25 although the development of whorled chambers is visible in the region surrounding the proloculus, the crossed spirals are not evident in this equatorial section.

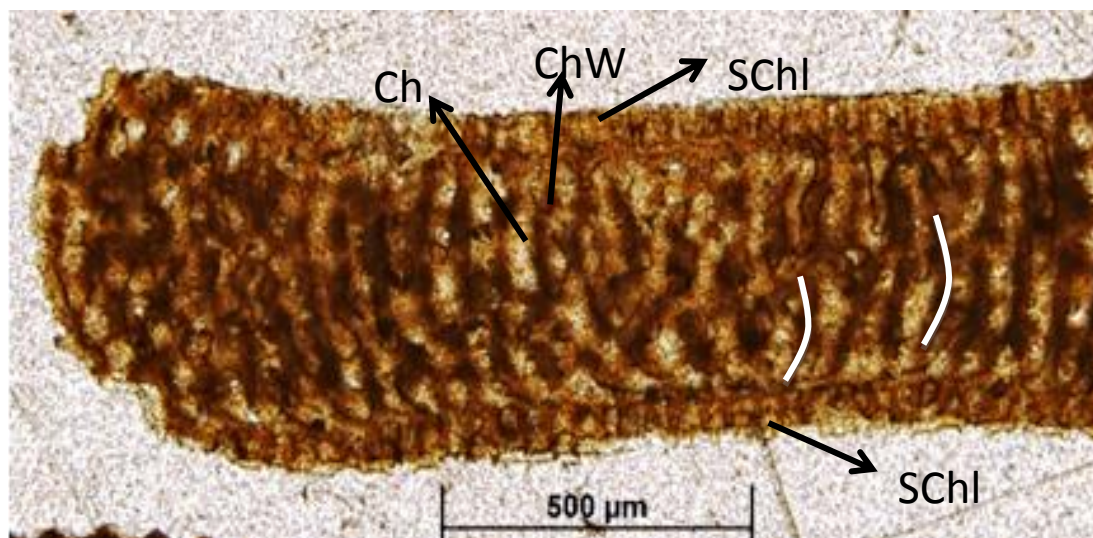


Figure 26 Transverse thin-section of partial disc of *Marginopora* sp.

Ch: chamber; ChW: chamber wall; SChl: surface chamberlet. The white lines shows whorls or annuli.

In Figure 26 a transverse section is shown at approximately one-third of the depth of the discoidal test of *Marginopora* sp. In thin-sections a view at this depth reveals the surface chamberlets on both surfaces of the disc, the chamber walls and the 2D curved elongate bulbous morphology of the chambers. The chamber walls are clearly visible as alternating regions to the chambers' 2D curved structures consisting of constricted and bulbous regions. In the central region of the lower surface of the disc a convergence of pairs of oppositely curved chamber walls is discernible.

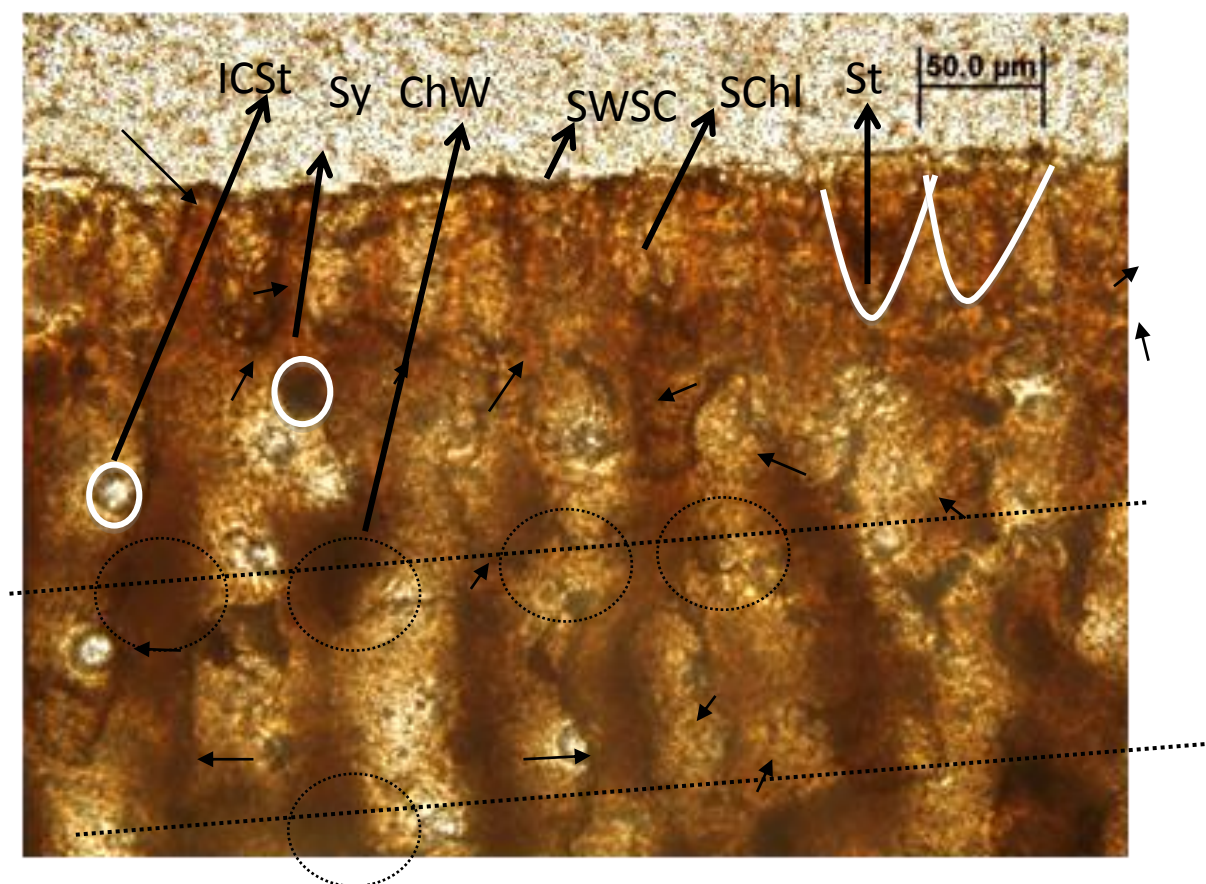


Figure 27 Microstructures of *Marginopora* sp. in transverse thin-section.

ICSt: Intercameral Stolon; ChW: chamber wall; SWSC: surface wall of surface chamberlet; SChl: surface chamberlet; St: stolon; Sy: symbiont. White lines highlight outlines of microstructures; black dotted circles indicate denser walls; dotted lines indicate the trend of positions or alignment of dense periodic wall structure across the test

In Figure 27 a higher magnification optical microscope image of the transverse thin section at a shallow depth is presented which reveals the intercameral stolons or tubular pores which connect the circular chambers (Lucitti, J.L., Jones E.A., Huang C., Chen J., Fraser S. E., Dickinson M. E., 2007). Several stolons can be seen in approximately the same horizontal plane and at lower horizontal planes. A symbiont (light circle) is visible inside a large chamber lumina (cavity-lighter region). Surface chamberlets appear as cone shaped structures approximately 45 μm wide and 52 μm long (in this sectional view) with a single opening or stolon at the constricted end of the crystalline walled structure. The length of the stolon is greater than its diameter. The stolon appears connected to the elongated chamber directly beneath the surface chamberlet. The surface chamberlets have a curved surface wall which appears slightly convex or concave at different points. The darker (black) lining on the surface may be an organic lining. A similar darker lining, perhaps organic, is visible at the bottom of the surface chamberlets and along the walls of the chambers (small arrows). It demarcates the shape of the chamberlets. The lining is also clearly visible at a higher magnification along the entire upper and lower surface of the test and walls of the chambers (Figure 27), but is broken in some regions. Crystalline walls between the surface chamberlets appear lighter. The central regions of the vertically aligned walls appear a darker brown suggesting a higher density of crystals in a horizontal band(s) across this section (indicated by dashed lines). Within the darker regions there is a further variation of intensity; a

very dark smaller central patch is apparent in almost each of the regions (as shown by dotted circles).

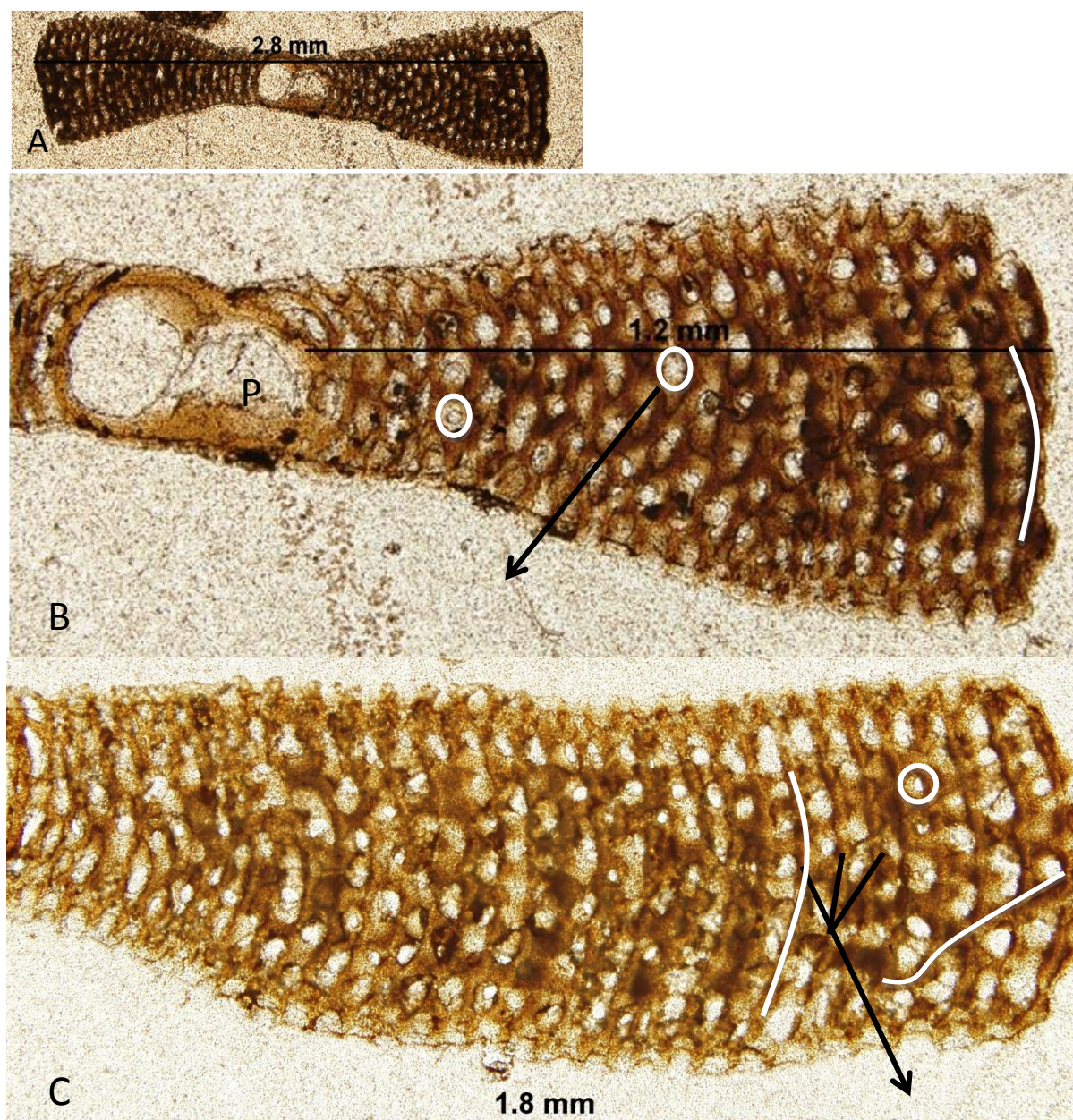


Figure 28 Axial thin-sections of *Marginopora* sp.

White lines indicate the curvilinear annular onion ring denser wall; black arrow indicates periodicity; circle shows stolon.

Figure 28A presents a thin-section in which the entire discoidal form is visible. The section is axial through the centre of the disc. In Figure 28B, a staggered pattern of the wall and chamber is evident. This view also shows the staggered horizontal separation of the chambers (arrow) by the wall into discrete chamber lumina. The structural pattern of the walls appears to follow a gradual ascending straight line slope from the central region to the periphery. This staggered arrangement coincides with the (darker) curvilinear crystalline walls. Circular-shaped stolons are visible; the arrangement of these also shows an ascending straight-lined slope towards the

periphery. The crystalline walls surrounding the surface chamberlets show a distinct cup-like morphology. In Figure 28C concentric curved walls extending vertically in a continuous distinct repeated form from the upper surface through to the lower surface are evident. The chambers appear as large cavities divided into amorphous shapes by horizontal short walls and rib-like vertical walls. The continuity of the horizontal walls and the convergence of the upward and downward curving walls are visible in some regions of the thin-section (as indicated by arrows and white lines). The higher density of crystals as inferred from the darker brown shade in patchy regions; these can be delineated as occurring at the possible intersection of the discernible horizontal bands and the upward and downward angular straight lines.

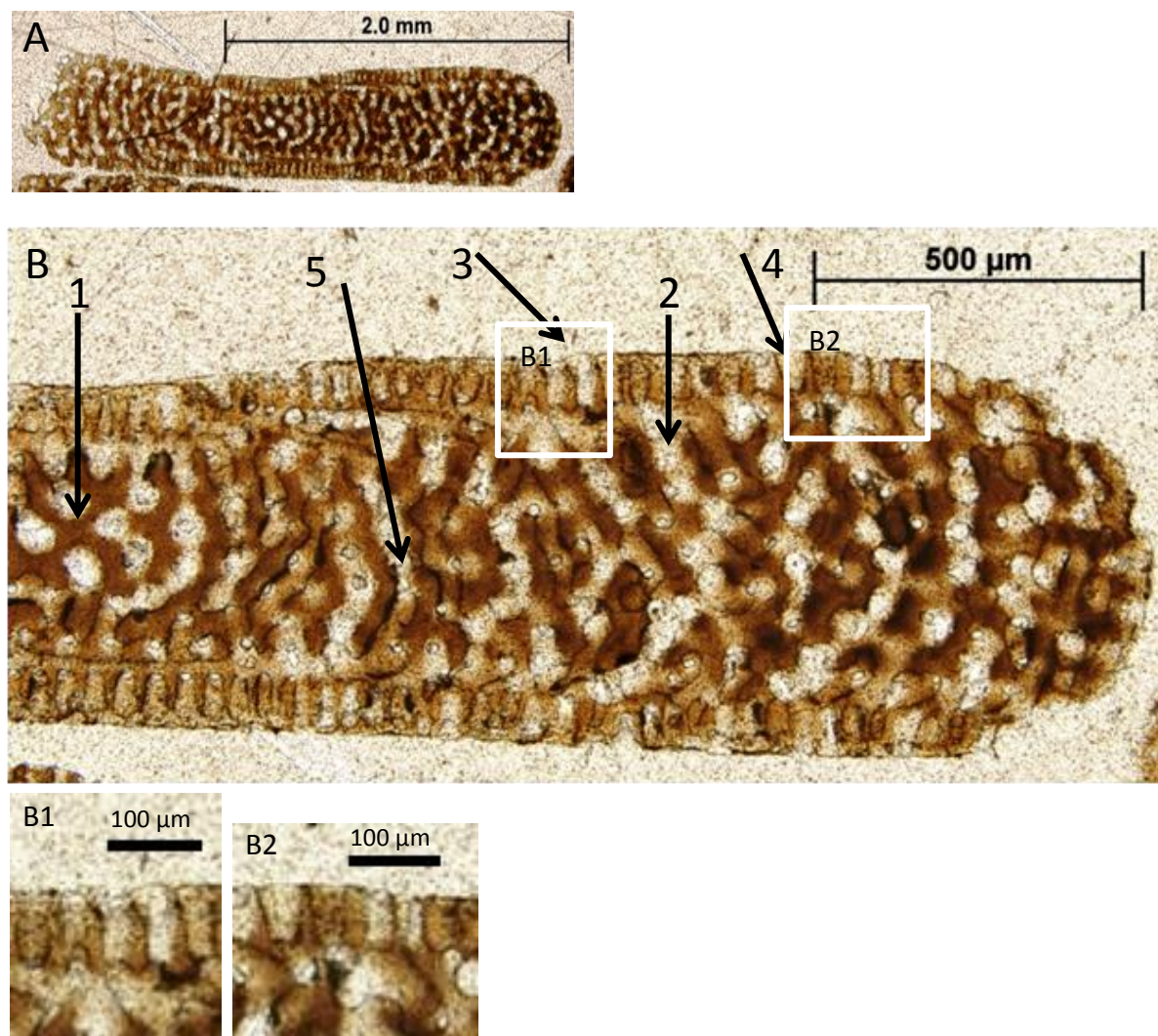


Figure 29 Transverse thin-section of *Marginopora* sp.: view from centre to margin. Region marked by white boxes are B1, B2.

In Figure 29B, a higher magnification view of the disc (Figure 29A) thin sectioned approximately two-thirds towards the centre of the disc is presented. 2D views of the morphology of several microstructures are simultaneously visible. The configurations of the walls and chambers are visible: the interlocking walls (1) in the inner zone, a continuous chamber extending from the upper chamberlets to the lower chamberlets and (2) with circular constrictions (stolons) and chamber lumina and organic lining with symbionts. This view reveals another facet of the

morphology of the surface chamberlets (enlarged in B1 and B2): the surface chamberlets appear to have an anisotropic or asymmetrical form in this view. The cross-sectional forms of the chamberlet located near the inner zone of the test (5) are different from the cross-sectional forms proximal towards the outer zone of the test. Also visible is a dark lining along the wall surfaces that may be organic in composition.

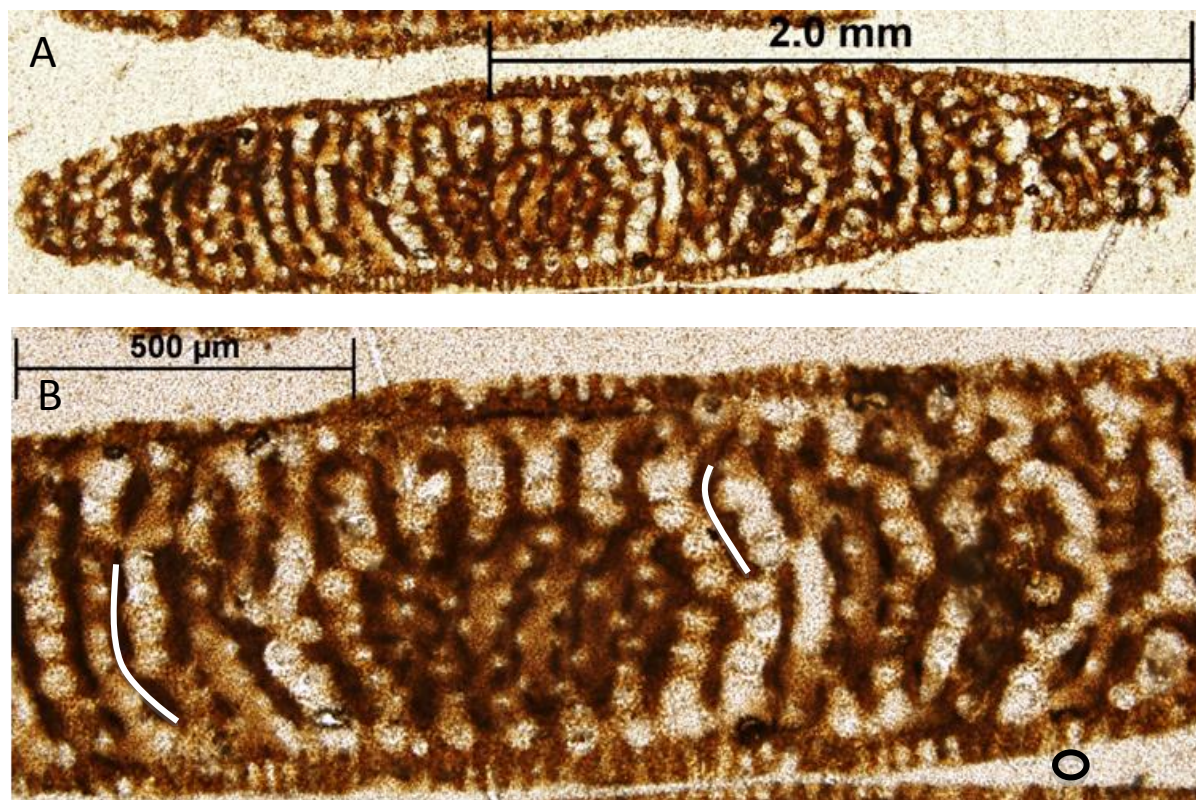


Figure 30 Transverse view thin-section of *Marginopora* sp.: view towards embryonic apparatus.

In Figure 30A and B a view across the cross-section of the disc of the crystalline wall's vertical orientation alternate with the luminae of the chambers is presented. It provides a qualitative indication of the solid (crystalline) vs. void (chamber) fraction of this particular section of the test. The cross-section of a solid crystalline wall is visible in the central region of the embryonic apparatus. The embryonic apparatus is positioned at the lowest elevation in the cross section of the disc of the test. This cross-sectional view of the wall also shows the multitude of stolons originating in the wall of the prolocular region. Also clearly visible is the annular growth of the test in the form of chambers-wall symmetry. The differences in density of the walls of the upper chambers and the thicker denser walls of the individual annular growth chambers is apparent from the different intensity of the brown tint. Lighter brown walls are visible in the background as a portion of the thin-section; the horizontal and angular lines of the crystalline assemblages are visible.

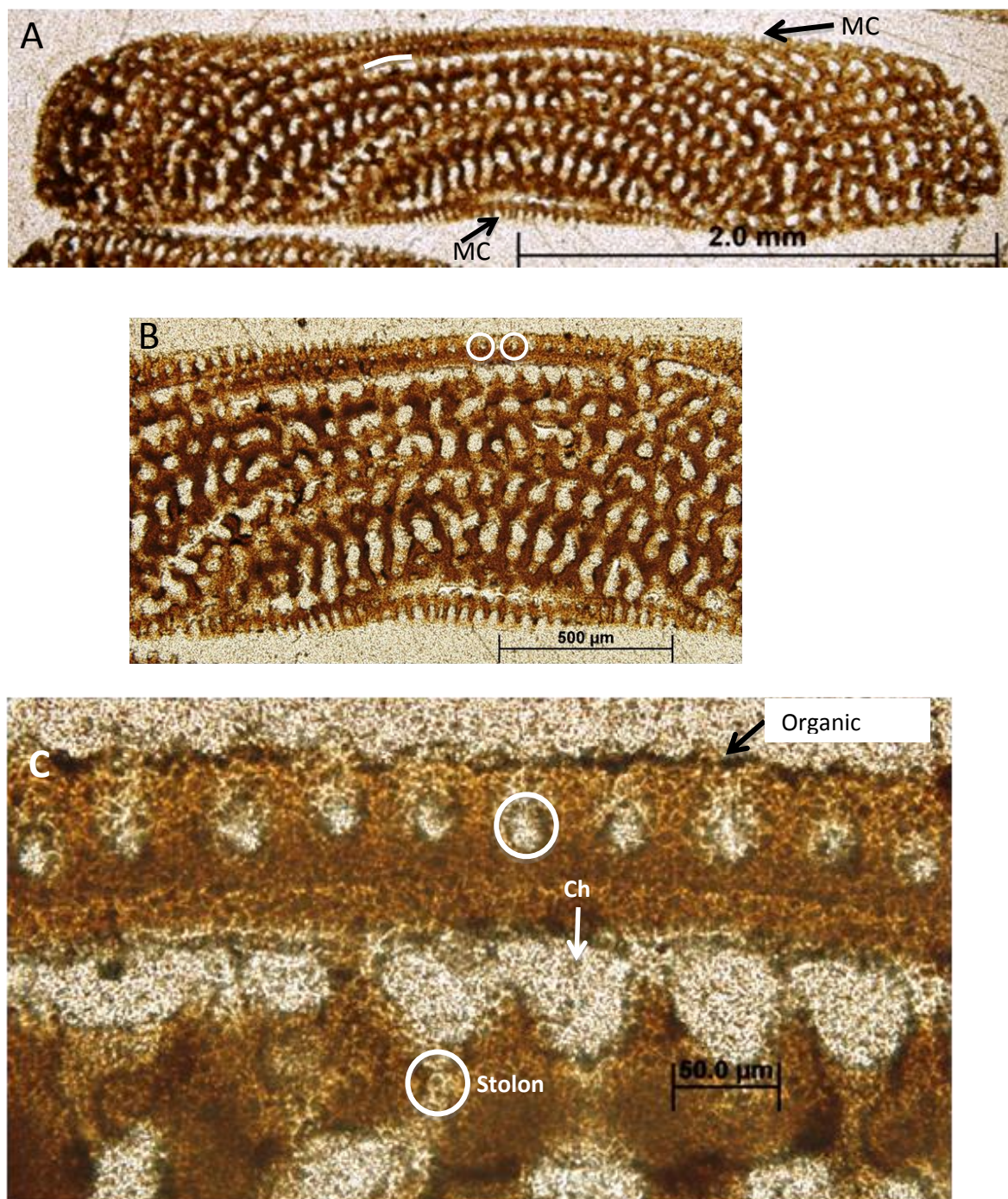


Figure 31 Partial equatorial angular transverse thin-section of test of *Marginopora sp.*

In Figure 31 an angular or oblique view of a section of the discoidal test commencing from the marginal chord or circumferential margin and ending at the surface of the disc is presented. The section clearly illustrates the alternating wall and chamber pattern of annular or concentric growth (A), of curved crystalline walls originating at the inner zone and extending to the marginal chord (B) and the regular pattern of stolons ending at the marginal chord (C). The alternate pattern of chamberlets in one concentric chamber, the immediate intercameral crystalline wall and their relative dimensions are approximately 56 μm (C). In this view, also visible are intercameral stolons and the equatorial planar cross-sectional morphology of the chamberlets formed by the division of the chamber lumina.

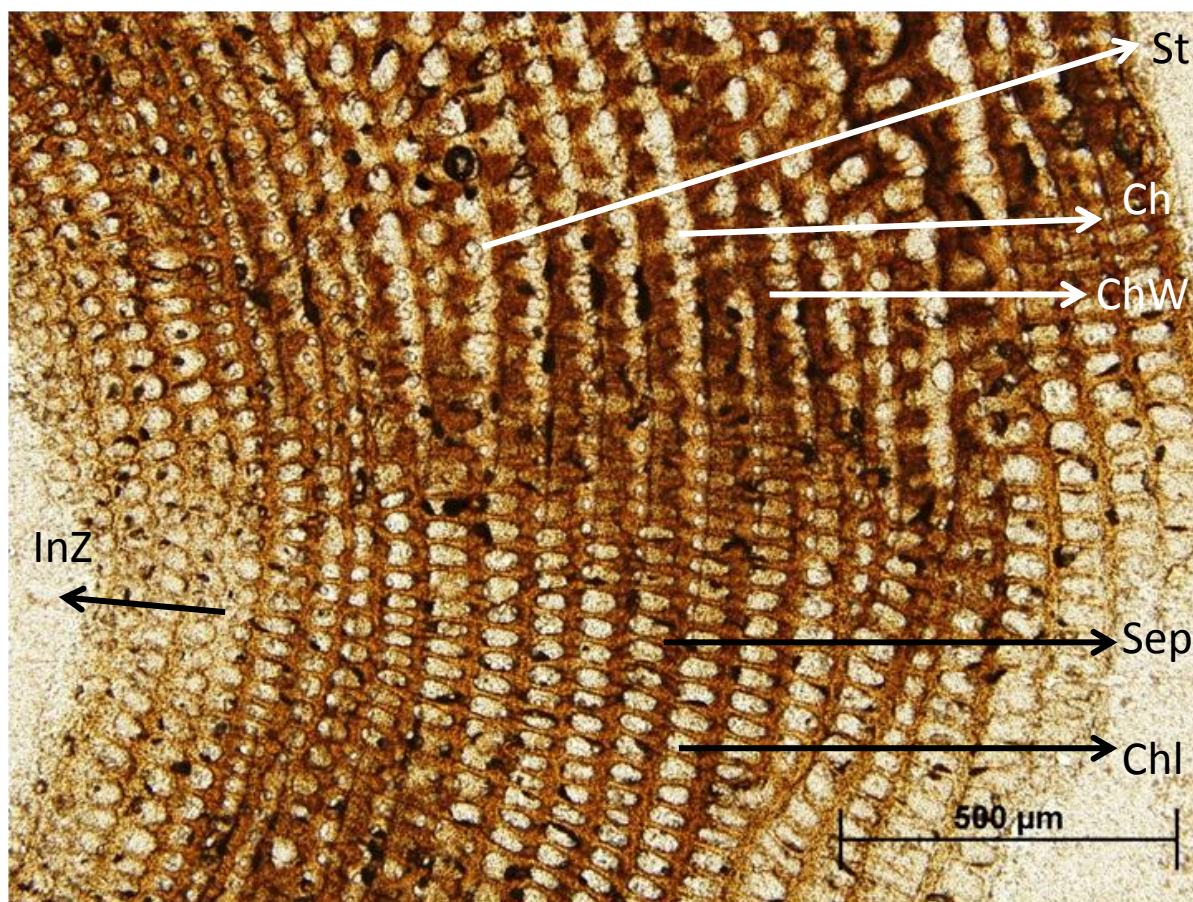


Figure 32 Equatorial surficial thin-section of test of *Marginopora sp.*

In Figure 32, a horizontal planar surficial view of the morphologies of several microstructures is presented: showing chambers, chamberlets, intercameral walls and intracameral stolons. The microstructures of the inner zone are partially visible, the surface chamberlets (Chl) in the middle zone are complete including the septal (Sep) walls. However, the surface chamberlets are not visible in the upper half of the thin-section. Thicker chamber walls (ChW) and the concentric chambers are visible (Ch). Circular microstructures associated with the chamber stolons connecting the surface chamberlets and the chamber lumina are visible (St).

3.1.2 Discussion

I have presented thin-sections of the test showing details of microstructures in many different planes comparable to the detail in 2D provided by the Hottinger technique. Each resultant thin-section reveals the complexity of the test but allows for limited understanding of the architecture.

In this study using thin-sections, the observations of pristine specimens allow for an understanding of the structure of the *Marginopora sp.* test in the equatorial plane and in the transverse planes. Various microstructures are identifiable by their shape and location. A change in the elevation of the test with an increasing diameter of the test and the annular anisotropy of the test can be inferred: in a planar equatorial thin-sectional view the microstructures that are located at different depths or elevations in the test are visible in the same thin-section. Microstructures of the test approximately 25 μm in diameter are clearly viewed, and layers of the

test's walls, organic linings ($\sim 3\text{-}5\ \mu\text{m}$) can be distinguished through differences in density and shades of colouration.

Lee et al.'s (1997) study notes that the dorsal surface may be organic as the acid used in etching away the calcitic test to produce the epoxy cast had not etched away the dorsal surface (Lee, Morales et al. 1997). These observations confirm that a possible organic lining is also visible in the images of thin-sections of the pristine test. Images of sections (Figure 23) in which a particular plane of the entire test is visible reveal patterns in the construction of the walls and chambers. The patterns and the microstructures are complex, periodic, varied in morphology - the different periodicity and 2D shape of the surface, equatorial and lateral chamberlets and chambers and of two types of pores or canals that connect the void of the chambers and chamberlets are discernible. However, the limitations of the thin-section method and of the Hottinger cast method are that a synthesised construct of the patterns and the connectivity of the structures can only be inferred. Each technique reveals the complexity of the test but allows for an incomplete understanding of the full test architecture. Further, crystals, crystal aggregates and their morphologies are not resolved.

The construction of the walls and chambers of biomineralised calcitic crystals, the presence of algal symbionts and the shallow marine environment of *Marginopora sp.* allow the notion that the architecture of the test has an adaptive function. This adaptive functional architecture would interact with light, with marine environmental mechanical stresses and with the symbionts (Briguglio, A. & Hohenegger, J., 2011a; Hallock, P. & Anonymous, 1986; Marszalek, D.S., Wright, R.C., & Hay, W.W., 1969b). In order to advance an understanding of the structural organisation of the test and its interaction with the environment, a better visualization of the units of construction and the framework of the structural organisation must be determined (Briguglio, A., Hohenegger, J., & Less, G., 2013).

Ultra-thin sections ($\sim 1\text{-}5\ \mu\text{m}$ thick) can be used with polarizing optical microscopy to reveal crystal orientations. The same sections, transparent to high voltage electrons (300 - 800 kV), were used with higher resolution electron microscopy to resolve the individual crystals, the morphology of the crystals and of the crystal aggregates. These are the fundamental units of construction of the biomineralised test of *Marginopora sp.* Results are presented in the following sections. Following the presentation of those results 2D high resolution images of the variety of microstructures and of the complete test are used to develop a novel conceptual framework of its structural organization, i.e. its architecture.

3.2 Polarized Light Microscopy of ultra-thin sections of *Marginopora sp.*: Chamber walls, orientation of walls and polarization of incident light

3.2.1 Introduction

The structure of porcellaneous, calcitic crystalline walls of miliolid foraminifers has been reported as a thin 2D veneer of rod-like flattened crystals on the surface covering randomly arranged rod-like laths with c-axes at high angles to the surface (Hay, W.W. et al., 1963; Hemleben, C.,

Anderson, O., Berthold, W., Spindler, M., 1986; Wood, A., 1949). This random arrangement of crystals results in the porcellaneous appearance of the test in reflected light. Most studies with optical and electron microscopy which report this observation did not evaluate the walls of large symbiotic miliolid benthic foraminifera, but provided observations of *Miliolinella subrotunda* and other smaller miliolid foraminifera (Lynts, G., Pfister, R., 1967), *Alveolinella quoyi* (Conger, S.D., Green, H.W., & Lipps, J.H., 1977) and *Spiroloculina hyaline* (Angell, R.W., 1980); these may have similar types of walls but have very different architectures. However, in an SEM study of complete (unbroken) specimens Ross added to this description and differentiated the test of *Marginopora vertebralis* further into an additional wall type. He described the *outer walls* of the equatorial chamberlets and outer walls of the lateral chamberlets as “intermeshed set of bundles of calcitic rods...in each bundle a few rods overlap and are cemented to adjacent bundles to form a structurally rigid framework...anastomosing porous structure” (Ross, C.A. & Ross, J.R., 1978). In addition to documenting a previously unreported type of wall, this observation offered a first mechanical perspective to the structure of the external wall, suggesting an adaptive strengthening function of the bundles of rods and calcite that may have allowed *Marginopora vertebralis* to build large tests to house more symbionts. The structure of the extensive internal walls of *Marginopora vertebralis* was not observed in that study or in previous work. In this study, which builds upon the transmitted light observations (Section 3.1.2) of the thin-sections of the pristine test, polarizing light is used to evaluate ultra-thin sections of the pristine test of *Marginopora sp.* to investigate at a coarse scale the orientation of the crystal fibres in the internal walls.

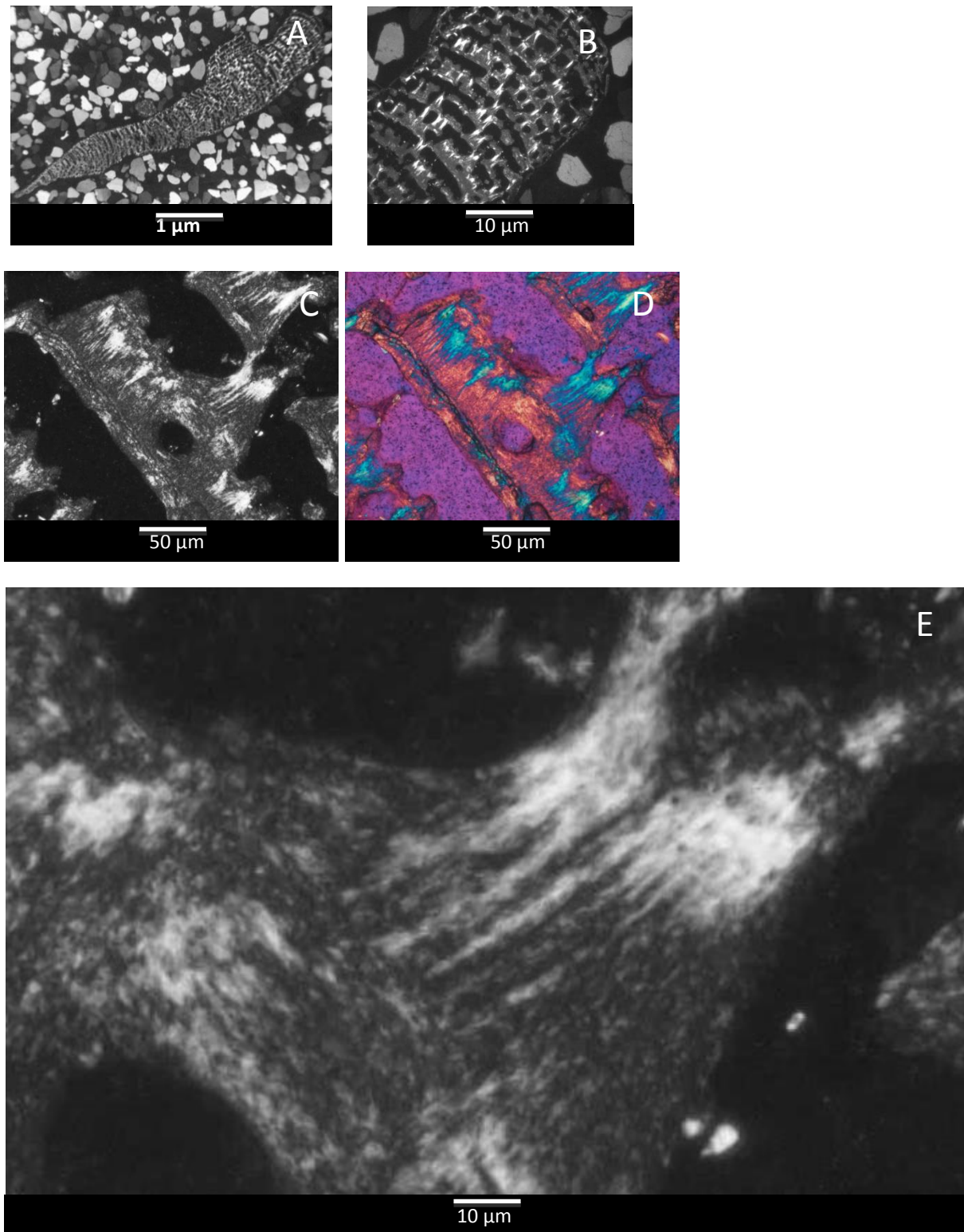


Figure 33 Low magnification images of thin sections of *Marginopora sp.* viewed with polarising microscope.

A: Transverse section 1.25×; B: Transverse section 5×; C: Transverse section 20× cross polars; D: Transverse section 20× cross polars plus lambda plate; E: D ×500.

3.2.2 Observations

Observations were carried out on an ultra-thin transverse section cut across the centre to the margin (Figure 33A-C show the observed region) of the discoidal test and on a parallel section cut one-quarter across the equatorial plane of the disc.

In Figure 33D and E, an optical interference plate was used to highlight or differentiate by different colours the contrasts of Figure 33C.

With the first-order red (550 nm retardation) accessory plate inserted, it is possible to discern the differing crystallographic orientations of the calcite crystals that make up the foraminiferal test. Higher-order interference colours (bright blue) indicate those regions in the photograph where the crystallographic (c-axis) of the calcite is aligned most nearly northwest-southeast (treating the photograph as a map view with north to the top of the page and east to right side of page). Lower-order interference colours (bright yellow) indicate those regions of the photograph where the c-axis is oriented most nearly northeast-southwest, and areas that appear bright pink indicate regions where the c-axis is oriented either north-south or east-west. Intermediate colours (between blue and pink and between yellow and pink) correspond to areas in the photograph where the orientations of the calcite crystals are intermediate. The chamber (septal) wall, highlighted brown, shows variable to near extinction, indicating their composition is of crystals of varying orientation, i.e. no preferred orientation. Along the margins of the chamber, crystallite aggregates or bundles of needle-like crystals are discernible in areas of near extinction to areas of light brown.

A possible organic material (black) is visible along the continuous length of the outer wall of the chamber and partial circumference of the stolon.

The walls that form the passages between each annular chamber show regions of high brightness (bright blue) i.e. a general orientation that is parallel to the a-axes of calcitic crystals. There are slight variations in intensity, i.e. differences of orientation within this region. This particular orientation is absent along the inner walls of the chambers but is visible frequently or dominates along the outer walls of the chambers (Figure 33B, C arrows). The same orientation occurs in very small patches adjacent to and along the length of the possible organic lining.

At a higher magnification (Figure 33E) fibrous bundles of elongate crystals constitute the majority of the structure of the intercameral wall and, crystals of a similar orientation constitute the entire section of the wall connecting two annular walls. Calcitic bundles with crystals of overall similar orientations occur interspersed throughout the wall; some crystals are oriented perpendicular or angular to the bundles. Large areas, in which optical extinction indicates an orientation of crystals parallel to the c-axis, include visible calcitic masses indicating opposing orientation to that of the larger area.

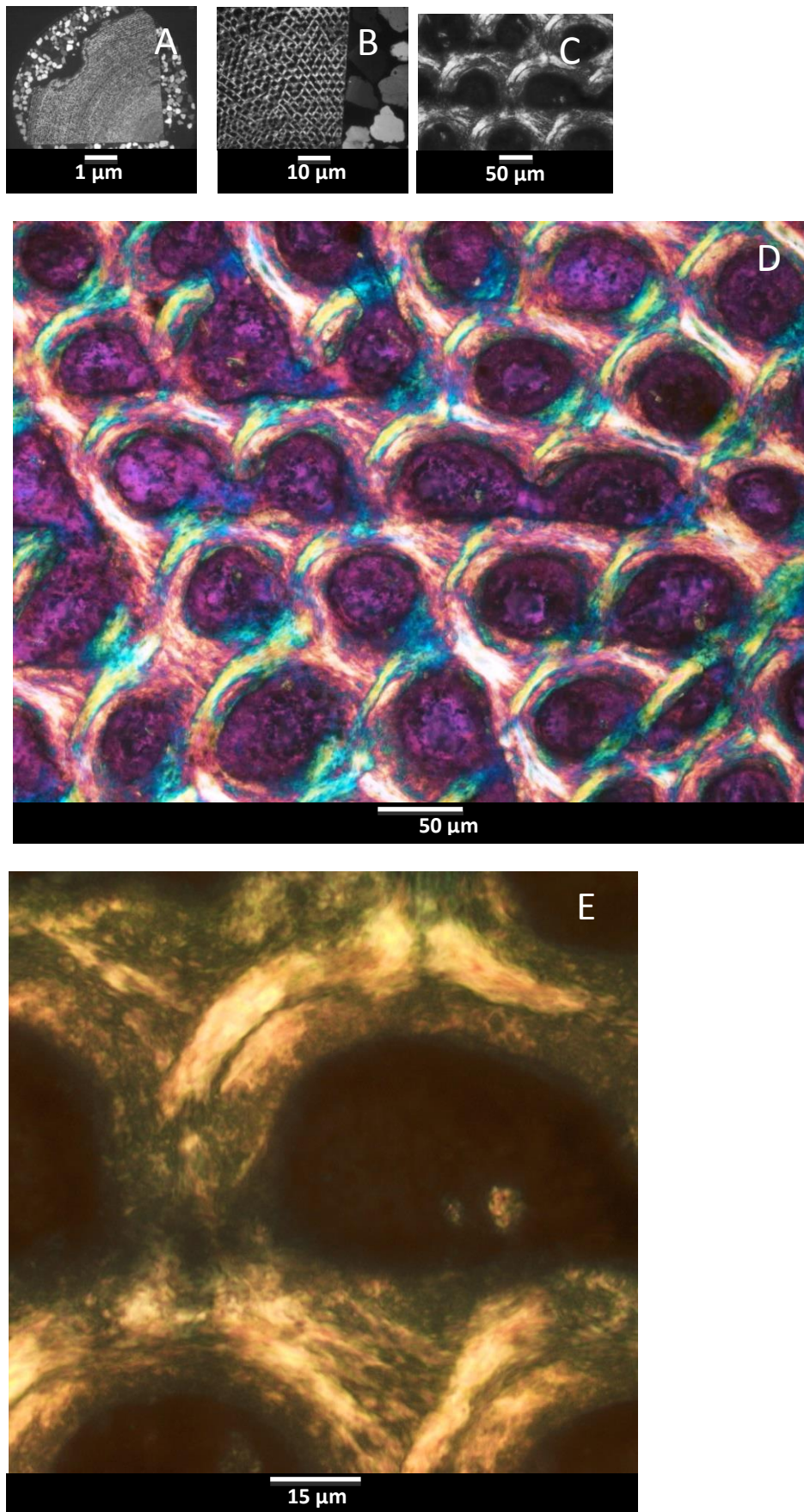


Figure 34 A: Parallel section 1.25x; B: 5x mag; C: 20x magnification; D: Crossed polars rotated 45; E: 40x crossed polars rotated 45 black white contrast.

In a parallel section of the chamber walls crystal fibres are oriented (Figure 34A-D). These oriented aggregates appear to form a periodic curved pattern (Figure 34C) across the test from the centre proceeding angularly towards the periphery. A similar pattern (line) occurs in the opposite direction perpendicular to the first line. Individual crystals in both fibrous regions are mostly oriented perpendicular to the c-axis of calcite as inferred from the areas visible brighter when viewed under the rotated polarizer (Figure 34E) and further highlighted in colour (Figure 34D). In other regions surrounding the apparent circular-section chamber void, the crystal fibre orientations occur in a random or highly variable orientation.

3.2.2 Discussion

Optical polarizing microscopy images of the internal intercameral walls in section indicate a directed orientation of aggregates of crystals or crystal fibres in specific areas encircling the void of the chamber. Further, the orientation of the fibrous bundles appears observable in a similar position at each subsequent chamber, i.e. it is not entirely random. Thus it may represent a motif or a pattern in the process of deposition of the crystallite fibres through the ontogeny of the test. The discernment of the same pattern in a perpendicular position and with similar crystalline positions in the bundles with respect to the surface of the section is an additional feature of interest. This would result in an intersection of two perpendicular lines of orientation of crystalline bundles at a region of the internal wall that would separate three chamberlets. Such an orientation has not previously been imaged or reported in the literature.

The thin-sections allow visualization in two dimensions at a relatively coarse resolution and limit the region that is visualized to a few microns of the thickness of the test's internal microstructures. It may be possible that the images viewed represent only the microstructure at the region of which the thin-section is representative. Thin-sections of a concave discoidal shape and the anisotropic test of *Marginopora sp.* may offer very limited inspection of regions; a pattern discerned may be isolated rather than propagated throughout the test. However, these images do offer limited evidence that the reported microstructure exists in the internal walls of 5 annular growth chambers.

The perpendicular appearing orientation of the c-axes of the calcite crystals in the described regions is counter-intuitive: they appear to be perpendicular to the dominant direction of orientation of the crystalline fibres. The birefringent properties of calcite imply that the higher brightness areas are highly birefringent, i.e. display an optically-slow vibration. The areas of lower birefringence appear duller in the presence of the optical interference plate. However only limited inference can be made with the data obtained from this study. Higher resolution images of the internal walls, showing the crystalline fibre orientation and views of several regions of the test would be necessary to advance an understanding of the pattern observed and suggested here.

If the inferred crystal orientation at the intersection of three chamberlets were confirmed at high resolution it would add credence to the proposition of a structural adaptive value to the pattern. Such bundles of similarly oriented calcite crystals could add an internal strengthening mechanism to the test- a relatively porous structure- creating a “reinforcing matrix” patterned of fibres of mineral crystals.

The interaction of light with the observed orientation of the crystals in these thin-sections of the test of *Marginopora sp.* with respect to the c-axis of calcite and its effects on the symbionts is another interesting aspect that warrants study. In this structure, the interaction of light with the overall crystalline architecture and the wavelength level interaction, with peculiar effects if any, of the nano-sized birefringent crystals would be topics of further study in optical physics.

3.3 High resolution electron microscopy of surface wall structure

3.3.1 Introduction

Focused ion beam (FIB) milling with simultaneous *in situ* imaging at high resolution has become an accepted instrumental technique in the materials sciences community. It rapidly has gained acceptance because of the topographic contrast available in imaging, the accuracy of position and precision of the cross-sectional cut that is possible with the use of the technique. It has gained widespread usage in the semi-conductor industry for its capacity in sectioning, depositing conducting materials at high resolution and the stress-free sectioning of metals that would otherwise be affected by fracture induced damage (Phaneuf, M.W., 1999). Beam induced damage including blurring, charging and amorphising of surface layers are known disadvantages that can be minimized, particularly in soft biological material, by adjusting (lowering) the voltage, beam current and milling angle parameters used during milling and imaging (Kudo, M. et al., 2010). Here I demonstrate a proof of concept: a one-off experiment performed with FIB SEM. Unfortunately, limited access prevented a wider application. But the results indicate that the technique is effective with the biological calcitic tests of foraminifera.

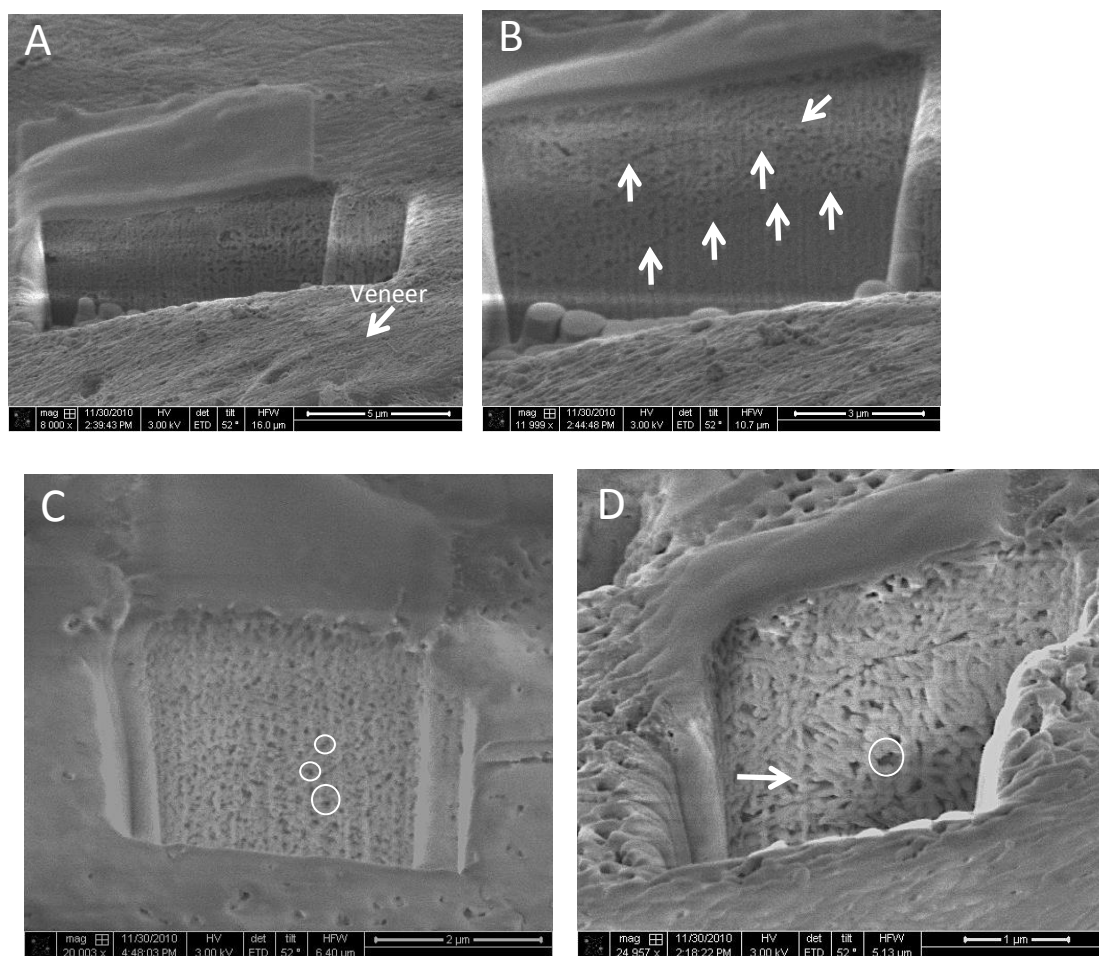


Figure 35 Focused ion beam milled surface of *Marginopora sp.*

A, B: Progressively larger milled area *in situ* to a depth of approx. 5 μm creating a cut-out block on the surface of the test and simultaneous imaging in the SEM. C, D: Higher magnification view of another milled area of the test revealing loose random packing of crystals of surface wall. Circles indicate inter-crystalline porosity.

3.3.2 Observations

The images in Figure 35 show the equatorial surface of the test of *Marginopora sp.* with a section precisely milled by a focussed ion beam *in situ* in a SEM chamber. In Figure 35A, a veneer of elongated but apparently rounded crystals is visible in the foreground (arrow) as a flattened surface layer. Inside the cavity created by the ion beam milling process, the upper region of the surface wall is visible to a depth of 3 μm . The rod-like crystals appear randomly oriented (Figure 35B). In Figure 35B at a depth of 4 μm the crystals appear flattened (arrow) below an apparent fracture line, as a consequence of beam damage or as an artefact induced by charging during the imaging. At a section milled at an adjacent location on the surface (Figure 35C) a similar organization of the crystals is visible to a depth of 2 μm . There is a high contrast between the crystals and pores. At a higher magnification (Figure 35D) $\sim 25000\times$ and high image contrast the inter-crystalline porosity is clearly visible. A rounded elongated rod-like form of the crystals is distinguishable. Most crystals appear to have a rounded terminal region and can be discerned to be a composite of smoothed fused spherical-shaped elements. Crystal morphology and packing appears similar in orientation but hydrated compared to images of specimens prepared for SEM using standard fixation and graded dehydration procedures for calcitic foraminifera studies. The

crystals of random orientation appear to be uniformly dense in this upper region (depth 2 μm) of the dorsal wall of the surface chambers. It is difficult to demarcate the exact length of a single crystal as a consequence of the random orientation in the packing of the crystals but most crystals are at a minimum 800 μm long.

3.3.3 Discussion

I applied a microscopy technique (Focused Ion Beam SEM) that is gaining popularity in materials sciences to view the upper surface layers of the chamberlet wall of *Marginopora sp.* to determine the packing and morphology of the crystals in a pristine specimen that is not fractured. I showed for the first time that this technique is, to the best of our knowledge, suited to viewing the internal and surface microstructure of calcitic foraminiferal tests with high-resolution SEM. A degradation of the microstructures through fixation and dehydration was avoided. Specimens required minimal preparation for examination. FIB-SEM allows for controlled cutting and simultaneous observation at a high resolution of any selected region(s) of interest. It prevents the development of fractures and likely damage such as dislocations of microstructures induced by the physical sectioning of the specimen by a blade.

At a sub-micron resolution in the SEM the individual crystals appear to be a rod-like shape with apparently convex surfaces or anhedral habit and of lengths less than 1 μm . Such a surface texture of the crystals is unlikely to be a consequence of an artefact of the imaging nor of any specimen preparation procedure such as dehydration or staining, which are commonly applied in the electron microscopy of biomineralised structures. The absence of visible sharp edges could also suggest an amorphous layer or coating to the crystals. Amorphous calcium carbonate (ACC) as a constituent of foraminiferal calcitic tests has not been reported in the literature (Erez, J., 2003). However, a crystallite-like amorphous substance “substance organique amorph” or colloidal calcite, has been described as the constituent of calcitic crystals in the tests of milioline foraminifers *Quinqueloculina sp.*, *Miliolinella cf. dilututa* *Spiroloculina excavata*, *Quinqueloculina semi-Nulu*, *Purriu bradyi*, *Pseudotriloculina lueriguta* and *Miliolinella sp* (Debenay, J.P., Guillou, J.J., Geslin, E., Lesourd, M., & Redois, F., 1998; Debenay, J.P. et al., 1996). The same authors and others have also reported similar “crystalline units” in the tests of hyaline foraminifera (Lipps, J.H., 1973). Although the FIB-SEM images obtained of this pristine specimen of *Marginopora sp.* provide an unprecedented *in situ* confirmation of the descriptions of “smoothed coalescent globular units” by Debenay et al., the resolution of the images presented here does not confirm that the individual crystals could be composed of such colloidal crystallites. However the technique and images provide a clearer view, *in situ* and undisturbed, of the inter-crystal porosity and the arrangement of the crystals than reported in earlier work through images of replicas or of thin-sections. However despite the 3D interface that is viewable and that lends a marginal field of depth, imaging is limited to presenting a static, 2D visualization of the packing arrangement and morphology of the crystals.

The FIB-SEM technique can be effective in a systematic examination of the continuous morphology of microstructures, including crystalline orientation and connectivity along any two planes of interest. Individuals or small numbers of specimens may be examined to explore the micro- and nano-structures at the surface and interior of the test. Thus, this method can provide considerable advantages over the methods of thin-sectioning and Hottinger araldite casts previously used in examining the microstructures of the foraminiferal test. A further advance in

the examination of the organic-inorganic matrix and the process of chamber formation and crystallisation in foraminifera could be achieved by preparing specimens by systematic precise FIB milling for cryo-SEM and cryo-TEM rather than by sectioning specimens with a blade or by crushing frozen samples. FIB milling of surfaces of a block of the specimen and imaging with SEM also can be used to generate slices of data used for 3D imaging of an entire 3D section of the specimen.

The advantages presented by this technique have been effectively used for TEM sample preparation of biological non-conducting materials, such as calcitic lenses of trilobite eyes (Lee, M.R., Torney, C., & Owen, A.W., 2012), silica bodies in the bristles of plants (Dietrich, D., Bäucker, E., & Marx, G., 2003), calcitic prisms of the noble pen shell *Pinna nobilis* (Wolf, S.E. et al., 2012), human molar and incisor teeth (Xie, Z., Kilpatrick, N., Swain, M., Munroe, P., & Hoffman, M., 2008), the larval shell of a pearl oyster, *Pinctada fucata* (Yokoo, N. et al., 2011), the dentine of ivory (Jantou, V., Turmaine, M., West, G.D., Horton, M.A., & McComb, D.W., 2009) and the nacre of *Haliotis discus hannai* (Mukai, H., Saruwatari, K., Nagasawa, H., & Kogure, T., 2010). Calcitic foraminifera tests are very difficult to fracture in a controlled manner because calcite has conchoidal fracture, the tests are porous and exhibit an anisotropic morphology. This technique overcomes the inherent disadvantages of preparing thin-sections by ultramicrotomy of a densely packed calcitic test with a small fraction of organic material - which result in the calcitic crystals flying off the base of the embedded epoxy (Towe, K.M. & Cifelli, R., 1967); my experience confirms this. However the tests can be prepared relatively easily for systematic investigation with TEM using the methods developed in the material sciences and applied to selected biological materials. Very recently, the calcitic test of *Amphistegina lessonii* has been prepared using FIB milling for TEM and Near-Edge X-ray Absorption Fine Structure (NEXAFS) spectroscopy in a study which showed that Mg is uniformly distributed for Ca in the calcite mineral lattice (Branson, O. et al., 2013). Mg/Ca ratios in foraminifera tests are widely applied as proxies for ocean temperature (Nürnberg, D. et al., 1996). The FIB milling technique aided in the study to make an important contribution in understanding the calcification mechanism across the foraminifera test.

Higher resolution instruments that can spatially resolve upto 5 nm are now available which could examine nanoscale structures and connectivity in foraminifera architecture. The study of foraminifera nanostructures, microstructures and the *in situ* imaging of the organic-inorganic matrix at high resolution with this technique could contribute to the understanding of pathways of biomineralisation and the hierarchies in the construction of biomineralised structures. Similar applications in the life sciences have been described by Hayles (Hayles, M.F., Stokes, D.J., Phifer, D., & Findlay, K.C., 2007).

3.4 Electron Microscopy of *Marginopora sp.*: 2D visualization of calcite crystal morphology, dimensions and orientation in the region surrounding a chamberlet

3.4.1 Introduction

In the previous section an *in situ* view was presented of a milled cross-section of the upper wall of the surface chambers of *Marginopora sp.* The morphology of the calcitic crystals was visible and described as rod-like and randomly oriented in section with a veneer of crystals laid flat on the surface.

A vast body of literature describes the use of walls of foraminiferal tests for the taxonomic classification of foraminifera (Cushman, J.A., 1959; Hansen, H.J., 2002; Lipps, J.H., 1973; Loeblich, A.R., Tappan H., 1974; Wood, A., 1949). Studies that reported electron microscopy of carbon replicas of the porcellaneous walls of milioline foraminifera (*Archais*, *Quinqueloculina*, *Spiroloculina*, *Peneroplis*) provide descriptions of their crystals: rod-like, rounded needle-like, lath-like and of their random orientation in the wall structure (Hay, W.W. et al., 1963; Lynts, G., Pfister, R., 1967). In another early electron microscope study Stapleton compared hyaline benthic foraminifera wall ultrastructure with data from light microscopy (Stapleton, R.P., 1970). In their detailed exposition of the crystallographic aspects of wall ultrastructure of foraminifera, Towe and Cifelli presented a SEM study of the porcellaneous wall structure of *Spiroloculina sp.* and *Quinqueloculina sp.*, but questioned the random orientation (“three dimensional disorder”) of crystals in the porcellaneous wall as a rare and unusual case of biological calcification (Towe, K.M. & Cifelli, R., 1967); biological inorganic phases are normally organized in some orientation of the crystallographic axes. The authors noted that the thickness of the crystals and the orientation remained unknown. By also noting that in the granular walls of foraminifera crystals were never observed to be parallel or perpendicular to the surface of the wall, Towe & Cifelli argued that the granular wall, usually described as randomly constructed, was not so. Further details of crystal structure in porcellaneous walls were revealed in an SEM study of *Quinqueloculina sp.* which showed images of needle-like crystals in an organic mass on the surface of a test. These data were used to support a suggested mechanism of the formation of the morphology of needle-like crystals and their suggested coalescence to form flattened aggregates of the surface veneer: that crystallite precursors of crystals were the first biomineralised units (Debenay, J.P. et al., 1998).

SEM studies of *Marginopora vertebralis*, a porcellaneous-walled foraminifer closely related to the species studied here, have been used to differentiate between two types of walls (Ross, C.A., 1976; Ross, C.A. & Ross, J.R., 1978), characterise its symbionts (Lee, J. et al., 1997; Richardson, S.L., 2001) and describe through images a few of its microstructures (Lee, J., 2011). Only Ross’ study showed for the first time a second type of wall and differentiated two types of calcitic crystals. The first type of crystals described in earlier works as rounded rod-like randomly oriented crystals formed the walls of the chambers and a flattened surface veneer. Ross further described elongate needle-like parallel crystals in bundles forming porous walls along the apertures to the lateral chamberlets. Reid’s systematic SEM study of the walls of a large porcellaneous symbiotic benthic foraminifer *Archais angulatus* first suggested that despite numerous past studies the porcellaneous wall structure was more complex than had been

reported for five decades (Macintyre, I., Reid, P., 1998). Importantly, the authors identified some evidence of parallel orientation of crystals in the internal walls and the research characterised a recrystallised form (minimicritic $<1\ \mu\text{m}$) of the rod-like Mg-calcite crystals in the walls (Macintyre, I., Reid, P., 1998). The authors reported that its distribution increased in the test as the test size increased. Using these data, Macintyre and Reid provided explanations to support their contention that the rods were the fresh crystals and transformed to a minimicritic form with the aging of the walls i.e. the rods were recrystallised to “the colloidal calcite” reported by Debenay et al.

Very limited high resolution data of crystalline material for only a few asymbiotic smaller porcellaneous foraminifera has been presented in previous work to support a proposed mechanism of biomineralisation in a large superfamily of foraminifera. Only a single TEM image of the crystals of a small asymbiotic milioid foraminifera *Alveolinella quoyi* was presented in a comparative study of walls of hyaline and porcellaneous foraminifera; it showed the rod-like crystals and proposed that they contained fibrous core and inclusions of organic material or water (Conger, S.D. et al., 1977). Similarly, a single TEM image provided evidence to show that the hypothesis of epitaxial growth of biomineralised crystals failed for porcellaneous foraminifera; that in fact elongate crystals formed in a vesicle of *Calzituba polymorpha*, a single species of a porcellaneous foraminifera (Berthold, W.U., 1976). Again, very few authors have reported on the use of the cryo-SEM technique in investigations of foraminifera tests: allogromiid foram tests were investigated for the ultrastructure of the organic linings and the relationship with the agglutinated layers (Goldstein, S.T. & Richardson, E.A., 2002); characterization of the morphology of the organic “cement” of some species of the agglutinated foraminifera identified this as strands, mesh-works and foam-like masses (Bender, H. & Hemleben, C., 1988). Bowser and Travis refer to cryo-fractured specimens to obtain 3D-like images of cellular ultrastructure in their description of methods for studying the soft parts of foraminifera, while another study reported the use of cryo-SEM to study the tubulin structures of the reticulopodia in eight species of foraminifera (Bowser, S.S. & Travis, J.L., 2000; Habura, A., Wegener, L., Travis, J.L., & Bowser, S.S., 2005).

Compared to the relatively limited capabilities of the instruments used in previous research, the present SEM and TEM instruments allow a much higher magnification and resolution of structures; backscatter modes of detectors provide additional data. The research presented here explored the crystalline structures of *Marginopora sp.* in order to obtain at higher resolution improved views of the complexity and variety of the basic structural units of the test of a large symbiotic foraminifera and, to supplement previous studies and suggested mechanisms of the biomineralisation of a porcellaneous test. The micronic and sub-micronic structures at the surface and internal wall of the test were investigated. Here are presented selected high resolution SEM images and TEM images of tests of several pristine specimens of different growth stages of *Marginopora sp.* fixed chemically *in vivo*.

3.4.2 Observations- SEM

A systematic SEM study using flash frozen (cryo) and dehydrated (graded ethanol and critical point drying) pristine specimens of embryonic, juvenile, adult and mature reproductive stages of *Marginopora sp.* resulted in a large number of observations of the surface, fractured walls and microstructures of the ontogenic stages of *Marginopora sp.* A series of images was obtained of

crystal forms and microstructures of several specimens; each specimen represented a sequential ontogenic stage of *Marginopora sp.* The observations of the ontogenic series (Appendix B) provide the expanded detail and context from which are abstracted the images that are presented here.

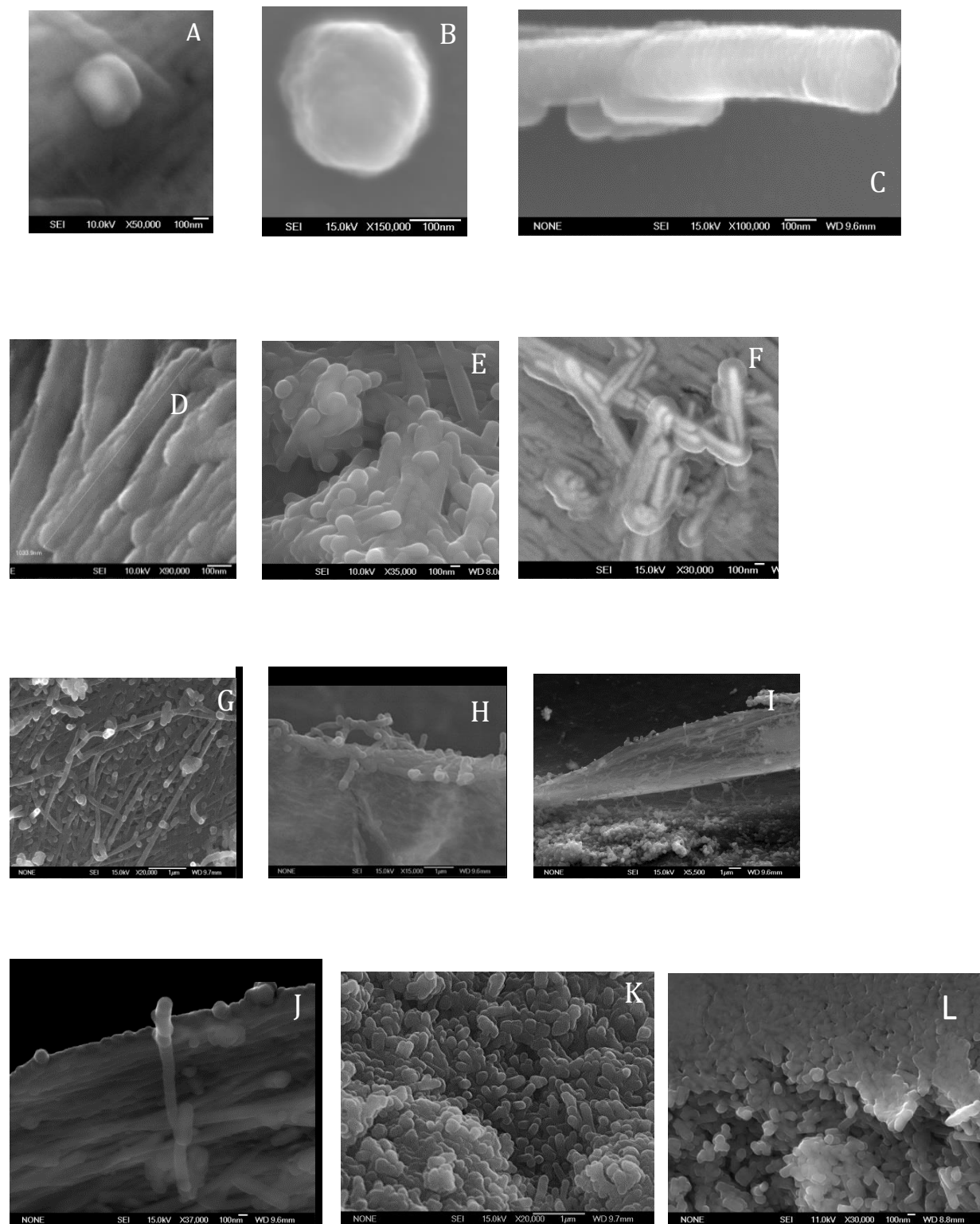


Figure 36 Colloidal crystallites and crystal morphology during biomineralisation.

Figure 36 is a high resolution SEM (bar: 100 nm) view of a collection of crystals scattered within organic material on the surface of the test of an ontogenically early stage of *Marginopora sp.*

A: The single crystallite structure consists of a distinct electron-dense core (confirmed by EDS – not shown – as calcium, magnesium carbon oxygen) that has a cross-sectional area 10,566 nm² (47-70 nm wide) and an outer sheath of electron-lucent material that has an area of 39,133 nm² (37-50 nm wide).

B: In high resolution in SEI mode a large crystallite is imaged; the surface is bumpy textured and the edges are roughly rounded, average diameter of 280 nm and an approximate cross-sectional area of 60,700 nm².

C: The crystallites appear to be growing one-dimensionally in faintly circular wave increments that are fused and form an elongate crystallite. The cross sectional dimensions of the crystallite is 135 nm x 71 nm and area of 9,660 nm² and a distance of 9-16 nm between successive “wave”-like growth lines.

D: Elongate crystallites appear to be of variable lengths; however approximately 800-1000 nm appears to be an observable range of lengths (this image).

E: The bulbous ends of the crystallites and a clumped aggregation of crystallites oriented in different directions are observed frequently.

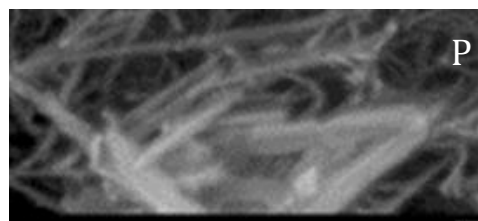
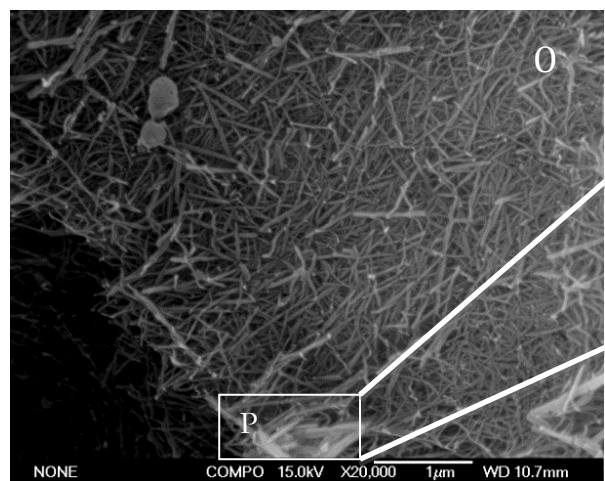
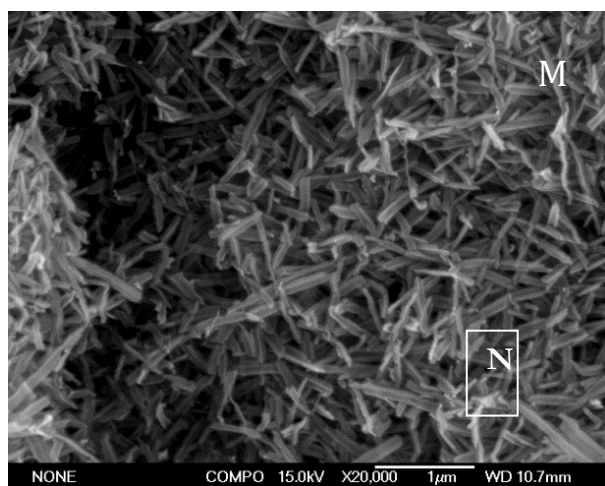
F: SEM image reveals the internal structure of the 1.4-1.6 µm long crystallites to consist of a 1.1-1.2 µm long core that terminates in a bulbous form. The diameter of the bulbous form is slightly larger than the baton-like rod. A 100-200 nm sheath of electron-lucent bumpy material covers the entire length and bulbous end of the crystal.

G: The wavelike or globular fusion of elements appears to grow to over 2 µm in length. The fused colloidal crystallite elements appear flexible and are able to bend over each other. A bright drop-like end appears on most of the linear elements. The fused elements appear closely linked to the organic lining (also clearly visible at high magnification in H).

H: An organic lining lifted or stretched back along a wall by dehydrating processing shows a mass of the same shorter crystals

I: At higher magnification these shorter crystals appear globular and fused to form clumps of 3 or more units.

J, K, L: The shorter crystals appear to be held together in an apparent mat or clumps by the adhesion of the sheaths or by an organic material. These crystallites appear to be cohesive.



M: At high resolution in backscatter mode, a view of a region on the surface of the same test at the edge of the prolocular region and the developing annular chambers (in a growth zone) shows an organic material covering a large clump of needle-like crystals; a mass of disoriented needle-like faceted crystals appear in the growth zone.

N: At high magnification these faceted crystals show an electron dense (emitting) thin core and sharp edges. Similar faceted crystals also exhibit may appear more flexible, more electron translucent and have a brighter tip.

O: In backscatter mode, these faceted crystals show a larger electron dense core with an electron lucent sheath i.e. enclosed in a possible organic mass.

P: At higher magnification of the region boxed in O the electron dense core is clearly visible and appears linear. Some charging artefacts of imaging are apparent.

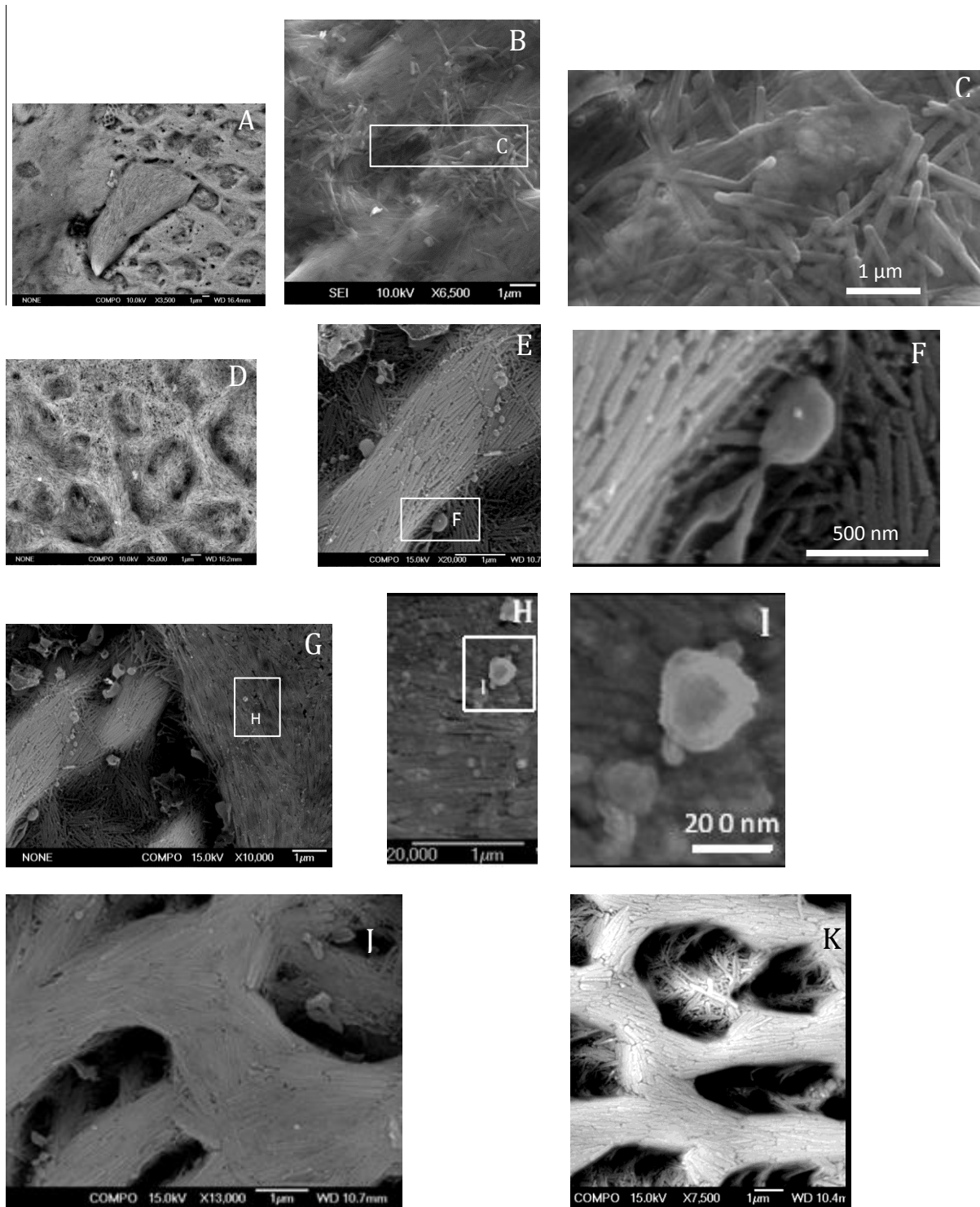


Figure 37 Crystal formation in vesicles, transport and construction of walls.

In Figure 37, high resolution FE-SEM observations of the test of a juvenile or neanic (2 mm diameter) test of a pristine specimen are shown.

A: The edge of the prolocular region (arrow), a large apparently bundle of fused elongate crystals on the surface of the test packed and fitted in a section. The surrounding area consists of an anastomosing flow-like mesh or network of crystals with depression-like gaps between raised bridge-like smoothed accumulations of crystals.

B: A collection of loosely scattered elongate needles or crystallites on the surface covered by a transparent organic mass or membrane, possibly a vesicle. The needle-like crystallites appear to be flowing into or aligning with other crystals that are organised into the smoothed structure.

C: At higher magnification, needles show a brighter core, bright tips, bending over each other, translucency; disc-like crystallites occur in a denser organic sac-like mass.

D: In backscatter detection mode the crystalline elements of the structure are highlighted; crystals appears densely packed and oriented in clumps and splayed over to form the structure; the smoothed surfaces are not evident in backscatter mode.

E: A higher magnification at the surface of the beam- bridge like structure of the mesh shows assemblages of finer crystals of apparent different density than the built up beam are visible at the lower and upper corners. Several large circular or globular crystallites of different sizes appear along the edges of the structure.

F: The beam like structure and a smaller, similar structure appear to be fusing through the “filling” in of crystals; circular vortex-type assemblages of bundles of finer crystals are visible adjacent to the structure. The right hand side of the images consists of an apparently smoother structure packed with crystals with needles that appear flattened and thickened. A difference in intensity is apparent between the two sets of crystals in the image.

G-H: The flattened euhedral needles appear at high magnification to have a boudinaged appearance; circular layered small crystallites appear in clusters and in large single units.

I: At high magnification, the circular crystals show a rougher texture and a layered core is apparent.

J: An anastomosing beam mesh of aggregated flattened crystals with the voids in between filled with randomly oriented crystals appearing to add to the existing structure.

K: The surface of the structure appears smoothed and a similar but less dense structure is visible at a depth suggesting the storeyed construction of the walls proceeds in 3 dimensions with the construction of the mesh of bridged structures that are gradually assembled, increased in density, smoothed and expanded to broaden and fuse; the gaps or voids appear to be regions of a supply of crystals and are eventually filled in with crystals.

3.4.3 Cryo-SEM and TEM Observations of Selected Microstructures

The juveniles contained in an organic transparent mass of viscous fluid that was removed from the surface test of a large specimen of *Marginopora sp.* that had reproduced asexually were flash frozen and used with high resolution cryo-SEM microscopy. Selected images of structures from hydrated specimens at very early stages of growth (< 0.5 mm) complement the observations presented.

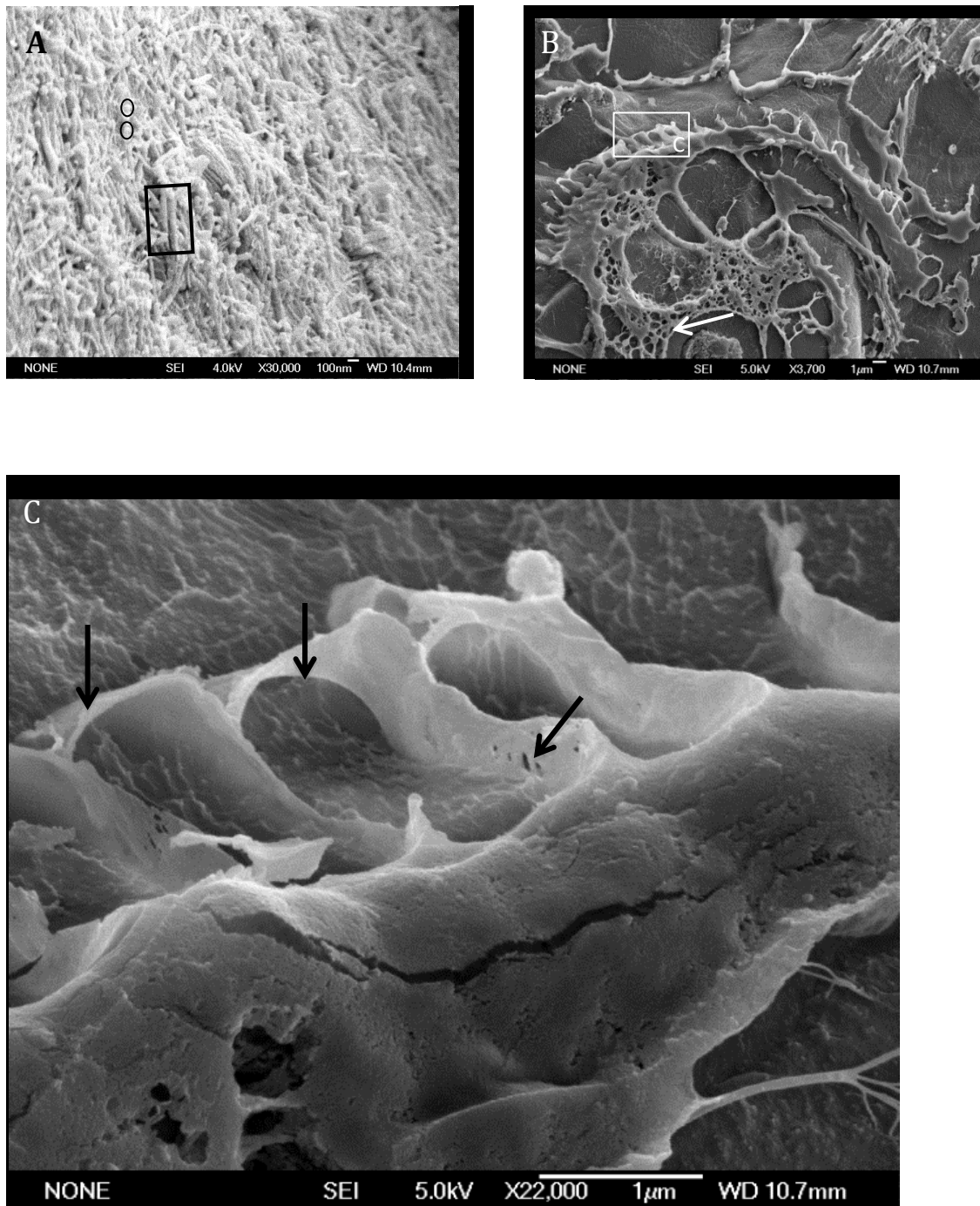


Figure 38 Cryo-SEM image of organic structure of early ontogenic stage of *Marginopora sp.*

A: A fractured specimen showed an organic lining visible under a dense matting of crystallites and crystals stuck or embedded in the lining. Since graded dehydration procedures were not performed, it is unlikely the organic material had peeled back or shrunk carrying with it crystallites that may adhere to it during any shrinkage. The beaded or globular nature of the crystallites is clearly visible (box) and globular stand-alone crystallites are abundantly scattered (circles).

B: A fractured area of the frozen fluid mass revealed an unusual non-crystalline structure probably of protoplasm with a dense nucleus-like structure at the centre (arrow). The structure resembles in cross-section a template of a cross-section of the test of the juveniles of *Marginopora* sp. but a calcified test is absent; neither are crystals nor crystallites embedded or fused with the structure. An organic form of an apparent annular chamber divided further into chamberlets, of which some are fully intact and others partially intact, remains attached to the larger mass of amorphous material. It is not possible to confirm that the imaged structure is that of *Marginopora* sp.

C: At higher magnification the morphology of the chamberlet-type structure is evident partially in 3D; these convex, arched and walled non-crystalline structures and the adjacent continuous organic structure are serially connected. Some areas of the structure are partially damaged by the electron beam (arrows).

Ultra-thin sections of the walls of pristine adult specimens were used to visualize the microstructures at high resolution using TEM. Selected results are presented here:

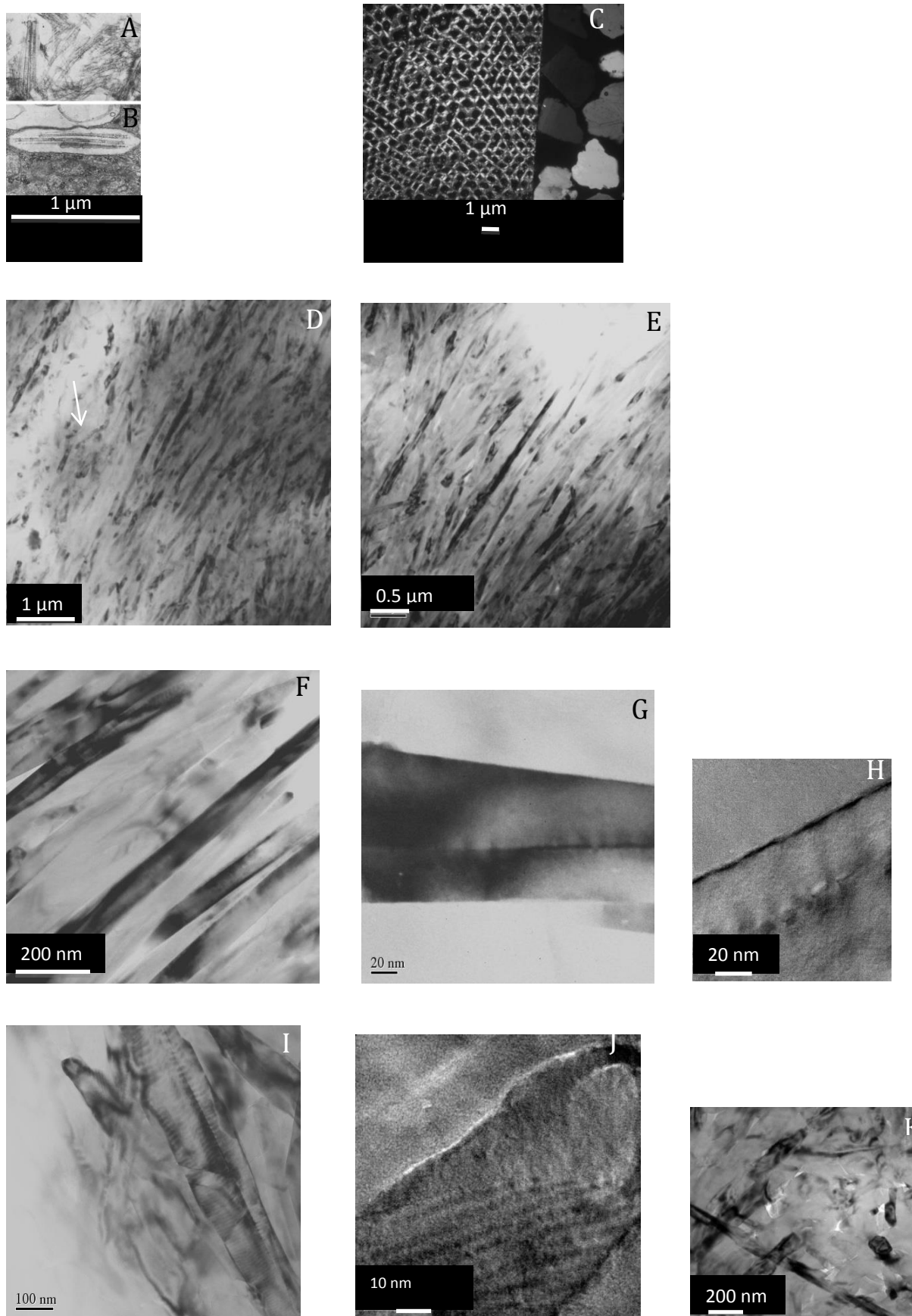


Figure 39 TEM image of crystal orientation and porosity in *Marginopora* sp.

In Figure 39A-B, TEM images of crystals in the test of *Calzituba polymorpha*, a miliolid foraminifer (presented for comparison) are of low resolution but show in a TEM section crystals in random orientation and within a vesicle (Berthold, W.U., 1976).

TEM observations of the crystalline structure in approximately 5 μm^2 area of a parallel thin-section (Figure 39, B, C(Figure 39C-E) show crystal lengths to be variable (0.7-2 μm and width approximately 0.04-0.08 μm). In this region of the wall there is a roughly parallel orientation of crystals in an area; crystallites and masses of crystals appear in a possibly organic mass (arrow - left upper corner). Sets of roughly parallel crystals (at least 6-7 in one set) occur (D). There is a variability in intensity - dark and light- among crystals and within individual crystals (D;). Crystal morphology appears rhombohedral but variations in morphology are frequent (E). Facets are clearly visible and interfaces between crystals are sharply delineated (F-G).

H: Higher magnification views of the facets indicate a series of suture-like less dense regions which may be defects along the facet; these could also indicate the presence of another facet or could be inclusions aligned linearly within the crystal or may indicate that one crystal has penetrated another.

I-J: Moiré fringes are also observed as shown in a high magnification image of crystals of the wall. The formation of these Moiré patterns may be due to double diffraction from overlapping of crystallites with minor dislocations of crystal lattice.

K: In an adjacent area, crystal orientation appears random or criss-crossed or interspersed with cross hatching. The inter-crystal porosity is apparent and the variability in crystal habit is evident in cross-sectional views of several crystals.

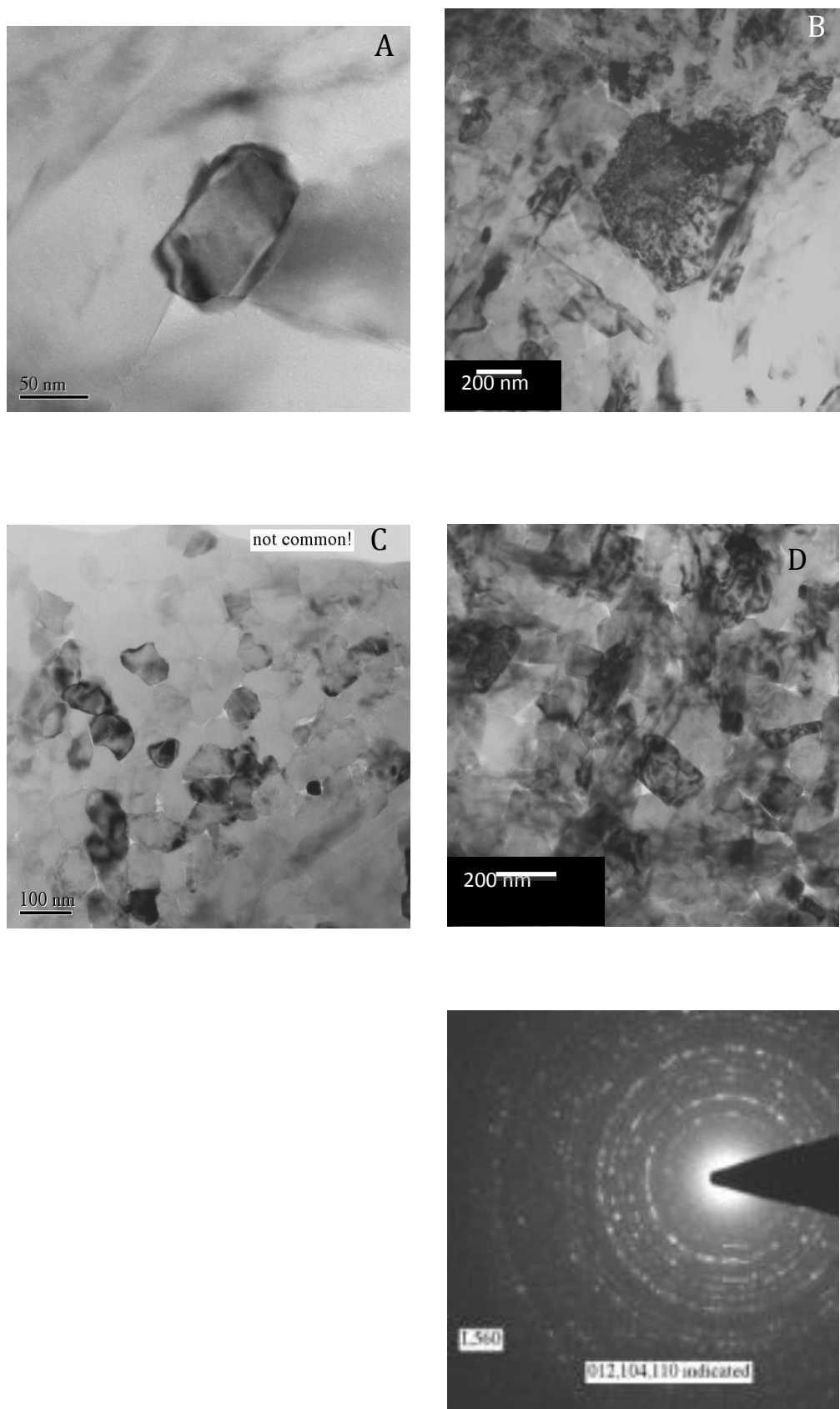


Figure 40 Variable size density and morphology of crystals.

In Figure 40 A: An equatorial view of the faceted end of a crystal or crystallite shows its approximate rhombohedral habit and cross-sectional dimensions of 59 nm x 119 nm and area of approximately 346 nm²; an apparent lining, possibly organic, 4.9-9 nm wide is visible along the edges (arrow). Adjacent crystals are oriented in various directions but their facets are visible. These facets are 52-80 nm wide (measured perpendicular to the edge of a facet).

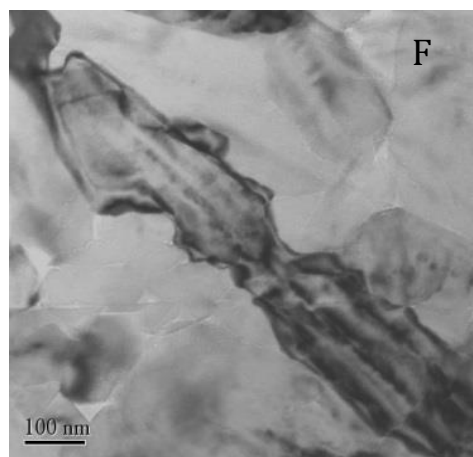
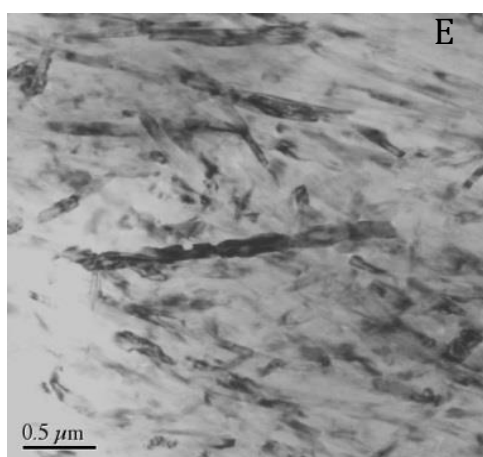
B: An unusually large (638 nm x 929 nm) crystal facet with internal variations in density (intensity) and numerous dark inclusions of granular matter- possibly organic material or water.

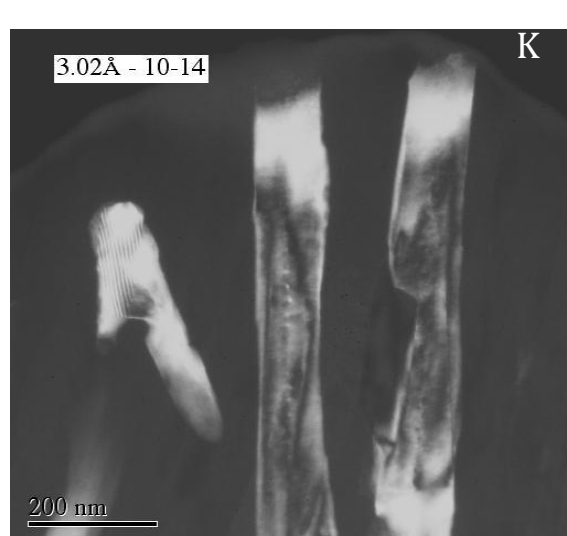
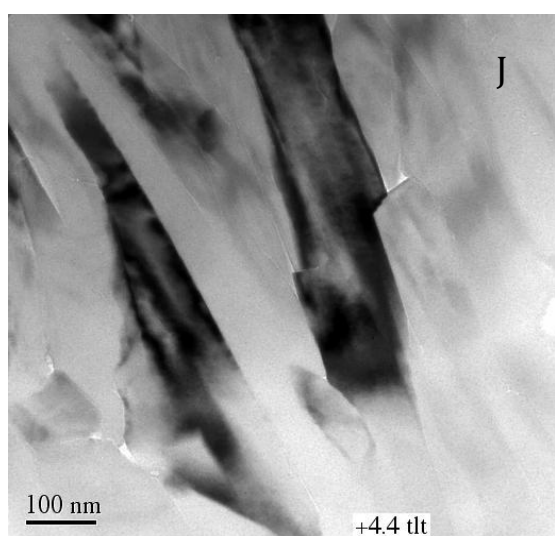
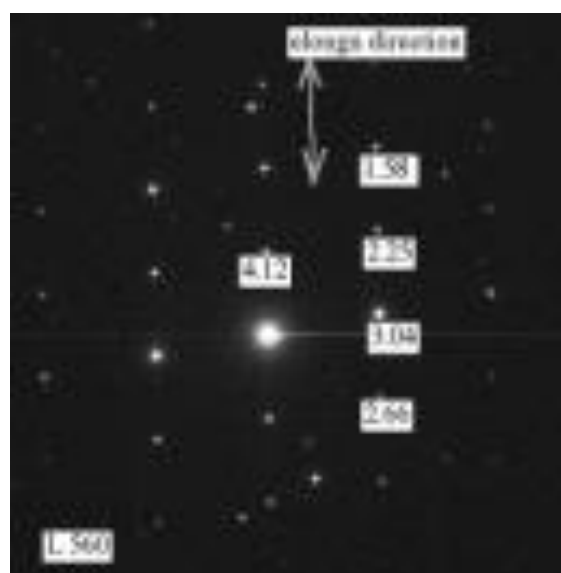
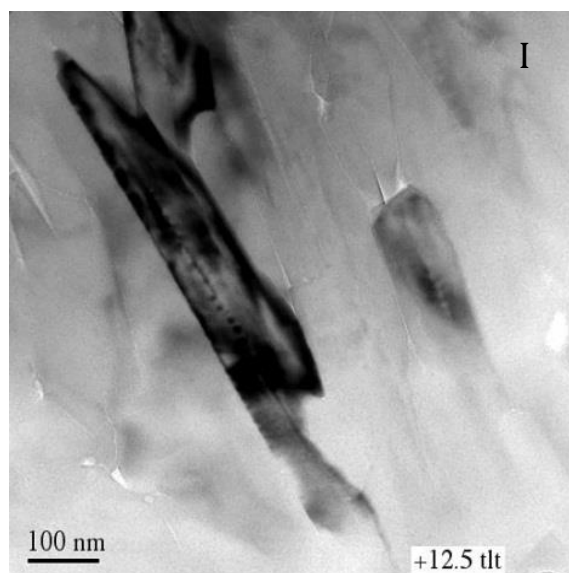
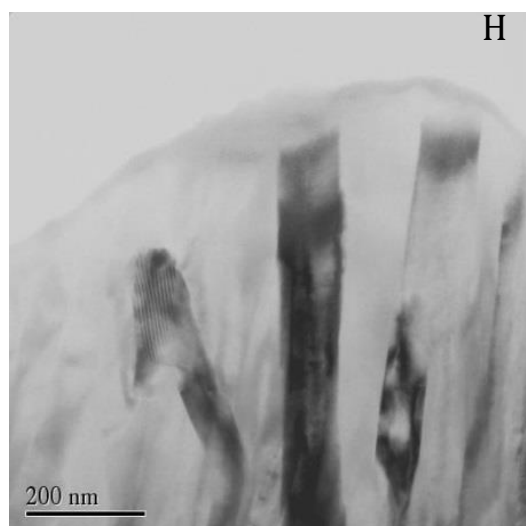
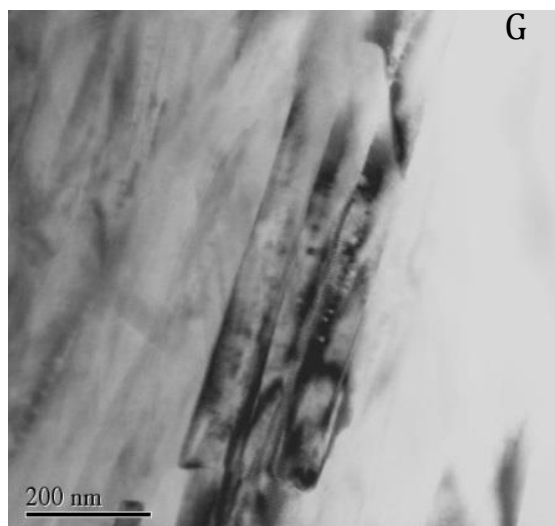
C: End-on view of apparent cross-sections of crystals indicating a packing of similar orientation i.e. oriented as a bundle with the c-axes of the crystals in the bundle parallel to each other. Variations in the habits of the crystals are apparent. There is a difference (increase) in the intensity at the periphery of each crystal- i.e. outline of each is apparent. An interesting feature is that numerous cross-sections show curved regions and an amorphous-like morphology (arrow) rather than angular facets predominate. Large differences in density (intensity) are visible in the aggregate like mass.

D: Several crystals of different cross-sections, lengths (> 2 μ m) orientations indicated polycrystalline and of several orientations in the diffraction pattern.

E: An unusual morphology- several elongate crystals of corkscrew-like appearance may be defects in the crystal structure. The structure is of general uniform intensity so it is one crystal.

F: A higher magnification view of a “defective” crystal showing a thin fibrous line running along and in the centre or core of the crystal and possible striated particle-like inclusions. Thin horizontal striations also occur along the face of an adjacent crystal (arrow).





G: A set of 5 crystals of similar length and orientation with closely packed facets. Some contrast within is evident showing a possible porosity within the crystal. The crystal facets are sharp and allow differentiation of individual crystals. The area between the ends of two crystals appear to be “filled” in with possibly organic material (circle), 3 crystals of darker intensity appear to have sharper facets while others appear bumpier. A linear set of less dense areas are visible located along the c-axes may be possible organic inclusions or defects (arrow).

H: Bright field imaging shows crystals of similar orientation, size (102 nm wide) and nearly parallel – the set of crystals appear enclosed within an organic envelope or vesicle. Sections of the crystals have very high intensity possibly being too thick (large sized or dense) for the beam to penetrate and others low.

I: A tilting of the sample while imaging provides a view that is parallel to an interface and shows the crystal and inter-crystal interfaces to be sharp. The diffraction pattern shows an intense central core indicating a possible crystalline core but its nature still is unresolved. Particle like inclusions occur along the core and striation-lines occur along the edge of the crystal.

J: Similarly, the sharp facets of the crystals and the variable intra-crystal density are visible.

K: In the dark field image the distribution of bright areas is towards the ends edges and noticeably in the spot-like inclusions of the crystals indicating the occurrence of heavier elements. A Moire pattern is discernible at the end of the crystal which may indicate some lattice misorientations.

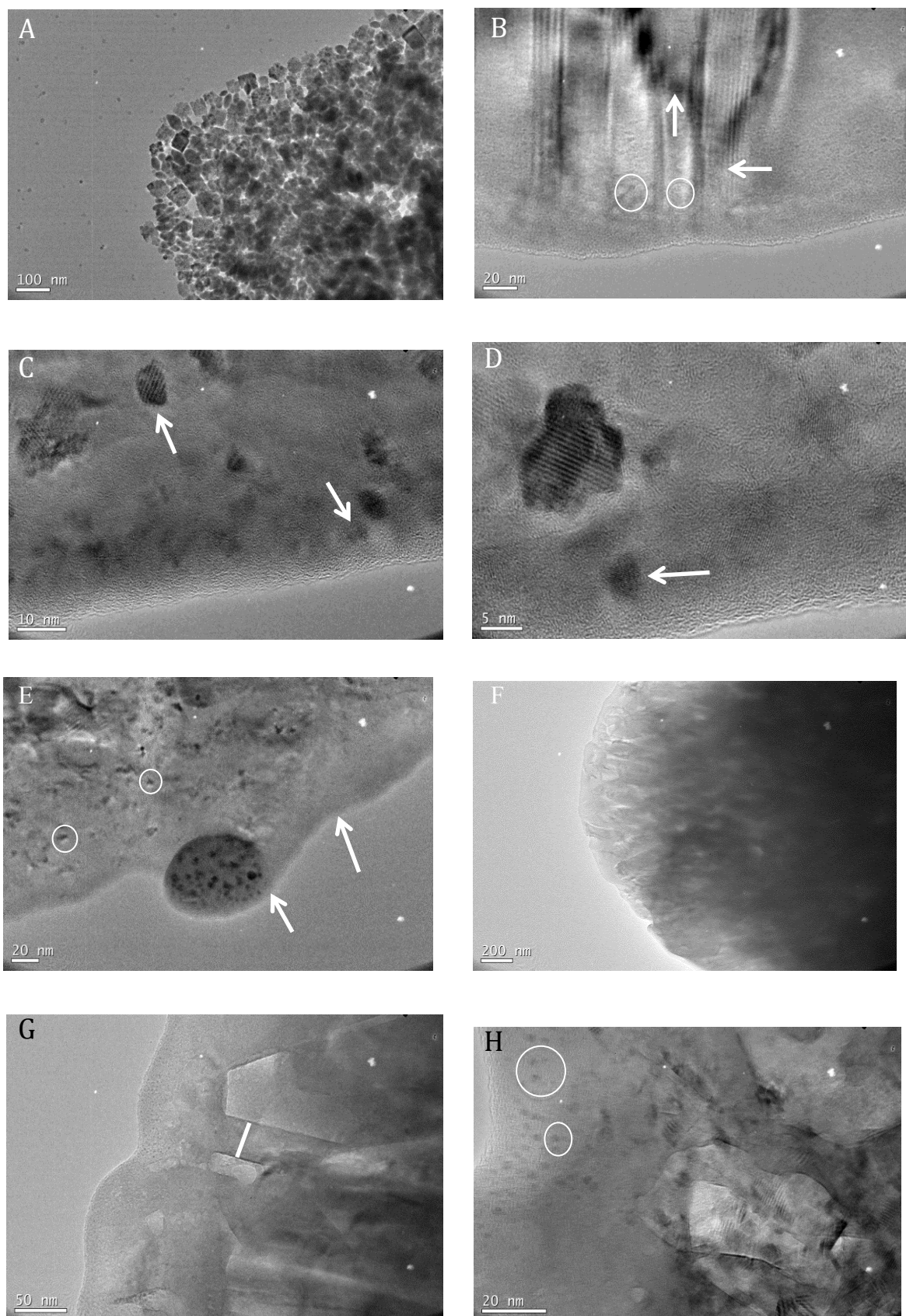


Figure 41 High resolution images of Crystal organic interface.

(Camera artefacts appear as white spots on these images; circles : crystalline inclusions, arrows: organic material).

TEM examination of walls around the pore (Figure 41 A, B). Observations of the thin-section at very high resolution reveal clearly the granular type electron dense inclusions in the large area of crystalline material indicated by lattice fringes and the edge of a lining of an organic material.

In C: At high magnification, several crystal lattice fringes are visible uniformly distributed across darker crystalline particles which appear in the grey organic material indicating these particles are single crystals. The grey areas in part could be organic but lattice fringes are visible in these areas also indicating they contain less electron dense crystalline single particles.

D: Crystal lattices are apparent in electron dense crystals embedded in the amorphous material. Crystalline lattice fringes are clear in very electron dense large particles of 14 nm- and also visible in an adjacent less dense particle which at very high resolution shows a visible outline.

E: Other inclusions of dark colouration including possibly oval dense cellular vesicles approximately 88 nm wide and 291 nm² in area has numerous very electron dense 2 – 4 nm sized particles included appear to be embedded in relatively widespread organic material. This vesicle is at the edge of the organic material possibly in the process of inclusion or expulsion. Numerous electron dense (2-3 nm) particles and an approximate 40 nm crystalline particle with an elongate electron dense 20 nm inclusion are embedded in the organic material outside the vesicle.

F: Elongate possible crystals in a virtually parallel orientation appear enclosed within an organic material with a curved sac-like profile indicating it may possibly be a vesicle. Lattice fringes are not apparent.

G: The sharp facets and edges of the structures of variable dimensions, 19 nm – 44 nm wide, are visible at high magnification with organic material occupying approximately 25 nm space between the structures. Very small (2 nm) particles are visible enclosed in a electron lucent possible vesicle.

H: A variety of structures appear meshed in a region that is dominantly layered of organic material. 2 - 4 nm particles with lattice fringes occur in rows at the edge of the organic material. Crystalline lattice fringes appear in numerous larger electron dense crystalline particles. Electron lucent enclosed areas – amorphous and of straight edges overlay the crystals. It is difficult to ascertain the nature of these electron lucent areas.

3.4.4 Results in Summary

This study's findings of the test of *Marginopora sp.* showed that:

1. The primary biomineralised structural sub-micrometre scale units are approximately spherical colloidal-crystallite nanostructures (CCN) that in cross-section or plan-view appear disc-like. The nanostructures appear layered, consisting of a heavier core that is inorganic (calcium based) of average diameter 20-26 nm (larger 130 nm) and a total average diameter in the range of 40-48 nm (large 238 nm), i.e. with a possible organic lining or envelope. However, smaller particulate electron-opaque units less than 10 nm in cross-section length occur in crystalline and amorphous frameworks. Amorphous globular aggregated Mg-CaCO₃ nanostructures also occur on the surface of the test.

2. Data show that the CCN appear assembled in increments to form linear and curved sub-micron structures i.e. linked structures that appear in flexible or rigid forms.

3. Mg-calcite crystals are polymorphic. During the biomineralisation process the Mg-calcitic elongate crystals possibly appear in different forms:

- a) an extruded form that appears fused, flexible, longer than 1 µm, rod-like elongated anhedral crystals with convex surfaces, a rounded end, a bright tip;

- b) less than or approximately 1 µm long linear baton-like crystals with a head that is larger or the same size as the baton. Both these forms have an electron dense core and an electron-lucent covering sheath structure;

- c) an elongate euhedral (sharper faceted) form of crystals containing a fibrous long core enclosed in organic material which is visible in early growth stages; these crystals also appear to have a crystalline electron dense core that thickens during biomineralisation; but elongate crystals can be comprised of fused elements (boudinage) in some microstructures, are noticeably flattened in those microstructures and can be aggregates of more than one elongate crystal.

Extruded rods, boudinaged rods, clumped aggregates apparently composed of these crystallites and faceted needles with a core are imaged on the surface and as constituents in the internal microstructures of the early stages. These were observed only on the surface of mature stages (see SEM images of ontogenic stages in Appendix B). The layered CCN frequently occur on and in areas composed of the boudinaged rods.

- d) elongate smooth faceted minimicritic crystals are visible in the internal walls of the adult and mature specimens. A core is not apparent at the resolution of SEM when the crystals appear shorter "minimicritized" in most areas of the internal walls of later ontogenic stages; TEM images reveal a core in these crystals.

4. At resolutions of tens of nanometres the euhedral elongate crystals show varying lengths, densities, internal porosities, intra-crystal porosities, monocrystallinity and polycrystallinity, dislocations or overlapping of the crystal lattices, varying cross-sectional morphologies, a possible crystalline core and regular spaced dense particulate inclusions mostly of unresolved composition, crystalline as indicated by lattice fringes, and a possible organic envelope- i.e. a

heterogeneous and composite structure exists at the nano-crystalline level. However the cross-sectional dimensions of all forms of the crystals shows a consistent range of size (65-95 nm).

5. Organic material as a lining is likely a constituent of the euhedral faceted crystals and possibly as inclusions of the crystals; it also occurs in intra-crystalline voids and vesicular forms containing particulate crystal material, and faceted elongate crystals. The primary CCN observed on the surface of the test of very early ontogenic stages and mature stages of the test appear to crystallise within or are associated with the organic material (possibly cytoplasm and pseudopodia). Organic material appears to form a sheath in all forms of the observed crystallites and crystals and possibly between adjacent crystals arranged in a layered or bundled orientation.

6. In addition to the previously described random orientation of the crystalline units of the wall, the test is constructed in part of directed, oriented bundles of euhedral crystals. This directed orientation of crystals in the microstructure of the internal walls (septal) between the chambers and chamberlets, visible in polarised light, is confirmed by electron microscopy at a scale of several microns; also a common orientation of crystals is observed in the walls at the sub-micron (200-600 nm) scale.

7. Flash frozen sublimated microstructures of juveniles of *Marginopora sp.* revealed extruded and baton-like forms of the crystals associated with organic membranes. A structure resembling a not mineralised ontogenic early stage (possibly amoeboid) was observed to have a cytoplasmic template resembling chamberlets.

3.4.5 Discussion

The multi-scale observations of the microstructures of the ontogenic stages of *Marginopora sp.* revealed unreported details of the structure of its test.

3.4.4.1 Colloidal crystallite nanostructures (CCN)

Although *Marginopora sp.* has been studied extensively for a century, here it is shown for the first time that CCN occur as subunits of high Mg-calcite crystals in the walls of the test and on the surface at growth areas through ontogeny of the test. It is easily conceivable that juveniles at early stages of ontogeny would actively biomineralise new material for the construction of all elements of the test and mature adults would add new material to the surface. The observation in such specimens of a cytoplasmic organic material which serves as a possible sheet-matrix within which CCNs were observed indicates the biological control to this CCN mineralization.

Studies of biomineralised crystallites in porcellaneous (Debenay, J.P., Guillou, J.J., Geslin, E., & Lesourd, M., 2000; Debenay, J.P. et al., 1996) foraminifera mostly have relied on the smaller benthic and planktonic foraminifera. In a study of recrystallization of the large soritid *Archaias angulatus* the authors referred to Debenay et al.'s images of colloidal calcite (Macintyre, I., Reid, P., 1998). Neither studies presented details of CCN, probably as a result of inadequate resolution or detection capabilities. However, Bentov and Erez described cytoplasmic granules, extracellular low Mg-CaCO₃ spherulites and extracellular high Mg-CaCO₃ microspheres in amoeboids and tests of *Amphestigina lobifera*, a hyaline symbiont bearing large foraminifera (Bentov, S. & Erez, J., 2005). The current work extends to an unprecedented detail the observations of CCN in foraminifera and in a large foraminifer that is the most recent of the porcellaneous soritids. Details of the morphology, dimensions and assembled forms and

locations of the occurrence of these CCN on the surface and in other regions of the test were previously not documented in a large benthic symbiotic porcellaneous foraminifera; this study fills the gap in that knowledge.

New high resolution observations presented here of CCN assembled into varied elongate structures indicate the CCNs essential role and dominance in the mineralization of the test. Askeletal minerals are precipitated by bacteria and intracellularly in enclosed regions such as vesicles in biomineralised eukaryotes (Raven, J.A., Knoll, A., 2010). However, in the small porcellaneous foraminifera *Calzituba* sp., *Quinqueloculina* sp. and *Cyclogyra* sp. calcite crystals have been shown to be deposited in vesicles which are emptied at the site of wall mineralization, i.e. by exocytosis, rather than by epitaxial growth as in hyaline foraminifera (Berthold, W.U., 1976; de Nooijer, L.J. et al., 2009; Hemleben, C., Anderson, O., Berthold, W., Spindler, M., 1986). Observations of this process in the latter two species of foraminifera were performed using optical microscopy to view visual signs of intracellular calcification and tracers of elevated intracellular pH; detailed observations of vesicles and the morphology of the calcified units were not reported. Although the data presented here do not distinguish at high resolution that CCN are deposited specifically in circular or elongate vesicles, it is shown that cellular organic material is the matrix in which CCN appear singly, clumped, and assembled into linear nanostructures which are identifiable as crystals in the microstructures of the test. In this large porcellaneous foraminifer, the mineralization of CCN may represent an example of a broad phenomenon observed in the evolution of eukaryotes: internal deposition of skeletons followed by exocytosis.

The observation that CCN are precipitated in large quantities by the earliest ontogenic stages supports the ballast effect of the mineralization in benthic foraminifera. The assembly of the CCN at a consistent cross-sectional size into various forms of the elongate crystals raises a question of the characteristics of a possible template of that size. Although EDS showed that Ca, Mg, O, C were the elemental constituents, the precise chemical composition and structure of the CCN in the test of *Marginopora* sp. remains undetermined in this research. Infrared or Raman spectroscopy or diffraction patterns of the CCN would confirm the composition. If this is amorphous calcium carbonate (ACC) then it may be an example of stable ACC existing with calcite; whether it is separated by a membrane or is mixed is unclear from the current data.

Oddly, in the transformation of ACC to *calcite*, the ACC does have a “nascent calcite-like order”, which makes confirmation by observation of order tenuous (Weiner, S. & Addadi, L., 2011). An ACC phase has been described as a precursor to biological low magnesium calcite in sea-urchin spicule (Beniash, E., Aizenberg J., Addadi, L., Weiner S., 1997) and vertebrate enamel (Beniash, E., Metzler R., Lam R., Gilbert P., 2009) and is found as a deposit in spicules, granules, corpuscles and cuticles in gastropods, bivalves, sponges and crustacea (Addadi, L., Raz, S., & Weiner, S., 2003) but it has not been reported in the calcification of foraminifera. In the test of *Marginopora* sp. it may be likely that ACC would play a role in the high-Mg content of the calcite crystals subsequently formed.

In vivo studies of the calcification process in *Marginopora* sp. would shed further light on the mineralization of CCN in vesicles and their transformation to elongate mature crystals. Importantly, such studies would provide an elucidation of the established inference that elongate crystals are the first formed crystals in vesicles in porcellaneous walled foraminifera based

primarily on Berthold's and Angell's observation of *Calzituba* sp. and *Spiroloculina* sp., respectively. The relatively large size of the juveniles of *Marginopora* sp. would make this foraminifer a taxon of choice for tracer studies such as those that were recently conducted to demonstrate the role of elevated intracellular pH in promoting calcification and observation of lowered pH in the microenvironment during calcification (de Nooijer, L.J. et al., 2009; Glas, M.S., Langer, G., & Keul, N., 2012). Combining such methods and cryo-SEM, FIB-milling preparation of the sample for TEM, followed by TEM and EDS of the native pristine specimen would provide one approach for a detailed characterization of the CCN, organic vesicle, matrix and crystal association.

3.4.4.2 Biomineralisation

Biomineralised elongate crystals in porcellaneous foraminifera have been observed as formed in vesicles, while crystallization in hyaline foraminifera has been described as an epitaxial growth process (Erez, J., 2003). In the calcitic tests of large hyaline symbiont-bearing foraminifera, intratest variability of Mg in the test, i.e. presence of high and low Mg-calcite, has been suggested as an indicator of different pathways of biomineralisation (Bentov, S. & Erez, J., 2005). In their electron probe microanalysis study of Mg and Sr in the test of *Marginopora* sp. specimens from Lakshwadeep Islands, Raja et al. found that there was "high heterogeneity" (7-23% mmol/mol) in the intra-test Mg/Ca ratios (Raja, R., Saraswati, P.K., Rogers, K., & Iwao, K., 2005). It is conceivable that simultaneous different biomineralisation pathways could occur in *Marginopora* sp.

Three observations presented in this research could indicate such pathways. First, the observation in cryo-SEM of juveniles of *Marginopora* sp. that revealed an un-mineralised amoeboid template including chamberlets in an annular chamber provides a previously undocumented view of an organic lining and template of chamber formation in *Marginopora* sp. The organic template of the form and size of a chamber with chamberlets formed by the amoeboid cytoplasm could indicate that this is the "true organic matrix" inside which deposition occurs by spontaneous nucleation created by the organic matrix. Although not observed in that specimen, investigation in cryo-SEM of the same set of juveniles revealed a single layer of fused rod-like and baton-like crystals against an organic matrix. In other SEM data-sets, similar arrangements have been observed and CCN were observed in association with such an arrangement. This could indicate primary crystallization occurring along the matrix surface. Arnold reported a similar observation in his light microscopy study of the living miliolid porcellaneous foraminifera *Spiroloculina hyaline*. He described mineralization as beginning at the base of the matrix and expanding upwards and laterally in repeated waves (Arnold, Z.M., 1964). However, his observations did not elucidate at a high resolution the structure of the constituents in that process. Bentov and Erez report that numerous primary high Mg-CaCO₃ microspheres were deposited on both sides of the organic membrane (of a hyaline foraminifera) forming a very thin wall with the "typical morphologic shape of a normal chamber". They described that this primary wall was high Mg calcite while the subsequent "lamella" deposited by calcification is low Mg-calcite and suggested that the higher Mg-calcite was acquired from the high-Mg microspheres (Bentov, S. & Erez, J., 2005). The data presented in this study: organic matrix of the morphology of a chamber wall;

occurrence, distribution and elemental composition of CCNs, assembled fused extruded rod-like structures; and elongate faceted crystals observed in the early ontogenic stages allow the possibility that a similar pathway occurs in the formation of the crystalline high-Mg porcellaneous walls of *Marginopora sp.*

The occurrence of such a pathway does not exclude the formation of elongate crystals in vesicles and the subsequent release of crystals (the established description in literature of the mechanism of miliolid porcellaneous wall crystallization). That the control or lack of control of the orientation or setting of the mature crystals in the wall is controlled not by the mineralization pathway but primarily by pseudopodial action of the foraminifera (Angell, R.W., 1980) also permits the notion of multiple pathways.

Second, the observation of a loose deposit of needle-like crystals covered by a thin layer of organic lining on the *surface* wall of the test of *Marginopora sp.* showed that the needles were constituted of smoothed primary CCN. It can be inferred that the CCN reorganizes and forms new crystallites. Debenay et al. reported that a “double process” of reorganization and mineralization takes place “sometimes by epitaxy” when they observed a deposit of needle-like crystals in a layer of organic matter on the surface of *Quinqueloculina seminula*. The findings reported here validate their observations with a greater level of detail observed.

Third, 2-10 nm crystalline nanoparticles indicated by lattice fringes observed by TEM within larger crystals and fibrous striations observed in the crystals allow the possibility that mineralization may occur inside organic macromolecules in the crystalline structure. Crystalline nanoparticles of these dimensions have not previously been imaged in the tests of foraminifera. Nanofibres of organic membranes may create the demarcated biomineralisation space. The requirements for crystallization would be performed in the space of a few nanometres. Such a possibility is described by the nanospace theory of biomineralisation (Katsura, N., 1991).

Each of these observations and suggested pathways could be further investigated using a combination of instrumentation-based analytical techniques. Exceptions to trends observed in the biochemical compositions of foraminifera tests of similar systematic classifications are not uncommon; exceptions to mechanisms and processes by which the tests are formed are also observed. In a study of a large porcellaneous foraminifera, *Archais angulatus*, Wetmore reported that video microscopy revealed the formation of an anlage during chamber formation prior to calcification of the walls. The formation of an anlage had previously been a feature of hyaline walled foraminifera; this suggested a possible evolutionary link between two large orders of foraminifera (Wetmore, K.L., 1999). Importantly, this research documents the presence of CCN, of vesicular involvement and possibly of organic lining mediated biomineralisation.

Researchers have used cryo-SEM to compare test and cell body ultrastructure of three modern allogromid foraminifera and noted that better quality fixation could contribute to an improved understanding of systematics - which is based upon test composition and ultrastructure. While it is possible that the amoeboid structure observed here is not of *Marginopora sp.*, such a likelihood is reduced because observations were made of juveniles which were attached to the reproductive chambers of the mature specimen and were observed by optical microscopy (Goldstein, S.T. & Richardson, E.A., 2002). It is unlikely that the structure is an artefact; such a structure was not

observed through numerous observations using cryo-SEM of *Marginopora sp.* specimens of various sizes. In this research employing cryo-SEM the specimens were fractured; however, systematic examination of the specimen using FIB cryo-SEM would be very useful. That the reported crystalline nanoparticles are artefacts or impurities of the process of sample preparation is possible but unlikely because they have been observed in views of different locations, orientations and in different sizes and distributions.

3.4.4.3 Euhedral crystals

The higher resolution data in this study showed that the elongate euhedral crystals have a core and inclusions. Conger et al. had observed a core in a TEM image of crystals of *Alveolinella quoyi* and suggested that it was composed of organic material (Conger, S.D. et al., 1977). However several observations in this study of different specimens using SEM consistently show an electron dense and electron emitting core compared to the remainder of the crystals. The diffraction pattern obtained in the TEM was also indicative of a crystalline core. However the availability of a single diffraction pattern limits the force of this inference.

The particulate inclusions in high Mg-calcite crystals could be of different elemental composition. Crystalline and non-crystalline inclusions warrant further investigation at high magnification to differentiate organics between and inside the crystalline interfaces of high Mg calcite. The EDS data indicated the presence of high percentages of Ca, Mg, Sr and Mn in the crystalline rod but the resolution of the data was insufficient to show a correlation with the 3-8 nm sized particulate inclusions. Mn has been reported in concentrations up to 300 ppm in the tests of *Marginopora sp.*; it was suggested that Mn was included in the organic material and associated with the preservation of the inner organic lining (Langer, M.R. & Gehring, A.U., 1994). TEM of the sample at different tilts showed variation of shades of intensity in the crystals. This could be interpreted as one region being of higher element or doped with higher elements such as Sr, Mg, Ca, or could be organic and inorganic. Amorphous material would show as the same shade of intensity even at different tilts which indicates that the entire rod is crystalline. A TEM image (Figure 41C) of curved and rounded crystals with facets and different porosities could be interpreted as crystallites with organic sheaths, or as a cluster of elongate crystals viewed end-on; although an observation of curved crystals was uncommon, further interpretation is difficult because of the presence of layers of amorphous or organic material. The organic-inorganic composition of the euhedral crystals has implications for mechanical properties- an important aspect of structural units of the test. Artefacts evolved during TEM sample preparation by ion milling are discussed in a study of the amorphization effects of milling (Barna, Á., Pécz, B., & Menyhard, M., 1999). The observations made in this study did not discern such artefacts except that a camera-based impurity was evident.

As noted earlier, the crystals appear to undergo recrystallization in several stages and a high variability of Mg intra-test of *Marginopora sp.* has been reported. In the porcellaneous foraminifer *Archais angulatus* the recrystallized minimicritic crystals were reported to have a relatively unchanged Mg composition (Macintyre, I., Reid, P., 1998). An interesting similarity may exist between the observations of Mg in the eye-lenses of trilobites and warrant investigation in *Marginopora sp.*, a shallow water symbiont bearing foraminifera with a translucent crystalline upper wall surface and lens-like arrangement of the chamberlets. Lee et al. reported that the lenses of trilobite eyes had higher Mg and retained higher Mg than the cuticle through diagenetic stages

(simultaneous high- and low Mg-calcite). The recrystallized cuticle contained detectable Mn, Fe i.e. diagenetic alterations occurred in nanometre scale microstructures. They suggested an association of Mg with optical functions (Lee, M.R. et al., 2012).

Crystalline subunits and crystals of similar morphology and aggregation are found in biomineralised tissues or skeletons of other organisms such as corals (Bryan, W.H. & Hill, D., 1941), calcified sponges tissues or skeletons of other organisms such as corals (Bryan, W.H. & Hill, D., 1941), calcified sponges (Gilis, M. et al., 2013), and the tooth enamel of rats (H., W.F., 2005). Similar structures are also observed in calcium carbonate sediments, particularly in cemented regions around pores or voids of tests and shells (Bathurst, R.G.C., 1974), ooids (Folk, R.L. & Leo Lynch, F., 2001) and stromatolites (Andres, M.S. & Pamela Reid, R., 2006). Similar physical and chemical thermokinetic processes that apply to the formation of these minerals are also achieved by biotic control. Alternatively, a lack of biological control of the process results in a similar end result of crystallization.

3.4.4.4 Synthetic minerals

The morphology and size of CCN, the extruded form and the aggregated textured rod-like crystals observed in the test of *Marginopora sp.* are similar to CaCO_3 crystals synthesized *in vitro*. A number of approaches have been adopted in forming different materials that are similar to biologically mineralized materials. These approaches seek an understanding of the physical and chemical mechanisms controlling the morphology, composition and transformation of the mineral phases. Several of the methods, the targeted biological systems, and the *in vitro* results for ACC and crystalline forms of CaCO_3 were summarized and reviewed in literature (Addadi, L. et al., 2003; Gower, L.B., 2008; McGrath, K.M., 2001; Meldrum, F.C. & Colfen, H., 2008; Palmer, L.C., Newcomb, C.J., Kaltz, S.R., Spoerke, E.D., & Stupp, S.I., 2008; Raz, S., Weiner, S., & Addadi, L., 2000; Sondi, I. & Skapin, S.D., 2010). By comparing the morphologies and the mechanisms elucidated *in vitro* to those observed in the test of *Marginopora sp.* rapid advances may be made in understanding the biomineralisation pathways in foraminifera and vice versa. A biomimetic approach to formation of inorganic-organic colloidal crystalline nanostructures and organic-inorganic nanocomposites would benefit from the observations and further elucidation of the mechanisms underlying the observations in this study.

These electron microscopy experiments have shown information about the surface structure of the calcitic crystals and provided 2D projections of their solid structure. A better understanding of these structures could be provided by the use of 3D-TEM. The architecture and composition of these crystalline aggregates and individual crystals can be studied with nanometre scale resolution and would complement the information obtained here (Koster, A.J., Ziese, U., Verkleij, A.J., Janssen, A.H., & de Jong, K.P., 2000). An evaluation of the micro and meso porosity of the crystalline aggregates, the location and identification of possible organic inclusions within the aggregates and crystals and their relative sizes would be possible. The application of cryo-TEM to an investigation of the structure of the organic matrix and membranes in *Marginopora sp.* would likely reveal new insights. Such a structural study would complement a biochemical investigation of its organic matrix using HPLC and FTIR and provide a comparison between the structural and biochemical analysis of porcellaneous walled foraminifera and of hyaline foraminifera which have a different crystalline wall structure. Weiner and Erez reported on the constituents of the organic lining of a hyaline walled foraminifera

showing the distribution of soluble matrix proteins and polysaccharides and insoluble sulfated glycosaminoglycans by percentage weight in the matrix (Weiner, S. & Erez, J., 1984). A new view of the organic matrix of nacre was obtained using cryo-TEM which led to a reconsideration of the models of matrix structures and mediated crystallization (Levi-Kalisman, Y., Falini, G., Addadi, L., & Weiner, S., 2001). Similarly the use of FIB with TEM and FIB cryo-TEM would provide details not observed previously. Such work has been reported in the study of larger microstructures of ivory dentine (Jantou, V. et al., 2009), larval shells of the oyster (Kudo, M. et al., 2010), and smaller structures of *E. coli* (Marko, M., Hsieh, C., Schalek, R., Frank, J., & Mannella, C., 2007). Even further resolution and 3D characterization was demonstrated with FIB-EM nanotomography to provide new insights of ultrastructures of organic walled acritarch microfossils in a recent study (Schiffbauer, J.D. & Xiao, S., 2009). Such research could help elucidate the linkages in the composition and structure of the organic matrix and biomineralised crystals and synthetic or *in vitro* controlled growth of calcium carbonate crystals. Interestingly, further elucidation of the actual transfer of minerals in the test particularly of reabsorption and reformation of inner walls, could also shed light on the role of matrix-vesicle pathways for the transfer of minerals in the inner regions of bone and dentin collagen, which remains unresolved (Veis, A. & Dorvee, J., 2013).

3.4.4.5 Directed orientation of clusters of euhedral crystals

Ross described (Ross, C.A., 1976) a new wall type in the marginal chord regions consisting of clusters of parallel needles that “appear cemented”. (That wall structure is corroborated in the test of *Marginopora* sp. by images presented in Appendix B). Similarly, the description of the flattened surface veneer by Towe and Cifelli (Towe, K.M. & Cifelli, R., 1967), Ross and others is also confirmed by this study. In additional data presented also showed clearly the organic lining that covers the flattened layer. While the findings presented here do not warrant the categorization of an additional type of wall structure, it is significant that directed clusters of crystals are evident at different scales of measure. These orientations were observed under different conditions of electron microscopy of the tests of several fractured specimens of varying sizes; it is unlikely the findings are random occurrences. That polarising microscopy shows there is a possible pattern to this directedness across the sections of the test provides a context for further investigation of the distribution in the test of such an orientation of crystals. The data demonstrate that the test of *Marginopora* sp. is not entirely constructed of randomly oriented crystals and may modify the previously held observations of the past 60 years of such a lack of orientation of crystals in the walls of the tests of porcellaneous miliolid foraminifera. Recently Mikhalevich reported the discovery in Antarctic miliolid foraminifera *Pyrgoella* sp. and *Planispirinoides* sp. of outer walls similar to other miliolids but internal walls which had crystals organised into loose radial structures - randomly oriented crystals in the middle layer with parallel subtubular empty spaces i.e. an irregular pore network in the walls (Mikhalevich, V.I., 2009). The potential importance of this orientation of crystal aggregates in the architecture of the test theme is explored through the application of a complementary microscopy technique: X-ray microtomography in section.

3.4.4.6 Organic-inorganic composite

The existence of an organic-inorganic composite structure is a characteristic of the biomineralised structural units observed here at a submicron scale. The CCNs, the primary

crystals assembled of the CCNs, the baton-like crystals, the euhedral elongate crystals, further assemblages of flattened parallel ensembles or columnar bundles, all consist of organic material enclosing or sandwiched between inorganic units. It is uncertain whether the outer and inner linings of *Marginopora sp.* or the organic sheath of the crystallites and crystals have the same composition. It has been reported that the organic linings of the test and of the chamber walls consist of soluble glycoproteins and insoluble polymerized sulfated mucopolysaccharides and constituted 0.1- 0.2% of the weight of the test (Weiner, S., 1984). In agglutinated foraminifera with predominantly organic tests, these linings appear to resist dissolution by hydrogen peroxide and weak hydrochloric acid (Bender, H. & Hemleben, C., 1988; Lipps, J.H., 1973). The organic “cement” in decalcified specimens of *Marginopora vertebralis* was also reported to be insoluble in hydrochloric acid/EDTA solution (Lee, J. et al., 1997). In the test of *Marginopora sp.* the material properties of composite structural units would contribute to the requirements of the endoskeleton (test) to counter abiotic forces and grazers. Characteristics of the mineral phase and of the organic materials found in biological composite materials contribute to the mechanical properties of the aggregates and structures formed of these mineral phases (Meyers, M., Chen, P.Y., Lin, A.Y.M., & Seki, Y., 2008). Properties of abiotic calcitic crystals are well-established. However the mechanical and optical properties of biological calcitic crystals are associated with the organic material, their variable morphology, formation and aggregation; in foraminifera, including *Marginopora sp.*, these properties remain largely undetermined by experimental techniques. An understanding of the functional adaptive value of the test is predicated upon a better understanding of these properties.

At the sub-micron scale *Marginopora sp.* possesses a composite structure but it does not appear at this scale of observation to possess orientations in structural units that mimic those of the vertebrate bone or enamel, crustacean carapace, or bivalve shell; neither does the test have a similar mechanical requirement. The orientation of fibres in specific areas could be adaptive- a compromise providing a framework for the structural requirement of strengthening of the large annular discoidal test. The random orientations of crystals may allow for scattering of light for symbionts and resistance to mechanical abrasion at the surface. The existence, the mechanical properties and adaptive value of the organic-inorganic composite nature of similar primary structural units is observed and has been studied in skeletal structures across several phyla of the animal kingdom (Fratzl, P. & Weinkamer, R., 2007).

This research proposes that an interesting apparent analogy exists in the two biochemically different cellular processes: organic structural positioning and mineralization, both of which have a skeletal outcome. The formation of the organic lining and the development of the crystalline wall can be construed as consisting of broadly equivalent steps in *parallel* processes involved in the construction of the test by porcellaneous walled foraminifera. In the foraminiferal cell, the organic matrices are composed mainly of glycosaminoglycans. The completed glycosylated proteins are shed as secretory vesicles into the cytoplasm. Along microtubular strands of the pseudopodia the vesicles are transported to the cell membrane and either formed into organic linings or organic cements or are secreted (Langer, M., 1992). In porcellaneous foraminifera the process of crystallization occurs within vesicles in which ions are concentrated; the vesicles are transported by pseudopodia to the site of an inorganic wall under construction; the CCN are released, assembled into elongate crystals and fused into bundles or filled into depressions or

formed into walls (Berthold, W.U., 1976; Debenay, J.P. et al., 1998). In both processes microtubules (which comprise the pseudopodia) act as transport channels and scaffolds leading to the site of active test construction. That the microtubules are assembled of hollow parallel scaffolds is an arrangement of further interest.

3.4.5 Conclusion

An understanding of the formation and variation of the crystal morphology and its interaction with the organic matrix provides a bottom-up perspective on the microstructures assembled from these organic-crystalline constituents, and of their structural organization in the test of *Marginopora sp.* This study contributes a high resolution visualization of several constituents and steps of the process at different dimensional scales. A conceptual framework for the hierarchical organization of the constituents in the test is presented in the next section.

3.5 Results: Scanning Electron Microscopy 2D high resolution visualization of internal microstructures of *Marginopora sp.* assembled in a hierarchical structure

3.5.1 Introduction

Foraminifera are among the most interesting eukaryotic organisms for the study of the processes of biomineralisation (Weiner, S. & Lowenstam, H., 1986), their skeletons are important sources of information in the reconstruction of paleoceanographic scenarios, and their tests are a major contributor to sediments and the carbon cycle (Erez, J., 2003). Many eukaryotic organisms produce mineralized skeletons that are composites. The organization of the skeletons can be characterized by its composition and structure. Compositional constituents are organic and inorganic; the structures are often hierarchically organised. The organic constituents are often chitin, cellulose, collagen or matrices containing complex organic molecules and proteins, while the inorganic constituents are often amorphous and crystalline polymorphs of silica and calcium carbonate or calcium hydroxyapatite (Lowenstam, H.A. & Weiner, S., 1989). Hierarchical organization occurs at different dimensional scales: different constituents are found at each scale and similarly organized constituents are found at different scales or differently organized constituents are found at the same scale. Scale represents an important aspect in the biomineralised architecture of skeletons as it is indicative of different crystallographic and biological forces in small and large architectures (Mann, S. & Ozin, G.A., 1996); the position, movement, size, composition of organic templates such as vesicles, linings cells, organic foams, osteoblasts and time can set the patterns at each scale and stage of skeletal formation. Through their hierarchical organization, the skeletal forms and components represent a multifunctional organization of the constituents (Fratzl, P. & Weinkamer, R., 2007). Many skeletal components and arrangements offer protection against the environment, e.g. aragonitic and calcitic shells of molluscs; others provide structural support e.g. bones and spicules; some also have specialised optical or audio properties, e.g. spicules, otoliths; some may also provide an attachment for muscles, e.g. chitin-CaCO₃ armour carapaces of crabs and lobsters. Similar adaptive multi-

functions have been proposed for the high-Mg calcitic large test of the foraminifera *Marginopora* sp. Cocolithophores, foraminiferal and radiolarian skeletons represent evolutionary early forms of biomineralised self-assembled skeletons (Brasier, M., 1986). Self-assembly and self-healing or repair of skeletons by invertebrates (including foraminifera) using inorganic constituents usually from the marine environment, and by vertebrates using ionic constituents of body fluids are an important characteristic of biomineralisation in biological systems and contrast with abiotic mineralized structures (Weiner, S. & Addadi, L., 2011).

The hierarchical organization of skeletons of invertebrates and the hierarchies of the mammalian bone have been the subject of considerable research. In composite biological materials, the mineral-inorganic constituent provides strength but is brittle, and the organic component provides ductility. A composite structure and hierarchical multi-scale organization allows for a high energy absorption prior to failure of the material. Reports of investigations of and the state of knowledge of these inherent, defining features of rigid biological systems have been reviewed by leading researchers from a perspective of the biological, chemical and material sciences (Fratzl, P. & Weinkamer, R., 2007; Gao, H., 2006; Lakes, R., 1993; Mayer, G. & Sarikaya, M., 2002; Meyers, M. et al., 2006; Sarikaya, M., 1992; Weiner, S.A.L., 1997; Yao, H.-B., Fang, H.-Y., Wang, X.-H., & Yu, S.-H., 2011). These reviews of interdisciplinary recent applications of the principles of material science and engineering to the mature science of biological materials and systems provide an information base of principles or tools for the development of new materials and structures that are biologically inspired or biomimetic. Such investigations of biological systems also advance an understanding of the interactions between synthetic materials and biological materials in composite structures; this advances the development of biomaterials for use as substitutes or supplements in the human body.

In the materials sciences in the past there has been a separation of disciplines which is largely based on tradition. Materials were studied by materials scientists and structures by mechanical engineers. However, an inclusive view has gradually progressed in the materials sciences. The Arzt pentahedron, the most recent model of materials encapsulates the complexity of the systems through its five vertices which represent the five aspects of the uniqueness of biological materials: synthesis at ambient pressure/ temperature, multifunctionality, hierarchy of structure, self-assembly and evolutionary /environmental constraints (Meyers, M., Hodge, A., & Roeder, R., 2008). This approach has been applied recently to several biological mineralized systems.

The tests of foraminifera have been studied extensively over the past century by researchers with the objectives of identification, characterization and classification of their structures and investigation of their physical, chemical, biological, morphological properties. The outcomes of such investigations in the majority have been associated with the evolutionary position or significance, or taxonomic, stratigraphic, sedimentary, paleoceanographic, ecological and environmental value of the tests as constituents, contributors, indicators or proxies in the fossil record or in present ecosystems. Numerous researchers have posited the functions of the test, but a mechanical view of the test has not been developed. The foraminiferal test is mineralized and mostly calcitic. Among the eukaryotes, it is an example of an early form. A protist, *Marginopora* sp. has a large, complex and evolutionarily successful form; it is symbiotic - a complex association that may have allowed it to achieve an unusually large test size; and it displays adaptability in its survival in dynamic shallow coastal environments. The purpose of this section

is to adopt a fresh inclusive structural, materials sciences approach based upon the existing knowledge of the test of *Marginopora sp.* and upon new data obtained in this research to conceive of and develop an original perspective of the construction of the test. Here are presented selected results of a high resolution SEM study which show that in the self-assembled test of *Marginopora sp.*, there is a hierarchical organization of the biological composite material structures at nano-micro-meso-macro scales. The results presented here are related to a posited mechanical adaptive value of the test.

3.5.2 Hierarchical level 1: CCN

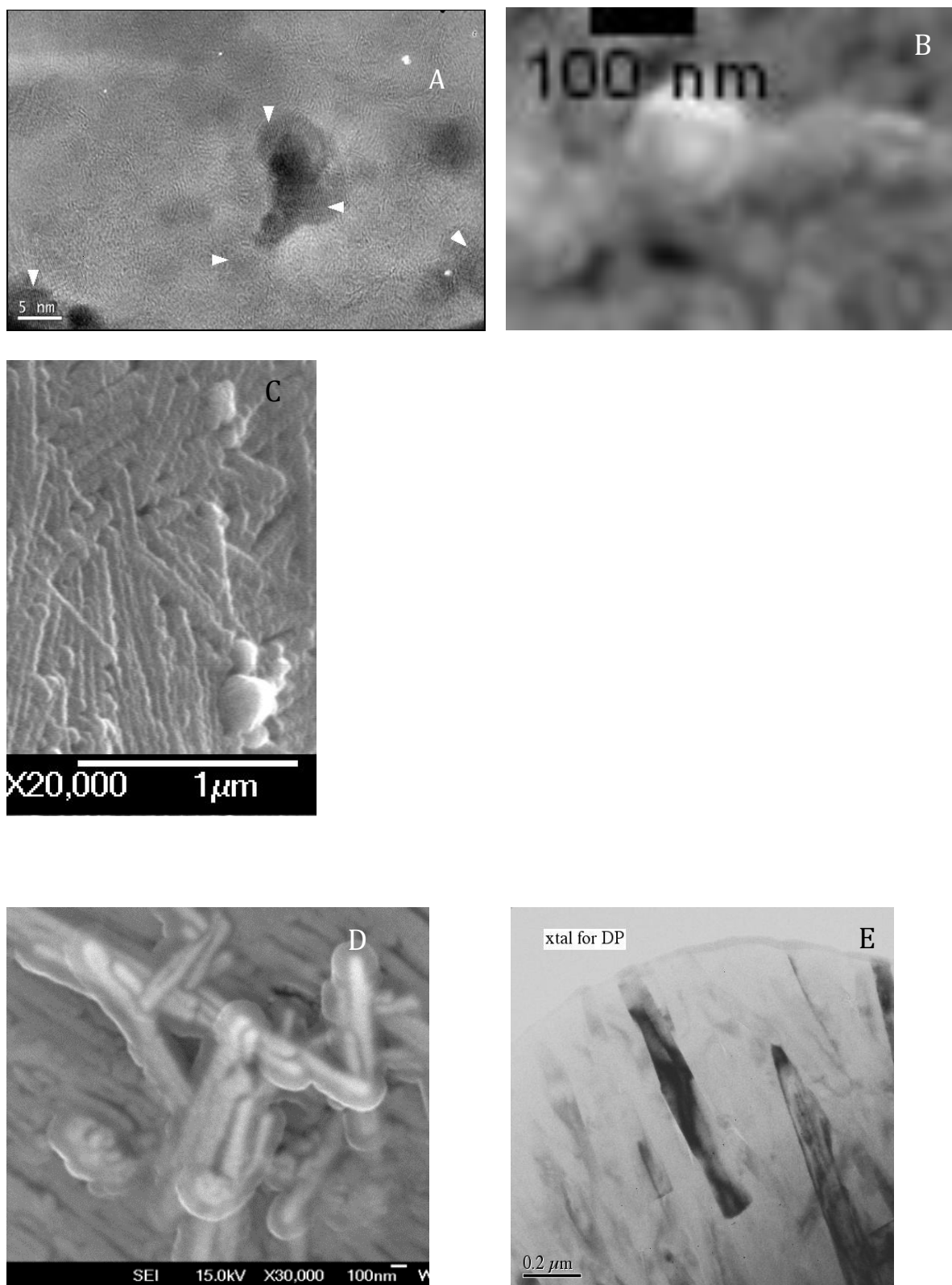


Figure 42 Single calcitic crystals.

TEM images (A, E) of crystals of inter-chamberlet wall or septa; B, C, D: SEM images of assembled crystals of wall.

The primary units of nanoscale particles comprise the first level of the hierarchy of the test (Figure 42).

A: As shown at the nanoscale, lattice fringes indicate the smallest crystalline particles of 2-5 nm, which appear embedded in the organic material: comprising a nano-level composite material- the first order biomineralised material.

B: Crystallites which are roughly 100 nm, spherical, and with a dense core 60-90 nm thick have an organic sheath approximately 10 nm thick, are assembled to form linked, chain-like bumpy crystallites.

C: The submicron elongate crystals are alternating inorganic-organic composites of conglomerates of the nanocrystalline composites.

D: The entire elongate crystal shows an integrated dense core and sheath.

E: Further, the crystals have variable internal densities indicated by varying intensities.

3.5.3 Hierarchical Level 2: Organic

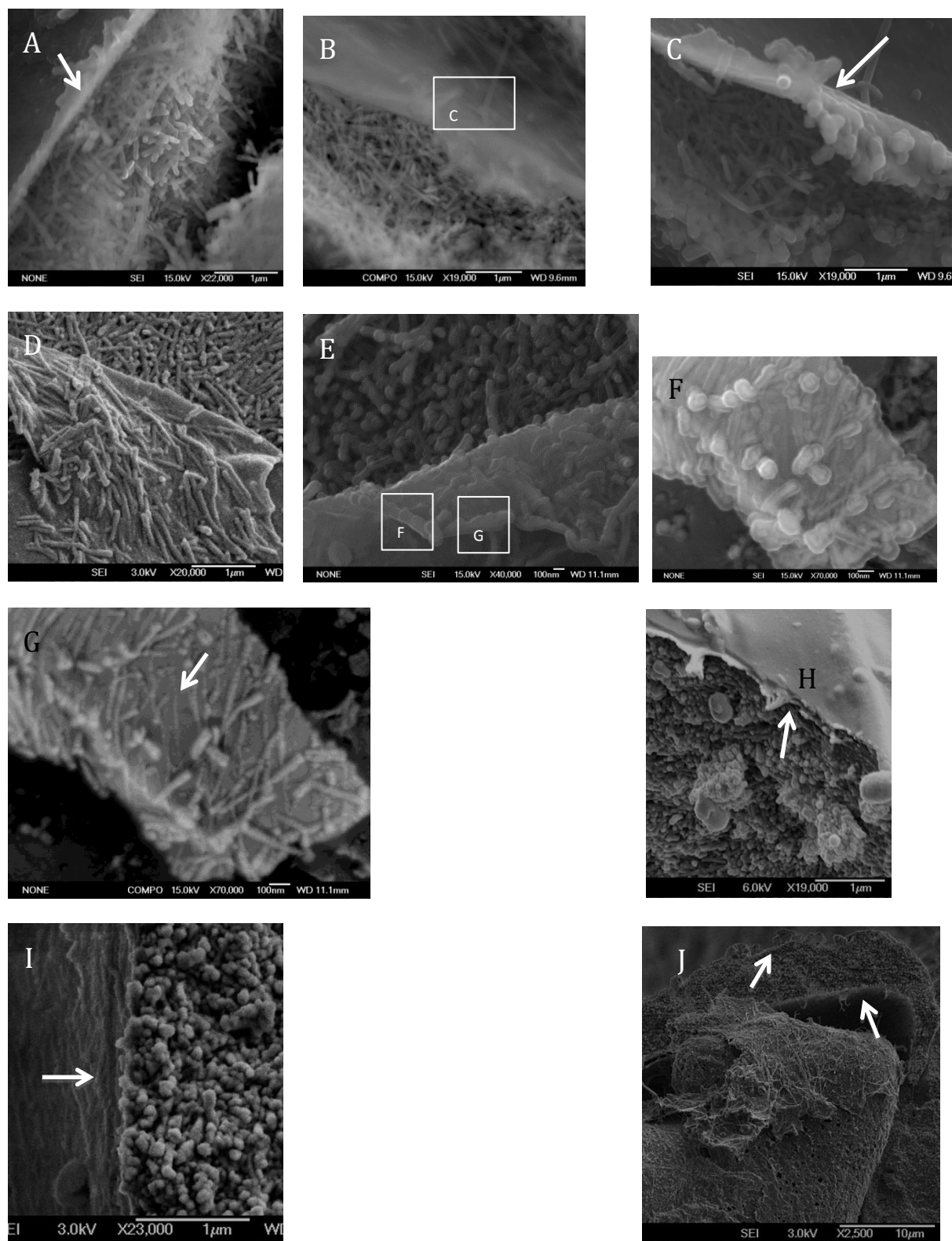


Figure 43 Organic lining of varying thickness and density with adhered crystals or covering packed crystals.

At the second level of hierarchy (Figure 43), high Mg-calcitic crystal microstructures are enclosed by a nanoscale organic lining, which is present in all ontogenic stages. The organic lining is visible on the inner and outer faces of the external and the internal walls of the microstructure and of the entire structure. It appears virtually electron transparent, translucent or opaque. Crystals appear to adhere to or to embed in the organic lining.

In Figure 43A, B, C, the organic lining appears to be lifted off the fractured internal crystalline wall of a test likely as a consequence of the specimen preparation dehydration process.

In Figure 43D, a tear in the organic lining or sheet results in a flap-like portion appears as if it were pulled back from the wall and with elongate crystals embedded in the lining.

In Figure 43E, elongate boudinaged or bumpy crystals appear less densely packed with intercrystalline spaces; the crystals appear stuck in the organic lining and

(in F) the same core-sheathed crystallites appear at the edges of the lining partly formed and assembled into aggregates. The organic material-lining appears permeated by the cores of the elongate extruded crystals visible as electron dense boudinaged rod-assemblages of the CCN (F-only visible in backscatter detector mode of the SEM).

In Figure 43G the organic lining is visible on the upper surface of the same wall.

In Figure 43H, the lining covers the inner wall of a chamber; the wall consists of densely packed calcitic crystal.

In Figure 43I the organic lining is associated with the internal crystalline walls of a chamberlet

In Figure J, the organic lining is visible as a sheet-like layer over the upper and lower walls of the approximately 5 μm thick surface wall of the test.

3.5.4 Hierarchical level 3: Bundles, Ensembles, Lamellae

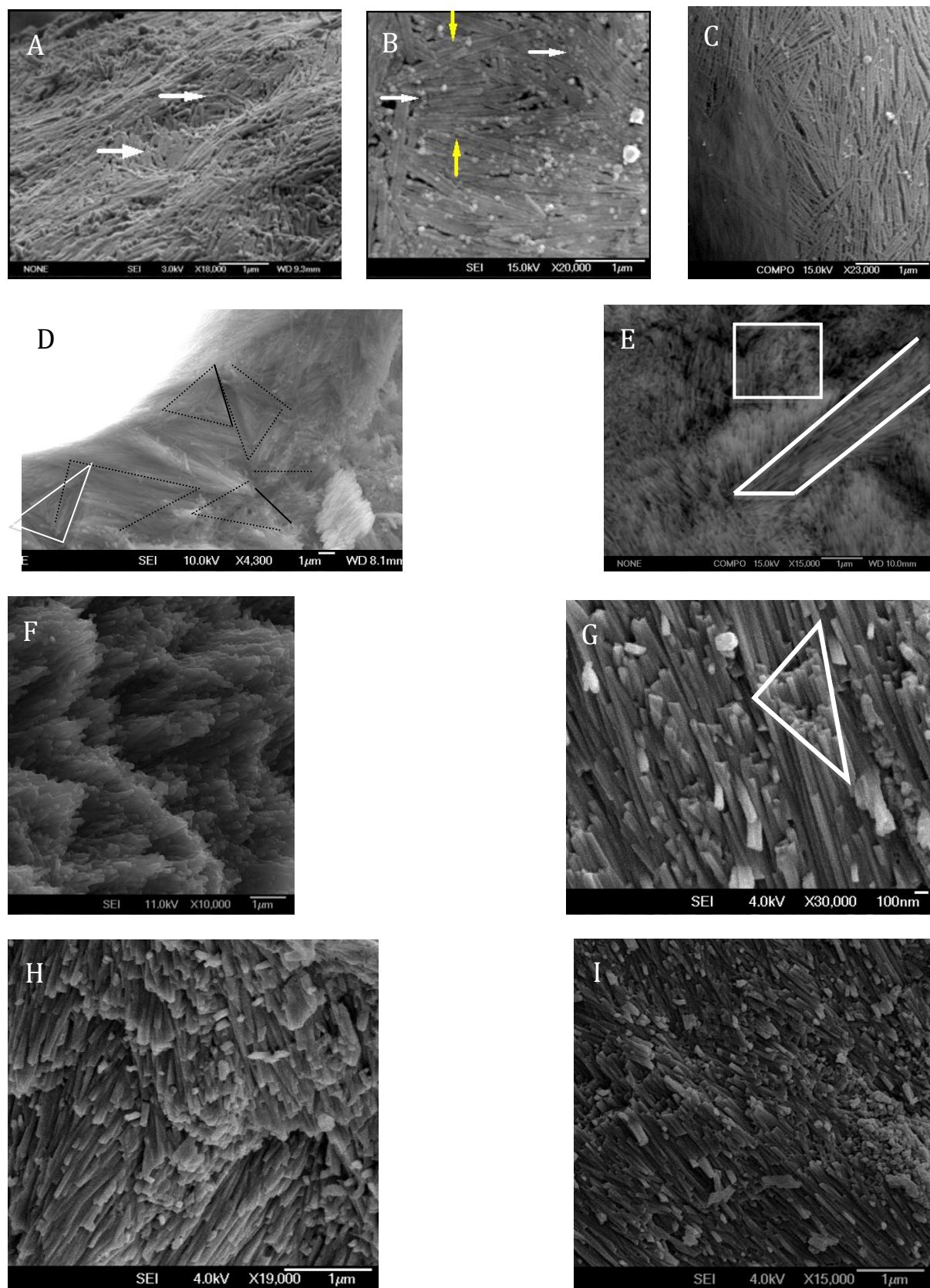


Figure 44 Meshed assemblies of calcite crystals of varying density or packing, orientation, overlap and flow patterns.

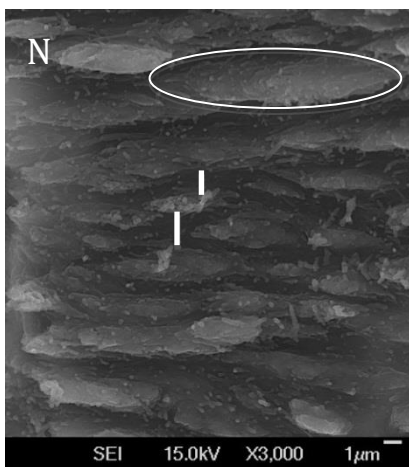
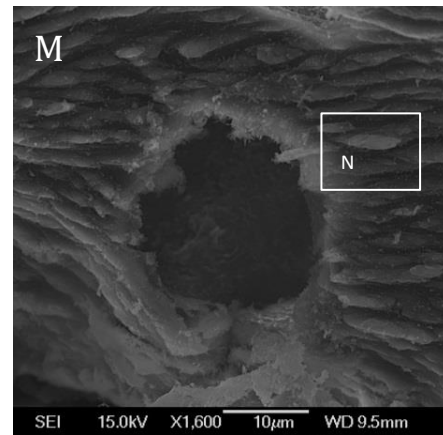
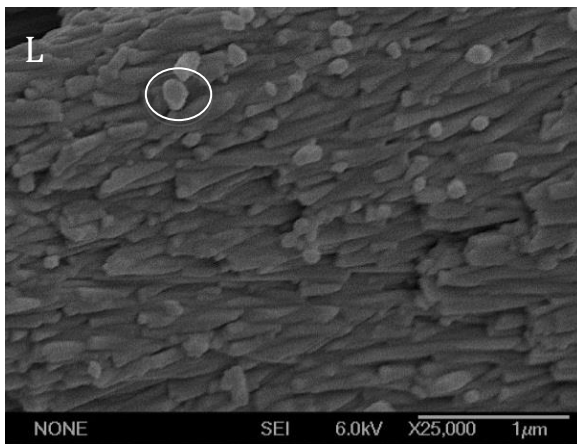
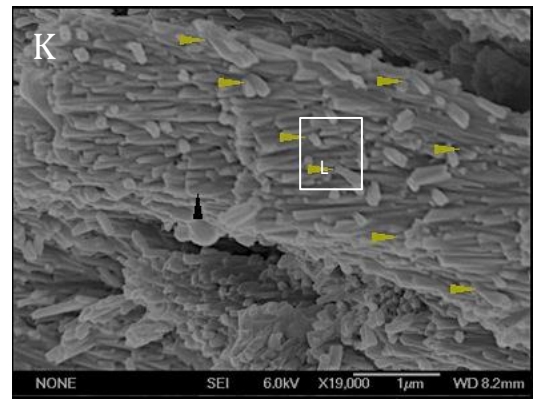
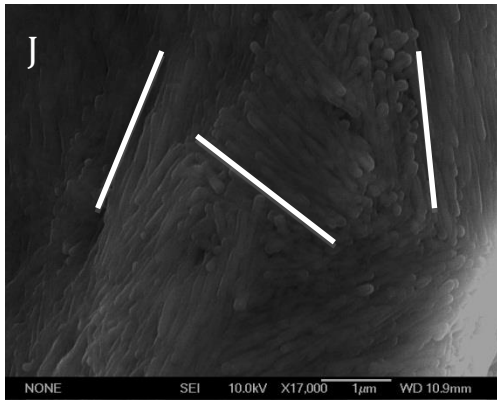
The third order of the hierarchical structure consists of the organization of the elongate crystal units into assemblies (Figure 44). A high resolution evaluation of the occurrence of the crystals in different microstructures reveals several forms of organization.

A, B: Elongate crystals occur on the surface of the test in circular “whorls-like” arrangements with linear and randomly arranged crystals filling in the areas between whorls. In curved internal microstructures, the elongate crystals are organized in polygonal arrangements. Polygonal sides range in length between 0.5-3.5 μm . These polygonal forms are usually one dimensional surface layers in which several elongate crystals (end-to-end) form the sides of the polygon; the area between the polygonal sides is filled in with end to end crystals of variable length but of equal widths (diameter).

C: Crystals may be organized as 3D polygons in some microstructures- resulting in polygons with a laminar structure and a microstructure comprised of a 3D tessellated arrangement of such polygons.

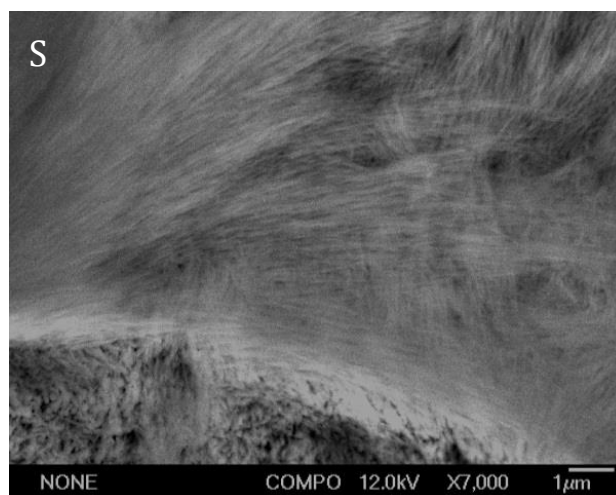
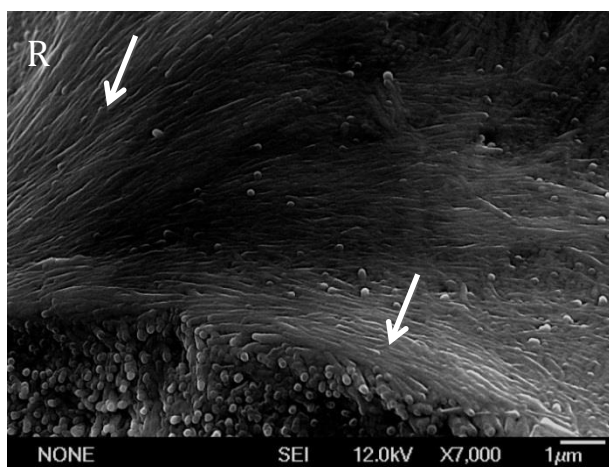
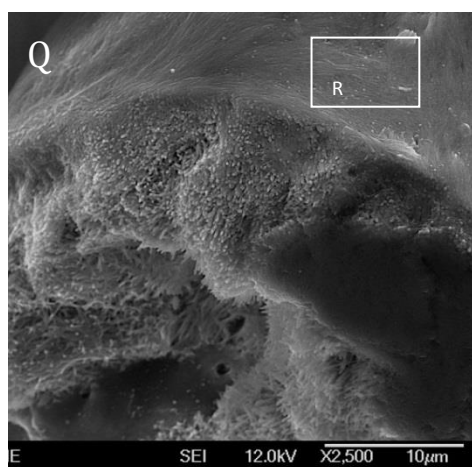
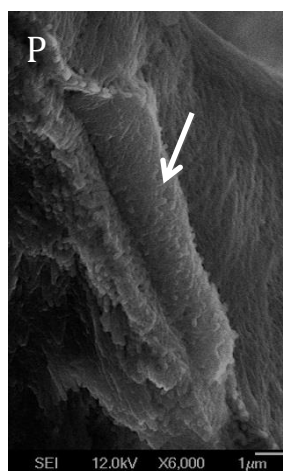
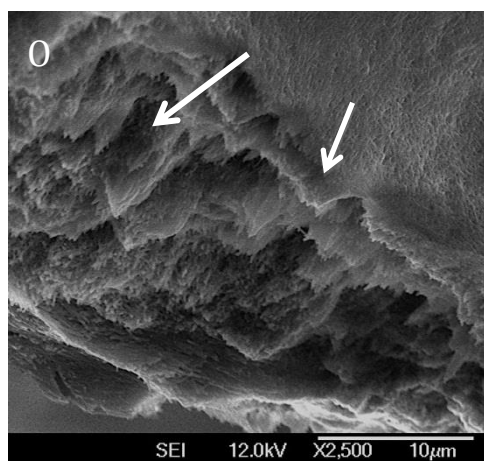
D-G: A second type of assembly of crystals consists of bundles of crystals, each bundle being approximately 1-1.5 μm *wide* oriented in the same direction. The bundles have similar densities. As the walls become denser with ontogeny, the density of the bundles increase and the bundles consist of foliated or tessellated assemblies.

H-I: These assemblies of elongate crystals are visible in bundles in a fractured chamber wall. Bundles of crystals are oriented apparently randomly. Note that bundles oriented parallel to the x-y or horizontal plane are not observed.



J, K: The dense bundles that comprise tessellated assemblies may contain loose crossed lamellar arrangements in which most of the crystals are oriented (black arrow) in one direction but cross-hatching (yellow arrows) is evident within the bundle.

L, M, N: A third assembly is observed in the earlier ontogenic stages where a terraced oval structure is grown consisting of the elongate crystals organised in a cross-hatched arrangement; terraced oval microstructures average 4-5 μm in length with a distance of 1 μm between structures. These structures are observed in the chamber walls of tests of pre-maturation stages of ontogeny.



O, P, Q: A fourth type of assembly of crystals is observed in the internal chamber walls of mature large tests. The densely packed crystals of apparent random orientation (at a dimensional scale of tens of micrometres) in vertical pillar-like regions of the chambers appear to have a lamellar nature consisting of sheet-like layers of randomly arrangement crystals intermeshed in a layer.

R, S: The lamellar nature of the overlying layer (R) and the orientation of crystals in this layer as differing from the orientation in the lower layers is evident in backscatter mode (S)

3.5.5 Hierarchical Level 4: Curvilinear, Meshed Microstructures

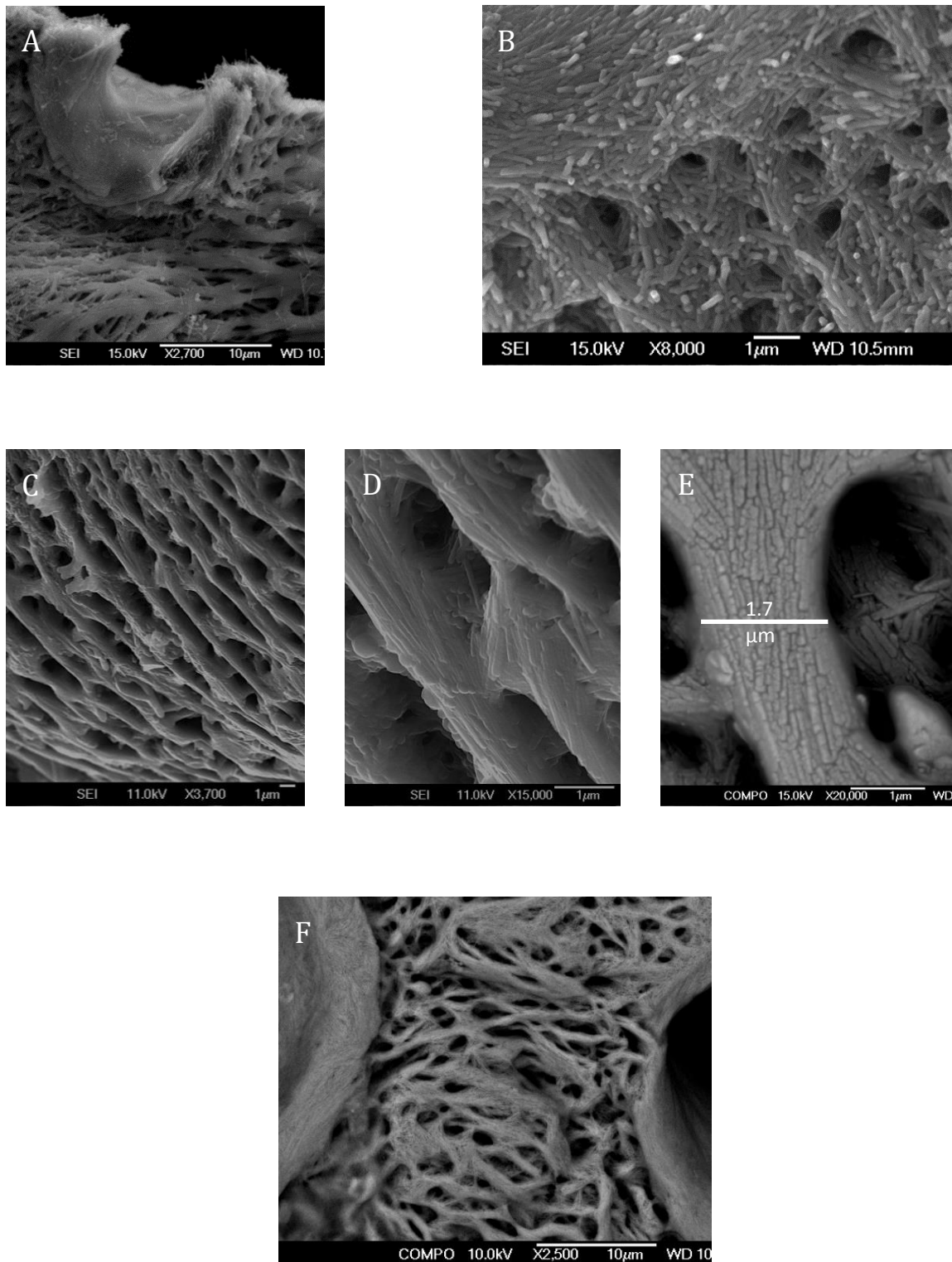


Figure 45 Circular port-hole openings and branched multicrystalline beams forming a mesh and margin.

The next hierarchical level of the test consists of the assemblies of elongate linear crystals organized to form circular and curvilinear microstructures (Figure 45). These structures are complex and exhibit an internal hierarchy consisting of internal lamellar and surficial flattened elongate crystals.

A-B: The circular microstructures i.e. pore openings formed on the circular margin of the discoidal test have diameters of 10-30 μm as size increases with ontogeny ().

C: The circular convex peripheral or marginal area of the test between the pore openings is comprised of curvilinear beams. Curvilinear beams along the periphery run in vertical direction between the upper and lower surfaces of the test, roughly parallel to each other, spaced 1 μm apart and are interconnected in a general horizontal direction by multicrystalline bridging beams.

D: Beams are comprised internally of lamellar layers of elongate crystals oriented in a perpendicular direction to the length or longitudinal orientation of the curvilinear beams).

E: A one-dimensional surface layer of flattened elongate crystals oriented longitudinally i.e. along the length of the beam covers or caps the entire beam. The density of crystals in these beams increases through ontogeny and increases in the size of the test.

F: At the pore-line along the margin of the test the vertical orientation of the beams changes to horizontal. A crystalline mesh of horizontally oriented anastomosing beams form a loose grid-like structure between consecutive pores. The crystalline fenestrated beam structure thickens with ontogenic growth to fuse in parts and close the fenestrations.

3.5.6 Hierarchical level 5.1: Crystalline solid and chamber void periodic structure

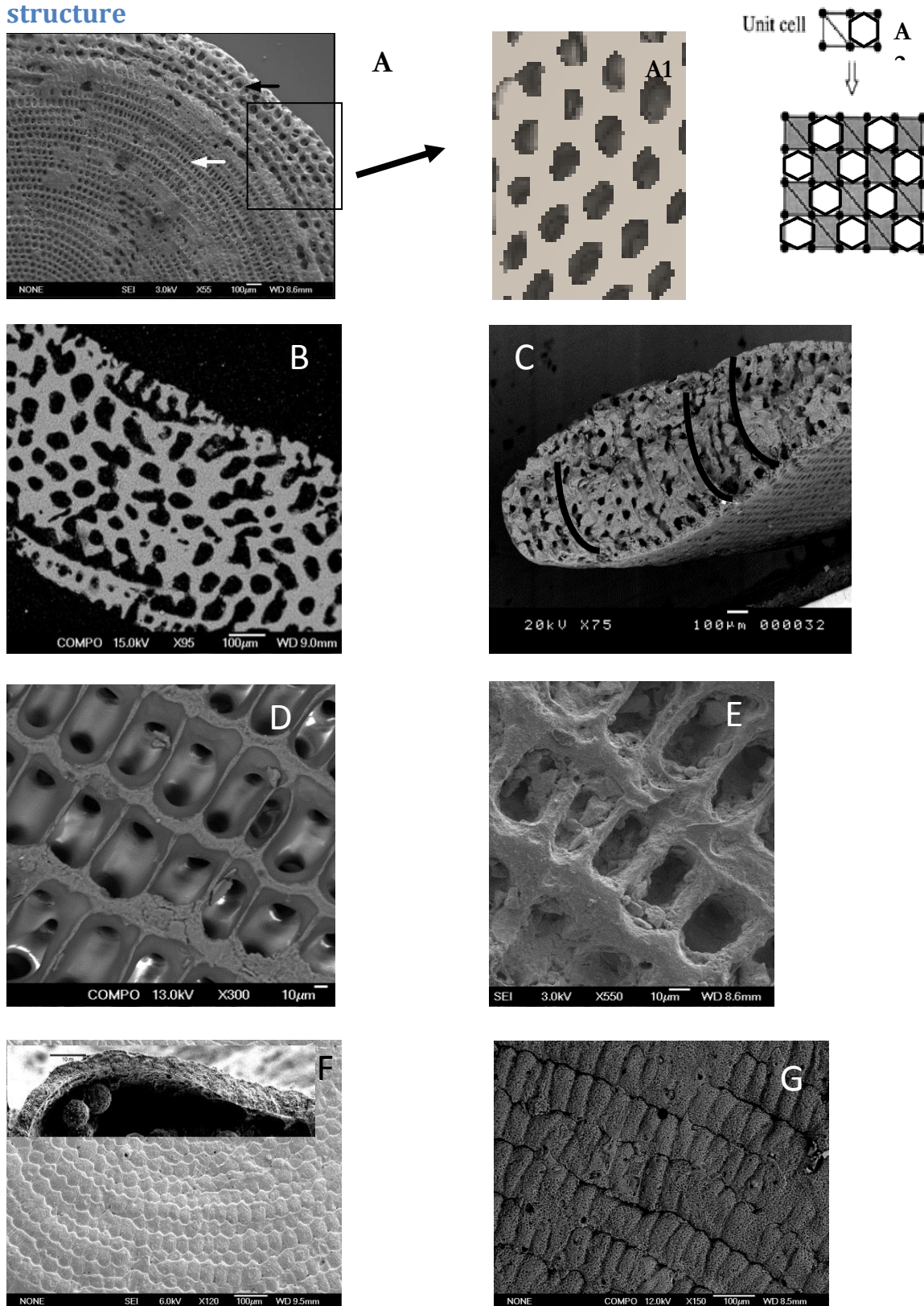


Figure 46 3-Dimensional alternating solid and void periodic structure of the test.

The fifth level of hierarchy is visible at the mesoscale (10-100 μm) in Figure 46. An alternation of void and solid microstructures forms a cellular structure comprised of inorganic-organic composite materials assembled in a grid pattern.

A: This rigid composite cellular structure is assembled and grows in an approximately square grid. This alternate void and solid construction is highly periodic in the xy or equatorial planes and extends in multiple layers through the thickness (z plane) of the discoidal test.

A1: As shown in a to-scale rendering of a cross-section through the equatorial plane of the test, a grid-like geometry is evident. Although the chamberlets-void spaces- do not possess square (or cubes) geometry as shown in the schematic Figure 46A2, a combination of polygons- hexagonal or pentagonal in cross section- more closely describes the arrangement. The solid or rigid space between the periodic void spaces consists of the elongate calcite crystals – partially ordered - in 3 directions- as shown in Figure 44 H-K and homogenized compacted crystals which fill space around the elongate ordered crystals.

The periodicity of the chamberlet-voids has two frequencies in the test. The uppermost layer of voids and solids (Figure 46B-white arrow) occurs at twice the frequency of the void and solid arrangement of the inner layers (black arrow). This higher (2x) frequency is repeated twice in the structure- at the upper most and lower most layers of the discoidal test.

In three dimensions, the structure grows in an annular addition of microstructures- displaying an onion ring structure. In Figure 46B, C is shown concentric layers of the voids (chambers) are demarcated by successive onion-ring walls (black arcs in Figure 46C). The annular chamber-void is divided into smaller convex voids i.e. chamberlets. The onion ring structure and chamberlets appear symmetrical in their distribution around the centre of the disc.

The upper most layer of voids are periodically arranged chamberlets-a fenestration of the surface of the test. Each chamberlet has two openings or stolons connecting to the lower or main chamber annulus below it (Figure 46D). The internal crystalline surfaces are smooth-covered by an inner organic lining. A similar organisation occurs at the lowermost layer of voids or chamberlets. The walls between these chamberlets resist dissolution and abrasion as seen in a specimen obtained from sediment (Figure 46E).

Although the structure of the test is a 3D cellular solid the void space is closed at the upper and lower boundaries (fenestrations of the test) by a series of microstructures. The elongate crystals form a 5-8 μm thick surface wall or roof (Figure 46G and H) over the fenestration of the surface chamberlets. This roof structure itself is a 2D cellular solid consisting of periodic tiled structures. The surface tiles elongate their shape through ontogeny as the morphology of the surface chambers changes with growth in large discoidal tests. In earlier growth stages the tiles are visibly hexagonal (~acute angled lengths 18-25 μm x parallel sides 33-48 μm). In cross section the tiles are crest-shaped or asymmetrical curved prisms (Figure 46G-inset: bar 10 μm). In mature reproductive stages of the test the tiles in plan-view appear more rectangular (~16-20 μm x 42-48 μm) with rounded corners.

3.5.7 Hierarchical Level 5.2: Chamber or void microstructures packed with organic fluid and amorphous solids

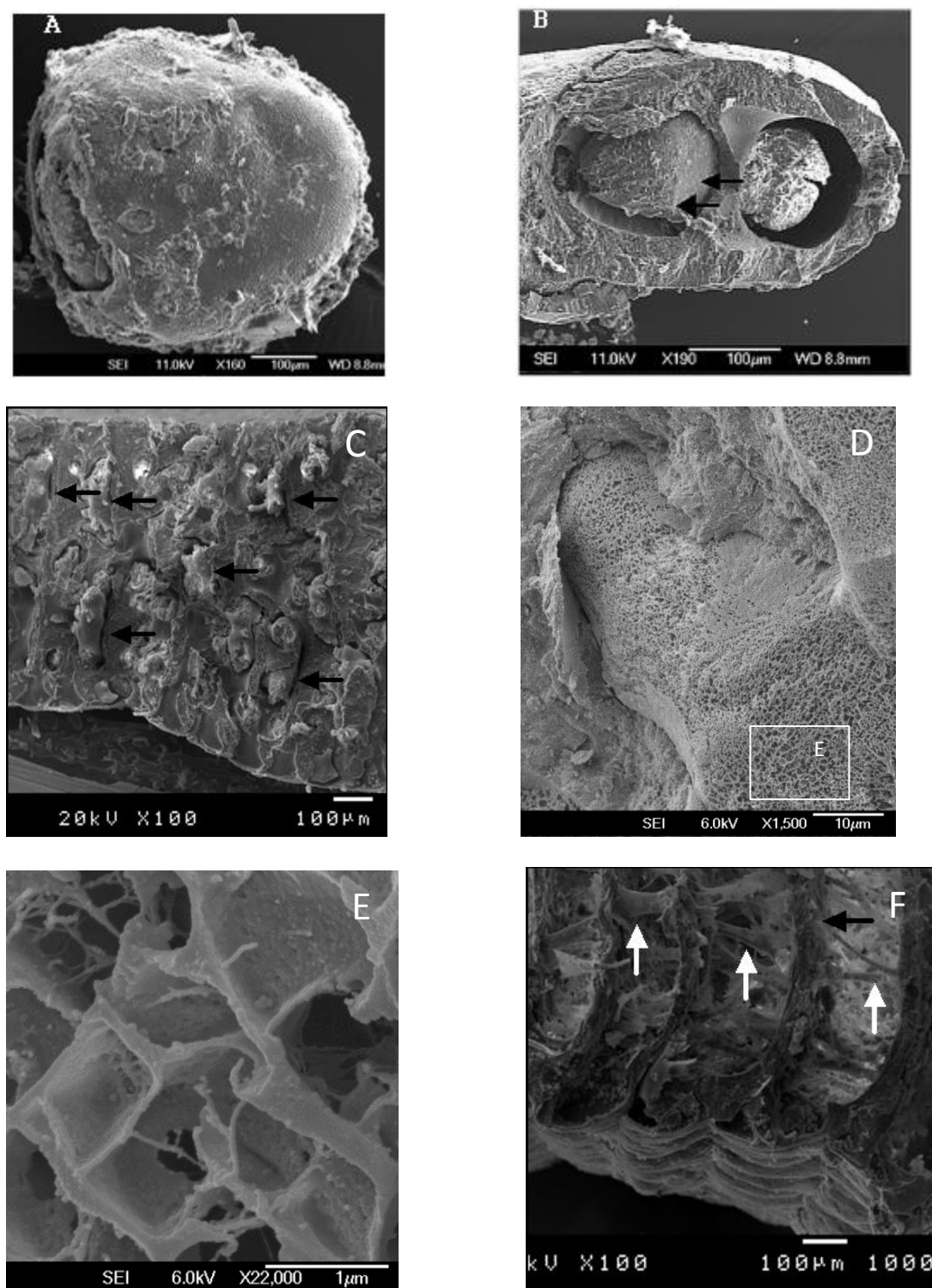


Figure 47 Amorphous and foam structure inside the void space.

A rigid cellular structure is usually a solid. In the test of *Marginopora sp.* a nested layer of hierarchy is visible within the inorganic cellular structure: organic fluids that may be foam-like, organic long fibre-like structures and amorphous solids are present within the voids of the solid cellular structure (Figure 47).

The earliest ontogenic stages of the test, in which annular chambers have not been added, are divided into three regions of void space by crystalline curved walls (thickness 31-51 μm). The entire void space is filled with protoplasm, pseudopodia and a few symbionts.

In Figure 47A and B a surface and cross-sectional view of the fractured test reveals the mass of dense protoplasm (arrows- shrinkage is due to dehydration artefacts in the preparation of the sample for SEM). The chambered voids in adult specimens are filled completely with protoplasmic mass or protoplasm containing symbiotic dinoflagellates.

In Figure 47C such masses of protoplasm are revealed as full sac-like structures (arrows) in the fractured test of an adult specimen. Protoplasmic structures viewed in a relatively native state using cryo-SEM reveals a dense foam like structure consisting of a closed cell foam; the cells are not connected to each other by throats, but by shared cell edges.

In Figure 47D the foam structure of the protoplasm appears preserved and in high magnification the cells of the foam have polygonal walled edges and a cup shaped interior. The walls of the cell are $\sim 38\text{-}68$ nm thick and cell wall edge lengths are $\sim 700\text{-}800$ nm.

The organic material shows fibre-like separation and neck-like elongation or stretching (shown in Figure 47E, white arrows) greater than $100\text{ }\mu\text{m}$ across successive chamber walls (black arrow) under tensile stresses of dehydration by graded concentrations of ethanol.

3.5.8 Hierarchical Level 6: Tubular and Flange structures

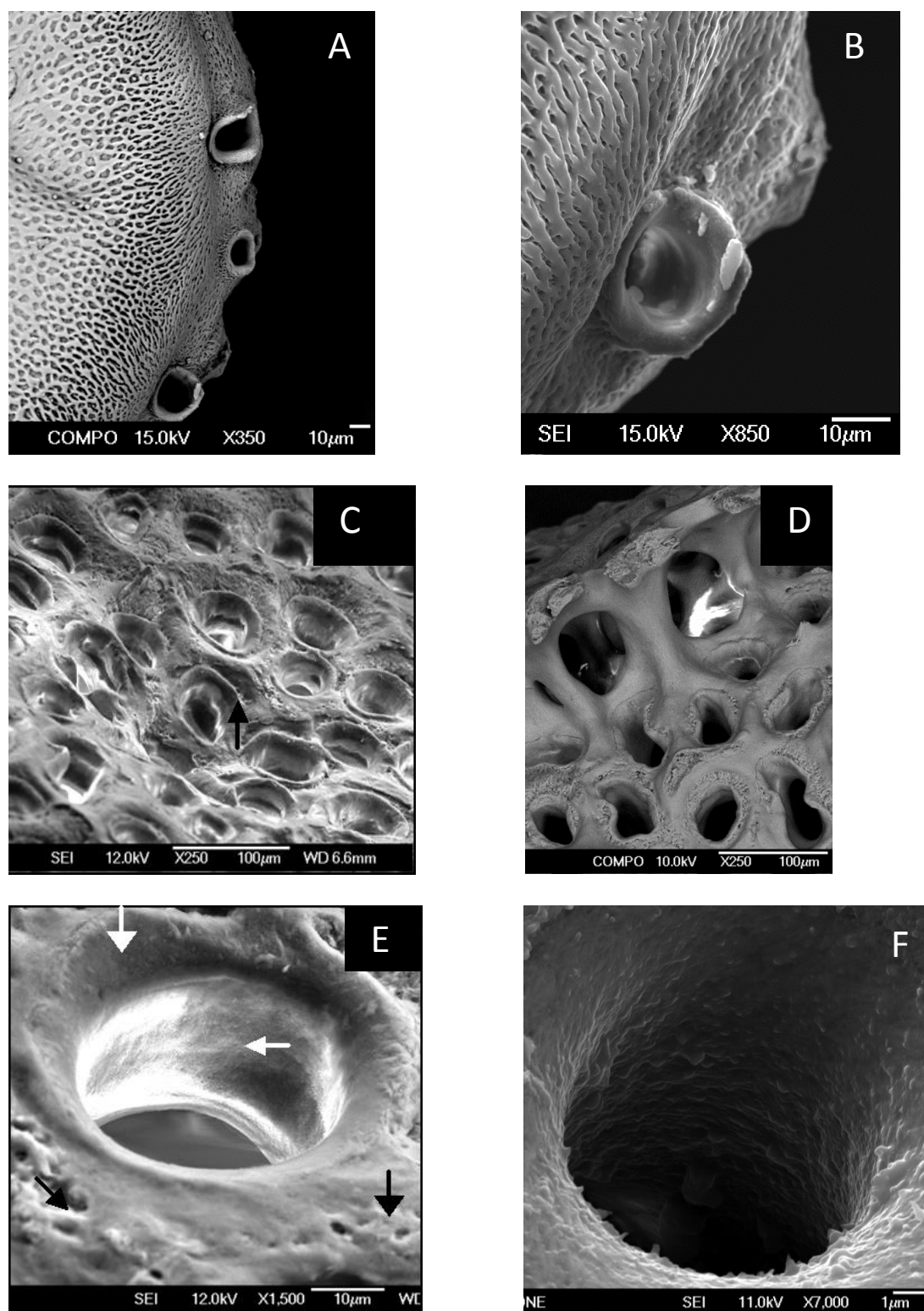


Figure 48 Dense flanged openings on the margin and dense smooth walled tubes connected to the interior of the test.

The next level of hierarchy is the construction and distribution of hollow tubular lengths within the test and flange-like circular openings on the periphery. A grid-like network of tubes criss-crosses the test in 3 dimensions. It connects successive annular chambers at periodic coordinates along the elevation (thickness) of the discoidal test and between internal chamberlets in the equatorial plane of the disc.

Figure 48A, B, C, D: The marginal chord or periphery of the disc is marked with numerous openings that have broad extensions that flare outwards in a circular form and fuse (black arrows Figure 48E) with the anastomosing mesh of beams between adjacent openings. Densely packed flattened elongate crystals form a circular straight tube; the smooth (white arrows Figure 48E) wall of the tube is covered with a thin organic lining.

3.5.9 Hierarchical level 7: 3D Porous Biconcave Disc Shape

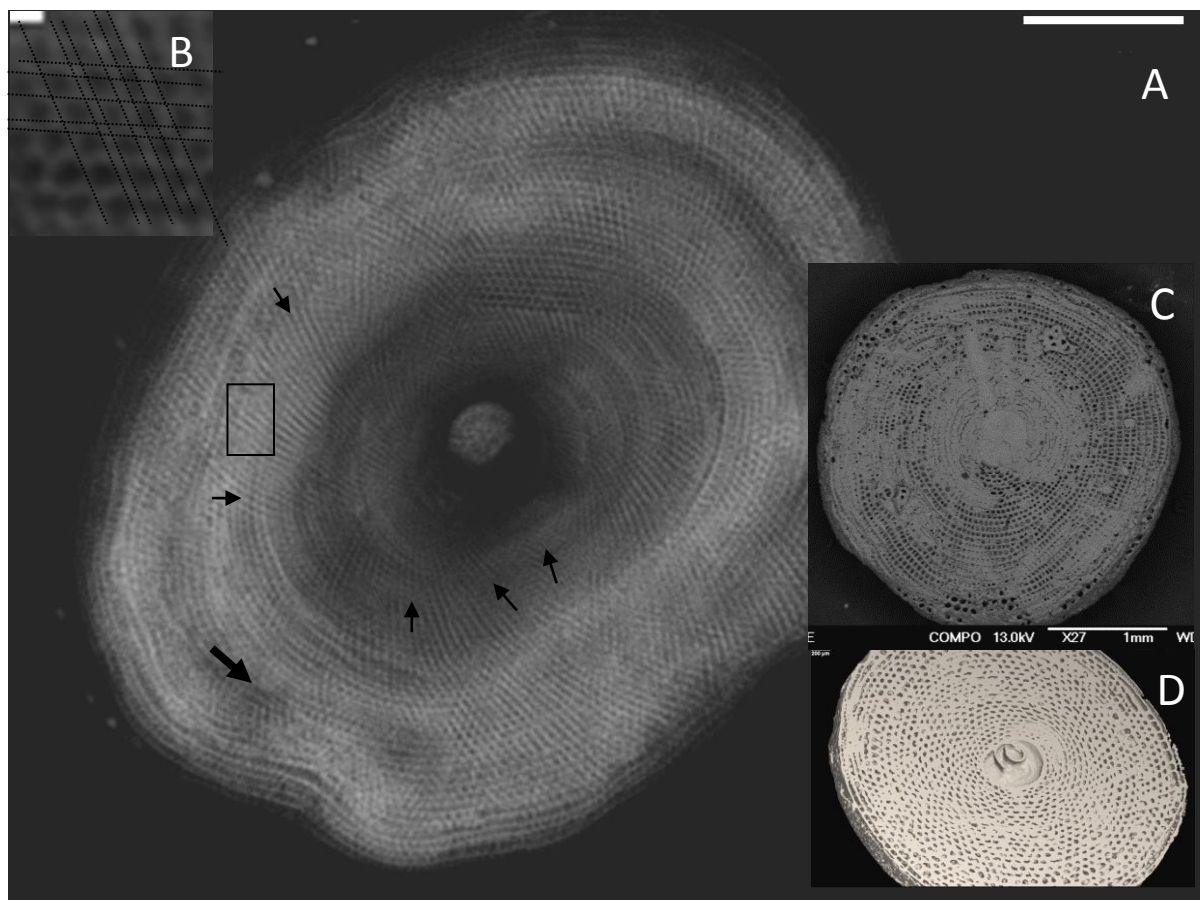


Figure 49 Anisotropic biconcave composite discoid with periodic internal void space and central soft region.

The last level of hierarchy is the macroscale integration of the submicron, microscale, mesoscale structural components. An X-ray image of the test of *Marginopora sp.* reveals, as shown in Figure 49A (bar 2 mm), the crystalline skeleton and displays the alternate solid-void-square grid hexagonal geometry (inset B bar 50 μm) integrated through the x-y-z planes of the disc. The surface of the test varies annularly in its curvature, i.e. it can be convex or concave at a microscale and is concave at the mesoscale. Some regions are saddle-shaped: the disc is not isotropically concave at any given radial distance, i.e. the disc is anisotropic in an annular direction along any chamber, as indicated by the small black arrows in selected sections. The marginal chord (large black arrow) also displays such an irregular contour. A multi-layered or storey-ed architecture is also evident at the marginal chord. In Figure 49, the difference is highlighted between the geometries of the denser and linear grid at the surface (C) of the test and in an internal view as shown in an equatorial cross-section (D) of the test. The gridlines are arc-like in the internal layers. The arrangement is an integrated 3D cellular grid which consists of rigid solid elongate units linked in the geometry of curvilinear arcs which radiate internally from the central region to the periphery of biconcave disc. In the outermost-bottom and top of the disc- layers the grid is organised at a higher periodicity. The void spaces create an interconnected porous cellular internal architecture.

3.5.10 Discussion

3.5.10.1 Hierarchical levels

In this study I show that the generally accepted picture of the structure of the skeletal systems - the tests - of large benthic symbiotic foraminifera must be refined. In this work it was observed in particular that the test's architecture reveals a more complex internal order of its constituent microstructures and nanostructures than has been commonly assumed. *Marginopora sp.* test is likely adapted to its tropical shallow coastal habitat. Recall from Section 1.3 that researchers have proposed several functions of the test. The characteristic sizes and construction mechanisms of the skeletal system are expected to be robust and tuned for these functions. The results presented in this section indicate a hierarchical constructional pattern in the architecture of the test. An organic-inorganic composite structural arrangement prevails through the nano-macro scale of dimensions of the test. Following evolutionary thinking, natural structures that are comprised of hierarchical levels of construction would be optimized at each level. Some hierarchy is visible at the level of optical light microscopy while other levels are visible only by the use of higher resolution and magnification.

3.5.10.2 CCN and crystals

The basic units of construction presented in this research are spherical-appearing nanostructures that are crystalline or possibly colloidal (CCN); it remains unresolved if these are ACC (see Section 3.4.4.1). These constitute the crystalline elements forming the first constructional level of the test. The CCNs and the crystalline matter 2-5 nm in size appear to be the lowest identifiable hierarchical level and these may be precursors of the rod-like crystals. At this hierarchical level these nanostructures are aggregated into rod-like crystals with smoothened or rounded edges; these may be further transformed into euhedral crystals. Several observations (see Section 3.4 and Figure 42) indicate that the rod-like crystals are composites with variable densities, with a range of sizes of occluded particulate crystalline matter and a fibre of organic material or water, and an organic sheath. Previous studies of these structures did not reveal these details. In the spicule of the sea urchin during larval growth stages, the spicule has rounded surfaces which are ascribed to the ACC that is shaped by the inner surfaces of the confining vesicle; the ACC then transforms to calcite (Beniash, E., Aizenberg J., Addadi, L., Weiner S., 1997). The composite structure of crystals, particularly the presence of organic material as a sheath, and as a filler material between crystals has been known to have strain absorption properties (Mayer, G., 2005).

A characteristic of composite materials is strong microstructural hierarchy. The stiff components (usually mineral) absorb the bulk of the externally applied loads; stiff nanostructures reduce crack propagation. The organic layers, in turn, provide toughness, prevent the spread of the cracks into the interior of the structure, and allow for recovery after deformation. While the chemistry of biomineralisation processes occurring in foraminifera have received increasing attention (Bentov, S. et al., 2009; Erez, J., 2003; Labaj, P. et al., 2003; Towe, K.M. & Cifelli, R., 1967) corresponding efforts not been placed on understanding the relationship between the structure and the mechanical properties of the tests of foraminifera.

3.5.10.3 Organic lining

Organic lining was observed within the composite arrangement as an envelope of the inner and outer walls of all chamberlets, tubular passages, and also the exterior of the test as reported in previous studies of *Marginopora sp.* (Ross, C.A., 1976); however in this study organic material was also observed at the nanoscale in the inter-crystalline voids. The question that remains to be answered is the mechanism by which the organics are occluded within single crystals. Here the suggestion is made that the organic material and lining has a mechanical functional value in the test; such a role in the tests of foraminifera this role has not been mentioned nor explored previously. That an organic sheath covers the crystals; that, the organic lining covers all internal and external walls of the test; that it, appears to show an adhesiveness to the crystalline (Figure 43) structure; and that it can stretch are all observations that support its mechanical functional value. In other biomineralised structures, including calcitic shells, the presence of layered or intra and inter-crystalline organic material is asserted to lead crack deviation and to stop crack propagation and to the distribution of hardness (Schmahl, W.W. et al., 2008). In nacre, the thin layer of organic material, mainly chitinprotein, between the stacked arrangement of platelet-like aragonite crystals arrests cracks; it can stretch in a “chewing gum-like” manner (Currey, J., 1999). In the mollusc shell *Conus betulina* the organic lining has been shown to be important in the transfer of bending loads and that the mechanical properties were considerably reduced upon removal of the organic layer (Liang, Y., Zhao, J., Wang, L., & Li, F., 2008). The amount of water, quantity of organic matter, the spatial arrangement and type of mineral content determine the mechanical properties of bone and the removal of the organic material that is wrapped around calcitic fibres reduces the fracture toughness in the tooth of the sea urchin (Currey, J., 1999). Aside from the spatial arrangement of crystals, these have not been quantified for foraminifera tests except that Weiner reported values of 0.1-0.2% organic matter by weight of the test in *Heterostegina depressa* (Weiner, S. & Erez, J., 1984). The spatial relations of the acidic and framework constituents of the organic linings are an open area of study which has implications for the biomechanical behaviour of the structure of the test. The composition of the organic linings is also relevant; it was observed that in the large symbiotic foraminifer *Heterostegina depressa* that the dominant soluble acidic macromolecules were similar to the enamel proteins of vertebrate teeth, which play a role in the hardness and fracture resistance of teeth (Weiner, S. & Erez, J., 1984).

Although the organic linings of the test of *Marginopora sp.* are a material that is a composite with the crystalline material and form a hierarchical level in the organisation of the test, it is interesting that in a biomineralised structure the organic material itself can exhibit a hierarchical structure. In the carapace of the lobster *Homarus americanus* hierarchy is observed in the structures of the organic matrix, starting at the molecular level; nano-fibrils of chitin-protein fibres, chitin-protein planes that are structured in a twisted plywood formation and a honeycomb structure (hexagonal) comprised of bundles of fibres arranged in horizontal planes; it contains a well-developed pore canal system perpendicular to the surface. This hierarchical arrangement is correlated to the mechanical properties of the carapace (Raabe, D. et al., 2006). The test of *Marginopora sp.* has a pore canal system perpendicular and parallel to the surface. In the carapace of the lobster, a marine benthic crustacean, the epicuticle is a thin waxy layer which acts as a diffusion barrier to the environment. An investigation of the composition of the outer organic

lining of the test compared to that of the internal organic lining found inside the chambers may reveal a similar functional value of the lining. *Marginopora vertebralis* is reported to survive in air at extreme low tides in the tropics (Smith, R., 1968); the role of the organic lining in preventing dehydration is unexplored.

3.5.10.4 Crystalline arrangements

Although the crystalline arrangement of the test is described in literature as a porcellaneous random type of test wall with possibly some local orientation, in this research the detailed examinations showed that crystals are arranged in several local orientations. These can be clearly distinguished into several different arrangements of groups of crystals that occur at either different ontogenic stages or in different regions of the test (Figure 44). These spatial arrangements were observed in several tests; meaning that chance observations of a random occurrence or mutation are minimized. Here it is proposed that the arrangements reported in this work indicate that the test of *Marginopora sp.* is very likely to possess similar mechanical properties as reported for other biomineralised structures. Importantly, *Marginopora sp.* is an early eukaryote, and one of the simpler biomineralised organisms, but several different crystalline arrangements observed in more complex organisms also occur in the test. This could indicate that the biomineralisation processes are sophisticated or that it draws upon numerous spatial arrangements and creates a robust test such that the resultant structure is an integrated compromise; no single mechanical property would be dominant. These structures, if they provide an adaptive or reproductive advantage to the individual, may be passed down to its descendants, and eventually become widespread throughout the species. However, the crystalline arrangements of the symbiont-hosting test would likely also have an optical adaptive function, which is not commonly associated with other biomineralised hierarchical structures. Specific arrangements of crystals in layers, lamellae, cross-lamellae, prisms, foliated polygons, homogeneous, tessellated, etc. are known in several well-studied biomineralised shell structures in molluscs, echinoderms, gastropods, crustacea, brachiopods (Currey, J., 1999; Mayer, G. & Sarikaya, M., 2002). These occur at different degrees of arrangement; different numbers of groups or different groupings of crystals or different numbers of layers in a group are possible. Such arrangements are an integral element of the hierarchical organisation of the biomineralised shells. Biomechanical studies have shown that the high mineral content, composite character and crystalline arrangements were associated with higher values of toughness than for the corresponding constituent materials. The nanoscale dimensions and high aspect ratio of the euhedral crystals (minimum 1:11) in the test of *Marginopora sp.* are consistent with the criteria that lead to a reduction of the possibility for fracture initiation and crack propagation (Gao, H., 2006). The high Mg content of the calcitic crystals of the test of *Marginopora sp.* and the composite structure of the calcite crystals also likely contribute to the hardness of the test and fracture resistance. In the feeding apparatus of the sea urchin the magnesium content of the calcite is directly related to hardness (Currey, J., 1999). A consequence of the often stated “random arrangement” of the euhedral elongate crystals and their nanostructure is that any cracks initiated cannot propagate in a single easy direction. The local arrangements noted (Figure 44) in the present study, the random -appearing arrangement of crystals in several regions of the test but particularly in the upper and lower tiled surface walls in which cracks may presumably be

initiated, and the composite structure of the crystals, are strongly suggestive of the adaptive mechanical value of the crystalline arrangement.

3.5.10.5 Meshed curvilinear structures

The linear crystalline elements are combined to form curvilinear structures which are observed at the marginal chord of the mature test, at the surface, in cross-sections and at the marginal chord the test at the early ontogenic stages. These structures would facilitate a rapid expansion of the test and allow the test to occupy a larger volume and has a greater surface area while a smaller volume of biomineralised calcite would be used in its construction than in a solid test.

Protoplasmic flow would be enabled through the mesh-like structure. It would also allow for rearrangement, addition, consolidation to solid walls and resorption of calcitic material by the cell. An outer fenestrated mesh-like marginal chord that binds the two surfaces of the test would reduce the rigidity of the test and allow for flexure. Fenestration has been shown to allow for an easier lateral movement of rudders (Penney, M.D., 1962); *Marginopora sp.* has a lateral motion as it “crawls” or pulls its test along surfaces in the marine environment.

3.5.9.6 3D cellular solid with fluid or foam filled void

At the next hierarchical level the microstructures are combined such that the void-solid organisation achieves the formation of a laminated (bi-lamellar) sandwich cellular foam structure. Observations of the layer of surface chamberlets on each surface sandwiching the equatorial chamberlets, the honeycomb-like structure of the cross-sections of the test with polyhedral cells indicate that the outer surface is a denser 2D tessellated structure which forms the roof. The lateral chamberlets supported by angular hollow struts form the denser tiled roof at a higher periodicity thus creating a stiffer compacted structure and form a larger surface area. Hollow struts are an efficient way of resisting buckling, look similar to the trabeculae in bone, and are found in the tooth plates of the cownose ray *Rhinoptera bonasus* (Currey, J., 1999). The angular struts support and maintain the lateral chamberlets in a vertical position and permit the movement of symbionts (this arrangement is visualised in 3D in Figure 63 in Section 3.6.2).

The interior of the test is a 3D periodic structure that forms a rigid mechanical grid. The particular periodicity of alternating solid and void squares forming a grid that is observed in the test (Figure 46 A-A2) has been shown in theoretical studies to be an economical, stiff-in-shear construction although only half the squares are stiffened with solid material (Deshpande, V.S., Ashby, M.F., & Fleck, N.A., 2001). Interestingly, the cross-section of the chamberlets (voids) in the grid structure is largely hexagonal. This would allow for a closer packing of voids in the volume of the test. The onion-ring structure of the test with the cross-cutting radial stolon tubes also could contribute as a stiffening strut mechanism for the entire test.

A cellular solid structure presents an interesting advantage that is conceivable advantage for *Marginopora sp.* in its benthic habitat on coral rubble and seagrass blades. It has been shown that a multiple connected porous structure will be heavier than a solid structure with the same overall mechanical properties, i.e. stiffness, strength or toughness (Gibson, L.J., 1989). This suggests that a biomineralised porous test is advantageous because it would be less buoyant and equally

strong or stiff but would have a lower minerals and energy cost to construct. A similar structure is evident in the stereom of the sea-urchin, which is benthic marine organism that exhibits pseudopodial movement (Currey, J., 1999). However, the architecture of the test does not suffice in that respect; *Marginopora* sp. attaches to the substrate with a cytoplasmic glue-like substance.

This cellular solid structure is further enhanced by the presence of a foam-like structured cytoplasm and symbionts in the voids; a fluid-filled void is denser. This cytoplasmic flow would keep the organic lining moist. The continuous wetting of proteinaceous organic material is known to have a plasticizing effect which leads to an increase in the work required to cause fracture (Mayer, G., 2005). An interesting surface feature is the hydrodynamic sinusoidal surface of the lateral chamberlets; it may have an adaptive value to facilitate micro-flow domains on the surface or to serve as an irregular surface that slows the movements of symbionts on the surface of the test. Studies of the thermal absorption properties of the symbionts and effect of the presence of the cytoplasmic foam on the mechanical properties of the test would add another dimension to the mechanical properties of the cellular crystalline test.

3.5.9.7 Tubular and peripheral holes

The construction of the tubular stolon system with linear crystalline elements is an essential element in the hierarchical construction of the test; it provides the connectivity of a microstructural network in the test and terminates externally at the marginal pores. A continuous marginal chord with mesh-like anastomosing crystalline structures could not be sustained over the length of the chord; solid anchors would be required at points along the chord. The locations of the reinforced pore openings indicate that they could serve as anchor points. The elliptical rather than circular shape of most pores could allow the pores to serve as stress distributing flanges on a disc; hole formation at the ends of ceramic elements is similar to stress whitening in polymers (Mayer, G., 2005). A continuous distribution of radial canals lined with the organic lining may serve to reduce friction in the flow of protoplasm.

3.5.9.8 3D biconcave disc

The test is not entirely a solid structure but its discoidal biconcave shape likely offers mechanical advantages. Stresses on biconcave discoidal shapes have been modelled using Finite Element Analysis (FEA), particularly in an attempt to understand the response of the test of *Marginopora* sp. The proloculus disintegrates during diagenesis such that the test retains a central hole. Although Song et al.'s study used a solid disc with a hole in its centre as a model, FEA showed that for several sizes the biconcave discoidal shape allowed for a decrease in the maximum bending stresses (Song, Y. et al., 1994). The *Marginopora* sp. test likely encounters such stresses in the rigorous inter-tidal habitat. A valuable experiment would be to perform FEA using an X-ray MCT based realistic representation of *Marginopora* sp.; a porous structure with less biomineralised material that has a similar mechanical performance as a solid discoidal biconcave model would forcefully demonstrate the adaptive value of the architecture of the test.

3.5.9.9 Levels of hierarchy

The framework conceived in this study shows the hierarchies nested within the macrostructure of the test scaled in dimensions to the nano-level constituent structures. It does not necessarily follow the same hierarchical classification of solely sequential or fractal nesting of structures as in several other studies of biomineralised structures described in a review by Fratzl (Fratzl, P. & Weinkamer, R., 2007). It draws upon the theme of hierarchy in structures while creating novel groupings that are peculiar to the architecture of the test of *Marginopora sp.* The levels of hierarchy described in the literature of biomineralised structures differ in numbers (two to seven) accordingly with the complexity of the structure and the level of resolution or structural detail revealed or considered in a study, the type of microstructures and materials, the morphology of the macrostructure and the patterns recognised by researchers. A model developed recently to indicate optimal levels of hierarchy as a function of mineralisation in biocomposites is an attempt to relate structure to maximum toughness of load bearing biological materials (Zhang, Z., Zhang, Y.W., & Gao, H., 2011). Hierarchy distinguishes complex from simple systems (Alessandro L, K., 1990) and at least three levels need to be considered.

In this study, unlike in most descriptions of the hierarchical construction of structures, the molecular level (of the calcitic crystals or of the organic linings of the test) was not considered. Its relevance is explored in Section 3.7 in the context of other patterns of the test. Another limitation is that a microstructure, the proloculus, has not been considered in the hierarchical framework presented in this section. A hierarchy of structures has been conceived; hierarchies in cellular or assembly processes have not been described. There are likely synergies between processes and structures; the effects of these are beyond the scope of this study.

However, in this study a qualitative explanation was attempted of the mechanical behaviour of the test in terms of its structure across scales of dimensions. The interpretations of the structural or mechanical adaptive values of nanostructures and microstructures and their arrangements strongly correspond with findings of either theoretical or experimental studies of biomineralised structures or in studies of the structural mechanics of materials. Such an attempt lays the groundwork for a progressive experimental evaluation of the assertions that arise from the correlations made here. In the biomechanical studies of bone and bone tissue, the most extensively researched biomineralised structures, different microstructures are related to the different mechanical properties of different structural elements. Yet, several structural-mechanical function relationships remain unproven assertions (Currey, J.D., 2010).

Very limited experimental evidence is reported in the literature regarding the mechanical properties of foraminiferal tests. Wetmore's studies showed that some test shapes correlated with high crushing strength (Wetmore, K.L., Plotnick, R.E., & Wetmore, K.L., 1992) but the test of *Marginopora sp.* was not considered; its discoidal shape does not suitably relate to the use of crushing strength as a parameter for its mechanical performance. *Marginopora sp.* exhibits hierarchies as a biological composite. But the extensive rotated plywood fractal hierarchies observed in bone were not observed in the test. A fundamental difference is the test of *Marginopora sp.* is likely not a load bearing biological structure in a strict sense. Since evolutionary processes tend to adapt biological systems to fit their functions, it can be assumed that the

hierarchical structures of load-bearing biological materials have been optimized for stiffness and toughness. Applied to the test of *Marginopora sp.* this proposition suggests that the hierarchical structure of this composite material may be optimized to allow for a mechanically robust test adapted to the shear and flexural forces imposed by the coastal environment. Based upon the hierarchy of the observed structures and the correspondence with the biomechanical properties of other biomineralised structures, it is posited that the test can be classified as a cellular solid that is a natural ceramic bio-composite. Numerous natural materials – cellular solids, elastomers, polymers and polymer composites and ceramics and ceramic composites- - such as cork, woods, timbers, seaweeds, cartilages, skins, silks, cuticles, collagen, shells, bones, corals, etc. are included in reviews in literature of extensive detailed analyses of mechanical properties and efficiencies of natural materials (Wegst, U.G. & Ashby, M.F., 2004). The tests of foraminifera are not. By revealing the structural hierarchy and different crystalline arrangements of the test of *Marginopora sp.* and their mechanical implications, this study initiates the study of tests of foraminifera in the material sciences.

3.5.9.10 Future research

From the preceding discussion of the correspondence of structure and mechanical value observed in the test and in biomechanical studies of other structures several modelling and experimental studies may be pursued. First, is the porous test heavier and does it have equal flexural stress responses as a calcitic solid test of the exact shape? Second, do the mechanical properties of the test match the properties of natural ceramics? SEM images of the crack and fracture surfaces and of the test and the tests of different large benthic foraminifera found in different environmental conditions compared to other biomineralised structures would also be another possible active line of investigation. As systematic micro and nanoindentation study of the test including that of the internal walls, crystalline aggregates and the organic lining would provide valuable data towards the mechanical evaluation of the test. These studies could open a path towards understanding the relations between the complex architecture of tests of large benthic foraminifera and their mechanical adaptations. Linkages to structures, processes and adaptive functions in biomineralised higher organisms could also be revealed. Similar analytical and experimental work with other biomineralised structures over the past 30 years has gradually revealed a wealth of information that is utilised for biomimetic technological applications (Mayer, G. & Sarikaya, M., 2002).

In this section, the interactions between the hierarchical architecture of the test and the mechanical adaptive value were explored. Factors related to the mechanical properties of the test: distribution of density, 3D structure, porosity, void networks and other constructional patterns are explored in the following sections.

3.6 Results of X-ray MCT: Qualitative Analysis of Ontogeny of the test

3.6.1. Introduction

In the previous section using high resolution EM images of various specimens of *Marginopora sp.* at different growth stages it was shown that there exists a hierarchical nano-macro scale architecture of the test. The EM technique offers a limited view of the development of the morphology of the test at the meso and macro scales because the minimum magnifications and resolutions of EM often preclude a macro-scale evaluation of specimens larger than a few millimetres. Also, a systematic viewing of the internal cross-sections of the test is possible only through the preparation of thin-sections. The obvious destruction of the specimen(s) and difficulties associated with the preparation of thin-sections of pre-defined or selected areas of calcitic tests, i.e. not of epoxy replicas, have been described earlier (Section 3.1.1). Both techniques, as used in this research, only provided observations in 2D.

However, the X-ray MCT technique offers the advantage of a non-destructive 3D view of the test. Further, selected areas of the same test can be “virtually thin-sectioned” in different planes; qualitative and innumerable quantitative analyses can be performed with X-ray MCT data. In order to demonstrate the application and advantages of the X-ray MCT technique in enhancing an understanding of the changes through ontogeny: (1) of the morphology of the test; (2) to provide rapid qualitative assessments of the levels of biomineralisation in different regions of the test; and (3) to view the development of the cellular and grid structures of the test, I present here the results of X-ray MCT experiments with a set of specimens of *Marginopora sp.*

These specimens were not the exact specimens investigated using EM but were selected from the same sample; these are reasonably equivalent or representative in ontogeny and origin. Additionally, data are presented here using the same experimental conditions as described in Table 2 of Chapter 2, for all the specimens, excepting data for specimen “old”. Data have been processed to present 3 views for each specimen. In Figure 50 and subsequently in Figure 51- 60 in each figure the views **A1-A3** are shown **X-ray MCT grey-scale** images of attenuation values in selected xy_yz_xz planes of an ontogenic stage of the pristine test; the yellow crossed-lines indicate the point-of-view-of-planes. In **Figures B1-B3** are shown grey-scale values differentiated or converted using ImageJ software to a “**thermal**” view in which the attenuation value of X-rays, i.e. density of mineral, is indicated by colours (violet- highest; orange-lowest). In **Figures C1-C2**: are shown **3D Volumetric renderings of the reconstructed 3D X-ray MCT** data “slices” of the tests. Figure C1 shows grey-scale renderings cropped in an xy section using Molcer software and, C2 shows a coloured 3D volume rendering cropped view produced using Drishti visualization software. These 3D renderings are cropped approximately rather than exactly at the same “slice” in the planes shown in the views in A, B, the views of the test are rotated to illustrate the 3D reconstruction of the morphology of the test and to permit a 3D view of the external and internal features. Circular rings (white arrows) are artefacts of imaging described in Chapter 2.

In the following section, results obtained with some variation in experimental conditions (Table 4, Chapter 2) and the use of higher resolution (and cost) equipment are also presented. Those results allow for a comparison of data and results obtained of selected growth stage specimens with images obtained from lower resolution data of similar specimens presented in this section.

3.6.2 Results

3.6.2.1 Specimen M111

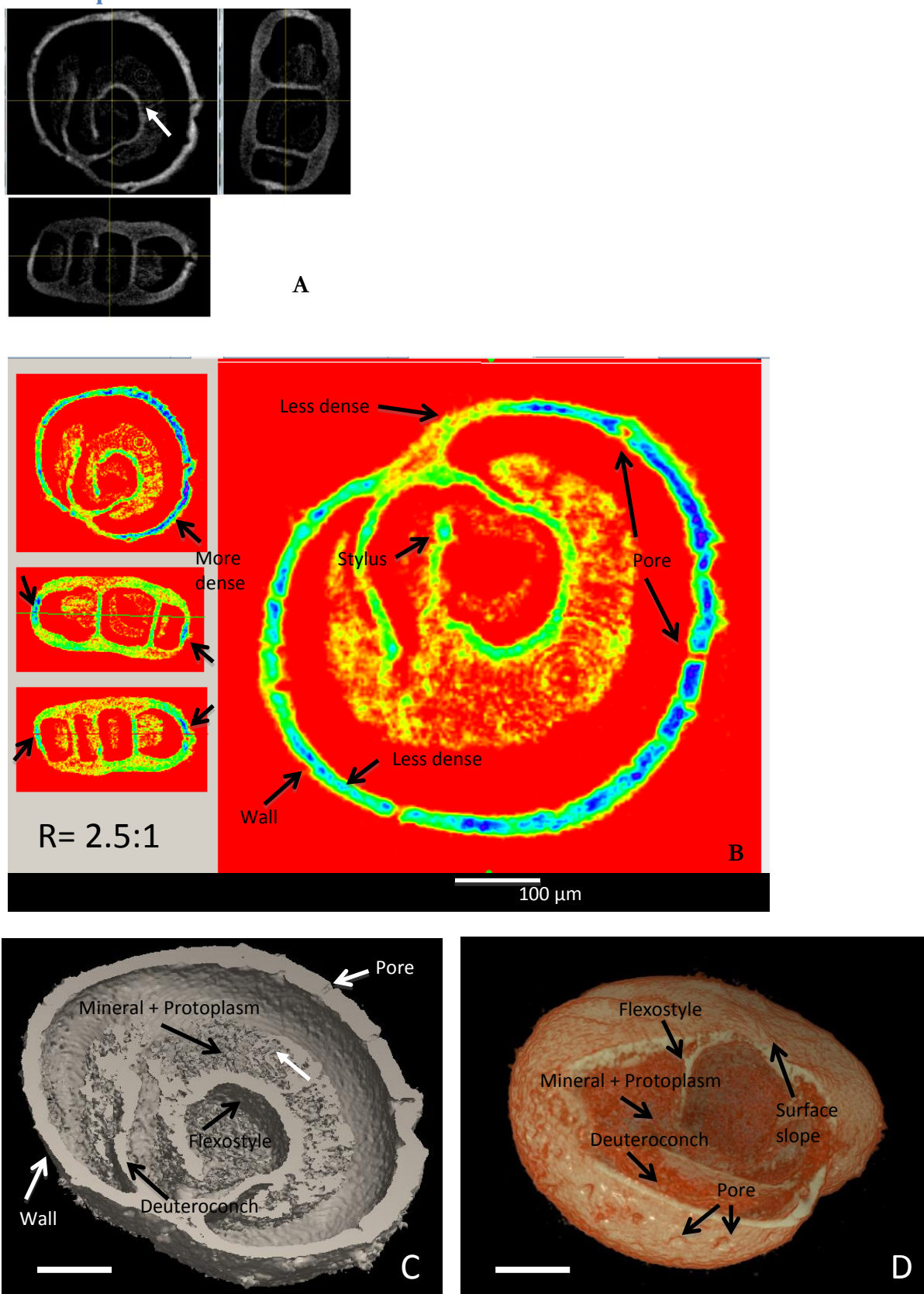
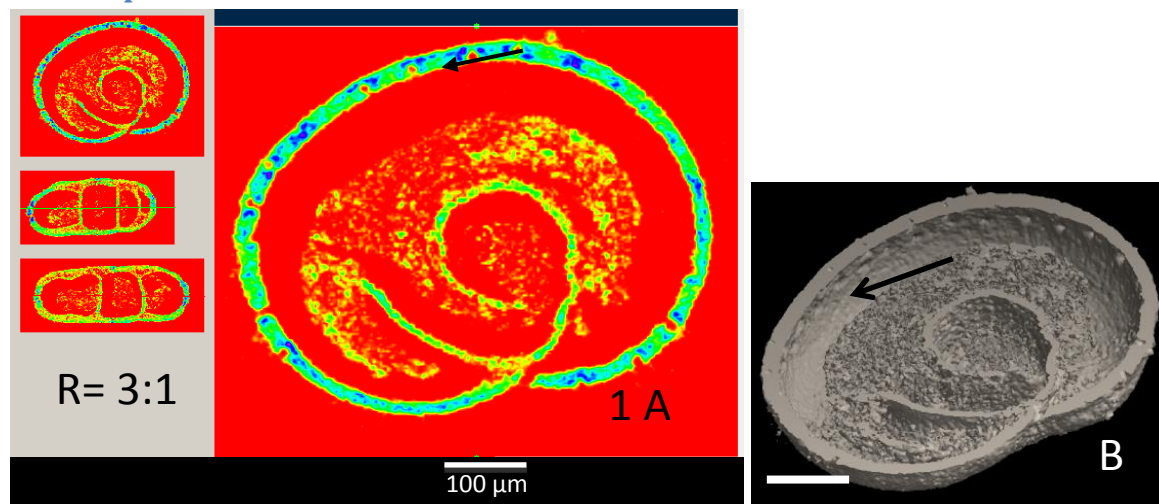


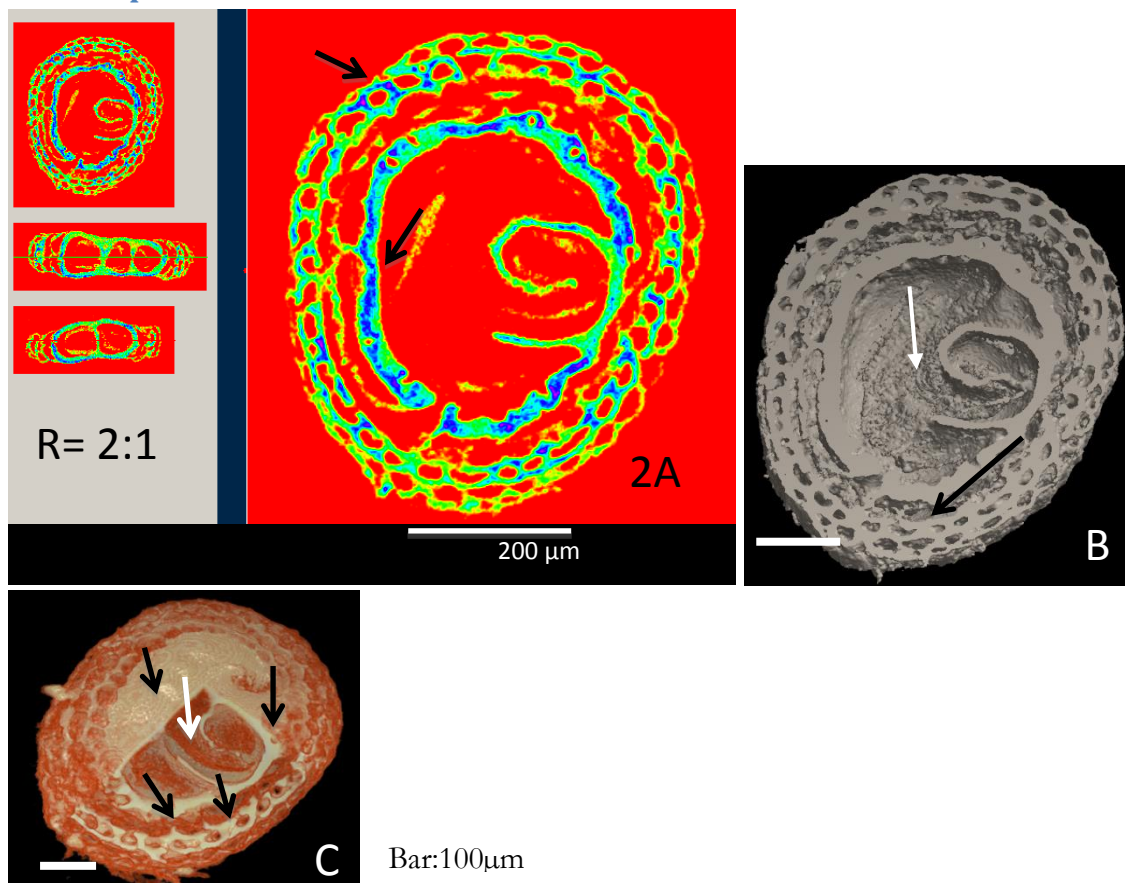
Figure 50 X-ray MCT images: A: Grey-scale, B: thermal colour. C and D: 3D volume renderings. Bar: 100 μ m.

In Figure 50A – D, a 3D view is presented of the early stages of the test. It is evident that the test is chamber-less. The thermal view (B) shows that the entire outer and inner margins of the test wall is less dense than the wall itself and is of a similar density as the region at the prolocular wall (dashed arrow in Figure 50 B4). The thermal views also reveal that the upper surface is not dense at the early stages of growth. Vertical walls of the test are denser or more mineralized compared to the structure of the test in a horizontal (xy) plane and appear to show higher mineralization adjacent to pore-spots. Pores are visible; these views show different degrees of penetration of the test possibly indicating an inclined stolon (tube) and their distribution. The volumetric view (D) shows that very early in ontogeny the pores are distributed at the margin of the test in a staggered periodic pattern. The test is asymmetrical; it is bean shaped and has a low aspect ratio (2.5:1) of length to height. The surface of test has a slope or that anisotropy develops in the early growth stages. The 2D X-ray MCT reconstructions and 3D volumetric renderings reveal X-rays attenuated by the material inside the cavity of the test; they show that the volume of the prolocular cavity is filled with intermingled amorphous material and reveal the distribution of the material. This material likely is protoplasm which contains mineralized matter of sufficient density that it attenuates the X-rays. At this resolution its morphology is not distinguishable. Volumetric views show the thickness and height of the deuteroconch and flexostyle within the cavity.

3.6.2.2 Specimen M112

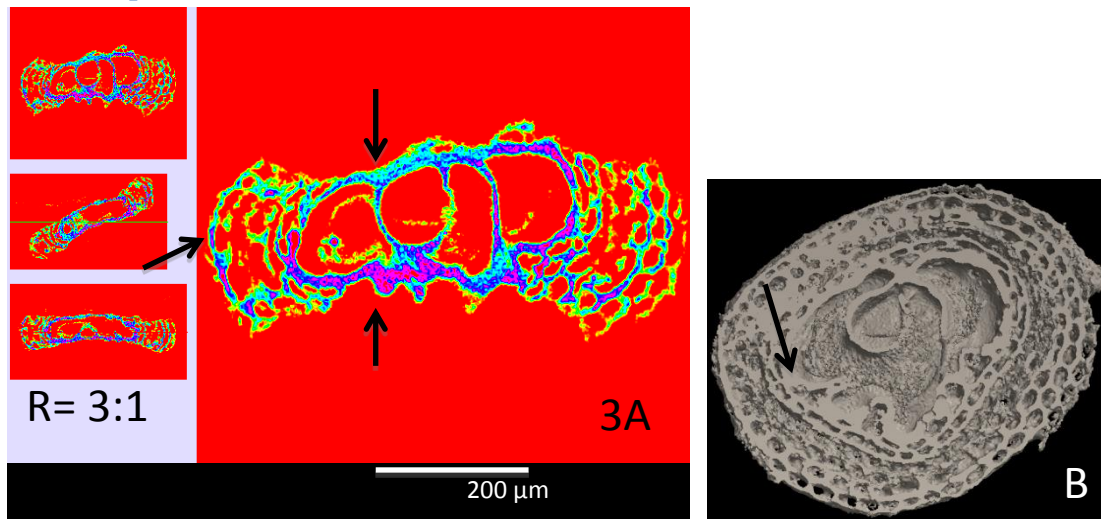


3.6.2.3 Specimen M331



In Figure 51 1-A, the chamber-less test shows a developed periodic pattern to the pores. In Figure 51 2-4 B, C, D a high degree of mineralisation is observed (arrows) at the periphery, lower areas, surface of the prolocular region and between chamberlets relative to other regions of the test. Test shape changes through addition of chambers- tending towards symmetry. Periodicity and a staggered chamberlet cellular structure is visible in 3D in the volumetric renderings (white arrow). Chamberlets are roughly polygonal.

3.6.2.4 Specimen M332



3.6.2.5 Specimen 441

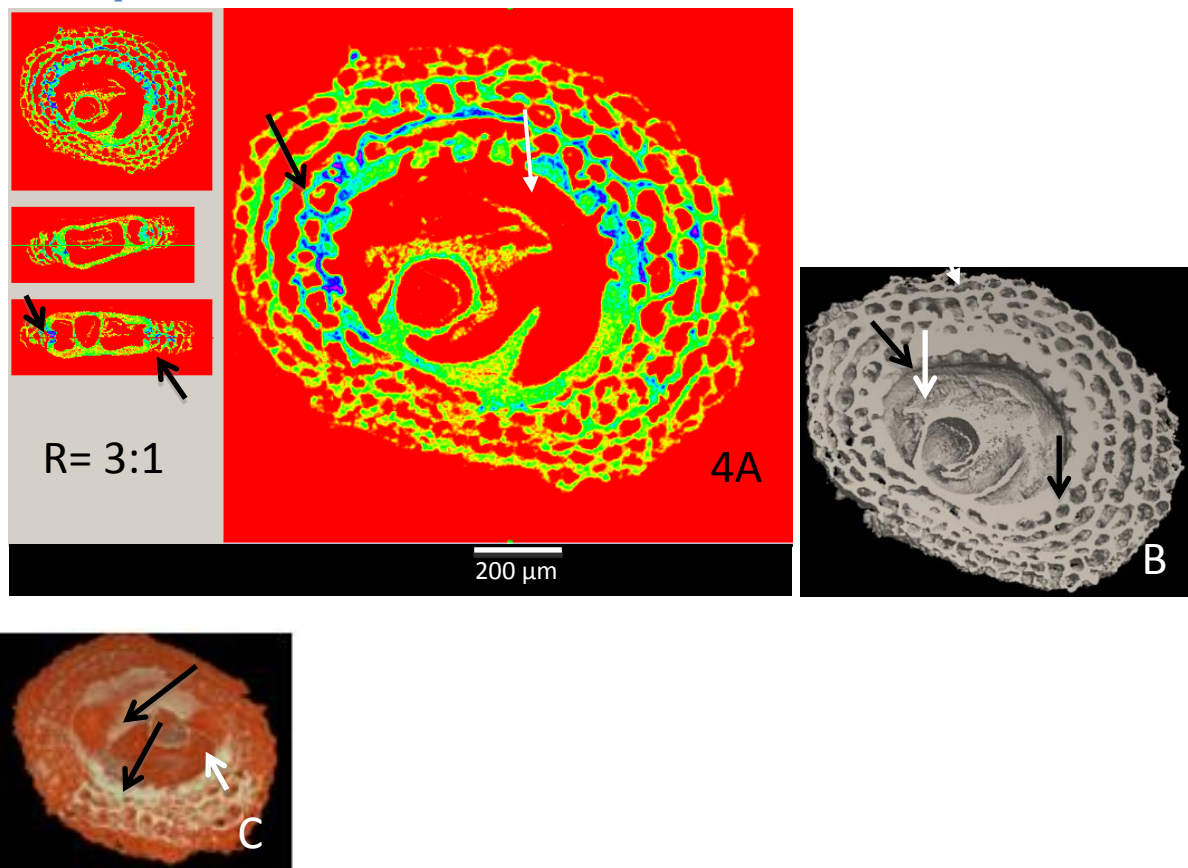


Figure 51 Early ontogenic sequence of *Marginopora sp.* revealing chamber formation, mineralization and change in shape.

In Figure 51 3-4 A-C, mineralisation appears to be increased, the chamber walls are thicker and periodicity of chamberlets increases (black arrows). Mineralisation is higher at the vertical walls and the prolocular (central region) surface of the test. The volumetric renderings reveal a solid aggregate-like mass in the prolocular region (white arrows).

3.6.2.6 Specimen M_smalllest

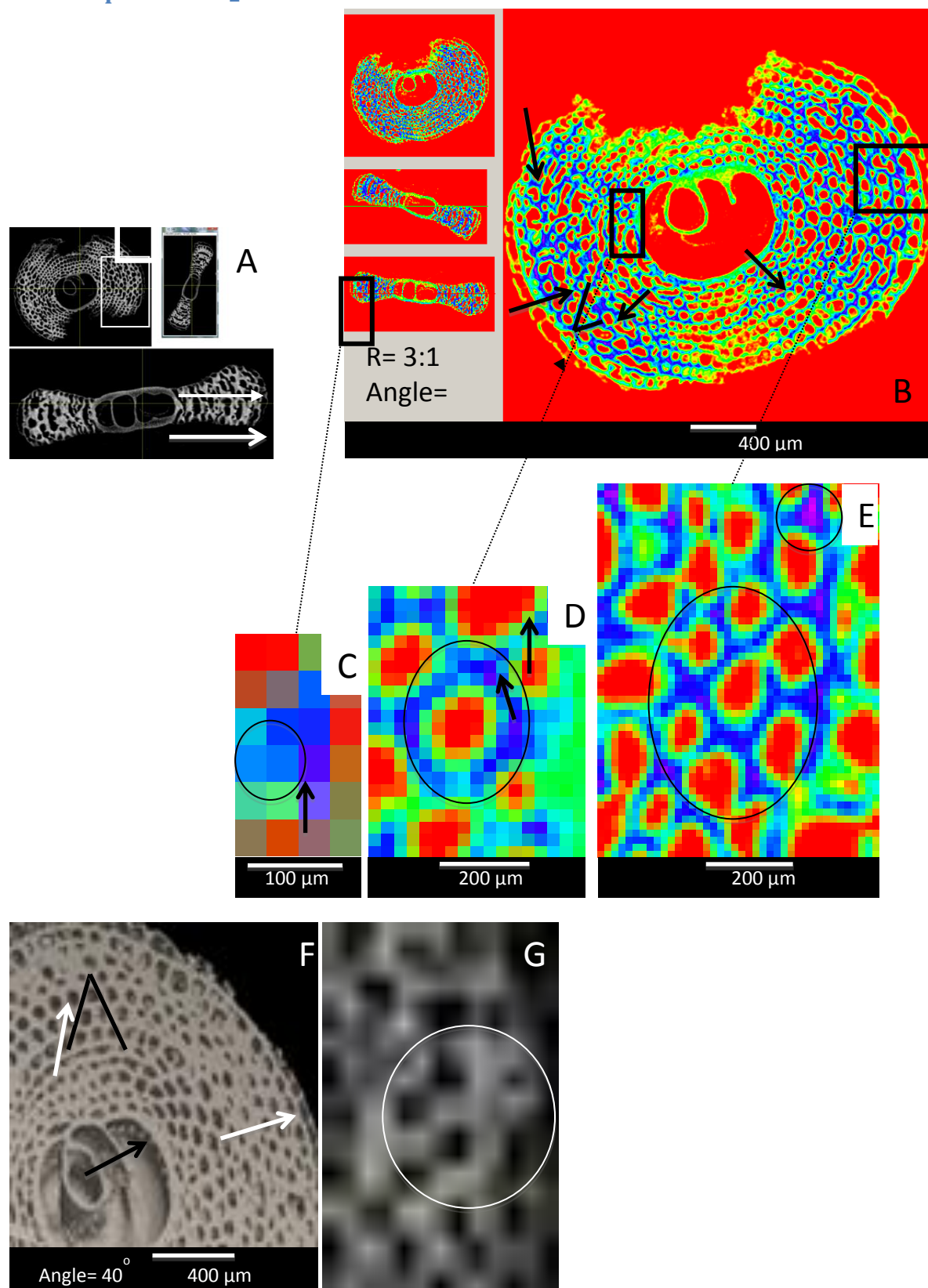
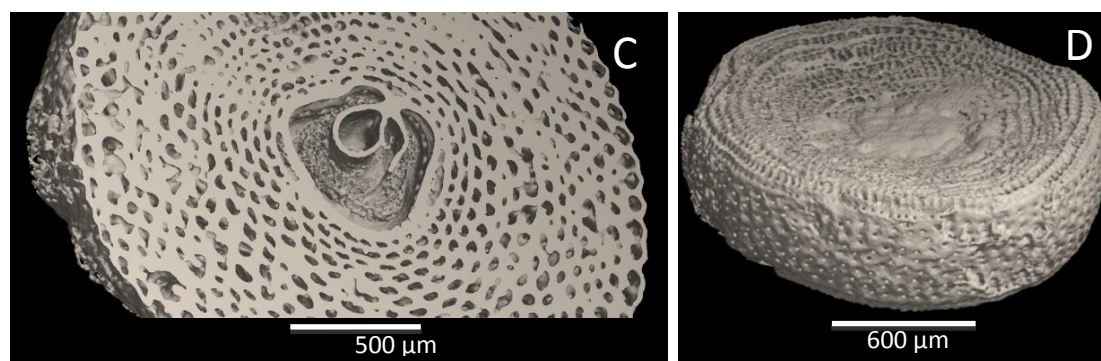
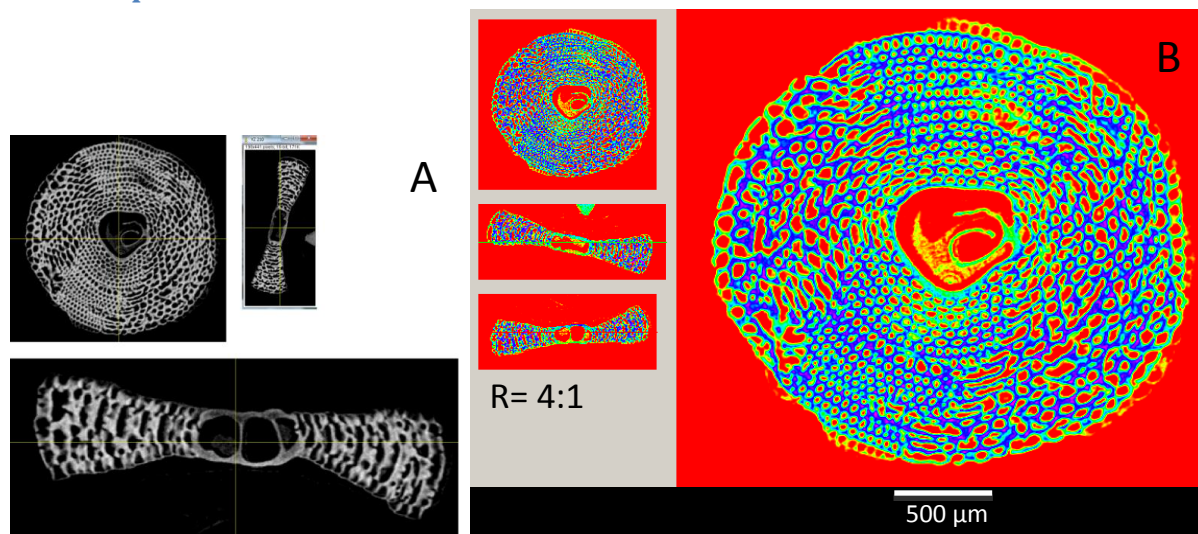


Figure 52 X-ray MCT pre-adult specimen.

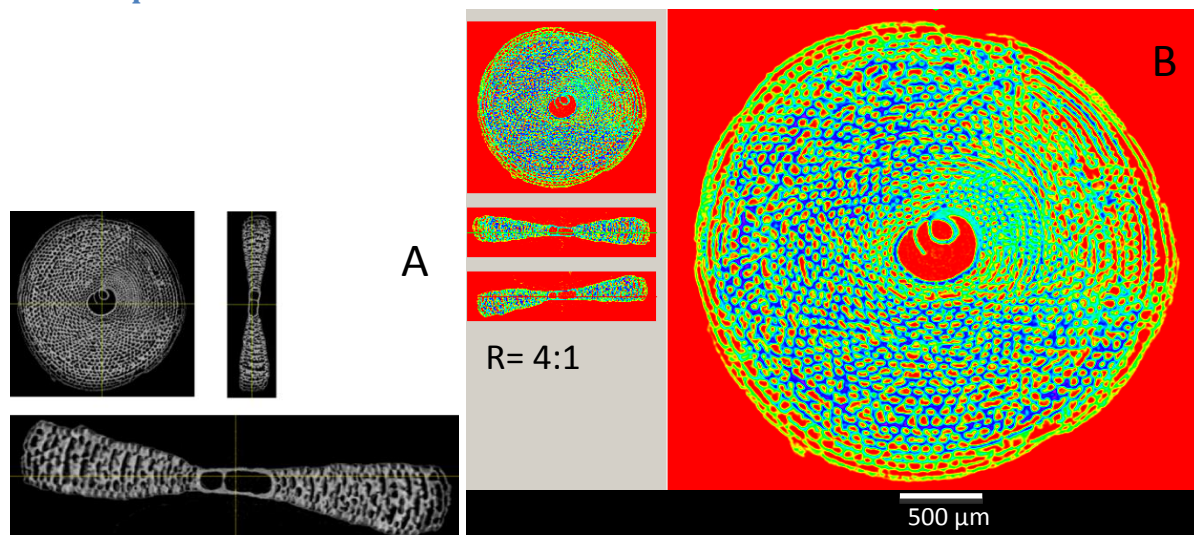
In Figure 52A is shown a pre-adult stage with a discoidal relatively symmetrical shape developed. In Figure 52B, the relative degree of mineralization appears higher in the regions between chamberlets such that a circular pattern of high density is evident (arrows in Figure 52 B). In most circular regions a central area of higher density is surrounded by a region of lower density on both sides (blue region with green periphery). Additionally, angular continuous lines (arrows) of higher density are evident progressing from the centre towards the margin in several regions of the grid like structure. In Figure 52F, the 3D rendering reveals the pores (stolons) at the prolocular wall (arrows) that connect the proloculus to the annular chambers, chamberlets and to the margin. The test is thinner at this region and increases in thickness (and 3D) towards the periphery (direction of white arrow).

In Figure 52 C, D, E, & G which are high magnification views of Figure 52B (boxes), a view (C) in the xz plane of a lower region of an outer chamber of the test, shows a high degree of density-mineralization (dark blue-violet) evident in a roughly triangular area (circled) linking the three chamberlets surrounded by a graded region of lower degrees of density (light blue green yellow) at the junction of three chamberlets (red colours) which are at three elevations. A linear region of higher density (arrow) is discernible in the chamber wall extending outwards towards the margin of the test between two chamberlets (red colours) which are in roughly the same vertical plane (dashed line). A high magnification view in the xy plane (D), of the thinner inner part of the test shows the degrees of density increasing from the chamberlets through to the inner regions of the walls. The density distribution appears as a thickened triangular region at the junction in this plane and extending through the walls (septa) from the inner to outer regions of the test in a linear beam-like shape that links with adjacent triangular high density regions to complete a clearly square-like interlinked pattern. A similar grid-like pattern with a similar density distribution is also visible at the outer areas of the test where the test is thicker (E). The triangular high density areas (small circle) with a graded decrease in density towards the chamberlets and an interconnected square grid is evident. The periodic hexagonal patterning of the chamberlets (circled area) is evident and the polygonal shape of the chamberlets can be discerned. For comparison, the corresponding area of the grey-scale reconstructed tomogram (G) is shown. The anisotropy of the test, i.e. the change in elevation with increasing diameter, changes in elevation in a circular direction, approximation of voxel attenuation values based on the algorithms applied during the transfer of grey-scale brightness (intensity) values of the reconstructed tomographic view to the “thermal view” result in an inexact match of the visible geometries in the two images. However, in both images, the patterns and subtle changes in density are discernible.

3.6.2.7 Specimen M_smaller



3.6.2.8 Specimen small



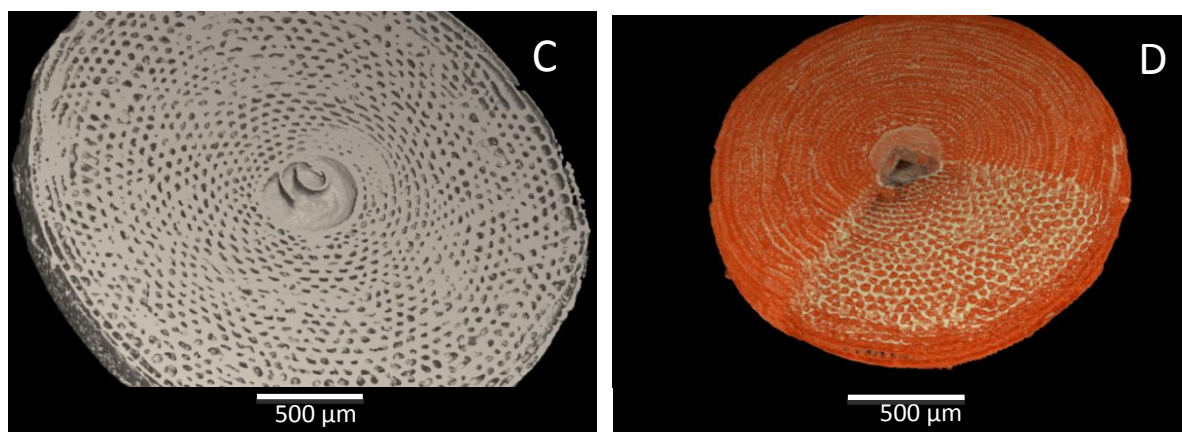


Figure 53 X-ray MCT mineral or density distribution in adult test.

The data presented in Figure 53 display similar features in two adult specimens with some variations. Since each view is not of an exactly corresponding “slice” in the xy plane of X-ray MCT data for the specimens there are variations in the views of the corresponding features that are visible. These data show the progressive increase in test size with concomitant increases in the development of and complexity of the cellular structure. Changes in aspect ratio of the discoidal form, development of cross-sectional near-symmetry, development of slopes of the upper and lower surfaces and changes in the slope across a single annular chamber of the test, development of the 3D layers - are particularly visible in the 3D renderings of a cross-section and complete test. An increase in the densities of the mineralized features across the grid structure of the test and the progressive refinement in periodicity is apparent in the “thermal” views of the test. Although there is an increase in the test diameter and 3D cellular structure, the width of the annular chambers and the chamberlets remain fairly constant through the increase.

3.6.2.9 Specimen M_551

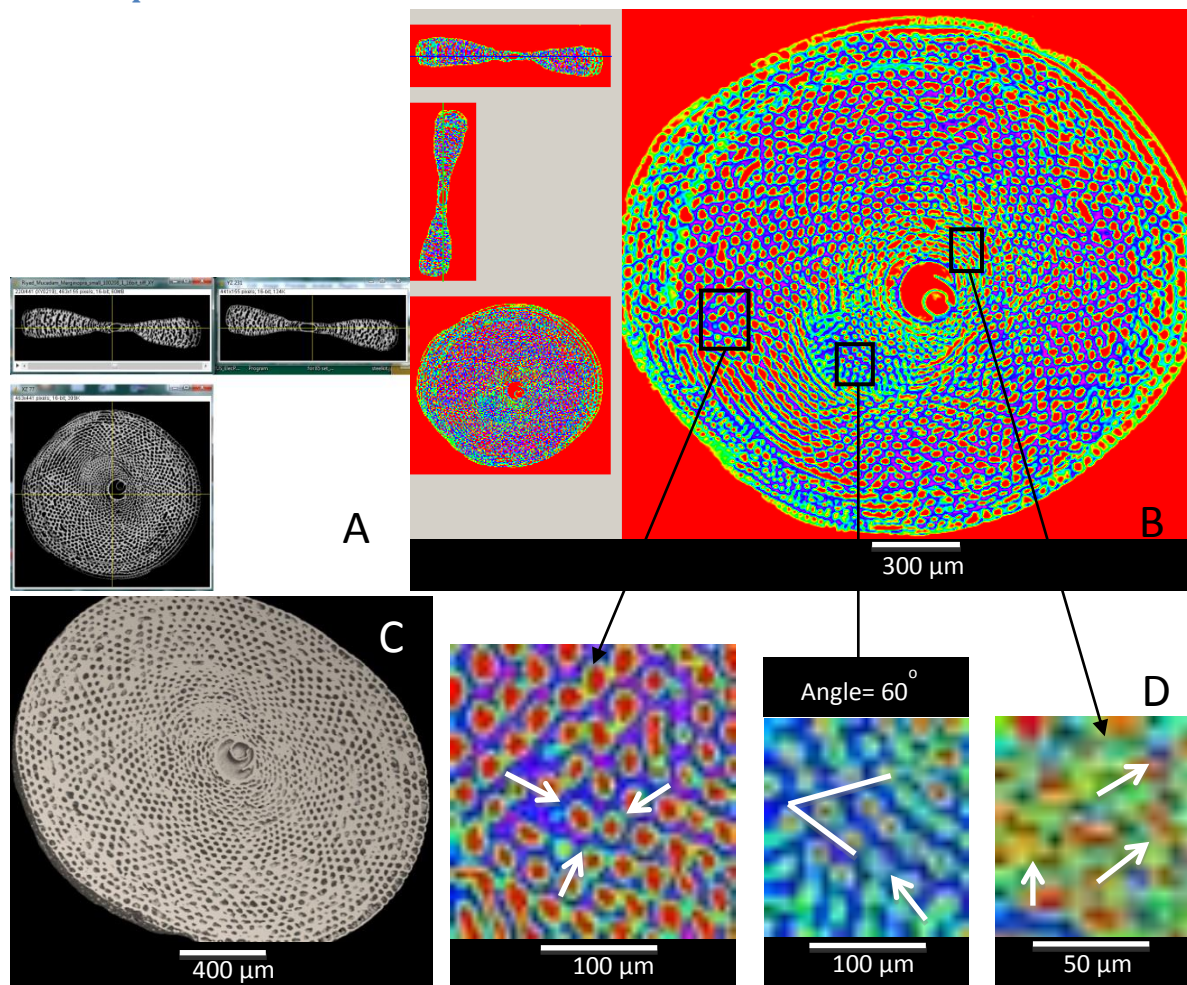


Figure 54 X-ray MCT density variation in intercameral walls and in adult test.

Figure 54 shows the data for specimen 551 which represents an adult test. The density distribution and its relevance to the grid structure is highlighted in four different views of the test.

In the adult test, represented by specimen 551 the mineralization of the grid structure appears well developed through all the annular chambers. Here the circular lines of mineralization, and the two lines of high mineralization in angular directions are clear. The 3D structure of the test is fully developed, there is regular chamberlet sizing at the inner, surface, middle and outer regions of the test. The magnifications of these regions show in Figure 54D a region from the middle section, with a well-developed triangular high density wall area between chamberlets linked in a linear circular direction. In the innermost region of the test, the periodicity of the high density aggregates or patches and their angular progression towards the outward region is visible (white arrows). In the outer area of the test, this structural arrangement and density distribution is well developed in its apparent connectivity in three directions. Here again, the anisotropy of the test shape and the angle of the “planar slice” of the tomographic view results in the visualization of different elevation levels of the test in a view of the complete discoidal test. This implies that all features which are microstructurally connected in the disc may or may not be viewable; however a change in the angle of the slice allows that the features of interest and their

connectivity be “captured” for viewing. This is illustrated in the 2D representations; this particular 3D volumetric rendering in this angular planar cross-section captures almost the entire disc and all the chamberlet microstructures in that plane, i.e., connectivity is not interrupted.

3.6.2.10 Specimen Middle

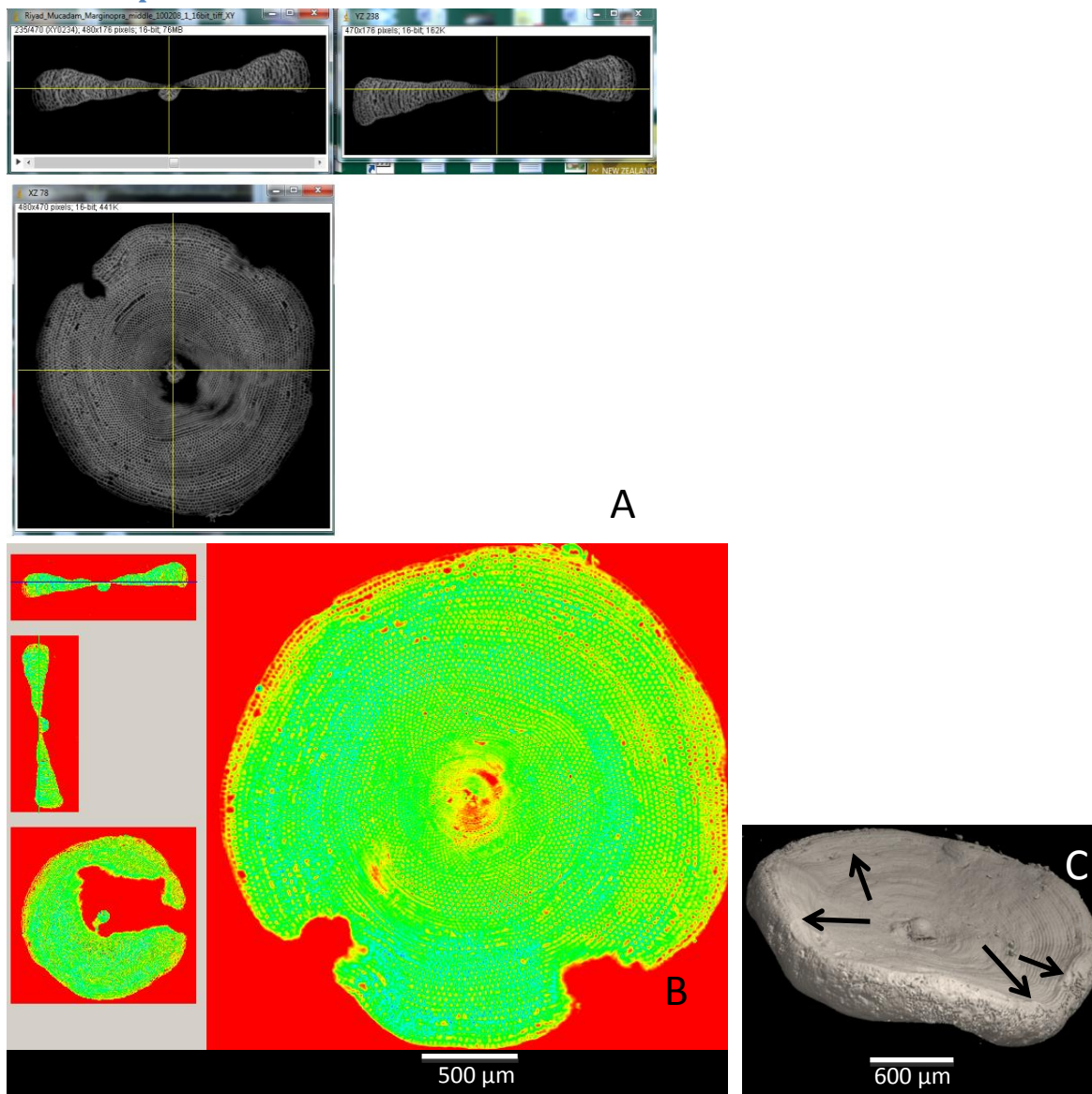


Figure 55 X-ray MCT Change in morphology of test at pre reproductive stage: curved margins.

The data presented for “specimen Middle” (Figure 55) show an obvious increase in the anisotropy of the test surface and a “wavy” or crenellated margin is apparent. A change in the prolocular region is evident- a globule-like mineralized material is visible and the morphology of the central cavity has transformed such that the test has a low density central hole-like region. Observations of several tests of different sizes indicate that this is an indication of maturity and the possible onset of the reproductive phase. The grid structure in the xy plane is highly developed in its periodicity; it is structured finely. In this image, the resolution of the X-ray MCT data (i.e. the voxel size) is sufficient to capture this periodicity and differentiate clearly between wall and chamberlet. However, the “thermal view” does not represent the same scale of densities as of the preceding specimens. During the processing of data, different thresholding values were applied to this set of data as the finer structural features of this test could not be distinguished using the thresholding values applied to specimens M111-M551.

In Figure 55 the discoidal test is roughly circular with a high aspect ratio but the anisotropy of the slopes of the disc which is in an annular direction appears extended to the marginal cord (Figure 55 C-arrows). The thresholding operation (assignment of different colours to different microstructures-solid/void) during data processing and the resolution of the data allow a precise visualization of the complex geometry of the structure. In this “slice” the periodicity and the annular chambers geometry are highlighted.

3.6.2.11 Specimen Largest

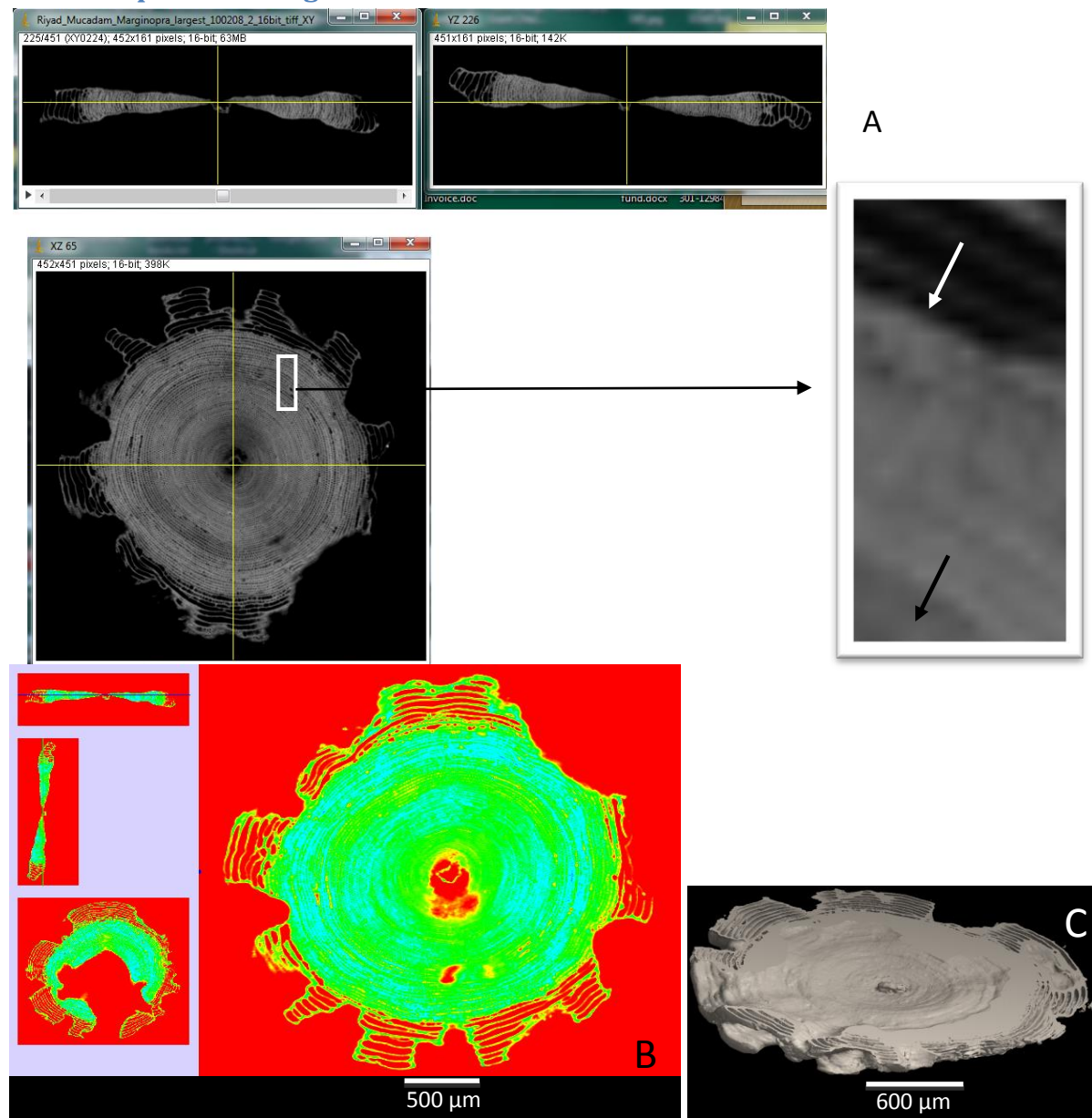
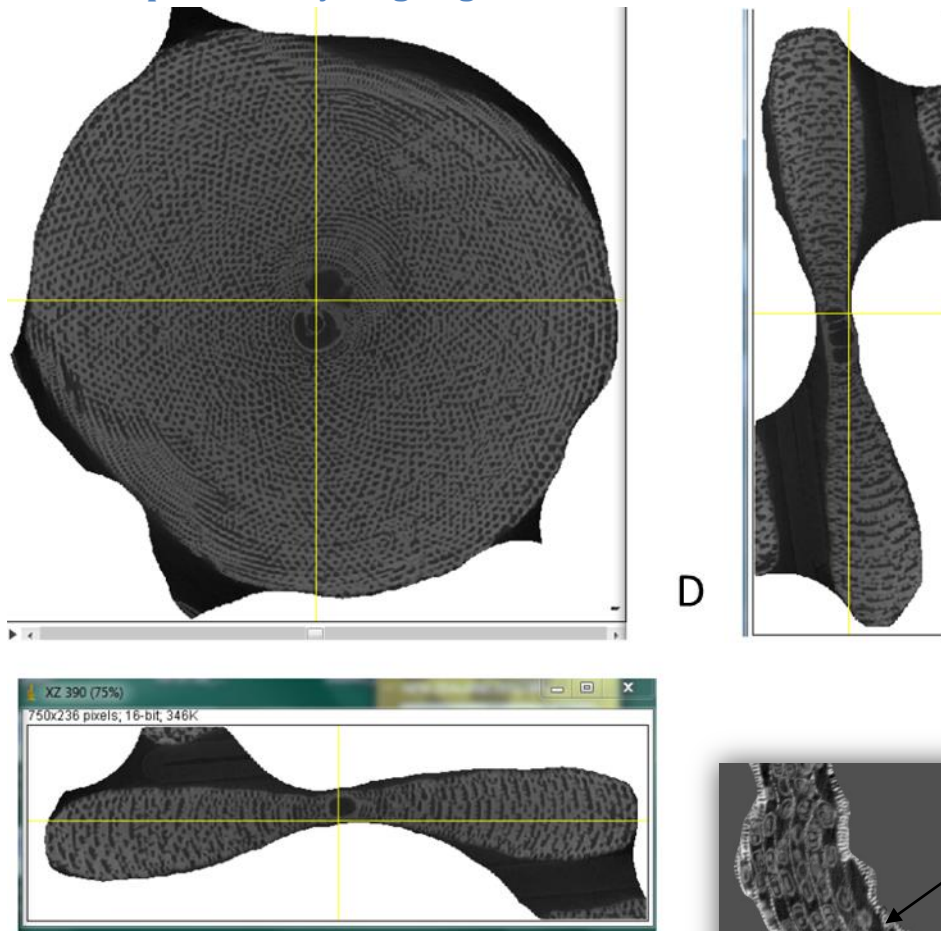


Figure 56 X-ray MCT of reproductive stage of test: unresolved details of chambers; variable density of test annuli.

In Figure 56 and Figure 57 are shown images of the reproductive stages of the test structure. The data in Figure 56 are of low resolution; Figure 57 shows high resolution data.

In Figure 56 the large size of the test and the low resolution (high resultant voxel size) of the experimental conditions cannot resolve the detail of the enormous number of chambers-chamberlets that define the structural grid of this test. The high magnification view of a region of the test demonstrates (Figure 56 A, black arrow) the closeness of the grid structure, the annularity of the chambers, the difference in structure-density and morphology- of the reproductive chambers (Figure 56 B, white arrow).

3.6.2.12 Specimen M_young: High resolution



3.6.2.13 Specimen M_old- High resolution

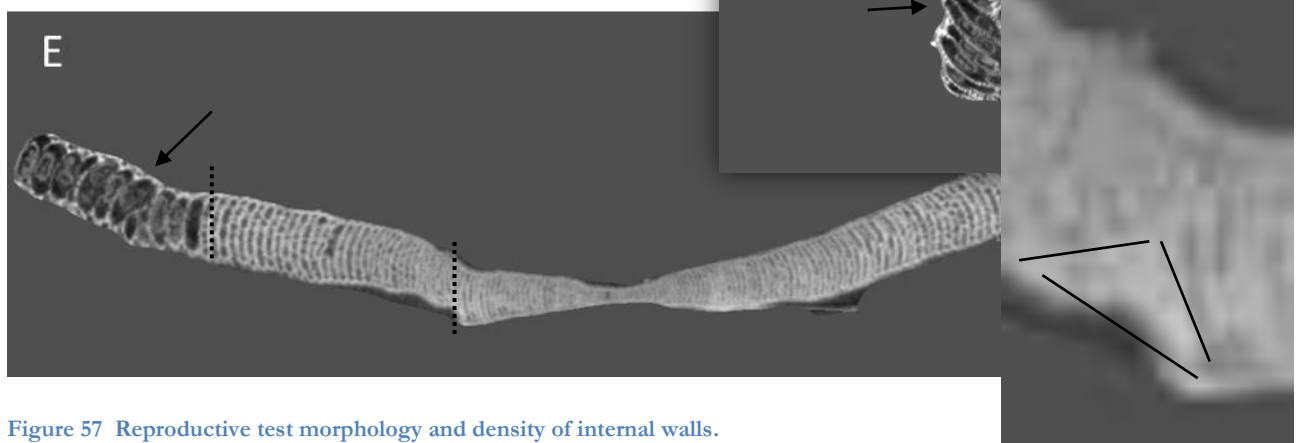


Figure 57 Reproductive test morphology and density of internal walls.

However, in Figure 57, is shown that was obtained using experimental conditions described in Table 3; the resultant voxel size of $3.1 \mu\text{m}^3$ captures the fine detail of the structure and the scanning conditions allowed for imaging of an adult (Figure 57 A-C) and a complete very large discoidal reproductive test (Figure 57 D-E) which is too large to view using EM. The resolution is high enough to view the contents of the reproductive chambers which are packed with

juveniles (inset: the internal structures and distribution of the juvenile are visible) and the higher density of the outer walls compared to the inner walls is evident. The test appears to have uniform thickness (as seen between the dotted lines) and a change in the curvatures of the original discoidal form is noticeable. In the regions of changes in curvature, the chambers appear fused (inset) and the walls are denser or consolidated (lighter triangular area in inset).

3.6.3 Qualitative Results: High resolution X-ray MCT data based volumetric renderings for 3D visualization of architecture

3.6.3.1 Introduction

The experimental conditions described in Table 3 and in Table 4 were applied using different equipment to obtain X-ray MCT data that provide a higher resolution of microstructures. The higher quality of the data is noticeable in the quality of the subsequently produced images and 3D volume renderings of the test. In order to provide a comparison with data presented earlier, and to illustrate the flexibility and applicability of this technique to calcium carbonate cellular structures and similarly composed structures, in Figure 58 3D renderings in different orientations of the test are shown. In several views a combination of cross-sectional planes, higher magnifications, virtual sections and visualization techniques such as material-based differentiation of structures in 3D are shown.

These visualizations are based on the digital tomography data represented in the grey-scale reconstructed tomograms of Figure 57. The separation of an entire volume of interconnected structures based on the solid or void phase composition of the structure is obtained through precise thresholding of the histogram of intensity (or attenuation) values of the X-rays. Subsequent processing of the tomogram data in 3D and the assignment of colours to the phases can show in isolation an entire phase of a structure in 3D. Here the interconnected chambers (void) or the crystalline wall (solid) phases of the test are isolated and highlighted (Figure 59). The views presented can be instantly rotated in any plane, sectioned (virtually), expanded or reduced in any sectional directional, colour coded or magnified etc. to provide a closer understanding in 3D of the connectivity, morphology of microstructures and architecture of each phase of the test.

Figure 60 and Figure 61 allow a visual, intuitive comparison of the quality of X-ray MCT of tests of similar ontogenic stages presented in Figure 50 and Figure 51. Figure 62 represents the reconstructed output of a single exploratory experiment with ultra-high resolution phase contrast X-ray nanotomography equipment. A $\sim 15\ \mu\text{m}$ section of the surface wall of the surface chamberlets of an adult specimen of *Marginopora sp.* was imaged to assess the potential for a very high resolution view in 3D of the crystal morphology, intracrystalline porosity and view of the orientation (or lack of) of crystals in the surface wall.

The same X-ray MCT based data are used to analyse quantitatively features of interest. In the test of *Marginopora sp.*, the surface chamberlets are potentially an exceptionally important microstructure: the symbionts are packed closely in the surface chamberlets, the surface wall of the chamberlets appear transparent to translucent; and the microstructures occur at twice the frequency as the chamberlets in the main annular chamber. In this research the use of optical

microscopy and EM showed at several scales of measurement various characteristics of this microstructure. However, a visualisation of the 3D morphology of surface chambers and details of their the connectivity with other microstructures remains largely elusive. This is elucidated in Figure 63 and Figure 64 through 3D volumetric rendering of the X-ray MCT data. Photographs of the solid model that was constructed using the same X-ray MCT data and a 3D printer described earlier (Figure 21). Together these allow a complete comprehension of the structure of the surface chamberlets. Surface area and volume are enumerated; these are key quantitative properties of this microstructure that are dependent on its distinct anisotropic 3D form. These values were obtained using the enumeration functions of Drishti and the X-radia proprietary software.

Further analyses that evaluate quantitatively selected important characteristics of the test of *Marginopora sp.* are presented in the section that follows.

3.6.3.2 Results

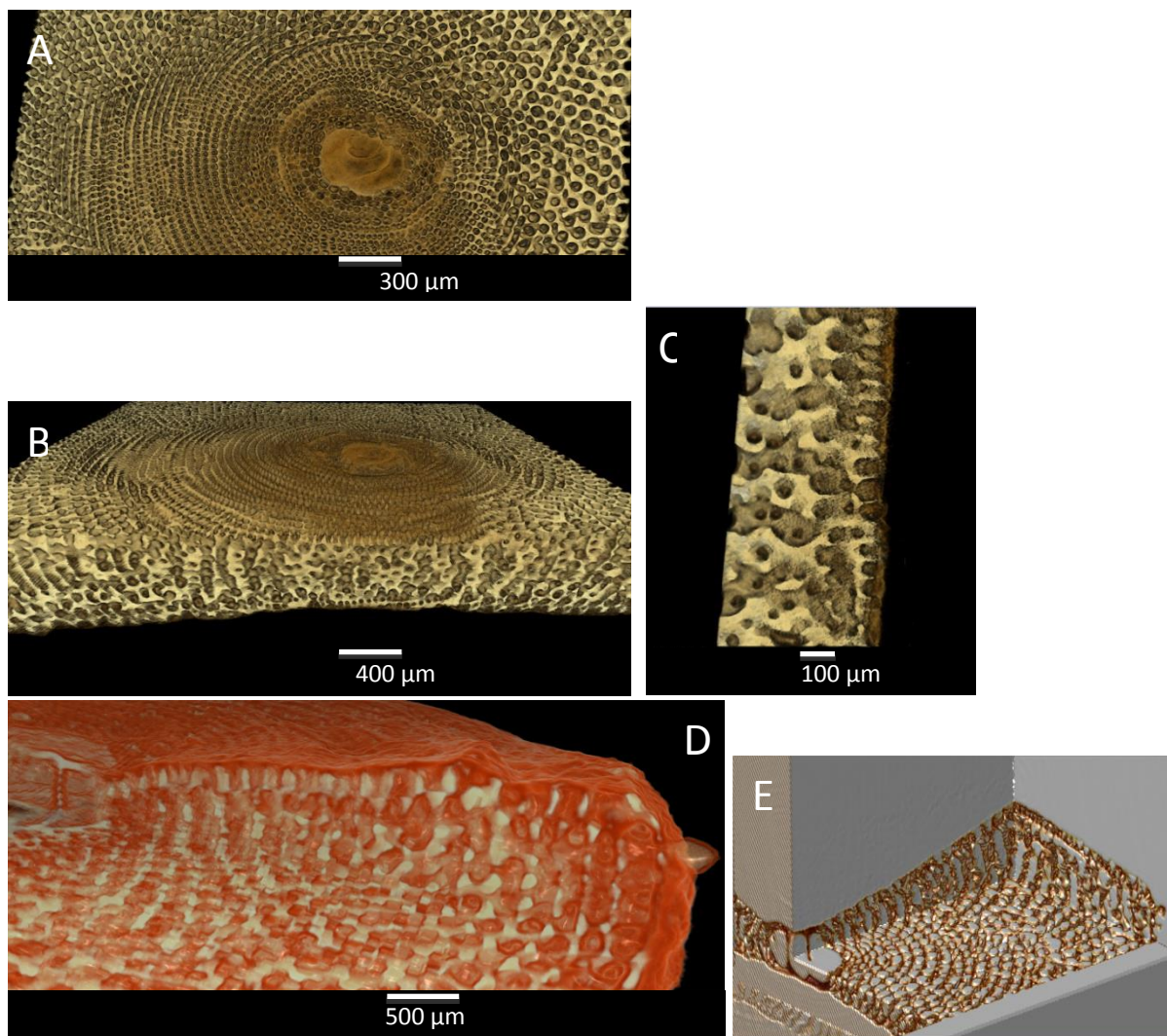
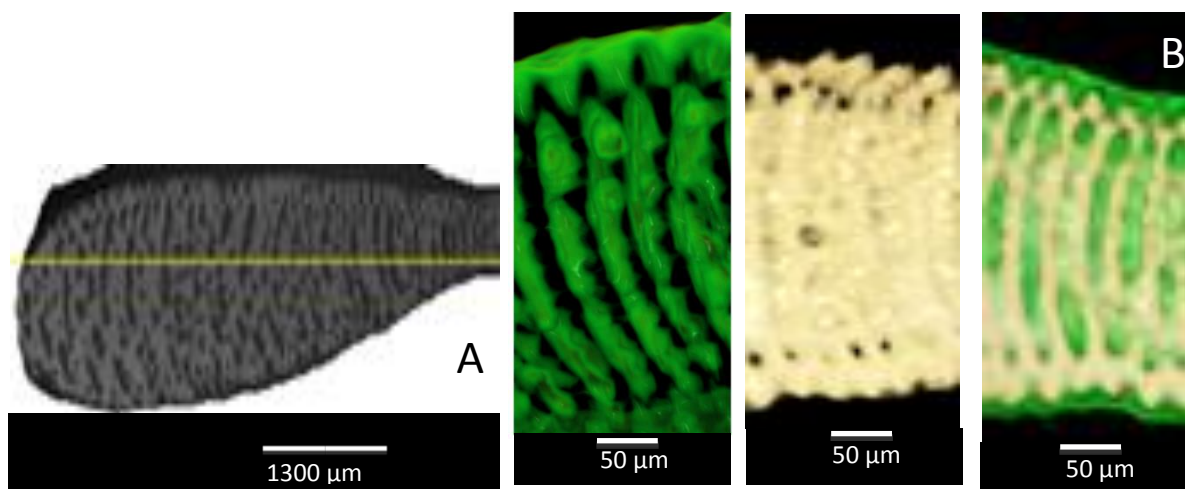


Figure 58 Specimen M_young: 3D renderings in different orientations of the test.

High resolution sections volume rendered with colour gradation (A-C); with solid and void phases differentiated by assignment of 2 different colours after thresholding (D); orthogonal view showing sections in 3 planes combined with solid fraction highlighted in a cellular view of the test (E).



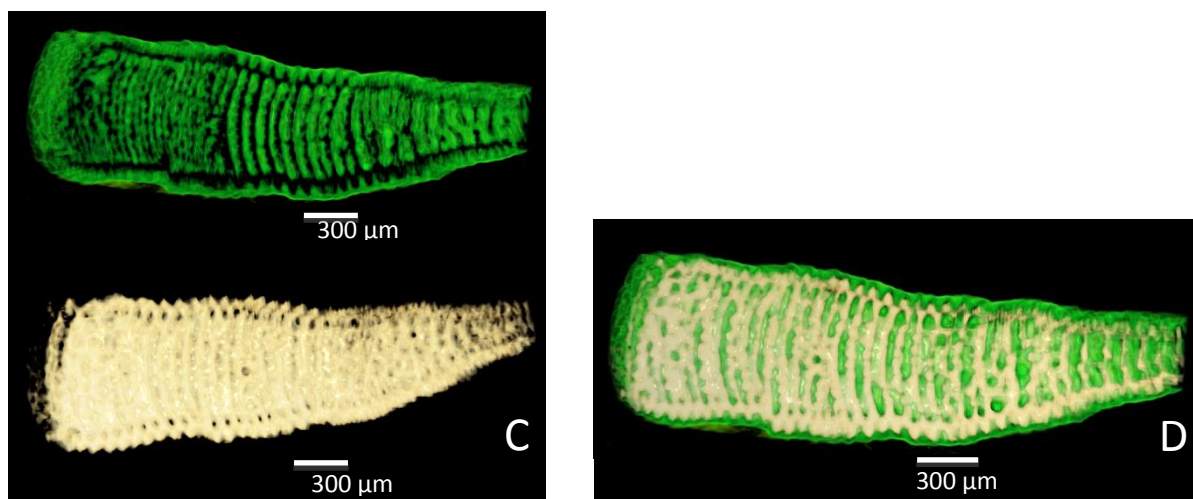
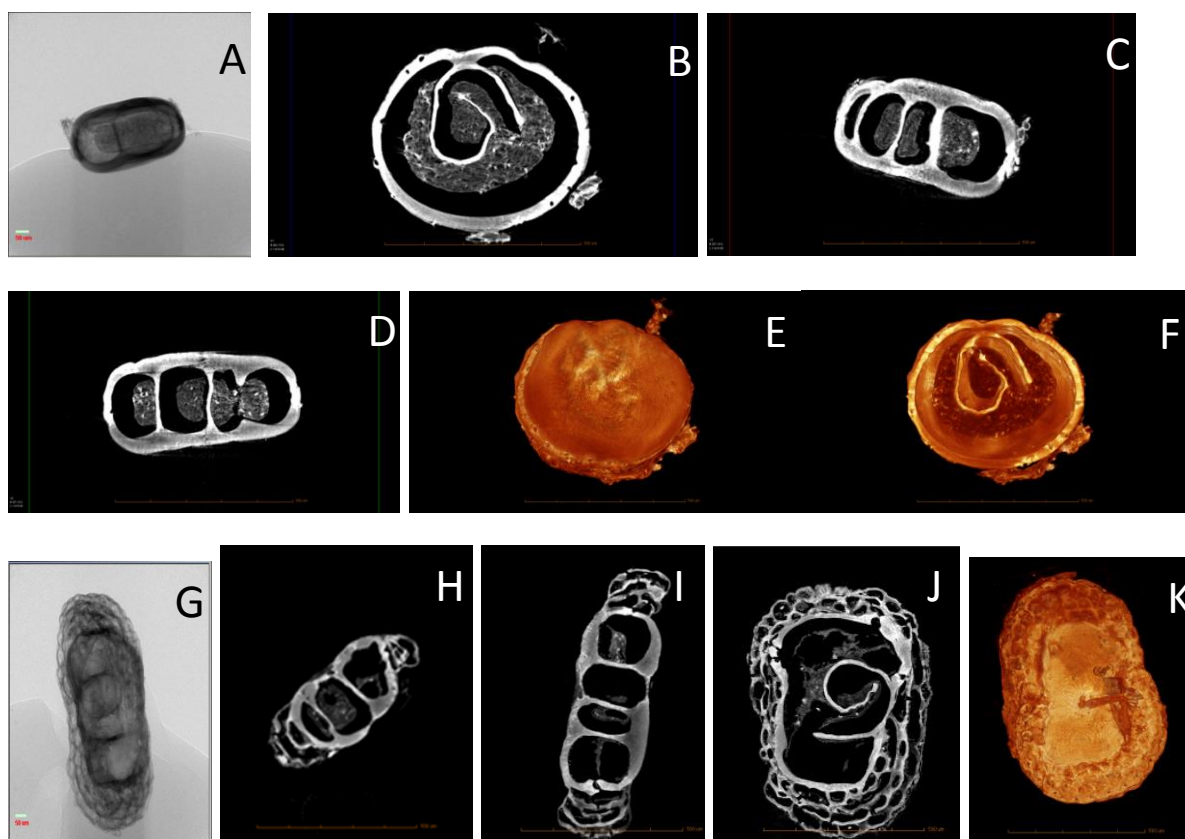


Figure 59 Specimen M Young: A reconstructed tomogram.

High resolution volume renderings of (B) void space, (C) solid fraction and (D) solid-void composite and corresponding detailed views.



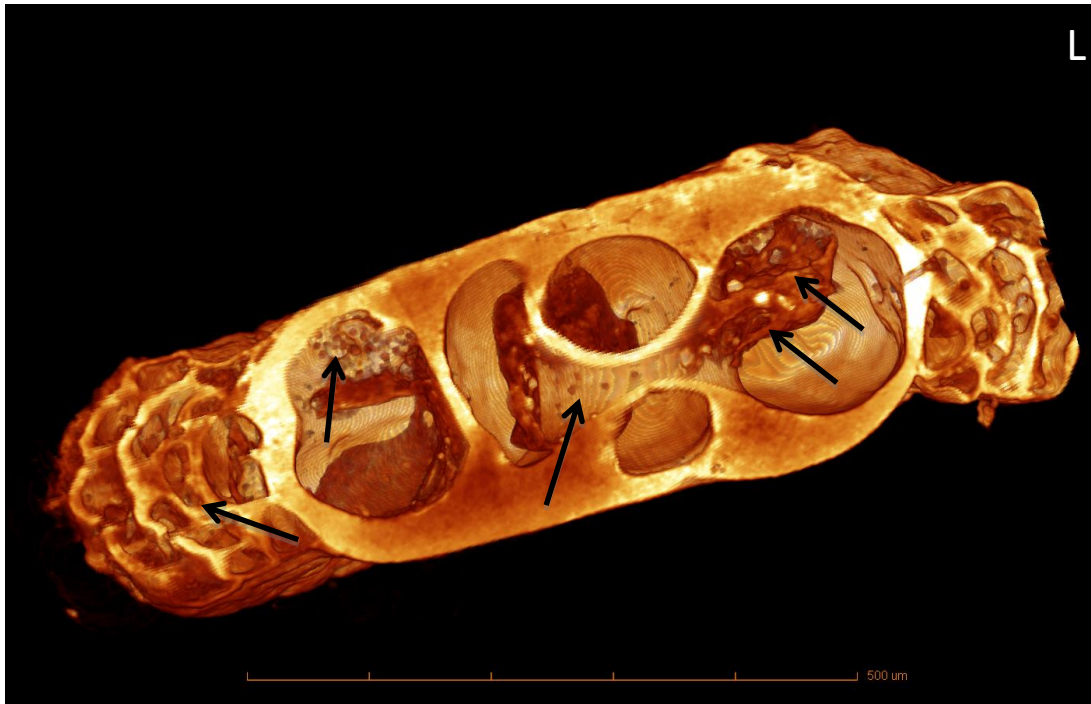


Figure 60 Specimen Foram Small and Foram 2.

Very high resolution reconstructed tomograms and volume renderings of early ontogenic stages of the test (white bar 50 µm and orange bar 500 µm).

In Figure 60L the symbionts are clearly differentiated and visible in 3D inside the test just below the surface, the 3D morphology of the septal walls including pillar-like construction is evident, small pores are visible, and the mineralized protoplasmic material adhering to the wall is visible; of particular interest are the apparent pore-like holes that appear within the protoplasmic material.

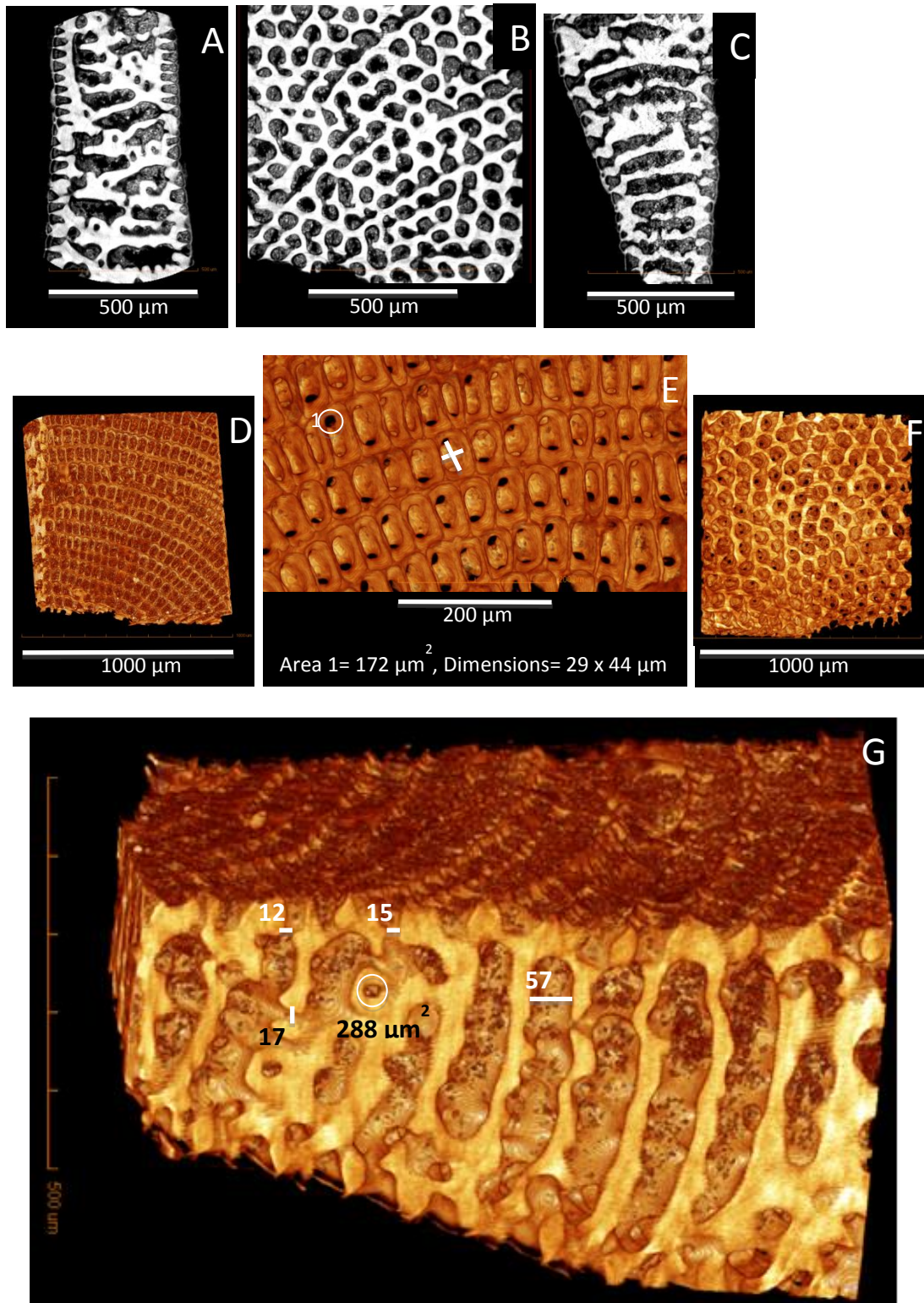


Figure 61 Specimen Foram Transverse section: very high resolution reconstruction and volume renderings.

The high quality of the reconstructed tomogram is evident in Figure 61A-C, which includes the surface wall, morphology and contrast of the surface chamberlets, the stolons, and symbionts-features that are 10-20 μm wide - are sharply defined. In Figure 61D-F the volumetric renderings show strikingly the detailed 3D morphology and distribution of the surface chambers, symbionts and the layered cellular solid structure of the test.

Specimen M 110: Ultra High Resolution (submicrometre) phase contrast 3D visualization

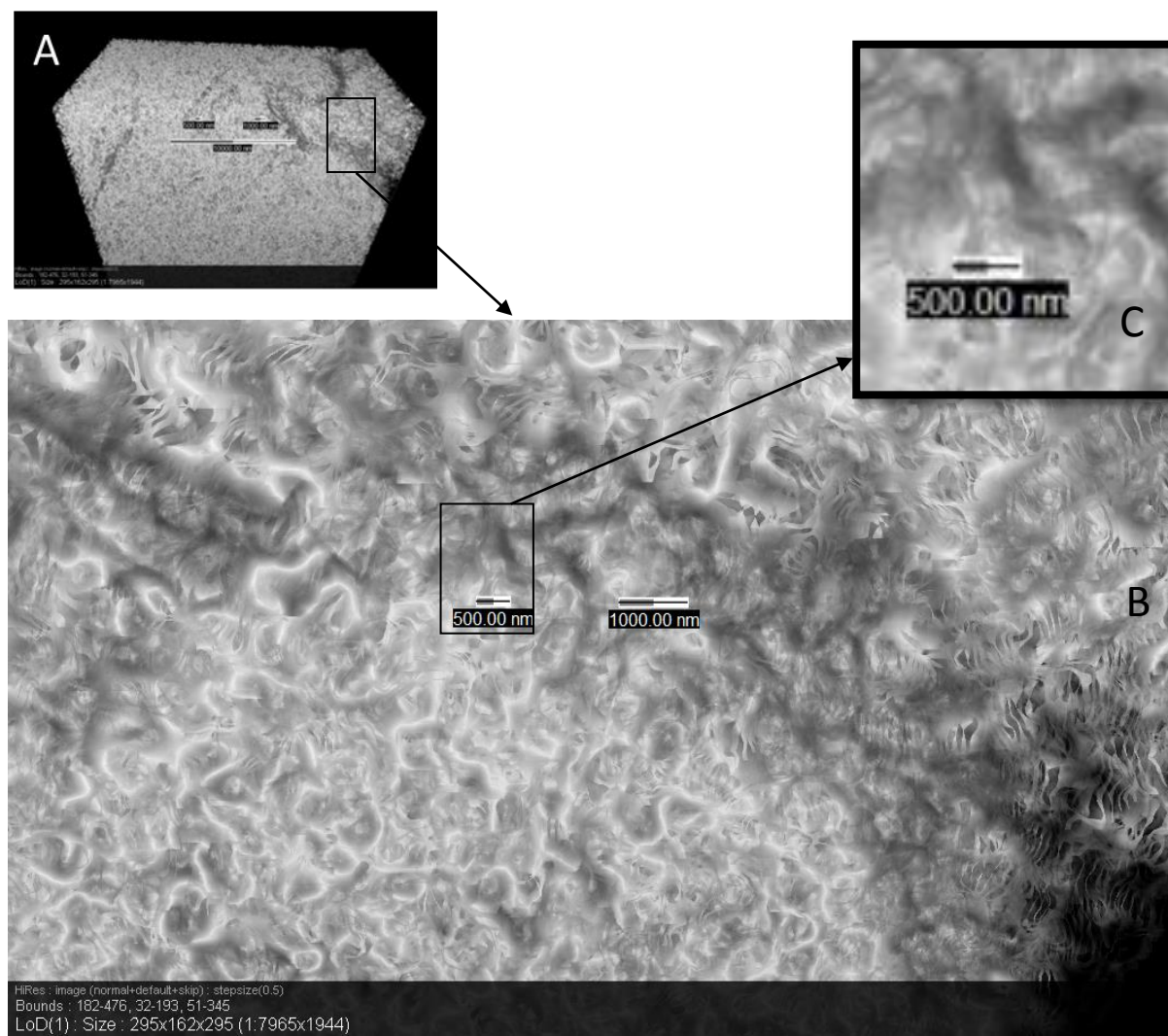


Figure 62 Nanotomography of the surface wall of the surface chamberlet.

The images in Figure 62 show a solid mass that appears as an agglomeration of disordered curved irregular closed shapes. Higher contrast bright irregular curved lines overlay these closed shapes. A darker region is visible in which the bright curved lines are not present. The inset shows a region in which high and low intensities are visible. If the crystalline material is X-ray attenuating then the darker regions represent voids between crystalline material. Although the resolution is in the submicron scale, it is not possible to distinguish any known features of the wall which were determined by the use of electron microscopy (EM).

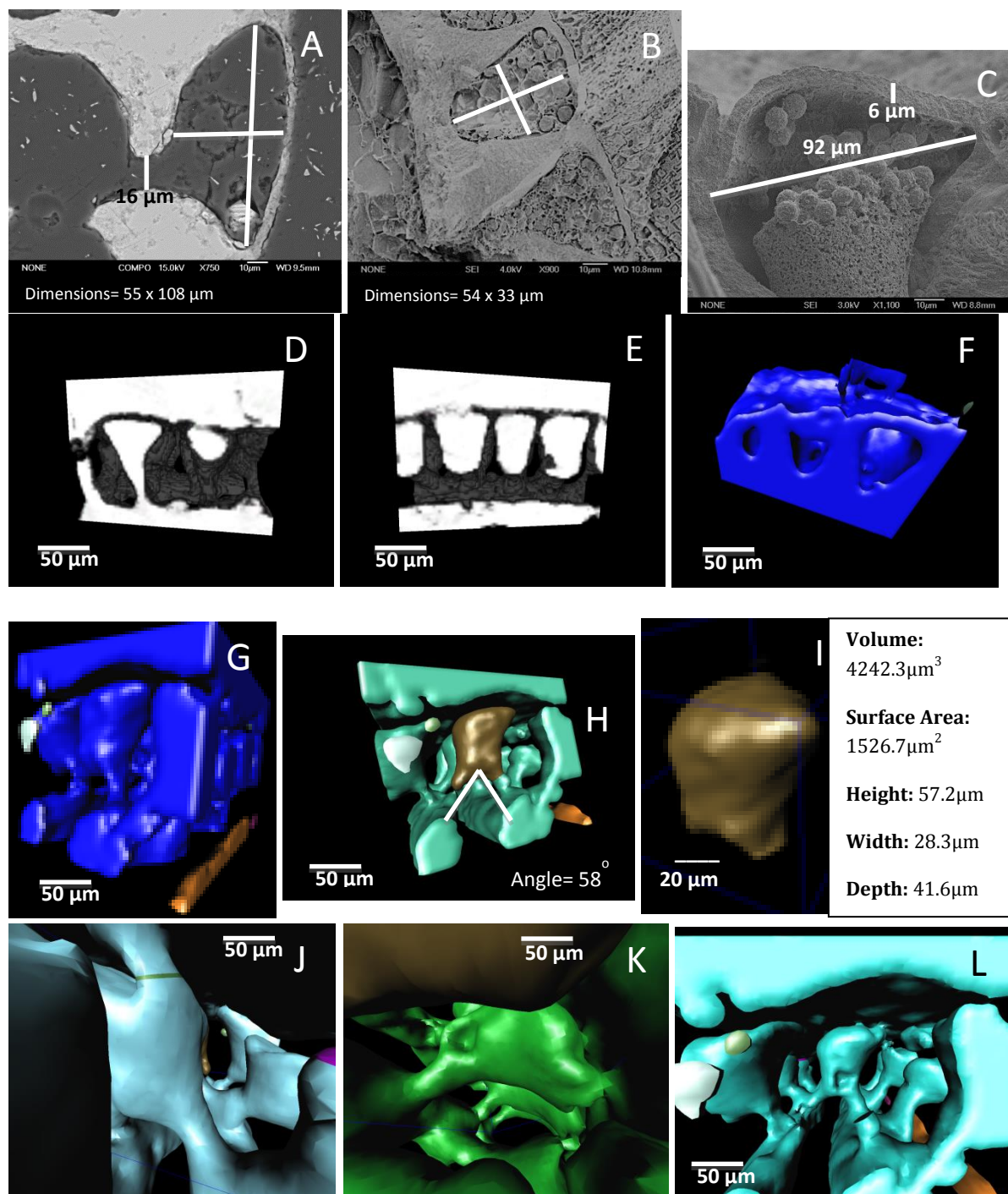


Figure 63 3D volumetric rendering of an isolated microstructural feature and quantification-surface chamberlet.

EM provide high resolution (micron and submicron scale) 2D views of the surface chamberlet and partial 3D views of components - e.g. surface wall and cavity - of its microstructure as shown in Figure 63A-C. The X-ray MCT data reconstructed in 2D and 3D volume renderings show a series of these structures (Figure 63D-F) and reveal their 3D morphology. However, the volumetric renderings of the same data with only solid phase and the void phase (Figure 63F, G respectively) selected and viewed in orthographic projections explicitly show the complete external 3D morphology of the microstructure- it is grossly similar to a molar tooth. There are two convex walls which show some concave regions and two concave walls which show localised convexity. The angularity of the stolons is 58° . Views in Figure 63H-L reveal the connectivity.

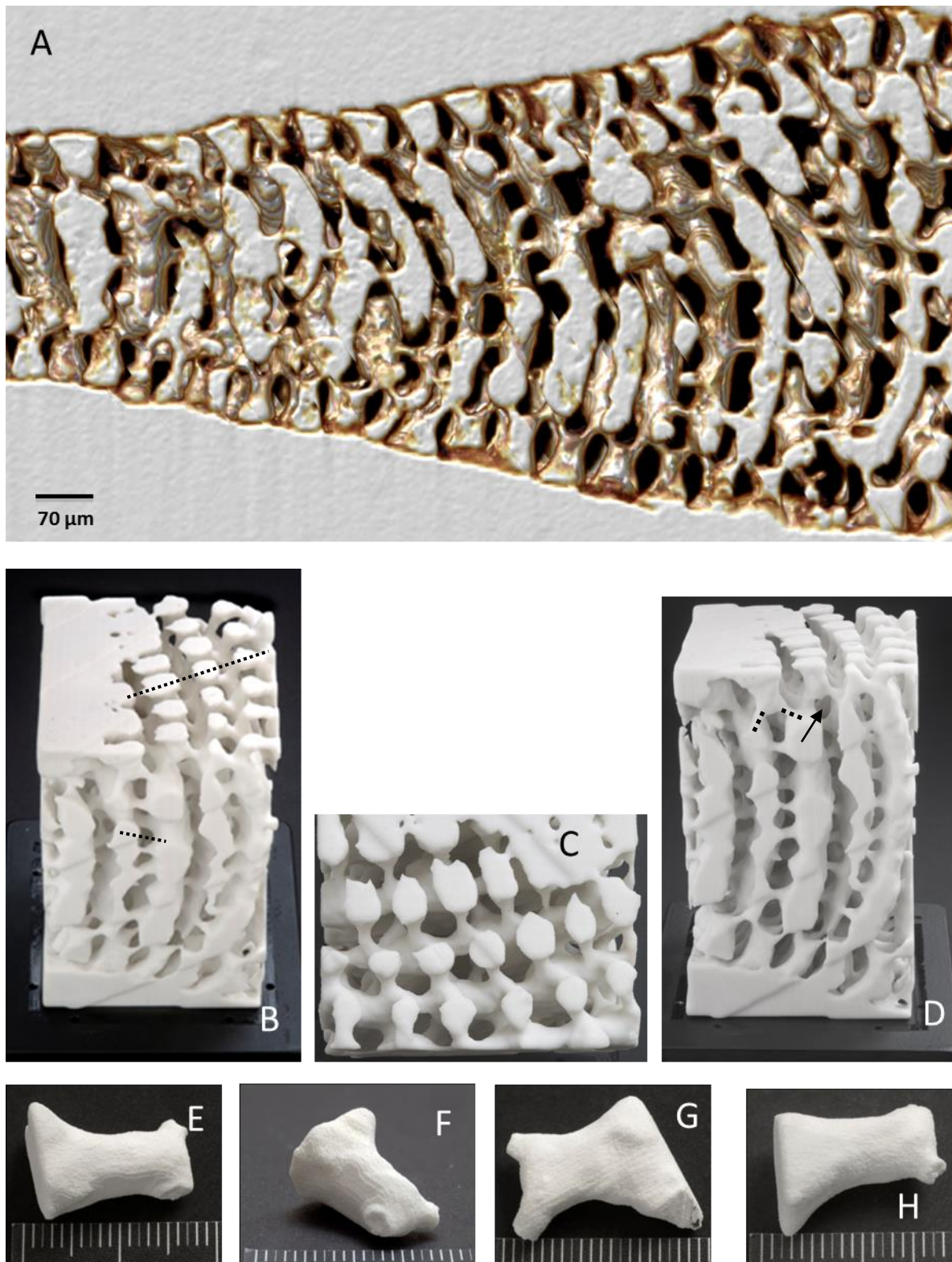


Figure 64 Rapid prototype 3D-print of internal structure of the test using X-ray MCT data: chambers, chamberlets. Here in a representative section is unambiguously visible the 3D the architecture of the test.

3.6.4 Results in Summary

3.6.4.1 Shapes of the test changes during ontogeny

The series of specimens of increasing size (i.e. diameter and number of chambers) representing increasing age through ontogeny examined using X-ray MCT in this study showed that the shape of the test changes in 3D from bean-shaped through roughly polygonal to discoidal. The 3D data allow for a view of the anisotropy of the slope of the surface of the test. Throughout ontogeny, as visible in the specimens in this study, the slopes of the surfaces of the disc change. The test is at first convex-shaped then gradually loses convexity and tends towards concavity. However, it remains locally convex in some regions. The 3D data reveal that at reproductive stages the test appears to have a wing-like expansion stage that is concave. Measurements made of the test in 3D views through virtual sections in the xy-xz-yz planes (Figure 50-Figure 57) indicate that the aspect ratio (diameter to thickness or height) of the tests of the specimens in this study changes through ontogeny. It varies approximately in the range 2:1 - 5:1. The shape of the test is approximately symmetrical when viewed along different orthogonal planes passing through the centre of the disc through juvenile to reproductive stages of ontogeny.

The 3D shape of chamberlets is revealed through the volume renderings of high resolution X-ray MCT data: the chamberlets are approximately pentagonal or hexagonal in cross-section, “sausage” shaped, curved and subdivided into 3-5 sections in the yz and xz planes of the discoidal test. Each subdivision ends in a constriction or stolon that connects to lower adjacent subdivision. The shape of the lateral chamberlets is very complex. Although in 2D a motif of the shape of the chamberlets is recognizable (Figure 63) the 3D X-ray data volumetric renderings and the 3D rapid prototype “print” model show that shape of lateral chambers- is highly anisotropic (Figure 64). Lateral chamberlets are broad, flattened at the upper end, bulbous; their lower regions are slender but are pillar-like. The cross-sectional shape of the chamberlets is variable throughout their length, width and height. A pair of stolons that connect the lateral chamberlets at their bases to the annular chamberlets are roughly orthogonal to each other.

3.6.4.2 Grid structure

The X-ray MCT data show distinctly a 3D a linear grid pattern of the crystalline structural framework at every stage through ontogeny. The grid structure is well-developed and periodic through the 3D form of the test; internal virtual slices reveal the same grid pattern at various depths or thicknesses of the test. Views in the transverse (xz and yz) planes also show the pattern and a cellular 3D structure in numerous views of the interior and reveal that the 3D cellular structure accommodates two sets of pore-tubes. The 3D unit structure is symmetrical such that it can be translated in an annular and a radial direction along the linear grid structure; it is modular in 3D.

3.6.4.3 Distribution density of calcite

X-ray MCT data represented in the reconstructed tomograms (grey-scale) and in the coloured thermal view in which differences in the grey-scale (attenuation of X-rays) shows in 3D the distribution of the density of the test. A virtual slice of the test in the xy, yz and xz plane shows the density distribution in a synoptic view for each specimen representing a stage in the ontogeny of the test. The outer and inner regions of the walls of each chamber are less dense; density is

highest in the central region of each annular wall and it is highest in the centre of the septa between the annular chamberlets; density of the vertical walls of the marginal chord (xz) is higher than the density of the walls in the xy plane in any particular virtual section. In the earliest stages of ontogeny it appears that regions adjacent to pores are denser than the remainder of the chamberlet wall in which the pores occur. During ontogeny the inner regions of the test appear to have a higher density compared to the outer regions in a particular xy section. X-ray MCT data with sufficient resolution that allows a magnified view of the inter-cameral walls and septa reveal clearly that the density distribution surrounding an annular chamberlet is graded: density is lowest closest to the chamberlet void and increases in annular ring-like regions towards the centre; a denser polygonal (rhombic) region is evident between chamberlets (Figure 52). Although it is not clearly resolved, some data show that the density in a xy direction between annular chamberlets is highest in a linear radial direction (Figure 52). The pattern of the densest regions forms a skeletal grid-like structure in the test in each of the specimens.

The distribution of high density regions appears as a flow-like pattern in one particular section (see Figure 57). It is not clear whether the distribution of density remains closely similar through the xz and yz sections of the test as observed in the virtual sections presented, i.e. progressively through the height or thickness of the test as it may be visible in the virtual sections presented. The distribution of high density regions appears as a flow-like pattern in a particular section (Figure 57). Sequential xz and yz virtual slices were not analysed to observe the distribution.

3.6.4.4 X-ray MCT resolution of viewable structural features

X-ray MCT data obtained using different equipment as shown in the low resolution, high resolution, very high resolution and ultra-high resolution illustrate the effect of voxel size and experimental conditions on the: resolvable microstructures, differentiation of density, sharpness of the 3D volume rendering, reconstruction of the structure, and viewable porosity of the test. High resolutions with voxel sizes of 1.9-3.1 μm resolve the smallest microstructures of the test- (including symbionts) that are also identifiable using optical and electron microscopy. Voxel sizes that are larger than 3.1 μm result in insufficient resolution of the microstructures and annular chambers of the larger specimens of the test (Figure 56). Ultra high resolution X-ray nano CT with an isotropic voxel size 50 nm does not resolve the calcitic nanostructure of individual nor the crystalline aggregates that comprise the walls of the test; experimental conditions and insufficient phase contrast do not permit sufficient differentiation and useful reconstruction.

3.6.4.5 Microstructure characterization

Different techniques- microscopy of thin-sections, SEM, X-ray MCT and 3D printing using X-ray MCT combined allow for a complete characterization of a microstructure of the test across all scales of measurement. In addition to the qualitative new visualizations that are not otherwise possible by other techniques new morphological information was visualized and reported about the lateral chamberlets and the annular chamberlets: the unusual complex anisotropic shape of the lateral chamberlets; the tubular sausage like morphology and polygonal cross-section of the annular chamberlets. Direct detailed quantitative measurements are possible of microstructures. Results (Figure 63) of the application of 4 techniques were shown for one important crystalline microstructure: the morphology or 3D structure of a lateral or surface chamberlet which contains symbionts was completely characterized and a direct enumeration of the geometric

dimensions at nano-macro scales of the test - surface area, volume, heights, thicknesses etc. was possible rather than through the application of approximations or models.

3.6.5 Discussion

3.6.5.1 Mineralisation and architecture

Results demonstrate that the X-ray MCT technique can be successfully applied in the visualization and qualitative analysis of the structure and microstructures of the biomineralised test of *Marginopora sp.* to reveal information that is not accessible directly by other methods. The most important contribution of its application as shown in this section is that the distribution of density in the test through several stages of ontogeny can be qualitatively evaluated. The variations in density can be construed to be variations in the mineralization or calcification of the test in different regions and of different microstructures. Using X-ray MCT data the observations presented of the test during its ontogeny allow a mapping of the gradual mineralization of the test.

The level of mineralization and localisation of mineralization patterns observed can be related to the mechanical properties of the test as it develops through ontogeny. This area of research remains almost entirely unexplored in the biomineralisation and structures of foraminifera. Stiffness, brittleness, hardness of the test and their relations with the mineralization and distribution of mineralization in the test are related. The level of mineralization varies in different biomineralised structures, but is usually high or low rather than in a gradation. If density of the test is not critical to test strength then alternatively the architecture of the test may compensate. A gradation or pattern of density in the architecture of the test would likely have effects on the mechanical performance of the test; this implies the possibility of differential calcification of different structures; more where it is effective mechanically for a resultant robust structure. Reports of research that mapped changes in density within the test and through ontogeny and its mechanical implications are absent in the literature. Wetmore's studies of the mechanical fracture of tests of *Elphidiella hannai* and selected small species explored correlations with motility, habitat and test shape. The studies indicated that some test shapes and nearshore habitats were related to crushing strength but motility was not, while density was not necessarily as important as test shape or some morphological characteristic (Wetmore, K.L., 1987). Wetmore's study of large benthic foraminifera in high and low energy environments reported that test weight did not differ significantly when compared to crushing strength despite notable differences in architecture (Wetmore, K.L. et al., 1992). This is in accord with the suggestion in this research based on the results of this study that the distribution of mineralization in and the architecture of the test are of importance to the mechanical properties of the test. Wetmore's studies did not consider the relation of density and different degrees of mineralization in the architecture of the test and any other mechanical properties.

That the mechanical properties of biomineralised structures are related to the degree and distribution of mineralization of the structures, the architecture and the hierarchy in the architecture is a well-studied relationship in several phyla. Summaries of several studies describing these relations in mammalian bone, seagulls legs and wing bone, echinoderm spines, mollusc shells, siliceous sponges and nacre are provided by Currey (Currey, J., 1999; Currey, J.D., 2005). In these studies Young's modulus, bending strength, fracture, mineral content and

density are experimentally determined parameters of the materials and of the architecture. These studies reveal that architecture is often “precisely adapted” to the interaction with the environment i.e. the loads and the material properties of structure. Younger bones of polar bears are less mineralized have lower Young’s moduli and lower yield stress; in calcified cartilages of rays (*Rhinoptera bonasus*) the tooth plates show a convergence with the structure of trabecular bone such that buckling is resisted. Results obtained in this research (Figure 51 through Figure 54) of density distributions revealed in different virtual slices in different planes of the test using X-ray MCT data show that in early ontogeny the vertical walls are more mineralised; later a pattern of high and low density areas forms that is repeated through the test’s microstructures in an apparent modular mode. The very high resolution volumetric renderings of early ontogenic stages show the pillar-like vertical structure of the internal septa of chamberlets (Figure 60); similar structures are observed late in ontogeny at the outer most chambers of the mature reproductive test. Both structures resemble internal views of trabecular bone. Both observations indicate the pillar-like supportive function of the septa early in ontogeny as chambers and the test are first mineralised.

An occurrence of the grid-like and rhombic patterns in the “thermal view” map of grades of mineralization that is revealed through the distribution of density is repeated and enhanced through ontogeny as the test size increases. Recall that in Section 3.4 the architecture of the test was described also in terms of a hierarchy of microstructures through several scales of dimensions. Evidence of the development of the pattern through the ontogenic stages of the specimens that are not necessarily the offspring of one adult but are of the same set of samples is stronger than an observation of a single specimen or only of adult tests. Observations of the presence of both these mineralization patterns support the deduction suggested here that the architecture of the biomineralised test of *Marginopora sp.* is adapted to mechanical functions in a coastal hydrodynamic environment; the mechanical value of these particular patterns in structures have been demonstrated (Deshpande, V.S. et al., 2001; Gibson, L.J., 2005) Experimental measurements of the mechanical properties and a comparison of results with other biomineralised structures would be valuable investigations that could help validate such a deduction. The separate and combined roles of the organic material, the organic-inorganic composite and the inorganic material which has not been considered in this section, in the mechanical properties of the tests could be investigated. Wetmore reported that the organic material of near-shore tests appeared to be more robust to dissolution than of tests found in calmer or deeper waters, suggesting that it may have a role in the higher crushing strength of the near-shore tests.

A limitation of the study was that a detailed map of density was not presented through all the virtual slices in 3 planes, i.e. 3D, for data sets of each ontogenic stage although the data obtained do allow for such analyses; the manipulation of large data sets was limited by the desktop computing resources. Parallel computing or large memory computing resources would easily overcome this limitation. An alternative method, which is cumbersome, is that each virtual slice of the tests could be converted to a “thermal view” to highlight the differences in the distribution of density and manually assembled in sequence to achieve a complete 3D density distribution map of each test. An internal view that captures as complete sections as possible have been analysed here. Also, the specimens investigated in this research were sampled at one site or

habitat. The biomineralised tests studied here could represent an ontogenic response of the organism to that particular habitat under the constraints of its genotype. A similar investigation of specimens of *Marginopora* sp. from different locations and observed possible variations may further inform the inferences of this study. X-ray MCT based density maps of different architectures of foraminiferal tests found in similar environments could also inform the mechanical functional value of the test architecture.

3.6.5.2 Visualization

Another important result of this study was the demonstration of the X-ray MCT technique's visualization capabilities in unravelling the morphology and connectivity of complex anisotropic internal and external microstructures without sample preparation or its induced artefacts.

Complete equatorial oriented sections of larger benthic foraminifera (LBF) with ring-shaped chambers are difficult to obtain due to the common waved geometry of the equatorial plane of the test. The value of X-ray MCT data used in 3D volume renderings and in virtual cross-sections is highlighted in views of the interior of the test and insights gained that are not possible or highly unlikely by other microscopy techniques: a simultaneous 3D perspective of the surface and in cross-section of the interior of the entire disc of the test or of three fused cross-sections of one test which reveals the periodicity of the solid walls in 3 planes; relative complementarity of the 3D structure of the solid walls and void chambers (Figure 58); transparency (very low or no attenuation of X-rays) of the upper walls of the lateral surface chamberlets allowing a view from the surface of the structure of the interior surface, position and high periodicity of the stolons and of the chamberlets; the texture or 3D topography of the surface of the test such that a series of wave-like periodic ridges is evident at the microscale which may prevent symbionts from rolling off the surface of the test or affect the scattering of light or both; a cellular foam like structure strikingly evident in a virtual 3D “block-cut” of the test (Figure 61); a close-up almost fly-in view of the interior of the test which allows a grasp of the nuances of structure as in the high resolution rendering of Figure 60. Although a 3D ultrahigh (nanometre) resolution of the lateral chamberlet's surface walls (Figure 62) was not effective in this study, future improvements in technology and of the technique may provide better results that would be most useful in studies of the optical performance of the walls of the surface of the test. The 3D characterization of the crystalline structural arrangement and the exact quantitative determination of the geometric quantities of surface area and volume, as has been achieved in this study using X-ray MCT data, would be essential parameters in such studies that could elucidate the optical role of the microstructures of the test.

To the best of my knowledge a 3D rapid prototype of the architecture of a test has not been reported. 3D rapid prototype (RP) model of the structure of the test and the 3D visualizations of the upper lateral chamberlets (Figure 64) reveal nuances of the morphology that are inaccessible by other techniques. In a study of the armor of *Gasterosteus aculeatus* (marine threespine stickleback) that used X-ray MCT data, the interlocking structure of the plates was revealed by using a 3D rapid prototype model (Song, J. et al., 2010). The 3D RP model of the test provides a synoptic, unambiguous 3D view of the internal connectivity, proportions, angularities, geometries of the microstructures and their positions in the architecture of the test. It indicates a compact, highly organized, modular, symmetric, sandwich 3D architecture; the unusual convex-concave walls and stylized funnel like structure connecting to the marginal canal

may represent an adaptive optical and storage microstructure that is part of the adaptive sandwich-architecture of the test in which the lateral chamberlets are packed closely at twice the frequency of the lower chamberlets, allow larger upper exposed surface areas to light, are supported by two strut-like stolons which positioned angularly (approximately 60° between struts) at their bases permit a wider stable structural footing and their hollow structure permits rapid transfer of symbionts in response to varying light conditions. The tubular structure of struts would support a compressive load. An interesting optical, microfluidics and biological experiment would be an *in vivo* observation of the intake and output of symbionts through the two stolons in response to varying light conditions on the surface of the lateral chamberlets. These are examples of the harvesting of features of interest in vast amounts of data and relating the features to the context of the architecture of the test, visualization of multi-fields at different scales (e.g. crystalline-void) and tracking the evolution of features (e.g. chamberlet formation, mineralization of the test).

The importance of visualization in science has been established in numerous diverse fields of research such as neuro-imaging, flow physics, aeronautics, meteorology, combustion; new ways and technologies of acquiring and interpreting data highlight the role of visualization (Oshima, M., 2001). Lipsa et al. provide a comprehensive review of work on visualization for the physical sciences including astronomy, chemistry, earth and atmospheric sciences, physics, simulation and modelling and computer graphics and point out opportunities for collaboration (Lipsa, D.R. et al., 2012). Visualization in science has been compared to theories which achieve an image-like status in their aims of organising, simplifying of data in a template and allowing for analysis. Metrics of the utility of visualization include memorability of phenomenon and structure (Borkin, M.A. et al., 2013), rapid understanding or time-saving (Chen, M., Floridi, L. Borgo, R, 2013), economical (high cost of alternative methods), natural or intuitive, aesthetic and precision (van Wijk, J.J., 2006). The appropriateness or particular effectiveness of visualization is in the analysis of multidimensional data, in observing similarities and differences in complex structures or trends or global vs. local similarities and differences. In a classic analysis of the role of visualization in mathematics and in science it was argued that visualization in pictures or images is, among alternatives, the “simplest way of representing the information and structure of a problem-usually thus aiding both its robust understanding and its solution” (Wimsatt, W.C., 1990). As in this research, in instances in aeronautics, problem solving, molecular biology, medicine and earth sciences, where large data sets are represented as imagery, visualization achieves through a preconscious, visual-system physio-neurological process “a competency and computation” that substitutes for conscious thinking (Gershon, N. et al., 1993). A criteria fundamental for robustness would be the detection and delineation of boundaries in the microstructures and architecture of an object. Visualization is particularly suited to this spatial representation, and provides robustness through a multiplicity and comparison of views. Different ways or techniques are necessary e.g. optical, polarizing, electron microscopy, X-ray MCT to combine information obtained from different perspectives on the same architecture of the test. In Section 3.3-5 the different size scales and levels of organization of the test were elucidated and in this section the distribution or level of mineralization in the test was visualized. The relationships among patterns uncovered in both sections can perhaps only be correctly understood by simultaneous multiple visualizations. Lastly, the use of visualization techniques is particularly suited to determine whether there is a common object, property or cause behind

apparently correlated patterns (Wimsatt, W.C., 1990). The mechanical adaptive value of the architecture is an emerging common theme related to the correlated patterns discovered in this research. The architecture of the test and patterns discussed in the last few sections are further explored in the following sections through analyses and visualizations of the networks of the test, the spatial organization and self-assembly of the test.

3.7 X-Ray MCT Quantitative Results: Porosity, Surface area, volume of the test

3.7.1 Introduction

Porosity is the void space fraction of a sample that is occupied by fluid. Porosities of the test of foraminifera have been reported primarily by researchers in palaeobiology, palaeoceanography and sedimentary geology. Researchers have shown that the test porosities of several species of planktonic foraminifera are related to oceanic surface water temperatures (Frerichs, W.E., Heiman, M.E., Borgman, L.E., & Be, A.W.H., 1972), and can be used for reconstructing palaeoceanographic conditions (Fisher, C.G., Sageman, B.B.,ASURE, S.E., Acker, B., & Mahar, Z., 2003); porosities of foraminifera tests are important in understanding the sedimentary evolution of atolls (Braithwaite, C.J., Taylor, J. D., Kennedy, W. J., 1973), in developing an understanding of the hydrogeology of coral reefs (Oberdorfer, J.A. & Buddemeier, R.W., 1985), and in determining the acoustic properties of sediments which are dominated by coral fragments and tests of foraminifera (Fu, S.S., Tao, C., Prasad, M., Wilkens, R.H., & Frazer, L.N., 2004). Foraminifera sediments react to the passage of sound waves as do solid particles but relationships between porosity and acoustic properties are complicated; intraparticle porosity is important for “correlating with acoustic properties”. In an early attempt to create a standard for measuring porosity of tests Bachman documented indirect laboratory measurements of porosity of tests using spherical glass beads as approximations and comparisons of tests because “no method was found to measure the internal void volume of a test directly” (Bachman, R.T., 1984). Porosity has also been an important factor in determining the density of the tests, an important parameter in the determination of the settling velocity of the test. The settling velocities of tests are important determinants of the distribution of tests in sediment; the unusual shapes and chamber morphologies of foraminifera tests require that the determination of densities and porosities be investigated by several methods in the laboratory (Severin, K.P. & Lipps, J.H., 1989; Wallbridge, S., 1998).

These studies have largely reported the use of measurements based on weight, volume, density relationships of the test with the use of water or acetone to penetrate the test under ambient or vacuum conditions. Scanning electron microscopy has been used to enumerate the pores and their sizes on and inside the surface of the tests (Constandache, M., Yerly, F., & Spezzaferri, S., 2013). Estimates of porosity based on thin-sections of tests in an equatorial plane are often not dependable because of the nonuniform 3D shapes of the tests. Limitations arising from 2D measurements transferred to 3D and of preparing thin-sections of *Marginopora* sp. have been mentioned earlier in this work. Instrumental analytical techniques such as mercury porosimetry and helium pycnometry are other methods which provide quantitative assessments of porosity. These methods are invasive, destructive of the specimen and do not allow a qualitative view of the distribution of porosity. Mercury porosimetry based instruments can resolve pore sizes up to 10 nm and provide rapid quantitative analyses of distribution of porosity and densities. In foraminifera tests this resolution may include the intracrystalline porosity but it leads to higher estimates of the chamber-stolon void space fraction; raw data have to be filtered for a particular range of porosities based upon a detailed knowledge of the dimensions of the voids in the test.

From Chapter 2, recall that the application of the X-ray MCT technique in several fields of research, including studies of foraminifera, was reviewed. Its applications included non-invasive research of the porosity and interconnectedness of the pores in rock cores and in the structure of trabecular bone. In the previous section of this work, X-ray MCT data of several specimens of *Marginopora sp.* were analysed to qualitatively represent the distribution of density in the test. In this section the data obtained with the X-ray MCT technique is analysed to quantify the porosity of the tests of the same specimens. The reconstructed tomogram data were analysed using ImageJ software described in Chapter 2 by the voxel-count method using the procedure described in “ImageJ BoneJ volume calculations” (Appendix A).

3.7.2 Results

Table 6 Threshold values for Figure 65 Porosity of tests of growth stages.

(Volumes in μm^3 , diameter in μm)

Sample	solid volume	total volume	void volume	Thresh. low	Thresh. hi	Porosity	average dia.
m111	15719017	37834279	22115262	7565	56735	0.584	490.66
m331	58103806	99644379	41540573	459	58559	0.416	807.33
m332	74284065	130269654	55985588	771	65535	0.429	955.82
m441	78337023	136860557	58523534	744	63199	0.427	929.29
m551	2.55E+09	3.56E+09	1.01E+09	9227	54719	0.283	3173.29
m smallest	391708383	621361977	229653594	6478	61183	0.369	1586.70
m smaller	700031942	1.03E+09	329090692	8270	60225	0.319	1877.21
m small	2.65E+09	4.34E+09	1.69E+09	15218	62591	0.388	3361.76
mmiddle	8.78E+10	1.08E+11	2.00E+10	10285	41631	0.185	10572.74
m large	1.45E+11	1.74E+11	2.85E+10	907	46271	0.163	15157.12
m largest	2.40E+11	2.95E+11	5.51E+10	1861	36511	0.186	16681.23
m young	863292884	1.09E+09	227566874	76	255	0.208	2154.19

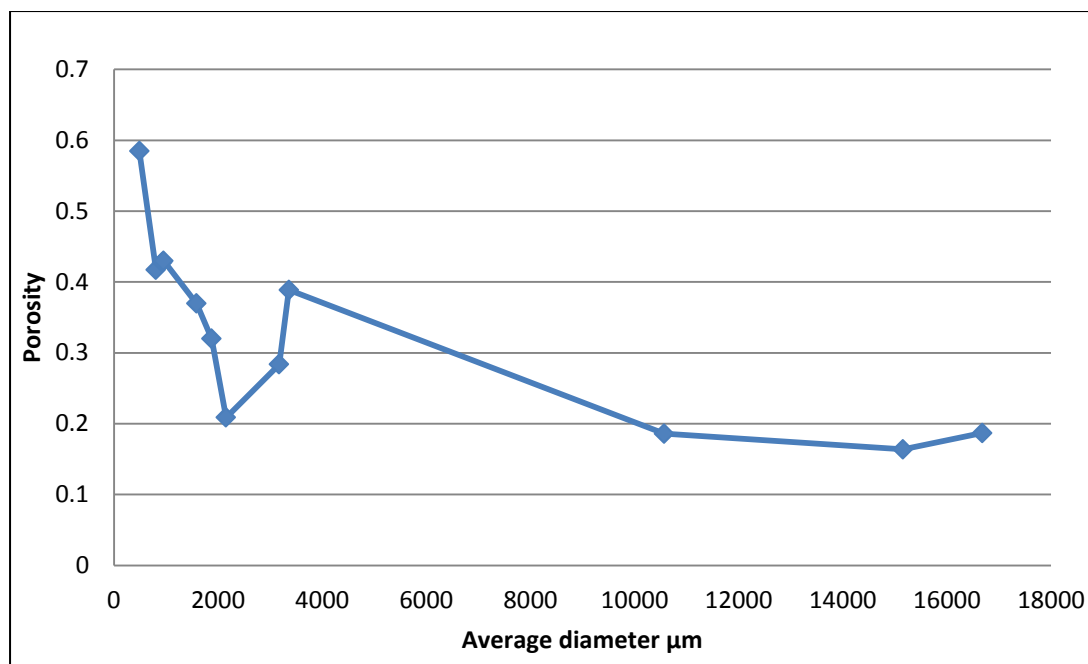


Figure 65 Trends in porosity with test size assessed with X-ray MCT data and ImageJ BoneJ.

For the specimens evaluated, the overall trend observed is that porosity of the test decreased as the size of the test increased (Figure 65). In the early stages of growth the test is highly porous (40-58%); porosity decreases rapidly through ontogeny up to a test diameter of 2.15 μm ; it increases up to 3.1 μm , followed by a gradual decrease as test size increases, although a 2% increase in porosity is observed as the test diameter increases marginally at mature stages (15-16 mm). The adult test (diameters ~ 3 mm or larger) has a porosity of 28-38%. Evaluated porosities vary between 19% - 58% across the range of diameters (~ 0.5 μm - ~ 16.5 mm) of the tests of specimens.

Porosity values reported here are based upon the thresholding values shown in Table 6. The voxel sizes of the images used for specimens M_331- M_small (Table 6 bold-face), were sufficient to resolve microstructures and clearly differentiate solid and void phases. Porosity of one specimen (M_young, diameter: 4.35 mm) was also quantified using the Mango software and different X-ray MCT experimental parameters (Table 3): porosity was 31.62%. This value differs notably from the porosity obtained by image processing with ImageJ (see discussion) but is consistent with the values obtained by mercury intrusion porosimetry for similar sized tests.

Table 7 Mean values of density and porosity for five tests (dia. 4-5 mm) using mercury porosimetry.

Bulk density at 1.00 psia	1.68622	g/mL
Skeletal or apparent density	2.71446	g/mL
Porosity	37.41046	%

Porosity was evaluated (Table 7) for five specimens of a similar size (diameters 4-5 mm) using mercury porosimetry, an instrument based analytical method described in Chapter 2. Limited availability of the instrumentation, the discoidal shape of the specimens and limits on the diameters of specimens that could be processed constrained the sample size and range of diameters of specimens that could be evaluated using this technique. Porosity values obtained (~38%) using the two techniques show good agreement for tests of equivalent diameters. However, in addition to a quantitative assessment of porosity, the gross densities of the specimens (tests) were obtained. Mean density values obtained for only the solid fraction (crystalline wall density) show good agreement with the density of calcite. The tests of foraminifera are bulk materials. Bulk density is related to porosity in that the void volumes in the test are accounted for and is an indicator of compactness. The mean bulk density (D_b = mass of dry solid / solid volume + void volume) of the test, skeletal density (D_p = mass of dry solid / solid volume) and porosity (P) are related by:

$$P = 1 - D_b \div D_p$$

The bulk density value of 1.68 g/mL indicates that the tests evaluated contain more crystalline material than pore space. The porosity calculated using the above equation and measured values in Table 7 is 38%.

3.7.3 Discussion

The usefulness of the X-ray MCT technique to quantify the porosity of a test was demonstrated: the porosity of the test of *Marginopora sp.* can be directly, quickly and non-destructively evaluated by the use of X-ray MCT data and image processing software. Porosity of the test was found to vary through ontogeny: for the specimens evaluated porosity decreased as the size of discoidal test increased. Porosity was found to be ~38% for tests approximately 1-5 mm in diameter. Validation of these findings was performed using mercury porosimetry for tests of a limited range of sizes. Recall that in Chapter 2 in a review of the use of the X-ray MCT technique for estimating porosity it was noted that good agreement has been found in several different applications.

The prolocular region is large compared to the diameter of the test early in ontogeny. As calcification occurs rapidly during the early stages of development of the test and walls are added rapidly, as shown qualitatively in 3D in Figure 51 in the previous section, the solid fraction of the test increases rapidly. Saraswati has noted in a study on growth of large coastal miliolid foraminifera that on the basis of weight measurements *Marginopora sp.* is a rapid calcifier (Saraswati, P.K., 2002). This may explain the high values of porosity observed in the smaller specimens and the observed decrease in porosity in tests that represented more mature specimens. Using indirect methods, including comparing volumes of spherical glass beads and volumetric infusion of toluene and water under vacuum into tests, and regression equations based on the changes in porosity with diameter, Bachman reported that intratest porosity of subspherical planktic tests of several species decreased from 73-61% as test diameter decreased and bulk density was estimated at 1.5 g/mL; planktic test diameters were 1 mm - 0.25 mm i.e. smaller than the smallest test of *Marginopora sp.*, a benthic foraminifera (Bachman, R.T., 1984). Interestingly, the planktic tests in Bachman's study were thin-walled, subspherical, buoyant, i.e. higher porosities are consistent with such structures. The test in early ontogenetic stages of

Marginopora sp. is also thin-walled, has an aspect ratio of 2:1, and has a high porosity (58.5%). The decrease in porosity with increasing test diameters of the adult test of *Marginopora sp.* could be related to and may be consistent with its complex internal walled structure and benthic habitat which are very different from those of planktic foraminiferas.

Porosity of modern planktic foraminiferal specimens is often relevant in studies of paleoceanographic parameters such as temperature of water masses. In their study that utilized electron microscopy and image analysis software to measure porosity, Fisher et al. point out that using that method they confirmed previous reports of the statistical sufficiency of five specimens of a sample in the evaluation of the porosity of planktic foraminiferal tests (Fisher, C.G. et al., 2003). Although *Marginopora sp.* is a large benthic foraminifera, the porosity values obtained by the two techniques reported in this work were in close agreement for at least five tests that have comparable diameters.

Knowledge of the bulk density of foraminiferal tests is useful in the reconstruction of the hydrodynamics of sediment deposition; bulk density of hollow tests replaces the grain density in calculations of shear stress velocity for sediment movement. Shape and bulk density of grains of biological origin, e.g. coral, mollusc, echinoderm and gastropod shell fragments and foraminiferal tests, are important factors affecting the distribution of grain-sizes of carbonate sediments in water (Smith, D.A. & Cheung, K.F., 2002). Bulk densities are also more important at larger sizes of particles (Maiklem, W.R., 1968). Bulk density is calculated using equations and experimentally determined using settling velocities of tests in seawater filled columns in which test shape is modelled by equivalent diameter spherical particles; but field studies do not usually affirm the transport relationships of foraminiferal tests and equivalent diameter particles (Oehmig, R., 1993). X-ray MCT data of planktic tests and image processing would allow for the direct calculation of bulk densities of tests of any shape and size by a quantification of the total volume of the tests, if the weights of the tests are known. Since the tests of planktic foraminifera are smaller, contain fewer chambers and are much less complex in their structure than the adult tests of *Marginopora sp.*, the limitations of large specimen size and loss of resolution associated with X-ray MCT would not apply. In this work, the values of the weights of the specimens evaluated by X-ray MCT in low-resolution were not recorded; regrettably, this error could not be rectified as the specimens could not be imported to New Zealand. If the values were known, the calculation of bulk density would be made trivial with the use of the solid and void volume data shown in Table 6.

The bulk densities of the tests of *Marginopora sp.* evaluated by mercury porosimetry are within the range (1.3-2.3 g/mL) of bulk densities reported for planktic foraminifera (Oehmig, R., 1993). Interestingly, the bulk density of cement (1.51g/mL) is lower. The bulk densities of large benthic foraminifera do not appear to have been reported in the literature, but specific gravity (1.2-2.3) for tests of *Marginopora sp.*, *Calcarina sp.* and *Baculogypsina sp.* was reported in a study of the settling velocities of reef sediments (Jell, J.S., Maxwell, W. H. G., & McKellar, R. G., 1965). Typical bulk density of sandy soil is between 1.5 and 1.7 g/cm³. This calculates to a porosity between 43% and 36%. Interestingly, the average intra-test porosities reported here fall within this range of values. Tests of *Marginopora sp.* and other large benthic foraminifera make up significant fractions of tropical carbonate sediments. Studies related to sediment transport in coastal lagoons, particularly of atolls and islands, in which large benthic foraminifera tests are a significant

component of sediments, would benefit from a quantification of the bulk density and porosity of the dominant foraminiferal assemblages of those habitats. Similarly, such a quantification using X-ray MCT data would help answer the question raised by Bachman regarding the effects of the unknown porosity and bulk density of tests on the acoustic properties of foraminiferal sediment (Bachman, R.T., 1984). The findings reported using the X-ray MCT data for the test of *Marginopora* contribute to such an effort. That the skeletal density of the tests evaluated in this study (as measured by mercury porosimetry) is virtually identical with the density of calcite is not surprising. The organic material in the tests which were evaluated was removed; only the inorganic structure of the high Mg-calcite tests was evaluated.

Possible limitations or difficulties associated with the image processing in the estimation of porosity of specimens used in this study are worth noting. Since the X-ray MCT data are evaluated using an image processing method that is dependent at first on a visual recognition of a solid vs. void phase through the thresholding operation during image processing, it would appear that the outcome may be subjective. While such a perception of the process is not entirely inaccurate, the thresholding operation in this research was rendered relatively uncomplicated because the structure of the test of *Marginopora* in the XY plane was clearly distinguishable as consisting of periodic repeating microstructures of similar size. Void spaces were clearly delineated by continuous connected walls; such a structure allows a rapid and relatively precise differentiation of void and solid space using the thresholding operations in ImageJ or similar image processing software. The thresholding values used in this work are displayed so that repeated analyses may be performed for a comparison and contrast of outcomes.

A variable in this study that could notably affect the reported porosities was the resolution of the structures in the original X-ray MCT data; resolution of the structures in the images is related to the voxel size of the resolved images representing the data in the reconstructed tomograms. The results reported here consist of data obtained using different experimental conditions with different voxel sizes (Table 5); i.e. 2.792-3.704 μm at high resolution and 24.46-40.92 μm at low resolution. Recall that optical microscopy and electron microscopy observations indicate that the smallest microstructural void space in the test consists of stolon tubular passageways that are approximately 10 μm in diameter. The cross-sectional width of chamberlets is approximately 45-50 μm . During the thresholding operation, it was observed that the voxel sizes in a range of 24.46-40.92 μm of the reconstructed tomograms were insufficiently small for the unambiguous differentiation of the walled microstructures of the chamberlets in tests larger than 10 mm. Thus porosities of the larger specimens (diameters 10 mm-16 mm) may be overestimated during thresholding when low resolution data (large voxel size) are used. In order to minimize this potential error, the thresholding operation was deliberately attempted to be performed such that the void phase was slightly underestimated. On the other hand, with high resolution data of large tests, i.e. a small voxel size that can resolve all microstructures, the resultant images fully capture the very high density periodic pattern void-solid structure or the “cellular grid” of the tests; i.e. a very large number of distinct chamberlets that are very closely packed. In this case, the thresholding operation in Image J was not able to efficiently distinguish between solid and void phases in the data as so as to avoid an excessive “fusing” of the void space of chamberlets with the adjoining walls. High resolution data sets for tests larger than 10 mm (as for specimens

M_young and M_old (isotropic voxel size $3.11\mu\text{m}^3$) could not be effectively thresholded. Another limitation arises from the very large data sets of high resolution X-ray MCT tomograms: the data for specimen M_young and M_old (reconstructed tomogram file size approximately 26GB and 20GB respectively) were not analysed because the available desktop computing resources were insufficient for handling or processing the data set. Parallel computing resources which offer 4-6 processors and a minimum of 96 GB of working memory is required for image processing operations with such data sets. For example, the use of these resources requires approximately 10-30 minutes of processor time to perform one segmentation procedure with one data set. A good match of the voxel size of the images with the microstructures that are to be resolved, the use of large computing memory resources and high resolution data with small voxel sizes could overcome such limitations of research in the future.

The porosity of the test would affect the material properties and performance of the test since porosity is a property of the structure of the test. In materials science, as reviewed by Matejicek et al. other methods, such as X-ray diffraction, electron probe microanalysis, and SAXS, may also be used to determine the porosity of abradable material in addition to mercury intrusion porosimetry, Archimedeian (weight-volume) porosimetry and helium pycnometry (Matejicek, J. et al., 2006). Each method offers advantages and may be peculiarly suited to the structure of the material and to the distribution of porosity and the pore geometry in that material. However, X-ray MCT offers the advantage of qualitative and quantitative 3D visualization analysis. Recall that in earlier sections the qualitative distribution of density in the structure of the test through its ontogeny was presented through the use of the X-ray MCT technique and discussed in the context of its architecture and patterns. An analysis of X-ray MCT data towards characterizing the distribution of porosity and its relationship to the structure of the test of *Marginopora sp.* is the subject of the next section in this work.

3.8 Networks in the test

3.8.1 Introduction

As has been shown in earlier sections of this study, the solid and void space in the test of *Marginopora sp.* consists of the crystalline walls and void space (lumina). A characterization of the crystalline phase has been presented in 2D and in 3D using a suite of microscopy techniques that allowed previously unreported features to be observed, described and analysed. Inorganic-organic composite walls, alternating with void space, were noted to have several micro-structural components. These components were formed at a range of scales and in a variety of shapes in the framework of the structure of the test. The void phase consists of interconnected spaces within the test; it can be viewed and analysed as a network within the cellular-solid structure of the test. The layout of the void spaces and their connecting passages - the chambers, chamberlets (lumen) and tubular passages (stolons and intercameral or interocular passages) can be described in terms of network topology.

The tests of foraminifera have complex canal systems. Canals interconnect chamber lumina or may form a tubular system rather independent of the lumina; both systems may interconnect through "loopholes". These canal systems have well-defined patterns, can be spiral or radial, and

are identifiable in similar groups of foraminifera (Hottinger, L., 2001). Hottinger integrated earlier descriptions and interpretations of the functional value of the test with descriptions of the canal systems (Hottinger, L., 1978). These detailed descriptive analyses of microstructures and their relationships were applied to the canal system in calcarinid foraminifera, which are the most complex of canaliculate foraminifera (Hottinger, L., Leutenegger, S., 1980). In another study of the canal system of a large symbiotic benthic foraminifera, *Heterostegina depressa*, Rottger et al. noted that it acts as a communication system, construction system for chambers, reproduction system, waste transport system and extrusion of protective sheath- using protoplasm flow from the apertures of the marginal cord (Rottger, R., Spindler, M., Schmaljohann, R., Richwien, M., & Fladung, M., 1984).

The possibility of common origins (homologies) and common functions of the canal system in different groups of foraminifera and, the construction of radial or spiral systems by similar or different microstructures remain of interest. In a key analysis of shell architecture Brasier provided models of the architectures of foraminifera and introduced the concepts of minimum and maximum lines of communication – MinLOC/MaxLOC (Brasier, MD, 1982). These related to the minimum distances from the central region (prolocular) to the nearest aperture connecting to the ambient environment and the distance from the penultimate chamber to the ambient environment. The tests of foraminifera follow several forms and modes of growth: planar, spiral, trochospiral, streptospiral, orbuline, annular, etc. In that analysis, MinLOC and MaxLOC were used as key parameters to show how the volumetric expansion of the test varied in different forms. In a review of the application of these concepts, Brasier emphasized a functional interpretation of the interlocular connection of void space using MinLOC and MaxLOC: the canal system provided internal lines of communication and with the environment of the test (Brasier, M., 1982). These functions included the internal movement of symbionts, protoplasm, vacuoles, pseudopodia, food and chemical signals and buffering of the stresses of the external environment. The diversity of test forms meant that this functional hypothesis linking the lines of communication with ecology and evolution could be tested through models of different forms. Importantly, the models were approximations - geometric shapes (circles for spheres, etc.) in 2D were used to represent 3D forms. Calculations were required to evaluate volumetric growth and linear measurements. While this was done for a number of selected forms, Brasier acknowledged that it was “immense labour” and devised a Parsimony Index (PI). The PI was an index for rapidly assessing the potential of tests for a short MinLOC (Brasier, M., 1982). Interestingly, among the forms evaluated using the PI, miliolid discoidal forms of the test (as is the test of *Marginopora sp.*) showed high parsimony.

“In summary, the MinLOC method provides another way of looking at foraminifera, from the inside. The MinLOC and PI methods can be used to study patterns of architecture through time (evolution) or in space (ecology) but these are likely to be the outcome of both internal factors (such as MinLOC and MaxLOC) and external factors (such as osmotic stress, substrate type, hydrodynamic properties and food source). The effects of these external factors could also be studied by modelling. But interpretation of the architectural patterns is a complex matter that will also involve further biological and ecological work”(Brasier, M., 1982).

X-ray MCT provides an alternative method of looking at the tests of foraminifera including - from the inside. The X-ray MCT data allow precise realistic representations of the test in 3D; linear and volumetric measurements can be performed quickly and precisely, and complex analyses can be undertaken to test hypotheses. This research used X-ray MCT data to characterize the canal system in the test of *Marginopora sp.* The hypothesis that the canal system of the test of *Marginopora sp.* is of functional adaptive value as a line of communication is examined. The techniques of a representation of the physical structure of the canal system by the topology of a network and a statistical analysis of networks were applied through the use of Mango network analysis software (Section 2.3.6.5) to the data obtained for specimen M_young. The canal system consisting of large voids (chamberlets of the annular chambers), passages between chamberlets within chambers, and intercameral tubular passageways extending radially to the margin were analysed as a distribution of pores interconnected by throats or a network of nodes interconnected by edges in the test. The edges represent the interactions or possible flows in the network of the test while the pores represent storage and connectivity. To the best of the writer's knowledge such an analysis has not been reported for any test of a foraminifer.

Graph theory and its results contribute to the quantification of the properties of a network in a few statistics. In section 3.8.1, selected network statistics which are relevant to the hypothesis are presented. In section 3.8.2 their interpretations are correlated with the 3D visual representation of the large voids and passages, i.e. of the canal system.

3.8.1 Quantitative analysis of the distribution of void space (pore)

The concepts related to network visualization and network analysis for biological systems are summarized by Nikiforova and reviewed by Barabasi (Barabasi, A.-L. & Oltvai, Z.N., 2004; Nikiforova, V.J. & Willmitzer, L., 2007). Only the very essential concepts of network analysis that are relevant to the results of this study are depicted in Figure 66 and Table 8.

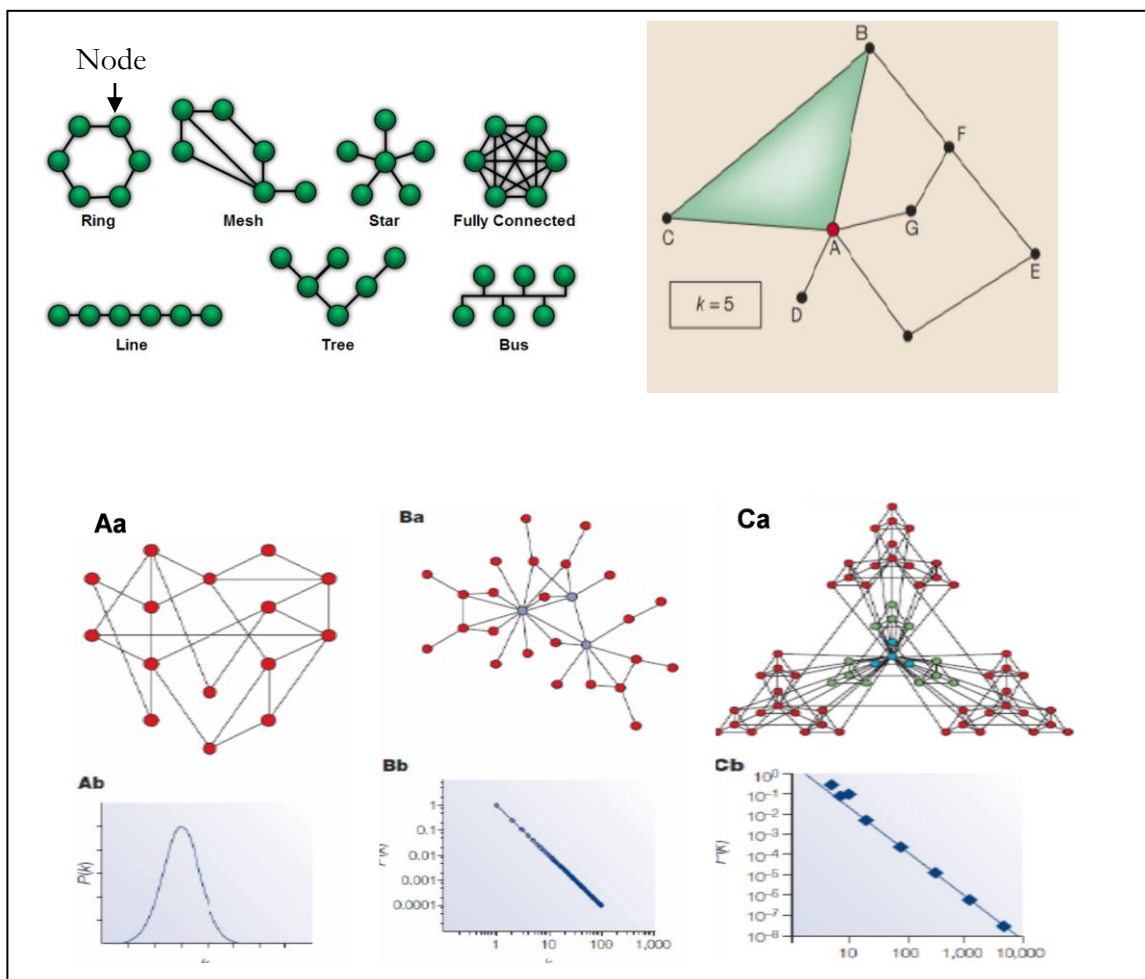


Figure 66 Basic descriptors of network topologies.

Top left: Different network topologies; hybrid topologies are possible. Top right: Nodes A-G are linked with edges, node A has 5 links or edges. Schematic Aa: A random network following a Poisson distribution (Ab); Ba: Scale-free network shows a power law distribution (Bb); and Ca: Hierarchical network which also follows a power law degree distribution (Cb). (Adapted from: (Barabasi, A.-L. & Oltvai, Z.N., 2004))

Table 8 Definitions of terminology used in describing network features of the test of *Marginopora* sp.

- **Coordination** number is the number of links or edges that are linked to a node.
- The **degree distribution**, $P(k)$, gives the probability that a selected node has exactly **k links or edges**. It allows us to distinguish between different classes of networks (see Figure 66 Ab, Bb, Cb).
- **Pores** are viewed as nodes in the network, i.e. nodes represent the large voids-pores-chamberlets (in the test of *Marginopora* sp.). **The size of a pore** is the void space in which a sphere is geometrically expanded to occupy the void space such that every voxel of the void space is included in the sphere.
- **Throat** is the narrower void (edge) linked to at least one pore. Throat and pore size are similarly calculated but throats are at *least* 3x smaller than the pores to which they are linked.

Shapes can be analysed by representations of their boundaries. Topological skeletons are thinned forms that are equidistant to the boundaries of the shape. Direction, connectivity, width etc. are properties of the shape that are maintained by topological skeletons. The medial axis is a topological skeleton which represents the shape of an object. In 3D space, as represented by voxels, it can be generated algorithmically by homotopic thinning, a skeletonisation algorithm.

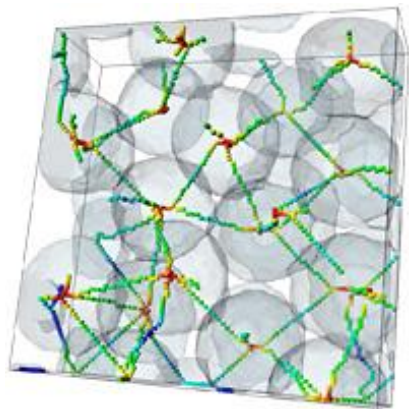


Figure 67 Skeletonisation: 3D medial axis of an object.

In the schematic (Figure 67) is shown that the medial axis can be used to create a skeleton of an object which consists of sphere-like components which are similar to pores. The different colours of the medial axis voxels represent the distance to the nearest voxel of the other phase, i.e. solid or void. Mango, a software package used in this research, employs a medial axis transform algorithm to generate the skeletal topology of pore-space in a volume. The 3D medial axis transform algorithm encapsulates, describes or can be used to reconstruct the complete shape of the object in the original domain. Therefore, the resultant skeleton is a complete descriptor of the shape of the object. This algorithmic method was applied to the X-ray MCT data of the test of *Marginopora sp.* to generate a topological skeleton of the void space in the test. The void space in the test of *Marginopora sp.* can be represented by pores and throats. Thus, the void structure of the test of *Marginopora sp.* can be represented abstractly by a topological skeleton.

A topological skeleton was created by processing the X-ray MCT generated voxel-data: reconstruction of tomograms, application of filters to reduce noise, segmentation of the data, and generation of the medial axis. It can be perceived as a graph of the voxel-data set. The properties of the topological skeleton, which is a graph, embodies the topological properties of the structure. The statistics of the graph can be analysed and visualized using software e.g. Mango, MIView, ImageJ, etc.

3.8.1.1 Results

The application in Mango of the filter “network statistics” to the segmented X-ray MCT data for specimen M-young yields numerous data files of statistics. Table 9 displays the statistics that are descriptors of the pore size, the throat size and the relationship of the pores with other pores, i.e. the number of links to that pore. It displays mean values -which provide a snapshot -of the dimensions associated with the pores and throats in the network of void spaces. The mean pore volume equivalent radius is 21.91 μm (diameters of $\sim 45 \mu\text{m}$), which indicates pore size is 3x larger than the mean throat radius of 6.05 μm (diameter $\sim 12 \mu\text{m}$). The value of the standard

deviation pore and throat dimensions does not exceed 2 voxels; the dimension of the isotropic voxel is 3.11 μm (Table 3). The mean total length of the throats that were enumerated is larger than the mean diameter of the pores. Further detailed statistics of these parameters are shown in Figure 68 through Figure 70. The distribution of the coordination number is such that most (mode) segmented pores have 4 links (Figure 68); of 50,606 pores a majority of the segmented pores have 3 (9,508) or 4 links (11,941) or 5 links (8,477). A notable number have either 2 (4,990) or 6-8 links (10,922).

Table 9 Mean values of selected network statistics of test of Specimen M_young.

	Coordination number	Pore Radius μm	Pore Volume Equivalent Radius μm	Throat Radius μm	Throat Total Length μm
Mean	4.9	14.19	21.91	6.05	67.18
Std dev	1.9	3.33	5.48	3.32	18.08

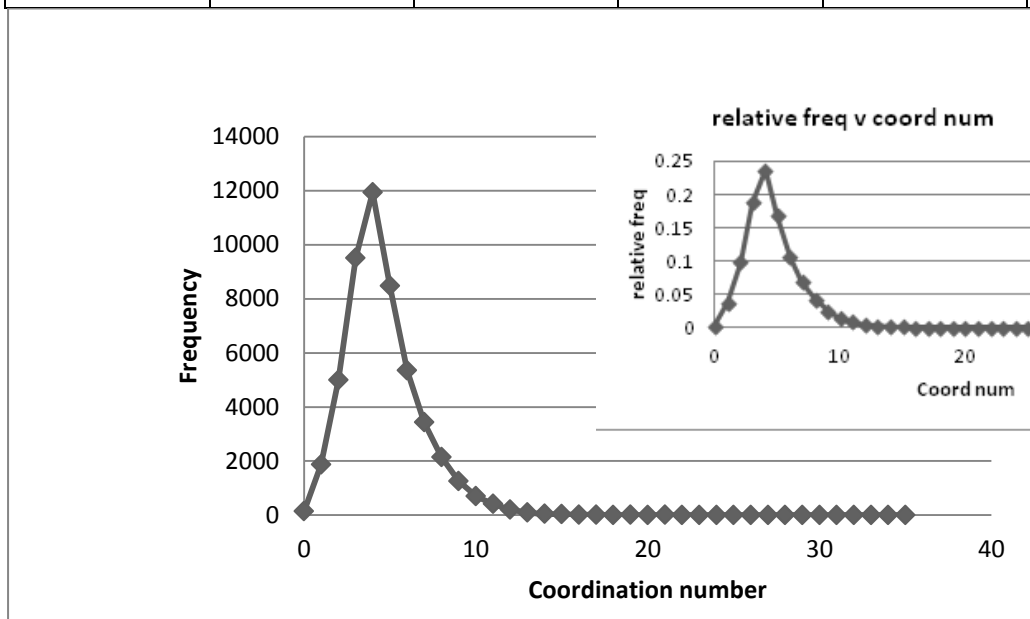


Figure 68 Frequency vs. Coordination number of pores.

Inset: relative frequency indicates occurrence as a fraction of total number of pores.

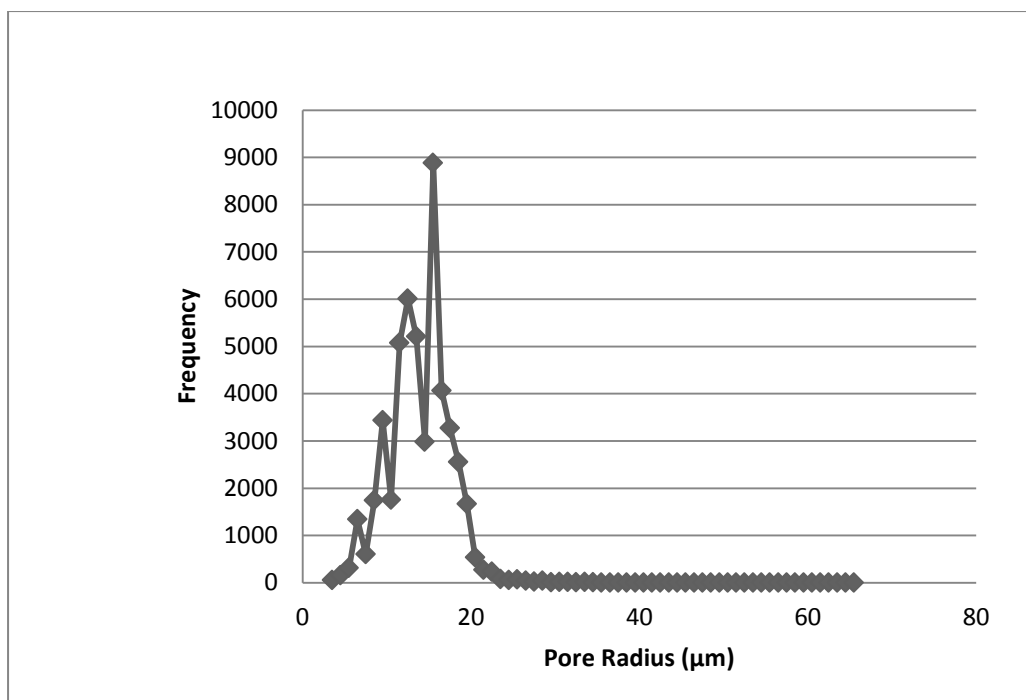


Figure 69 Frequency vs. pore radius.

The distribution of pore radius in μm and frequency shows a strong mode size of $\sim 15.5 \mu\text{m}$ (Figure 69). Segmented pores have radii largely in the $8.5\text{--}19.5 \mu\text{m}$ range; there is a gradual increase in pore size but distinct increases in the number of pores with radii at 6.5 , $8.5\text{--}10.5$, $11.5\text{--}13.5 \mu\text{m}$; there is a sharp decrease in the number of pores larger than $15.5 \mu\text{m}$; the distribution is asymmetrical. The segmentation and enumeration show that less than one-fifth of the pores have radii sized smaller than $10 \mu\text{m}$, or larger than $17 \mu\text{m}$.

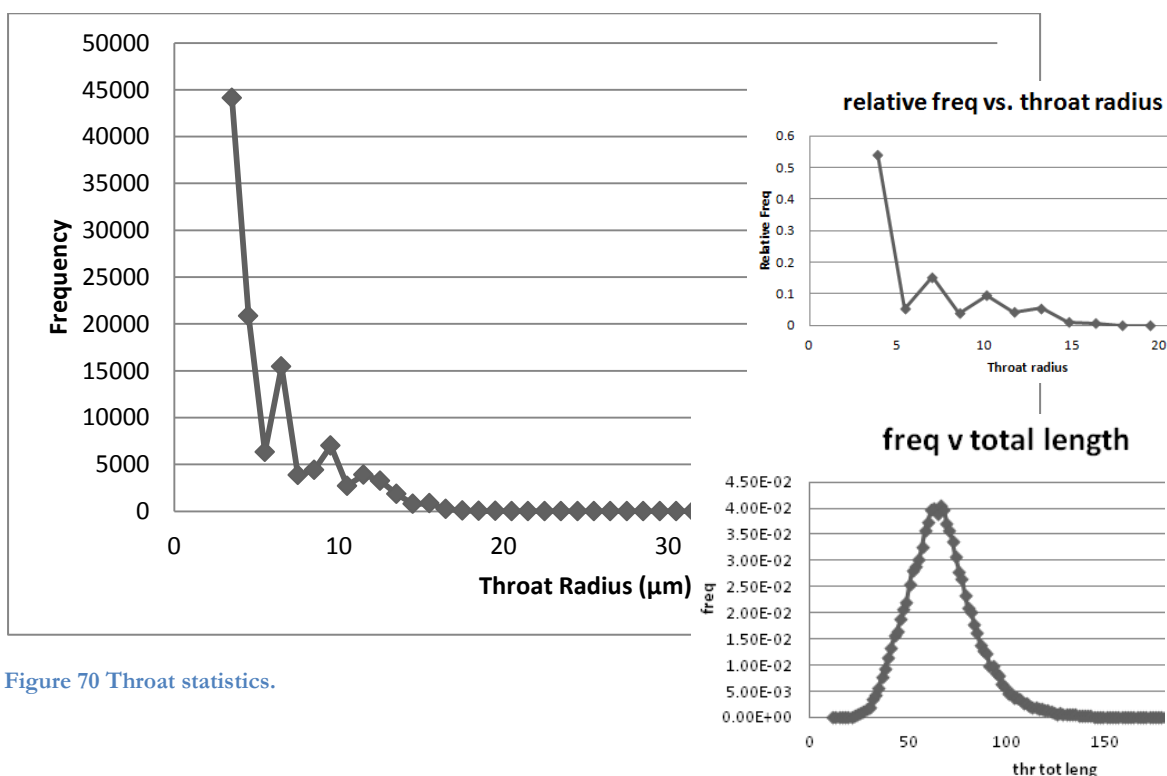


Figure 70 Throat statistics.

The largest number of segmented throats (45,000) have a radius of $\sim 3.5 \mu\text{m}$. Smaller radii are not recorded. This likely also represents the limit of the resolution of the throat size as the isotropic voxel size is $3.11 \mu\text{m}$. An approximately equal number of throats are enumerated with radii between $4.5\text{--}11.5 \mu\text{m}$ (Figure 70). Clearly a throat radius of $3.5 \mu\text{m}$ is dominant (55% of the throat radii -Figure 71). Notably the distribution shows that throat frequency falls very rapidly (exponentially) as throat radii increase; but modal trends are observed of larger radii distributed evenly in size between notably $5.5\text{--}7.5 \mu\text{m}$ and $8.5\text{--}9.5 \mu\text{m}$ with 4-18% and 10.5-14 μm (less than 4%) of the throat radii occurring in those ranges. Throat lengths show a symmetrical distribution. Most throats are $61\text{--}63 \mu\text{m}$ long (Figure 70).

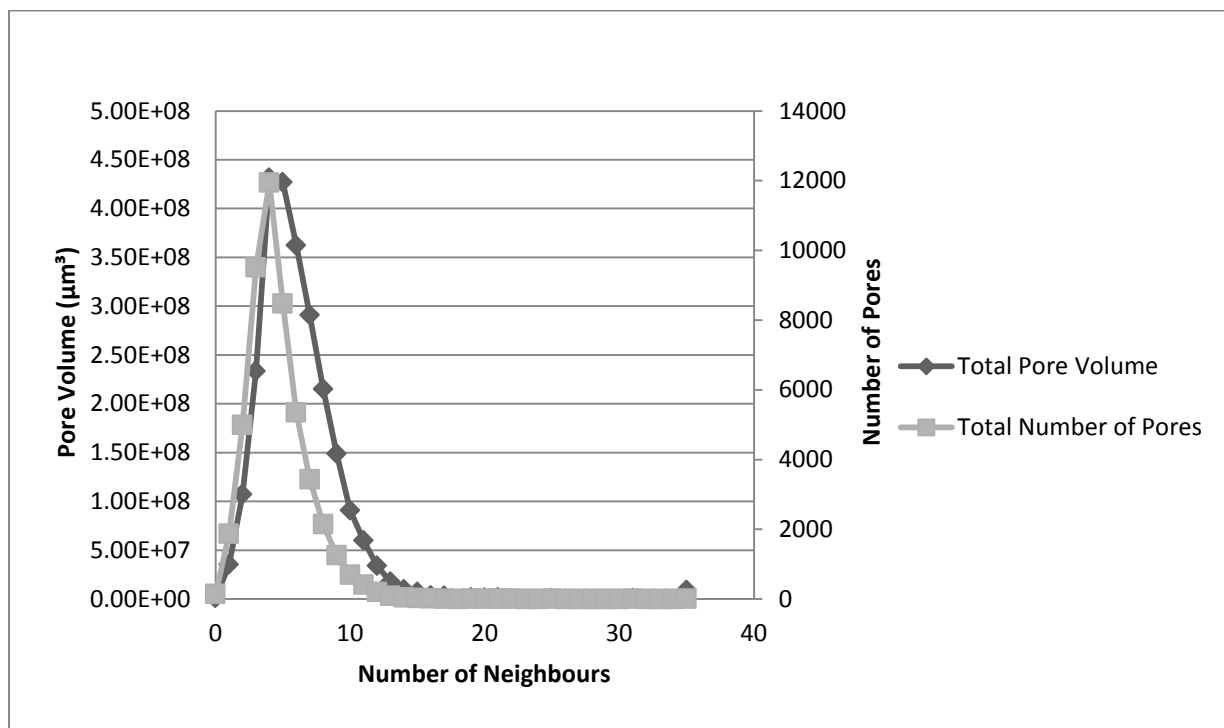


Figure 71 Pore volume and number of pores vs. number of neighbours.

Further detail of the distribution of pores is shown by a plot of pore volume vs. the number of neighbours (Figure 71). A comparison with the number of pores provides results similar to the distribution of the coordination number. Figure 71 shows that the distributions of the pore volume and the number of pores are unimodal and primarily symmetrical; the pores are distributed heterogeneously in size and number within the test. Notably, the largest pores (pore volume $\sim 4.3\text{E}+08 \mu\text{m}^3$) and the largest number of pores ($\sim 12,000$) have 4 neighbouring pores. Approximately equal numbers of pores of equal size have lesser and greater than 4 neighbouring pores. The distribution tails rapidly: beyond a particular decrease in size (pore volume) and neighbours (10) the pores are likely not differentiated or enumerated as pores.

3.8.2 Visualization of a network: the void space in the test of *Marginopora* sp.

The network statistics presented in the previous section showing the distribution in space of pore and throats – nodes and edges of a network - or chambers and interchamber tubular passages were a quantitative assessment of the networked void space in the test. In this section are presented visualizations in 3D of the networks of the test using X-ray MCT data and the outputs generated by network analysis and scientific visualization software (Mango and MayaVi <http://mayavi.sourceforge.net>). This qualitative assessment is an abstract representation (as shown in Figure 72) of the information presented in previous visualizations (Figure 59) of the pore space. The visualizations presented here are of a subset of the tomograms of the test rather than of the whole set. The entire data set is too large; computational memory size constraints and overcrowding of visualization space allow only limited data sets to be visualized.

The properties of the graph (topological skeleton) of the voxelised data representing the structure of the test are now visualized. The visualization of the topological skeleton of the void space employs a ball-stick model to represent the network of the pores and throats in the test. This model shrinks actual pore space volume to allow a “network view” in which balls represent distinct nodes i.e. pores-chamberlets and, sticks represent edges-i.e. throats. In this visualization in some views, regions of the large throats to some extent also represent part of the narrower actual chamberlet space.

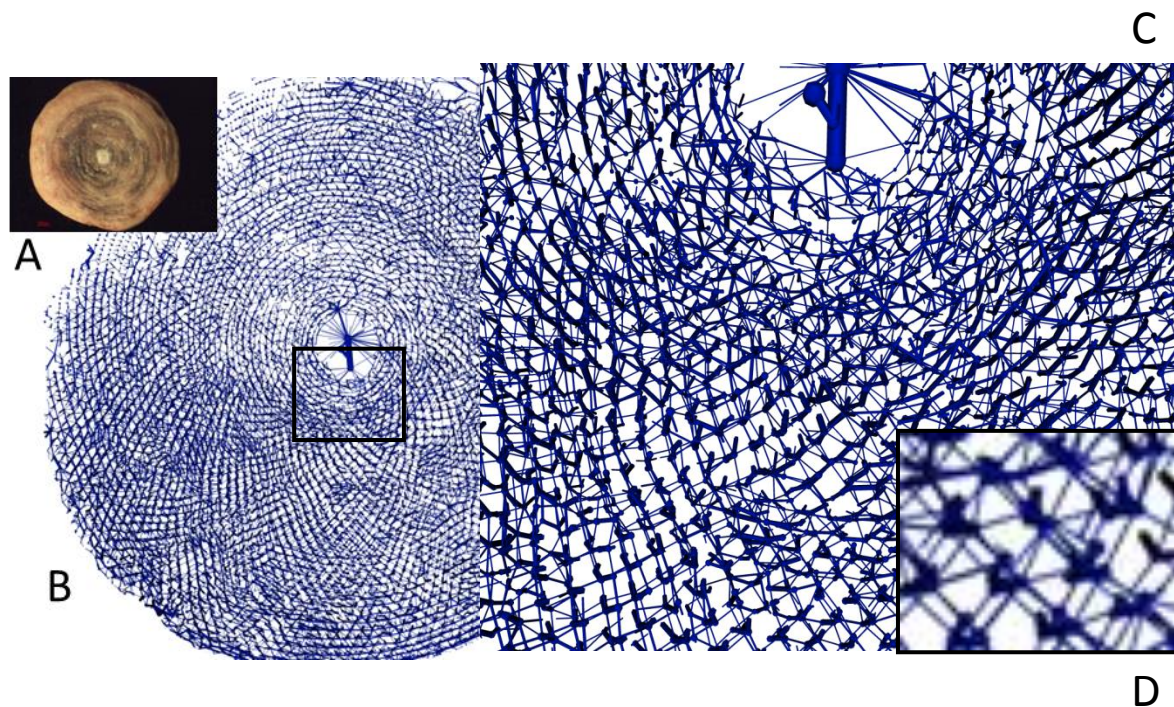


Figure 72 Pore space 3D visualization by network analysis of X-ray MCT data 9.

Figure 72A shows an optical micrograph of the complete test while Figure 72B show the physical topology of the pore network of the complete test. The intersecting arcuate topology is apparent. A magnification (Figure 72D) of a region of the pore network in Figure 72C allows a clear understanding of the periodicity of the pore network and the physical topology of the chambers in 3D space. The depiction by each ball-stick combination of the relative size of the

pore space is highlighted by the large ball-stick combination in the proclur region compared with that of a chamberlet in the annular chamber (arrows). Each sequential chamberlet (pore) is positioned in a linear extension of the previous position in each annular addition of chambers (as shown in the arrows in the inset). The linearity underlying the connectivity of the pore-throat (chamberlet-stolon passage) is magnified between pores in successive annular steps. Each pore is connected to others in a grid-tie system that is dominated by a truss-like (triangular components) system.

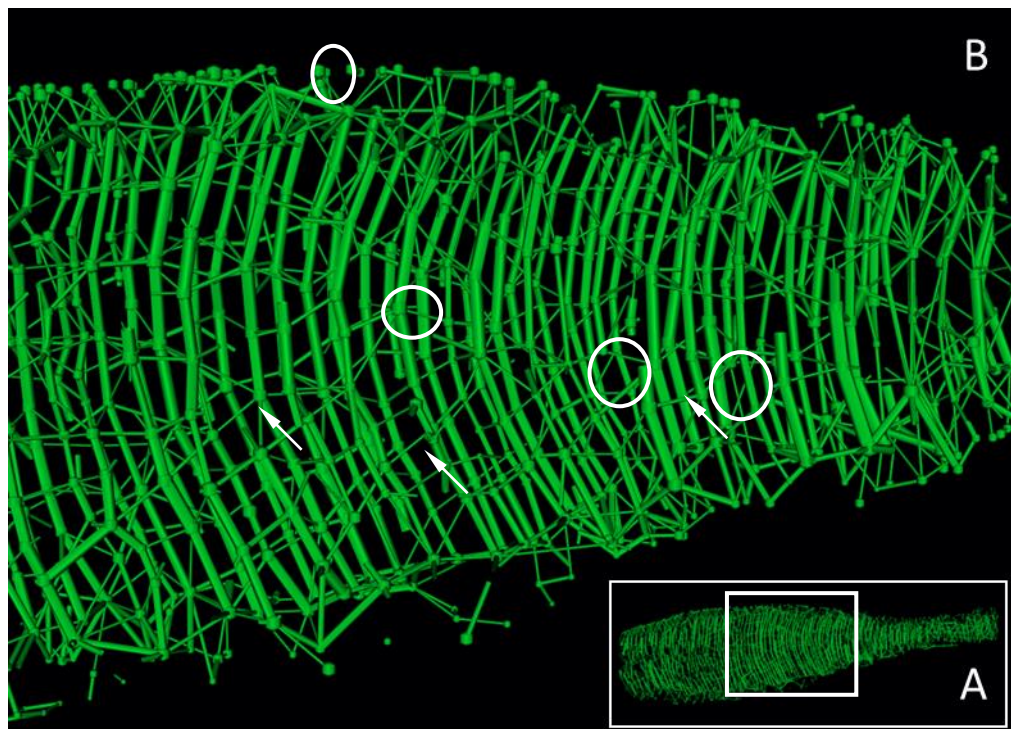


Figure 73 Ball-stick model of pore space in transverse section.

Further detail is revealed in Figure 74 A and B. A view of the pore network in a transverse section of the disk (A) is magnified in B and shows the depiction of surface chamberlet pores, chamberlets in a xz plane (circles), and interconnecting throats in the radial direction (thin white arrow). There are two dominant throat pore throat sizes; the radially directed throats or edges are smaller. The pores representing chambers are similar sized and the throats are smaller than the pores but are much larger than the radially directed throats. Some pores or throats are not connected; the ball-stick model visualization may not capture all the data in the network statistics when a subset of data (“slices of the set of tomograms”) are selected for viewing.

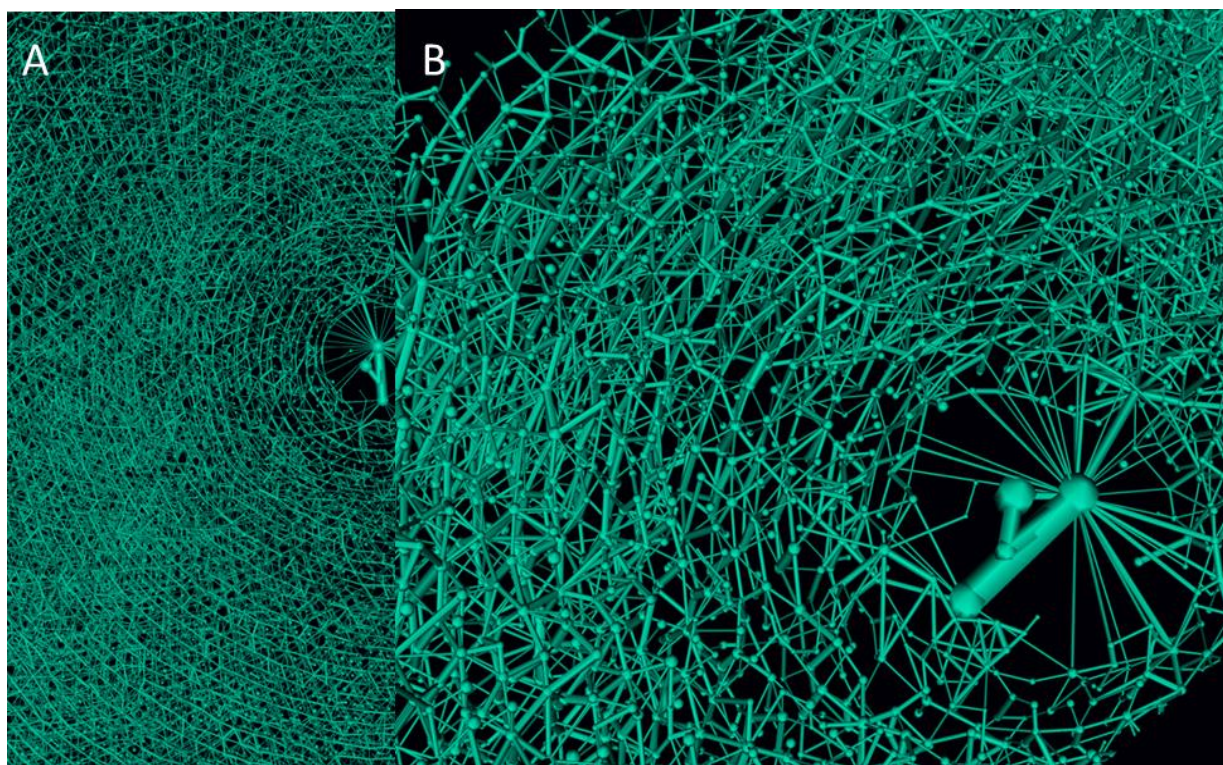


Figure 74 Pore network using ball-stick model of network visualization.

The flexibility offered by the technique is illustrated in Figure 74. The pore network can be magnified and sectioned, or viewed in any combination of planes. In Figure 74B the view presented in in Figure 74A is magnified and rotated along the z-axis: the ball-stick model provides a synoptic understanding of the connectivity and pore size distribution. Two sizes of throats (edges) are dominant; pores sizes are variable but a dominant mode is visible. A tubular annular network that forms a discoidal 3D structure is seen punctuated along each annular ring by relatively uniformly sized pores. The annular network is meshed in 3D with a radial tubular network.

In Section 3.8.1 statistics have been presented only for the pore (void) network; the X-ray MCT data were also analysed to obtain statistics of the solid (grain) fraction of the test. Based on the statistics a visualization of the ball-stick model of the solid fraction of the test is presented in Figure 75A to allow a comparison with the model of the void fraction. It can be seen clearly that the topological skeleton (magnification – Figure 75B) is represented by a configuration of trusses of equivalent linear dimensions. In Figure 75C the visualization combines the pore network (pink) with the solid crystalline wall or grain (blue) fraction.

Although the ball-stick model “shrinks” or “compresses” pore space and wall volume for an expediency of visualization, this graphical view abstractly represents the skeletal topologies of both networks. The potential symmetries of each network; i.e. the edge-node units or lattices which are repeated by discrete translations are visible. The complementary spatial organization of the hollow tubular chamber-canal system and crystalline-wall truss configuration in the architecture of the test is evident.

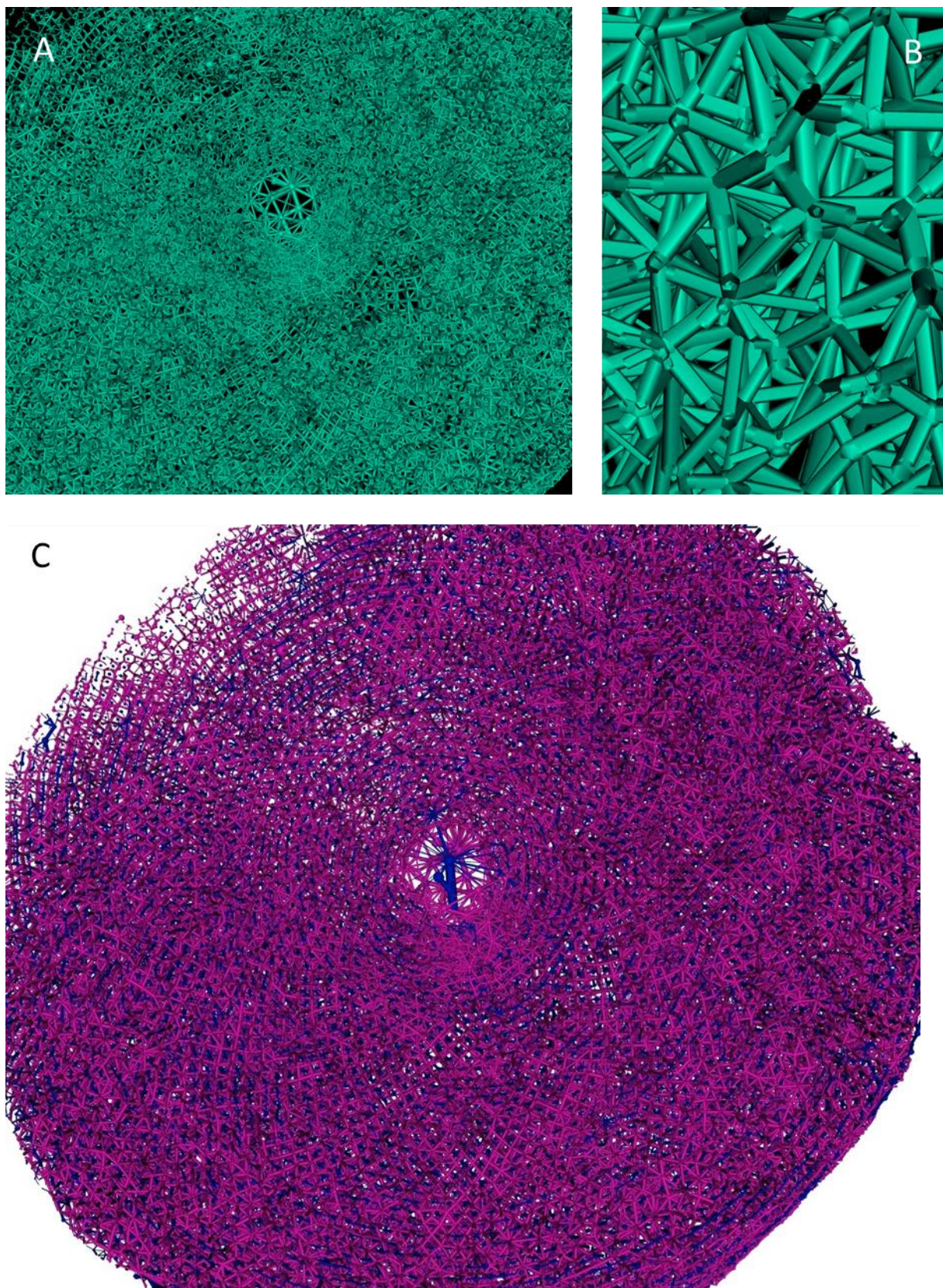


Figure 75 Visualization of (A & B) solid fraction skeletal topology and (C) combination of skeletonisation of pore network and grain.

3.8.3 Summary of Results

Results show that X-ray MCT data are useful to qualitatively and quantitatively characterize the distribution of the porosity of the test of *Marginopora sp.* by extracting a network of the porosity. Network statistics quantified salient features of the porosity of the test. The extraction of the network allowed a unique, view of the topology of the complete void space. The ball and stick model used to visually represent the network in 3D reveals and emphasizes the “skeletal morphology” of the porosity-network. The solid volume of the test, also illustrated as a ball-stick model of a network, has been integrated with the model of the porosity. These provide a novel insight: that the solid and void fractions of the test in their skeletal essence are grid-like structures that are integrated and that comprise the architecture of the discoidal test.

3.8.4 Discussion

3.8.4.1 Network Statistics

Network statistics provides a quantitative description of the distribution of pore characteristics. A visualization of the distribution often reveals the presence and connectivity of an unknown topological feature. These complementary techniques provide a wholistic understanding of the geometric characteristics or physical topology of an interconnected set of void-solid structures that can be represented as a network. Network statistics obtained by various methods have been shown to be useful in understanding the pore size distribution. Adsorption measurements of nitrogen on porous carbon (Lastoskie, C., Gubbins, K.E., & Quirke, N., 1994) and mercury intrusion porosimetry are physical instrumental methods which provide limited statistics. X-ray MCT based analyses are also a tested method for evaluating the quantitative properties of porous materials (Sheppard, A.P. et al., 2006). The extraction of simplified pore-throat networks with simplified geometries and connectivities from X-ray MCT data that represent the pore space have been compared with other computational methods and experimental data; good agreement has been shown for a variety of rock types and the most success in simulating flow has been achieved using these network models (Erickson, R.O., 1973). The quantitative characterization of the micro-pore characteristics helps in understanding the performance of materials at the structural levels at other scales of measurement; this multi-scale association of pore characteristics has been investigated in numerous types of porous materials, e.g. rock, cement, bone, scaffolds and tissue-engineered bones, macroporous alumina, paper etc. (see Chapter 2 review of X-ray MCT applications).

A coordination number with a strong mode of four and notable frequencies of five and six neighbouring large pores in the test of *Marginopora sp.* reasonably affirms the structural characteristic of the test, i.e. pattern of chamberlets, revealed by 2D thin-sections of optical microscopy and 3D volumetric renderings of X-ray MCT data (Section 3.6.3). Although the volumetric renderings allowed a visualization of the number of largest “visibly identified” pores i.e. the chamberlets, and their neighbouring “large pores”, only a few 3D sections were presented. But, the distribution of the coordination number obtained by quantifying the porosity represents the complete distribution of pores in a test. While the observed periodicity of the chamberlets in the test may indicate six neighbours for annular chamberlets, the lateral chamberlets were observed to be connected differently. Similarly the Poisson distribution (up to

eight links) may be indicative of the imperfections in the periodicity (number of links) of the chamberlets that are not identifiable in a view of the section of the anisotropic test. Network statistics capture the possible variability that exists in the connectivity.

This study has not validated the precision of the network statistics except that the porosity (31.6%) of the specimen is also an algorithmically obtained network statistic. Since this value is in fair agreement with the porosities of tests of comparable diameters measured using mercury intrusion porosimetry and different experimental conditions of X-ray MCT this indicates that the partitioning and enumeration of pore-space by the algorithms that generate the network statistics was reasonably representative of the physical structure. Indeed a validation of the statistics by other methods would require an application of different algorithms or variations in the image processing parameters; the benefit may hardly be imagined to outweigh the effort. The application of the medial axis algorithm and merge algorithms appear to have reasonably identified the pore-structure of the test. Unrealistic coordination numbers do not dominate the distribution. The application of the maximal ball algorithm, another network extraction algorithm often results in pores with very high coordination numbers. Also, forehand knowledge of the structure of the test obtained by complementary techniques is required to draw value about the local structural details of the network, e.g. to differentiate that lateral and annular chamberlets would necessarily have different coordination numbers. Again the network of the lateral chamberlets, if isolated from the remainder, would be represented by quite different statistics. That the network technique adequately represents the physical structures is most evident in Figure 73, which closely approximates the optical, electron microscopy and X-ray MCT derived images of transverse sections of the test.

The Poisson distribution of the coordination number, an important aggregate statistic, indicates that among current graphs a random or Erdos-Renyi type of graph (Figure 66A best describes this network. A discussion the construction properties and applications of various mathematical graphs describing networks is a vast subject and is beyond the scope of this section; a comprehensive review and summary was provided by Newman (Gibbins, J.R., Tilney, L.G., & Porter, K.R., 1969). It is noteworthy that biological networks are often modelled by random graphs. In such graphs, the mean path length is proportional to the logarithm of the network size, $l \propto \log N$. In the network of the test, using $N = \text{number of pores} \sim 50000$, $\log 50000 = 4.69$, rounded to 5. This mean path length varies (grows) as the logarithm of the number of nodes. For a smaller test with fewer chamberlets, mean path length would be smaller. Erdos-Renyi graphs have a small average node-to-node distance (or average shortest path) and a small clustering coefficient. The former is a property of a small-world network: most nodes, even if they are not neighbours of each other, can be reached from each other by a short number of steps. A local clustering co-efficient could be considered between 4 nodes or chamberlets in the xy plane or xz plane.

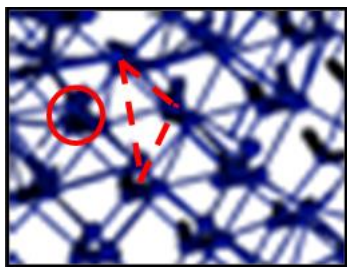


Figure 76 Clustering co-efficient of the pore network XY plane.

In Figure 76, for a pore (node/chamberlet- red circle), a local clustering co-efficient of $2/3$ is produced as 2 of 3 possible connections (dashed lines) between its neighbours are realized (blue throats-tubular canals) in 2D. If a clustering co-efficient is significantly higher than a random graph constructed on the same set of nodes then a graph is considered small-world: a probability of $2/3$ vs. $1/2$ is obtained for the nodes under consideration. However, the physical pore structure of the test does not exhibit several “hubs” in the network; highly connected hubs are an important property of small world networks. Also, a measure of the clustering coefficient in the network of the test of *Marginopora* is clouded by the effects of a large hub that the prolocular region represents; a global clustering co-efficient was not evaluated. The network of the test appears to have some but not all characteristics of a small world network. It appears to be a hybrid of a random Erdos-Renyi graph with Poisson distribution that represents the dominant annular chamberlet pore network and a hierarchical graph that represents the interface of the networks of the annular and lateral chamberlets. The visualizations of the network illustrate correctly the physical structure that reflects such a hybrid graph.

3.8.4.2 Pore and Throat sizes

The quantification of annular chamberlets in a test, the average chamberlet size etc. can be obtained rapidly. For example, a test with diameter 4.3 mm is partitioned into thousands of chamberlets of which the largest number measure approximately $0.42 \mu\text{m}^3$. A Poisson distribution of the pore volume may indicate that the volume of the individual chamberlets in the discoidal test varies as the 3D morphology of the test changes with its growth radially and in test thickness. The distribution could also represent the results of algorithmic excessive partitioning of the pore spaces; the visualizations of the ball-stick models do indicate that the partitioning does not correspond exactly but is a fair representation of the exact physical structure. Some edges of the network are not connected to pores; these should be discarded from the statistics but were not. A filtering algorithm may be applied but specific adjustments were required to the algorithm to accommodate the non-geometric morphology of the test.

However, two features identified by the statistics are of interest, corresponding to the measurements from complementary techniques used in this work and can be associated with the hypothesis relating to the chamberlet-canal tubular system (pore-throat network) as a line of communication. The modal diameter of pores is $\sim 31 \mu\text{m}$. The diameter of throats are indicated at $7 \mu\text{m}$ and $13 \mu\text{m}$. Radii less than $3 \mu\text{m}$ are not resolved in the data (voxel size was $3.11 \mu\text{m}$). Visualizations of the 3D pore-throat network in the test indicate that the larger sized canals are annular and the smaller canals are radially connected to chamberlets. The possible adaptive

importance of the 3D network and two different diameters of tubes oriented in different directions is discussed later in this section.

3.8.4.3 Visualization of pore-throat and solid fraction and adaptive value of network of the test

Visualizations in 3D of the skeletal topology of networks indicate that the grid-like pore-throat system and the grid-like skeletal system of the solid fraction are integrated in a mesh-like arrangement but differ in their topologies. The physical topology of a network in the test would be determined by the properties of the materials of construction of the test, the morphologies and adaptive value of the components (microstructures), the tolerance to environmental pressures during morphogenesis and self-assembly, and the energy cost of self-assembly of the network structure. Recall that in Section 3.5 it was shown that the inorganic and organic material units i.e. crystals and organic linings and membranes, of the tubular and pore-structures are the same as the constituents of the walls of the chambers. In an analysis of the shell cavity systems in two non-soritid families of foraminifera, Hottinger wrote:

“Pattern formation on the cell membrane as reflected and registered by pore distribution in the shell ...transport between chamber cavities is carried out by protoplasmic streaming supported by microtubuli, which have a linear extension. Thus, the connections in the shell’s septa have to be aligned. The axes of the intercameral foramina in successive chambers form basic patterns which are genetically fixed as deduced from their taxonomic importance on generic and higher levels” (Hottinger, L., 2001).

It is suggested that the results of this study reveal beyond the “transport...linear extension” noted by Hottinger, the pattern of a grid-like linear connectivity between successive annular chambers and the triangular truss-like “aligned” geometry of the pore throat network in 3D. These reveal the underlying or invisible structural pattern of formation or assembly of the annular chambers by extension of the linearity of the microtubules. Recall that in section 3.4 the role of the linear microtubules in transporting calcitic nanostructures and crystals was discussed. A similarity in the process of the delivery by microtubules of organic and inorganic constituents was observed. Also recall that the hierarchical arrangement of structures included an observed grid-like pattern formed by the inorganic crystalline structure at the macro level of the test. The pore-throat network of the void space reveals a similar grid topology. Moreover, the network of the crystalline structure reveals further details of the skeletal topology of the grid-like crystalline macro-structure. I suggest here that the results obtained through the application of a combination of techniques imply that during the morphogenesis of the test the microtubular extensions display a parallel process in the formation of the architecture of the test: similar grids are assembled in both, and the former is embedded in the latter. During the self-assembly of the test, the already-embedded pattern of the pore-throat network would facilitate the energy-efficient construction of the test walls. The solid fraction has a truss-like topology, despite the appearance of the curved walls of both the microstructures and the macro-level test. Based upon these results, an adaptive advantage produced by the pattern of pore-throat network and the triangulated truss system of the crystalline structure meshed together can be suggested: mechanical efficiency of a thin-shelled cellular (porous) disc structure. Interestingly, for cellular solids, the efficient mechanical value of precisely such a topology has been established through structural analyses of engineered artefacts (Gibson, L.J., 1989).

Hottinger observed that protoplasmic flow within the tubular network in the shell, and a reduction of associated transport distances, are an important additional functional requirement for the shell's architecture (Brasier, M., 1982). In a biological network, there is no conceivable reason for distances to be longer than necessary for achieving an adaptive value. If reduction of transport distances is important for minimizing energy expenditure by the organism, then the internal adaptive value of the tubular pore network would be related to the cell's metabolism and growth (including growth and repair of the test) rather than food gathering. In the test of *Marginopora sp.*, the chamberlets also are storage sites for symbionts. Annular and intercameral tubular passages are used to transport symbionts to the inner region of the test. SEM images indicate that the symbionts of the test measure approximately 3 μm (diameter). Measurements (from SEM images and from 3D Figure 61) indicate diameters of stolons in large tests are approx. 9 μm , intra-septal passages are 18-25 μm . Although network statistics and the visualization of the topology indicate lower values (77% of values obtained by SEM) there is fair agreement and reveal that the dominant two sizes (7 μm and 13 μm) are distributed in different orientations through the entire test. In a fundamental study of how networks may be used to circulate fluids extensively in composite materials such that fluid may reach any location of the structure, it has been shown that for a fixed volume the network grids that minimize the flow time are square and hexagonal grids (Bejan, A., Lorente, S., & Wang, K.M., 2006). (Lan, S. et al., 2014)(Lan, S. et al., 2014)In square grids in which two channel sizes occur, there is an optimal ratio of the diameters of the channels relative to the radial length scale of the porous medium. For the test of *M. youngi*, the pore-throat network exhibits both square and hexagonal configurations, and the distribution of diameters in the tubular throat network is bimodal. In this study, an analysis was not performed to evaluate whether the ratios of the two diameters observed is optimal. It is suggested that the pore throat network size distributions are correlated to the diameters of the symbionts and differentiated into larger and smaller diameters to allow an efficient movement of the symbionts and movement of the protoplasm-microtubuli cell material respectively. The value of two differently sized tubular systems in minimizing flow time in hexagonal and square grids correlates to the minimal communication distances hypothesis of the function of the canal system. A microfluidics-based experiment and simulation that models the network would be a way forward to test the validity of this correlation. Interestingly, an echinoderm, the sea urchin *Cidaris rugosa* has a calcitic skeleton that is fenestrated and consists of two interpenetrating but separate void-space networks that resemble a type of periodic minimal surface; it has been used as a template for fabricating macroporous copper (Lai, M. et al., 2007). A similar arrangement exists in the test of *Marginopora sp.*: the radial and vertical networks of stolons do not intersect in their geometric paths; but both paths share common nodes - the void space of the equatorial chamberlets – through which the paths transit.

The value of network thinking would be greatest when observations of the network, as has been achieved here, are modelled whole rather than only in part. Robustness, which is another property of networks, is likely to be an important feature of the network of the test. Removal of a single node (pore-chamberlet) is unlikely to have a significant effect on the network because the network encodes distributed robustness by allowing a few short steps to any node from any other node; the cellular structure and the composite nature of the material of the test would also be features that prevent an attack or fault in a part of the test from leading to catastrophic damage. Network thinking can also be applied to the networks of the reticulopodia

(protoplasmic microtubule movement) of the foraminifera during its feeding and motility. Qualitative and quantitative views of networks can both be used to determine the connection between structure, the adaptive values of the structure, and the potential efficiencies of the structure.

There are no studies known to the author of applications of network concepts to analyses of biomineralised foraminiferal tests. In a study of the skeletal pore network of a leuconid sponge (the structural make-up of which, like a foraminiferal test, is composed of a cellular network) based on X-ray MCT data, previously unknown areal cross-sections of the labyrinth of canals were revealed and that the network of circulating fluids could be considered functional to minimize fluid resistance (Hammel, J.U. et al., 2011). Results of that study were in part similar to the results presented here: the network was non-hierarchical. But the network of the foraminiferal test reported here is relatively uniformly branching as contrasted with the non-uniformly branching topology of the sponge network revealed in that study. In another study, the 3D network of the brain hemisphere of the fruit fly *Drosophila melanogaster* was extracted from synchrotron-radiation tomography microscopy data. An analysis of neuronal connectivity and distribution showed that a notable quantity of neurons could not be classified into groups and correlated those to the distribution of contacts between neuronal processes (Mizutani, R., Saiga, R., Takeuchi, A., Uesugi, K., & Suzuki, Y., 2013). These, and other studies earlier referred to in this work, demonstrate the application of network statistics and visualizations as a basis for understanding biological structure-function relationships.

Marginopora sp. is the most recent and complex of soritid large symbiotic foraminifera. Species of *Marginopora* which are similar in construction and morphology, have existed for million years and are an example of a evolutionarily very successful lineage and morphology. The characteristic of that pattern, self-assembly and another adaptive value are further evaluated in the next section of this work.

3.9 Analysis of the 2D and 3D spatial structure of *Marginopora sp.* using polygons

3.9.1 Introduction

The analysis and quantitative characterization of biological shapes is a difficult endeavour that has been attempted by naturalists, evolutionary biologists and palaeontologists. In order to characterize changing shapes “...In principle, if enough size and shape coordinates are included, we can describe the ontogeny of an entire individual” (Alberch, P., Gould, S.J., Oster, G.F., & Wake, D.B., 1979). Curved surfaces present a particular challenge; 3D space has been reduced to geometric shapes in most studies. Although advances in microscopy great facilitate measurements of structures at a high resolution and magnification recall that the limitations of optical microscopy or electron microscopy included, generally, a lack of 3D data. Although techniques were devised several decades earlier, as in the analysis of biological shape based on concepts of bending energy (Young, I.T., Walker, J.E., & Bowie, J.E., 1974), it remained cumbersome to acquire sufficient measurements in order to precisely represent and analyse shapes. The measurement of “sufficient coordinates” of a biological shape is increasingly made

possible by the availability of larger memory in current computing environments. Shape analysis and measurement is a specialty in the fields of computational graphics, pattern recognition and artificial intelligence; several advances in techniques and their applications to facial, organ, fruit, plant leaf and other biological shapes have been reviewed (Loncaric, S., 1998; Zhang, D. & Lu, G., 2004) in the literature.

Research of pattern recognition in the growth of plants, i.e. ontogeny, is encompassed by the investigation of phyllotaxis. A hugely varied multidisciplinary and enormous body of literature describes this widely prevalent tendency or pattern of self-assembly - growth manifested in particular spatial arrangements- in which buds and leaves appear in a precise order that is linked to a central position on the stem of a plant. Phyllotactic patterns were modelled by Bravais as lattice-structures. It was the study by L. Bravais and A. Bravais in the 1830s of the periodic structures and symmetries of plants that led to the conceptualisation of the invisible lattice structure of crystals, of which periodicity is a fundamental characteristic. In an era of important experimental work it which it was shown that the surgical removal of specific regions of the central stem inhibited phyllotaxis, and recent biophysical, biochemical and molecular investigations have advanced comprehension of the origins of these robust growth patterns. Reviews in the literature, which are too numerous to mention here, present mathematical, crystallographic, botanical and molecular genetic perspectives of the findings and analyses at progressive stages of research in the past decades; recent reviews by Kuhlemeier and Traas provide excellent summaries (Kuhlemeier, C., 2007; Traas, J., 2013).

Barabe and Jean refer (on pg. vii of their book) to phyllotactic patterns as the most “striking and puzzling” symmetry in plants (Barabe, D.a.J., R., 1998). Phyllotactic patterns are classified as distichous, whorled, spiral, multijugate. In distichous phyllotaxy (Figure 77A) two elements such as leaves or branches occur on each node. In whorled phyllotaxis (Figure 77B), two or more elements grow at the same annular node on the stem such that elements in an annular node are evenly spread around the stem, midway between those in the previous node. In spiral phyllotaxy (Figure 77C) elements grow one by one at constant angles from the previous one and, in multijugate phyllotaxy (Figure 77D) elements grow in groups of two or more spread evenly around the annular node, but each annular node is at a constant angle of divergence from the previous one. Pairs of spirals are known as families of parastiches (Figure 77E-F); their counts or numbers determine the type of spiral phyllotaxy. Pairs of spirals that represent numbers in the Fibonacci sequence describe a Fibonacci spiral phyllotaxy; other pairs of numbers of spirals are also observed but Fibonacci pairs are predominant. In a survey of 650 dicotyledonous families spiral phyllotaxy was observed in the majority of plants (~51%); exclusively whorled (~15%) and mixed (~34%) phyllotaxy was also widespread (Meicenheimer, R., 1998).

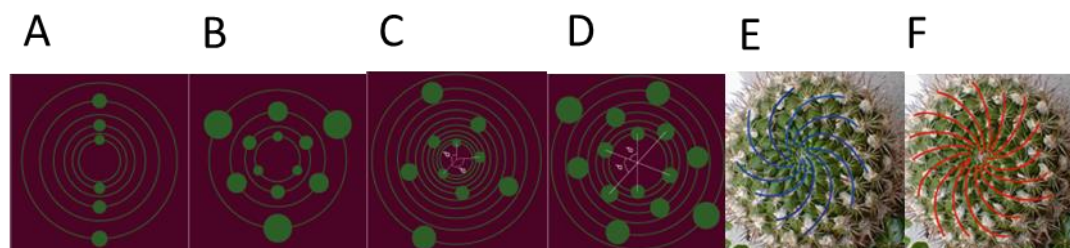


Figure 77 Types of phyllotactic patterns- circles represent elements distributed on annular nodes. (source: <http://www.math.smith.edu/phylo/About/Classification.html>)

Phyllotactic patterns occur not only in plants, although the origins of the word appear to restrict its use to botany. Using numerical simulations and physics laboratory experiments, phyllotactic patterns were shown to appear as self-organized growth that arises in an iterative process (Douady, S. & Couder, Y., 1992). In another study numerical and experimental evidence for spiral phyllotaxy in an experimental “magnetic cactus” (i.e. a cylinder of magnets with spines), validated in a non-biological system a model proposed earlier for the Fibonacci phyllotaxy observed in an elongate cactus *Mammillaria elongata* (Nisoli, C., Gabor, N.M., Lammert, P.E., Maynard, J.D., & Crespi, V.H., 2009, 2010). These studies strongly indicated that phyllotactic patterns had a purely geometric origin and could be found in other physical domains: the authors explained that the various patterns could be described by the simple fact that an element’s nearest neighbours in one dimension (e.g. along the stem) are not its nearest neighbours in three dimensions (i.e. around the curved surface of the stem). This insight added a new dimension to interpretations of the origins of phyllotaxy in plants, which had centred recently on the biophysical responses of surfaces of the stem to pushes from below or of expanding surfaces to lateral constraints of the stem which acted as a two layered sheet. However, that phyllotactic patterns in plants are, in addition to geometrical relations, a manifestation of the interplay of mechanical and biochemical processes such as the gradients of the hormone auxin at the apex of the stem also remains a widely investigated notion (Kuhlemeier, C., 2007). That phyllotactic patterns may be observed in convection cells on the sun’s surface or in plants and in polypeptides continues to make it intriguing and in biological tissues it remains “the grand-daddy of pattern-forming systems” (Newell, A.C., Shipman, P.D., & Sun, Z., 2008).

An important aspect of phyllotactic patterns is the distribution of elements or microstructures in space during the growth of the macrostructure. Recall that the complete test of *Marginopora sp.* was shown (in Section 3.6) to exhibit a gradual shift through ontogeny towards symmetry of a discoidal form and an increase in the aspect ratio of the test; the 3D skeletal topology of the pore network showed (as presented in Section 3.8.4.3) the circular and radial symmetry of pores and throats in two sizes and, the 3D skeletal topology of the solid fraction of the test was represented by triangles assembled in a grid-like configuration. In this research X-ray MCT data were analysed by geometric methods to advance an understanding of the basic pattern of the division of the 2D plane of the disc. In this section, the results of the analysis are described and correlated to an established pattern of morphogenesis and to the structure of the crystalline fundamental constituent of the test.

3.9.2 Results

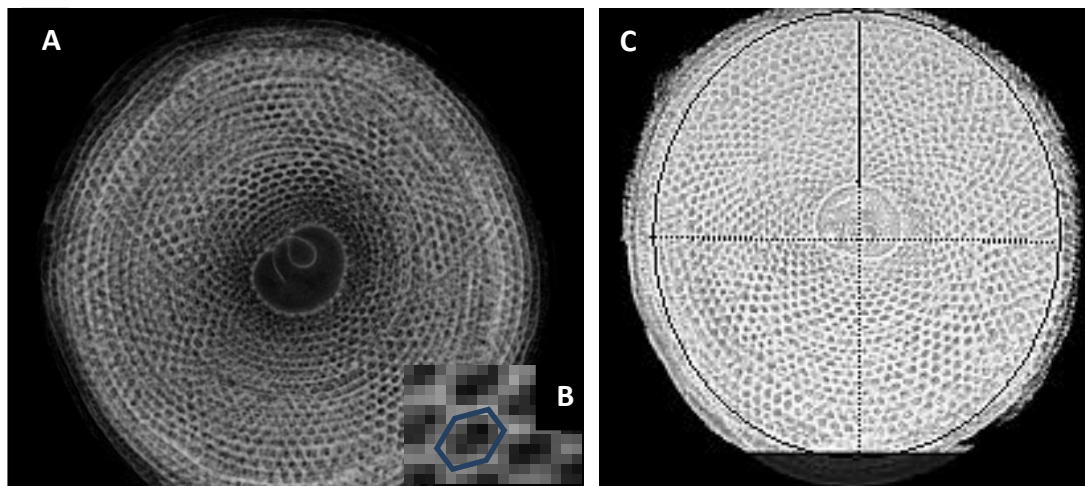


Figure 78 X-ray MCT (A) reconstructed tomogram view in equatorial plane and (C) rendered volume view of the discoidal adult test.

An X-ray MCT reconstruction of *Marginopora sp.* adult stage circular test in equatorial surface view of the entire structure in 3D shows (Figure 78A) a cellular structure comprised of approximately equal dimensions and equally spaced cells that divide the space of the disc into regions. Here, the plane of the disc is tessellated or divided into tiles or tilings. The cells are primarily hexagonal-shaped (inset); some are pentagonal. The 3D volumetric rendering of an equatorial section below the surface (Figure 78B) of the same test reveals the same regular cellular structure in one plane (region inside the circle). The discoidal shape is virtually circular and symmetrical along the dotted line.

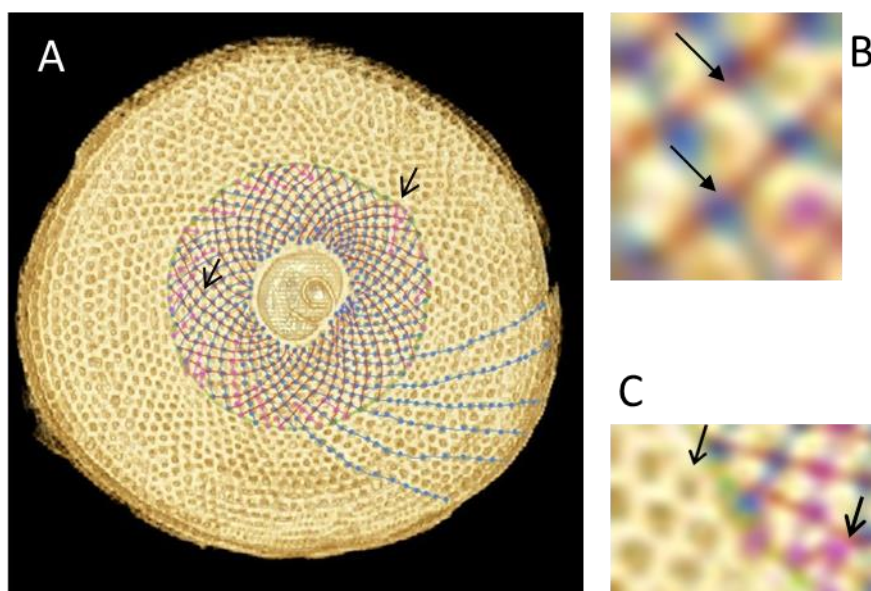


Figure 79 A: Pairs of spirals in the test of *Marginopora sp.*; B: Intersection of spirals; C: Changes in spirals.

At close examination, it is possible to define pairs of spirals or parastiches that traverse the cells which occur in the sequential annular chambers (as is shown by the green circle in Figure 79). This operation can be performed at each equatorial “slice” of the discoidal form and yields spirals in the partial section. In this particular “sliced section” in 2D, the pairs of spirals in the

clockwise direction (as shown by pink/purple lines) and counter clockwise direction (as shown by blue lines) trace trajectories across the entire area of the test. The pair of parastiches are visible opposed parastiches, i.e. at their intersection there occurs a cellular chamberlet (as shown in Figure 79 B). The angle of intersection of the pairs of parastiches is close to orthogonality in some regions but more often varies between 70° and 110° . The number of parastiches counted is dependent on the annular chamber at which parastiches are counted; e.g. numbers could be 39 and 47 if parastiches starting at the first annular chamber these are counted at the annular chamber marked with a green line in Figure 79. Perturbations occur at radial distances from the centre (as seen in Figure 79C); a single parastiche may bifurcate. Perturbations may result in an increase in the numbers of parastiches. Starting at the first annular chamber, counting in the clockwise direction there are 37 parastiches and in the counter-clockwise direction there are 38. The largest common divisor is 1. Counting again at the third annulus yields 12 clockwise and anticlockwise secondary parastiches (Figure 79A).

The angular shift for each consecutive annular chamber measured from the centre of the disc is constant at approximately 3° in the middle region of the test. It varies between 3° - 7° through the entire test; it is higher in the inner region of the test. Mean chamberlet (element) height is twice that of the thickness of the intercameral (between annular chambers) walls and no greater than four times. The positions of chamberlets in each consecutive annular chamber are determined by the angle of the stolons -intercameral tubes of the openings or foramen (Hottinger, L.C., 2000). By using the annular direction of the basal stolons which connect chamberlets in the same annular chamber as a line segment, and the angular direction of the intercameral stolons as another line segment that intersects the former yields an angle that is close to 137° (Figure 82D, obtuse angle between the thick and thin purple lines) ($N=10$, mean= 133.02 ; SD= 9.09 ; Min= 120.93 ; Max= 148.95). This shift or divergence angle is fairly constant through several consecutive annular chambers.

These features are congruent with the basic characteristics observed of whorled or annular phyllotactic patterns, especially of the majority of aquatic plants (Kelly, W.J. & Cooke, T.J., 2003). In addition, a non-Fibonacci form of a spiral phyllotactic pattern is observed in the test of *Marginopora* sp. This phyllotactic pattern has cellular elements and, in cross-section the elements are mostly hexagonal (Figure 78 B).

A visual interpretation of the data obtained by X-ray MCT displayed as the grey-scale reconstructed tomogram and 3D volumetric rendering showed that the equatorial planes of the discoidal test are divided into voids- cells with solid walls. Geometric methods that can be used to divide a plane or tessellate a region into tessellations include the construction of a Voronoi diagram (Aurenhammer, F., 1991). Here the method is employed to affirm with the use of a geometric algorithm the visual observations of the division of space and of the parastiches. The method uses defined seed points, and harvests all points in the region closer to a seed point than to any other seed point; an area around each seed point then defines the Voronoi cell around that seed point. The sides of the cell represent all points that are equidistant from the seed points of the neighbouring two cells; no space is left uncovered in the region. The tessellation of Voronoi cells of all the seed points defines the Voronoi diagram of the region. Its dual, the Delaunay triangulation, results in the maximum angles of the triangles that are formed by the seed points as shown in Figure 80.

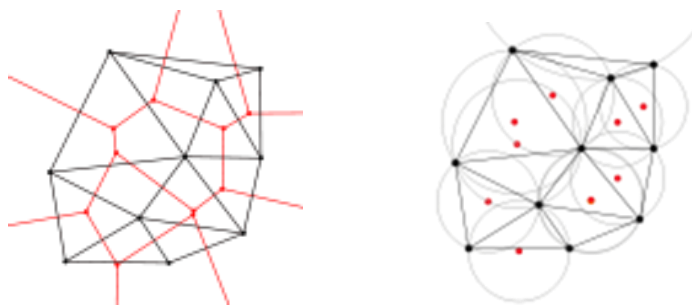


Figure 80 Sketch of concepts.

Seed points are black dots in the Voronoi diagram and cells are red polygons (left); its dual Delaunay triangulation (right).

In Figure 81 are shown a MATLAB generated Voronoi diagram which uses the centres of the chamberlets as seed points and, the Delaunay triangulation of the same planar section of the test of *Marginopora sp.*

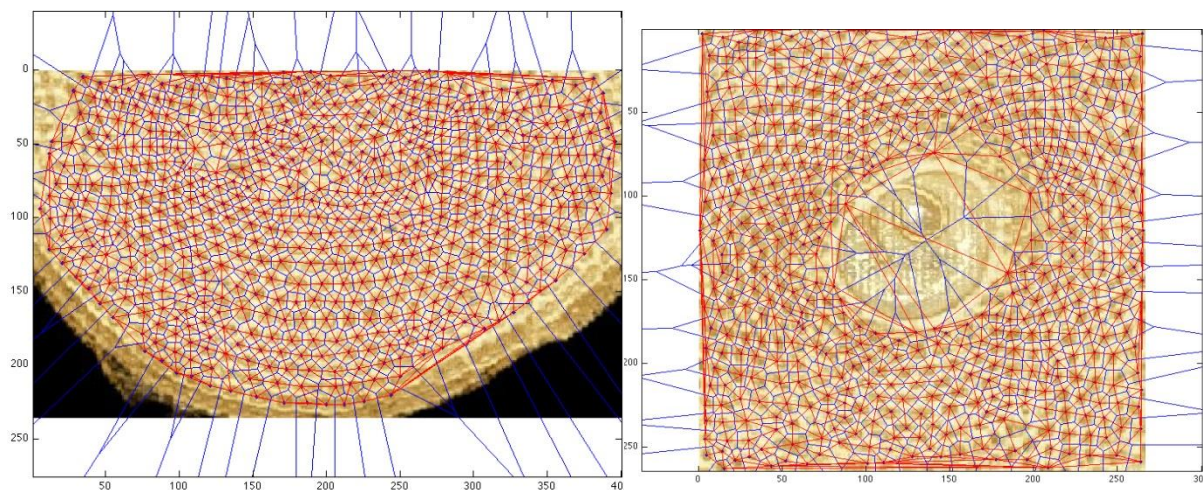


Figure 81 Tesellation of region of the test: Voronoi cells shown by blue lines; Delaunay by red lines.

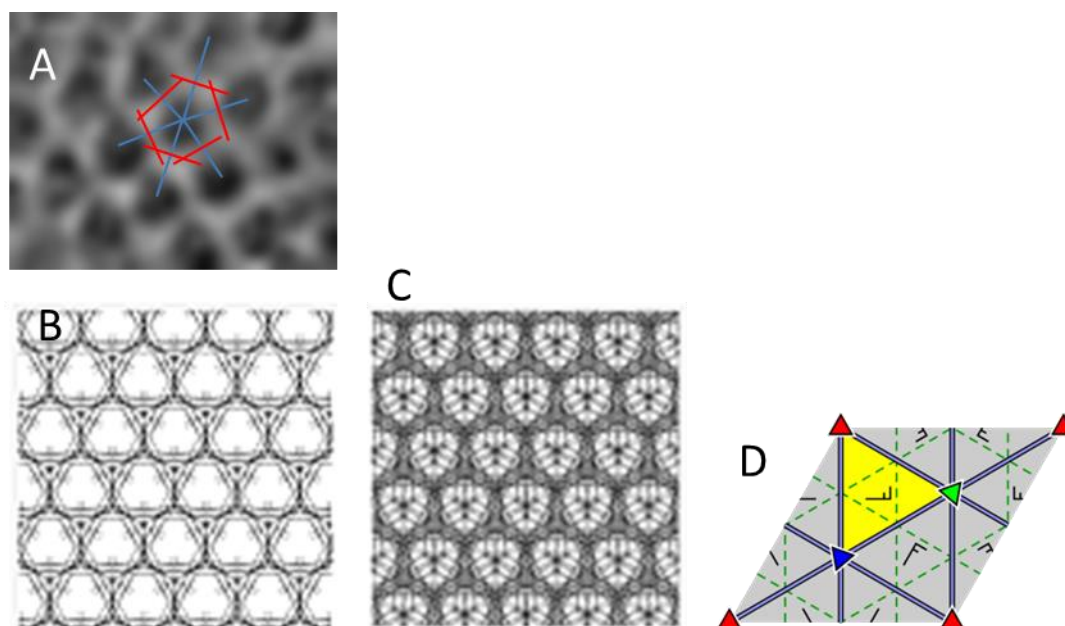
There are several features of interest in the Voronoi diagram shown in Figure 81. First, the generated Voronoi cells closely match the morphology of the walls of the chamberlets. Second, the hexagonal cell structure is less uniformly developed in the inner region than in the outer region of the test; most of the cells are hexagonal although pentagonal and septagonal cells are also visible. Third, within the regions shown, there are perturbations or imperfections. Imperfections occur either as variations in spacing or in sizing. Small changes in the position of the seed sites only result in small changes in the Voronoi cells (Reem, D., 2011). Fourth, the Delaunay identifies the parastiches and the circular annular chambers as geometric duals of the cells. Fifth, the central region of the test and the first annular chamber show an interesting, virtually symmetric, connection of the generated sides of the Voronoi cells in that area of the test which correspond perhaps to the pores in the prolocular region.

A phyllotactic pattern that is evident in the crystalline test forms a low-energy geometric lattice configuration of the macrostructure of the test. Each cell is also a low energy configuration- as shown in Figure 82A - in which the midpoints of the chamberlets are connected and orthogonal

at midpoints of the connecting lines form the cell; this form of construction of the Voronoi cell is known as the Wigner Steitz cell. In the Wigner Steitz cell the perpendicular lines (shown with red lines) indicate the Bragg planes of a region and the volume included corresponds to the first Brillouin zone. In the cellular structure of the test the position of these planes would coincide with the positions of the crystalline walls of the chamberlet.

The repetitive pattern of chamberlets and walls form a periodic tiling pattern. A lattice of evenly spaced parallel lines contains identical pieces of the tiling. This motif is compared now to the plane crystallographic groups, of which in two dimensions there are 17. In these groups the symmetries of translation, rotation, reflection, and glide reflections are maintained. Upon comparison, it appears that at least one motif or one fundamental domain of the tiling observed in the test of *Marginopora* sp. is congruent with the motif of the plane crystallographic group $p3m1$ (shown in two relevant variations as tilings and shown as in a single unit in Figure 82 B1-B3). One fundamental domain is shown superimposed in Figure 82C. In the macrostructure of the test, as has been described in Section 3.6, canals or stolons occur oriented in a radial and annular direction. The position of these canals which connect the chamberlets in both directions in the test has been shown in 2D and in 3D. The position of the canals and their parallelism is geometrically integrated in the identified fundamental domain (as indicated by the purple lines in Figure 82E and by red arrows in Figure 82D).

It is an established fact that the fundamental crystalline material constituent of the walls and the cellular structure is calcite (as Mg-Calcite). It is also known that the plane crystallographic group $3pm1$ is the symmetry frieze observed in the crystal structure of non-biogenic calcite. Here the correlation is observed and shown between the 2D symmetry of the cellular structure of the calcitic test and the symmetry of the calcitic crystals that constitute the test; i.e. symmetries at the underlying nanoscale and of the macroscale of the inorganic constituents of the test.



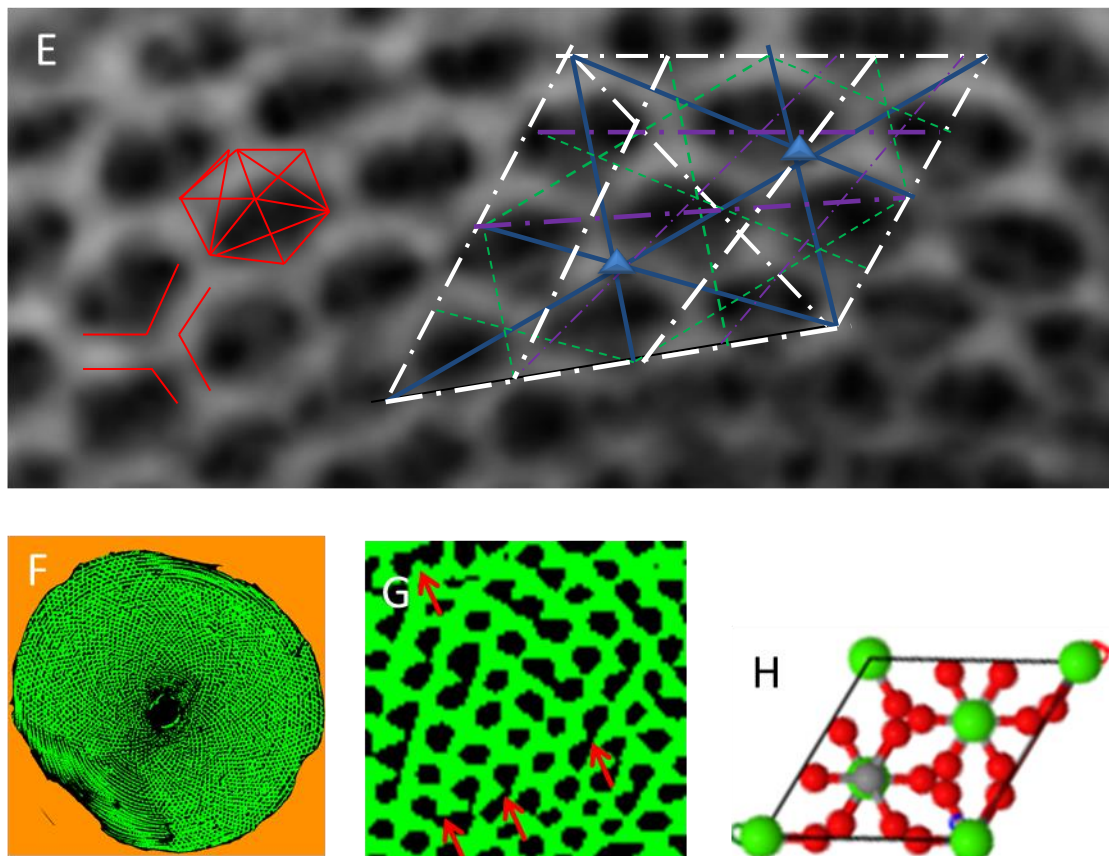


Figure 82 Plane symmetry group p3m1: the basic pattern observed at nano and macroscales of the test of *Marginopora sp.*

A: Blue lines connect midpoints of chamberlets and red lines are orthogonals drawn at midpoints of the blue lines; B: Motif of plane symmetry group p3m1 shown enlarged for clarity of illustration; C: Motif apparent in the cellular structure; Lines: White - crystalline walls; Purple (thick) - annular throats; Purple (thin) - radial throats; Black (solid): group p3m1 tessellation motif; Black (dashed): glide reflection axes; Blue (solid): reflection axes; D-E: Tomogram of test segmented to show void-chamberlets with radial and annular interconnecting canals indicated by red arrows; F-H: The unit cell structure of calcite.

3.9.2 Discussion

An analysis of the patterns of the test of *Marginopora sp.* using X-ray MCT reconstructed tomograms and volumetric rendering revealed the optical effect of pairs of spirals traceable in opposite directions of the 2D equatorial plane. An angular divergence that is close to 137° was obtained. In this study the suggestion is made that the observed pattern corresponds to a whorled mixed phyllotactic pattern. *Marginopora sp.* is an aquatic organism that hosts symbiotic dinoflagellates, which require light to photosynthesise. In their study of forms of phyllotaxis in aquatic plants, Kelly and Cooke argue that light-harvesting is a potential selection pressure on phyllotactic patterns. They note that in computer simulations light harvesting is maximised by whorled phyllotaxis, provided elements do not overlap and that the distance between elements equals element length (Kelly, W.J. & Cooke, T.J., 2003). Among hydrophytes whorled phyllotaxis is exhibited more than twice as frequently as in non-hydrophyte species of plants. These observations are consistent with the potential adaptive requirements of the test: efficient exposure to light in all areas of the test. A difference in the structure of the test and

hydrophytes that exhibit annular phyllotaxis is that there is a very large number of elements (chamberlets) in one annulus in the test and the intercameral distance does not always equal or exceed the size of the chamberlets; the application of the conclusions of the simulations that Kelly and Cooke rely upon to show the maximal light harvesting value of whorled phyllotaxis is weakened by this structural difference. However, the chamberlets decidedly do not overlap.

An important caveat should be noted: the phyllotaxis of spiral systems observed in plants is expressed by fractions; spiral phyllotactic patterns especially associated with the golden mean divergence angle of 137° are commonly and objectionably linked with the distribution of light on plant leaves. However, the spirals obtained in this study are not indicative of Fibonacci phyllotaxy in which the golden angle is very closely achieved by diverging elements. But Okabe notes that it is the vascular system that appears to be efficiently coordinated by this arrangement (Okabe, T., 2012). The fractional expression of spiral phyllotactic patterns derived from models of phyllotaxy in plants does not seem applicable to the spirals observed in the test because of the differences in the generative process of the elements in plants and of the test. In the test of *Marginopora sp.* the stolons inter-connected to the chamberlets fulfill an analogous function to the vascular system of plants, i.e. as a transport pathway through the test (see Section 3.8.2). The divergence angles reported in this study measure the angularity between the radial and annular stolons or tubular systems; the range of values of the angles measured (mean= 133.02°) is close to the golden angle 137° .

The pairs of spirals observed are often perturbed; natural systems show patterns that can be geometrically generated, but defects are common. The test of *Marginopora sp.* is a biomineralised structure that would likely exhibit responses of the cell to environmental conditions while constrained by the genetically and geometrically determined growth parameters. Defects are observed along the spirals where rapid changes in the elevation of thickness of the test occur. Dislocations or defects have been associated with contact pressures between elements.

In this study, a growth spiral was not generated using a spiral model of phyllotaxy. An objective was to analyse the patterns identified visually by seeking existing models across disciplines that could fit the observations. When the centres of the chamberlets are used as seed points (Figure 81) and a Voronoi-Delaunay algorithm was applied, the results closely resembled the morphology of the chamberlets. This allows the inference that a growth spiral probably does describe the geometrical growth of the test. But the Voronoi cells are not all the same shape and size which is a presumption of optimal packing models. Models of phyllotactic patterns suggest that Voronoi polygons can be hexagonal when they are fit to a set of points generated by a spiral model; the hexagonal shape allows for an optimal packing (Rivier, N., Occelli, R., Pantaloni, J., & Lissowski, A., 1984). The test of *Marginopora sp.* is not perfectly circular, nor is the equatorial section exactly planar. Perturbations, as mentioned above, also likely affect the chamberlet size and shape, which appear to be more uniformly hexagonal beyond the inner regions of the test. In the inner regions pentagonal and other planaforms are easily discerned. The angularity of the stolons may be greater through ontogeny as the diameter of the test and the thickness increase. The Voronoi-Delaunay algorithm is only applied in 2D but the test accretes in 3D. Importantly, the Delaunay also affirms the spiral growth or the angular extensions of the stolons based simply upon the tesellation of the plane and the allocation of seed points.

Optimal packing is not necessarily the dominant adaptive value of the architecture of the test of *Marginopora sp.* It is reasonable to conceive that other adaptive values and close-to-optimal packing advantages of non-Fibonacci or whorled phyllotactic patterns may be discerned in the architecture of the test. A mechanical adaptive value of the phyllotactic patterns in the test would be consistent with the structural hierarchy observed in the architecture of the test (as reported in Section 3.5.9). Cooke presents incontrovertible evidence that whorled phyllotaxis in plants, as is suggested in the phyllotactic pattern of the test of *Marginopora sp.*, does not involve Fibonacci formulae (Cooke, T.J., 2006). This finding supports the results of this study. It has also been suggested that a biological system is unlikely to be capable of self-organisation in response to a geometrical imperative (Cooke, T.J., 2006) such as optimal packing that is observed in high but not in low Fibonacci number phyllotactic patterns. Cooke suggests that Fibonacci phyllotactic patterns may be a consequence of “some other biological process” and that optimal packing is a secondary outcome. However self-organisation and optimal packing using phyllotactic patterns has been used in the analysis of structures in biological systems such as in the helicies in collagen fibrils (Charvolin, J.S., Jean-François, 2011), and in the tubular packing in biological fine structures such as in the arrangements of microfilaments of actin, and microtubules of some organisms (Erickson, R.O., 1973). Models that interpret the phyllotactic patterns as intrinsic and occurring naturally have also forcefully shown that compressive stresses, mechanical forces and energy minimizing buckling pattern of a shell versus the interior can lead to phyllotactic patterns (Shipman, P.D. & Newell, A.C., 2005). Importantly, these analyses have not encompassed a biomineralised skeletal system. The phyllotactic patterns observed in this study in the test of *Marginopora sp.* presents a novel challenge for further analyses.

A view of the test in another dimension shows the angularity of the walls across the thickness of the test. These form curvilinear spiral-like transitions through the test. Spiral-like connectivity of the annular chambers across the diameter of the test would add a stiffening mechanism to the structure. A 3D animation of this feature is available in the supplementary material in electronic form. The test exhibits a spiral structural pattern through its equatorial (xz) cross-section indicating that the spirals traverse the thickness of the test. Space structures are truss-like members that are linked in 3D to support curved structures such as domes. Spiral phyllotactic patterns as compared to non-spiral or linear arrangements of space structures have been shown in simulations to be up to 80% more efficient in reducing vertical displacements in the structural members under uplift loads (Choong, K.K., Kim J. Y., 2013). An adaptive value of such a structural pattern is relevant to the test of *Marginopora sp.*; it is attached to substrates and is subject to the hydrodynamic uplift forces of shallow marine waters.



Figure 83 X-ray MCT transverse section of test showing spiral-like connectivity of chambers.

Recall that in Section 3.5 the hierarchies observed in the structural arrangement of the test did not include a molecular level. The results presented here (Figure 83) draw a correlation between the macro level of the test and the nano level: self-similarity of a symmetry pattern. The walls of the test in cross-section mimic the low-energy geometric configuration (p3m1 symmetry) of the calcite unit cell. This result supports the notion that the repetitive modular constructional pattern of the calcitic test is derived from a self-assembly process that may share a common unifying principle with an abiotic established fundamental pattern in nature. Recall that phyllotactic patterns are also observed in non-biological systems and are an expression of self-assembly. Operative forces or processes in different balances under biological control and under abiotic or inorganic control (with an underlying mathematical structure) could be expressed in the test as a whorled mixed phyllotactic pattern and the repeated motif of the symmetry group p3m1. The transference or emergence of symmetry and periodicity from an atomic molecular and mineral level to different levels of biological structure, organisation and function has been discussed as molecular mimicry; i.e. biological periodicity is anchored on chemical periodicity (Lima-de-Faria, A., 1997).

In Section 3.4.4.6 a comparison was made of the delivery processes of organic and inorganic constituents and the role of microtubules during these processes in biomineralisation. In Section 3.8.4.3 a comparison was made of the structural arrangement of the pore network and grid skeletal structure of the crystalline phase and the role of microtubules in the modular extension of both phases. Here a suggestion is made that the growth of the test itself is accretive but results in a whorled phyllotactic pattern. Indeed, this research posits that the phyllotactic pattern would be the self-assembling over-arching genetically-determined pattern; the structural hierarchy observed in the test would represent the nano-macro assembly units of that pattern that provide a mechanical adaptive value (and other adaptive functional value) across dimensions of scale; the unifying underlying low-energy geometric motif is the symmetry motif of group p3m1. The architecture would be genetically-determined and the construction could respond to the environmental pressure-state. A hydrodynamic flow would be the environmental pressure-state to which the morphogenetic process responds. Microtubules respond to and sense the environmental pressure-state. The microtubules are the soft mechanical scaffold which provide a continuously assembling macro pattern according to a phylogenetic constraint, deliver the organic and inorganic constituents and guide the assembly of the calcitic nanocrystals along the soft scaffold (the microtubules themselves and the organic lining) for sequential chamber enlargement. The polygonal planaform tessellation of the plane of the test in an approximately hexagonal form could be achieved by the linear extension of the microtubules. Three cables (microtubular) consisting of pseudopodia could align in tension such that an angle of 120° is formed; extension along any cable at an angle of 120° would initiate an extension of the structure of a chamberlet. Microtubules and the aggregated rod-like crystals are linear structures that form curved surfaces and volumes in a complex 3-D architecture. The question of how linear microtubules may form curved structures may be resolved by the observations that when grown *in vitro* under an hydrodynamical flow (animal) microtubules bend and when tension is applied microtubule polymerization is promoted; the cytoskeleton can respond to mechanical stress (Louveaux, M. & Hamant, O., 2013). An assembly of the hexagonal or planaform chamberlets could be achieved by the geometric-tensional extension of the microtubule driven pseudopodia; delivery of the organic and inorganic constituents by microtubules would follow.

However, the distance or length of the extension of the pseudopodia would be related to the “seed” of the Voronoi; that distance would likely be developed as a “memory” held by the microtubules. Indeed, their hexagonal structure and that microtubules are the storehouses of memory and consciousness in brain neurons further is an intriguing aspect of the “constructional” potential of microtubules. Through collating this possible process and the discussions of microtubular activity in previous sections it is suggested that microtubule activity related to the architecture of the test may also exhibit a hierarchy of levels.

Marginopora sp. grows to a large size in a hydrodynamic mechanical pressure-state environment through microtubular activity at several levels of hierarchy of processes. It constructs a test of hierarchically arranged structures that indicate the test and the cytoskeleton are likely responsive to the same mechanical stresses. A testable hypothetical question arises from the model posited in the preceding paragraph: How does interference with the microtubular system in *Marginopora sp.* affect the architectural patterns of the test?

In this section, observed patterns in the test of *Marginopora sp.* have been correlated with phyllotactic patterns and their adaptive values have been discussed. A possible cellular process of assembly of the architecture of the test has been proposed. In the following section, an attempt is made to further refine the potential adaptive value of the test in the context of the patterns reported so far in this work.

3.10 Models for and of the test

3.10.1 Introduction

The present work was partly motivated by the problem of an incomplete understanding of the “functions” of the complex architecture of the test. A multi-scale and multi-dimensional characterization of the test has been performed in an effort to advance an understanding of the architecture of the test. Such a characterization would be a reasonable precursor to obtaining a detailed understanding of the complexity of the test. If form follows function; an enhanced understanding of form precedes and informs an understanding of function. The research contexts, perspectives and reports of novel multi-scale observations and multi-dimensional analyses of microstructures have been described in previous sections. Patterns formed by microstructures in the test of *Marginopora sp.*, which are a significant novel feature reported in the present work, have been correlated to the established mechanical efficiency of grids in cellular solids, to the vascularization of a grid of known volume, and to an accepted patterning process of self-assembled growth. The question raised in this section of the work is: do these patterns integrally contribute to the several conflicting adaptive values of the architecture of the test? If so, then primarily to which adaptive values?

Recall that in the introduction to this research (Section 1.3) it was noted that during the past fifty years researchers have proposed several “functions” of the test. The question of function could be answered through a very systematic arduous process of experimental work involving measurement, computing and hypothesis testing. It would involve measurements of numerous morphological, physical, and chemical characteristics of the test, and of the environment, and a systematic testing of numerous hypotheses in sequence and along different lines of inquiry. Recall that, in addition to the limitations of current experimental techniques, the anisotropy of the morphologies and the extraordinary complexity of test architecture of *Marginopora sp.* prevents meaningful results being obtained by experimental work and by using current numerical modelling techniques. That is not to say that experimental investigation of this question may not advance answers at present; the sophistication of instrumental analytical techniques available to execute experiments is rapidly increasing; concomitantly rapid advances are being made of the computing resources available to develop and test hypotheses using numerical or physical models. 3D data sets and accurate representations of structure, as obtained in this research, are indispensable to this process.

This process can be simplified by co-opting knowledge from other disciplines. It is proposed that the adaptive value of the architecture of the test of *Marginopora sp.* can be sought by examining existing models of similar architectures in biological and abiological systems for which functions are well-established. By doing so, the common elements, requirements, pressures and causal connections are deduced. This leads to the functional significance of the architecture of the test.

But, how do I decide what is a suitable model? In the first instance, I would have to find suitable ways to decide what is a suitable model. Recall that in Section 3.8 we found the skeletal topology, simplified and unravelled it, and visualized the intricately linked complexity of the microstructures of the test. I applied the established techniques of network analysis which have

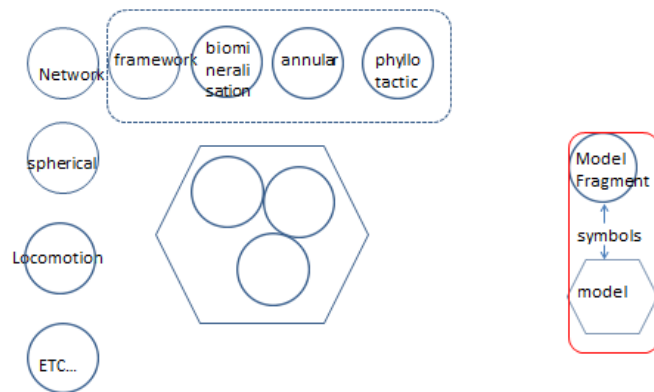
been tested on other structures with complex and similar features. Now, instead of finding suitable ways to decide what is a suitable model, I turn to a field of research in which that process is of fundamental importance, and in which the effectiveness or practicality of the outcome is crucial: artificial intelligence (AI) and expert systems. I rationalize the task.

The task is reduced to finding in AI research the established description of suitable models. In the research of AI an established idea is that effective problem solving requires the adoption of adequate models of that domain; abstractions and approximations are integrated in the adequate model (Amarel, S., 1968). The process of deciding which phenomena or features of the domain are relevant and which abstractions or approximations suitably represent the selected phenomena is “difficult, error-prone and time consuming”(Nayak, P.P. & Joskowicz, L., 1996). This difficult process is made more difficult by the problem of harvesting knowledge effectively. It is easy to conceive that nested within this problem are factors such as the amount of knowledge, its relevance, how to select just which knowledge, and how to process the knowledge such that it is quickly adapted to the task at hand. Research in AI develops strategic approaches to this problem. Major findings of AI research in this area showed that the amount of knowledge; the breadth of knowledge; analogizing general to “specific but far-flung knowledge”; avoiding “premature mathematization” or focus on “toy problems”; noting detail but testing falsifiable hypotheses on large problems are the important parameters of knowledge application (Lenat, D.B. & Feigenbaum, E.A., 1991).

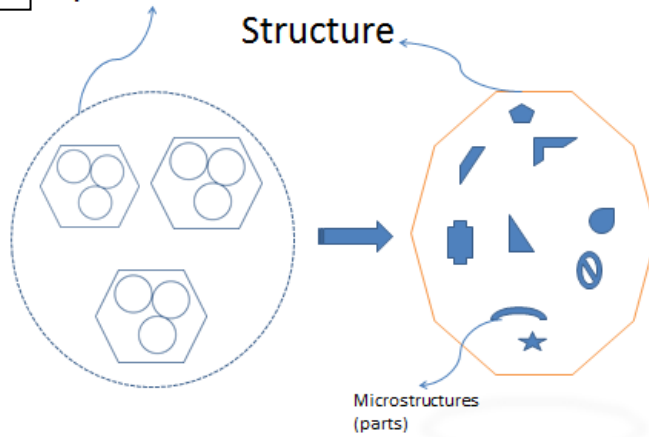
A major contribution to AI research in the adequacy of models was developed by Nayak and reported by Nayak and Joskowicz (Nayak, P.P. & Joskowicz, L., 1996). They elegantly showed that: a model is composed of model fragments; the space of the possible models of a system is defined by the structure of the system; the structure of the system consists of parts from a parts library and how the parts are put together. Each part is associated with a set of model fragments; model fragments describe different aspects of the parts’ behaviour; a model of the physical system is a subset of the model fragments that are associated with and describe each of the parts of the system; the space of possible models would be a subset of the model fragments associated with the parts of the system. Figure 84 (A-E) pictorially illustrates these concepts and their inter-relationships in the context of the test of *Marginopora* sp.

An adequate model would then be defined by the criteria of task, domain-dependent constraints and simplicity. A fundamental criterion of an adequate model is if it can provide a causal explanation of the task (or phenomenon). A causal explanation could be tested by the causal ordering of the parameters such that the causal ordering represents an informed notion of the causal dependency of the parameters of the system. If the ordering explains the dependency of the parameters then the causal explanation would be considered an adequate model. Domain dependent constraints refer to the constraints raised by the structure and behaviour of the physical system. Simplicity means that irrelevant phenomena are not included and complex models with irrelevant details are not created for relevant phenomenon, i.e. parsimony is valued. Searching for an adequate model would be made effective and efficient by making all approximations causal, identifying an initial causal model and reiteratively simplifying it by dropping a model fragment or approximating it. When simplification of the model means it is no longer causal then the model is a minimal causal model.

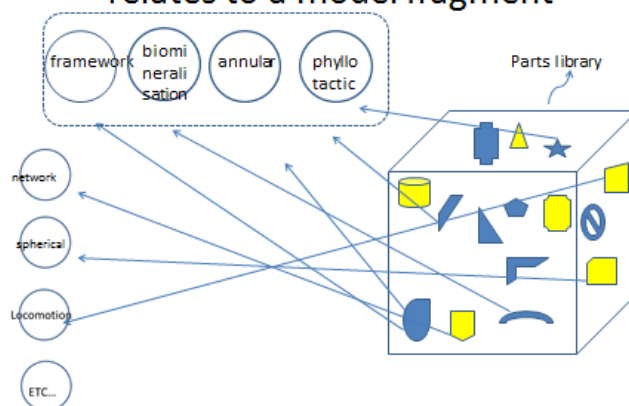
A Adequate models- concepts



B Space of models is a function of Structure



C Structural parts library: each part relates to a model fragment



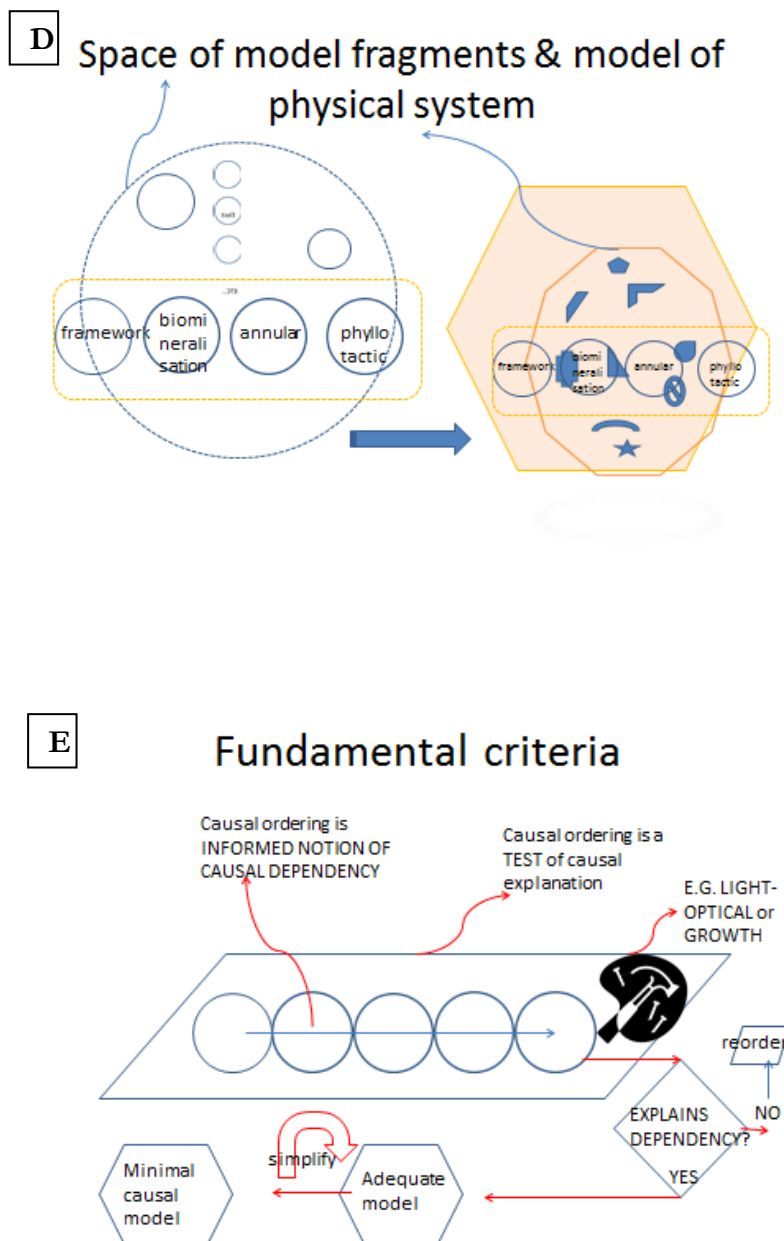


Figure 84 Schematic of concepts and relationships in adequate models.



A: Models (hexagons) are composed of model fragments (circles) that represent behaviours e.g. biomineralisation; note the fragments within the dotted rectangle are associated with characteristics of the test of *Marginopora sp.* B: A structure composed of constituent microstructures, nanostructures etc. that are represented by “parts” is related to all of the possible models or the “space” of models (dotted circles). C: Microstructures relevant (blue) to *Marginopora sp.* relate to model fragments that are also relevant to *Marginopora sp.* These and other microstructures or parts (yellow) constitute a parts library (box). D: *Marginopora sp.*’s test is characterised by biomineralisation, frameworks, annular growth and phyllotactic patterns; these model fragments and microstructures relevant to the test of *Marginopora sp.* constitute the model of the physical system (octagon), which is a subset of the model space. E: The algorithm of the fundamental criteria of a minimal causal model is pictorially represented as a flow-chart. The process (parallelogram) of the causal ordering of the model fragments (circles) towards achieving a task (hammer + nails) represents a test of whether the causal explanation is viable. Viability is tested by the criteria of dependency. If this fails (no) then the process requires a reordering of the model fragments. If it passes (yes) then the model is an adequate model. This can be simplified by removing fragments until causality would be compromised. That simplified model can be considered a minimal causal model.

In this work, the algorithmic netcasting process outlined above was used as a guide in a search for adequate models, then the space for models of the physical system (the test of *Marginopora sp.*) was searched and three existing potential models of the architecture of the test were identified; i.e. three unrelated biological and abiological systems that are *adequate causal* models for the test of *Marginopora sp.* The adequacy and the limitations of the models are discussed in the context of the findings and patterns reported in this work and the architecture of the test of *Marginopora sp.*

3.10.1 Results

Model fragments A brief explanation of the application or working methodology of the adequate model method and the resultant models are presented in this section.

Table 10 General reported parameters of the physical system of the test.

Fragment 	Form	Structural	Process	Task
Part 				
Elements Ca C O ₃ Mg	Atomic			
CCN	Spherical	?	Biomineralised	Growth
Calcite crystals in different stages	Solid agglomerate rhombic	Lattice Modulus Hardness	Biomineralised Self-assembly	Growth Light transmission
Euhedral crystals Walls Chambers chamberlets	Rod-like; bundles; oriented; not oriented; solid; curved; tiled; curvilinear; modular voids polyhedral	Composite structure Lattice Framework Sandwich structure; tesellated	Biomineralised Phyllotactic	Mechanical; Optical Barrier; Diffusion; Reflection/Transmission Volume for storage; Packing arrangement
Organic Linings	Lamellar	Composite; Template Hardness	Cell	Growth; Barrier; Light transform transmission; Diffusion
Symbionts	Spherical; oriented; distributed	Space filler	Incorporated	Packing; Light absorption; Biochemical
Protoplasm; Organic structures, vacuoles etc.	Organic	Space filler	Biomineralised Cell	Growth; Biochemical; Transport; Attachment to substrate;
Microtubules	Linear; hexagonal; reticulated	Network; Framework	Phyllotactic Self-assembly	Growth, Transport Communication
Canal & Stolons	Tubular	Network	Biomineralised	Communication Flow- Transport
Architecture	Discoidal Convex- concave; Annular- Anisotropy Discontinuous (pore-holes)	2 surfaces- one fixed one exposed; Cellular; Sandwich Hierarchical	Phyllotactic Self-assembly	Growth; Surface Area- Volume; Packing; Mechanical; Mobility; Optical; Barrier; Diffusion; Hydrodynamics

An initial causal model would consist of all fragments listed in Table 10 towards achieving all the tasks listed. This causal model would be simplified to the point where a model would retain causality. To illustrate the process, a simplified model consisting of model fragments would be: *biomineralisation>framework> composite >lattice > cellular> discoidal >2 surfaces> annular>growth*. The

model fragments <composite> can be removed to further simplify the model while retaining a causal ordering towards most of the tasks. I could remove the fragment <cellular> without compromising causality because per se its removal does not dissociate parts <walls and chambers> nor is cellularity necessary in the causal ordering towards most of the tasks; model fragments <lattice> and <framework> are also associated with those parts and in a causal ordering can be substitutes for cellularity. Similarly, <lattice> could be removed. If I chose to remove the model fragment <framework>, by considering its redundancy with the model fragment <lattice> I would be dissociating the part <microtubules> and disrupting causality for a number of critical tasks. Similarly, <annularity> is necessary for the critical growth task. Note that biomineralisation is retained as a model fragment to represent a biotic-driven (i.e. with any biological intervention) crystalline (inorganic parts) assembly process rather than represent a solely abiotic self-assembly as a causality to any of the tasks or to the architecture. The model would be a subset of these fragments. Note that the subject of the original question fragment <phyllotactic pattern> is missing although the notion exists that it is causal to several tasks. The effect of its inclusion as a model fragment is also illustrated in a resultant model (model 3).

3.10.1.1 Model 1

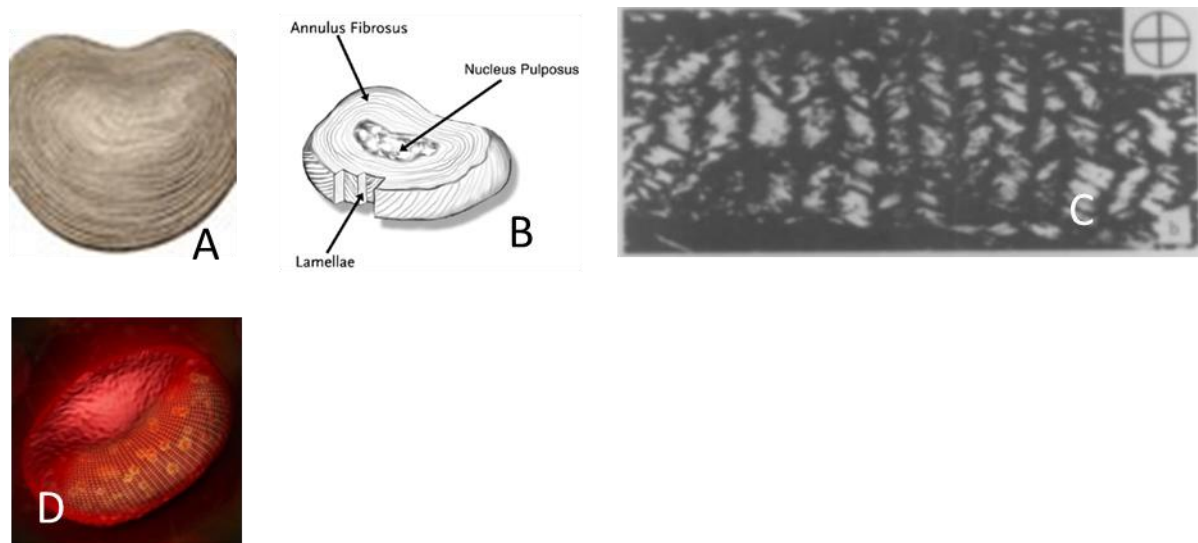


Figure 85 Structure of vertebrate disc.

A: Plan view; B: Orthogonal; C: Optical microscope cross-section through lamellae; D: Discoidal red blood cell.
Source: http://www.anatomyexpert.com/structure_detail/15113/884/; Reproduced with permission (Cassidy, J.J., Hiltner, A., & Baer, E., 1989).

Applying the simplified causal model illustrated above and searching the possible space of models results in the finding of the invertebrate disc as a possible adequate model. The intervertebral disc is biomineralised, discoidal, has two surfaces and has a growth mode that is annular. It has a complex internal structure consisting of collagen fibres organised in a hierarchical form in which the fibres are oriented in an angular opposite direction in layers (Figure 85C). An established, specialised functional value of the architecture of the inter-

vertebral disc is its response to compressive and flexural mechanical loads (Cassidy, J.J. et al., 1989).

If I remove substitute fragment <biomineralisation> to exclude the crystalline part and include organic lining as a part we could start with fragment <cell> and <organic> <discoidal> driving the process towards <diffusion> or <surface area-volume> as an end task. Another interesting biological model can be harvested: the red blood cell. The biconcave discoidal shape of the red blood cell has been shown to be related to geometries that have least bending energies and for large surface area to volume ratios (Canham, P.B., 1970).

3.10.1.2 Model 2

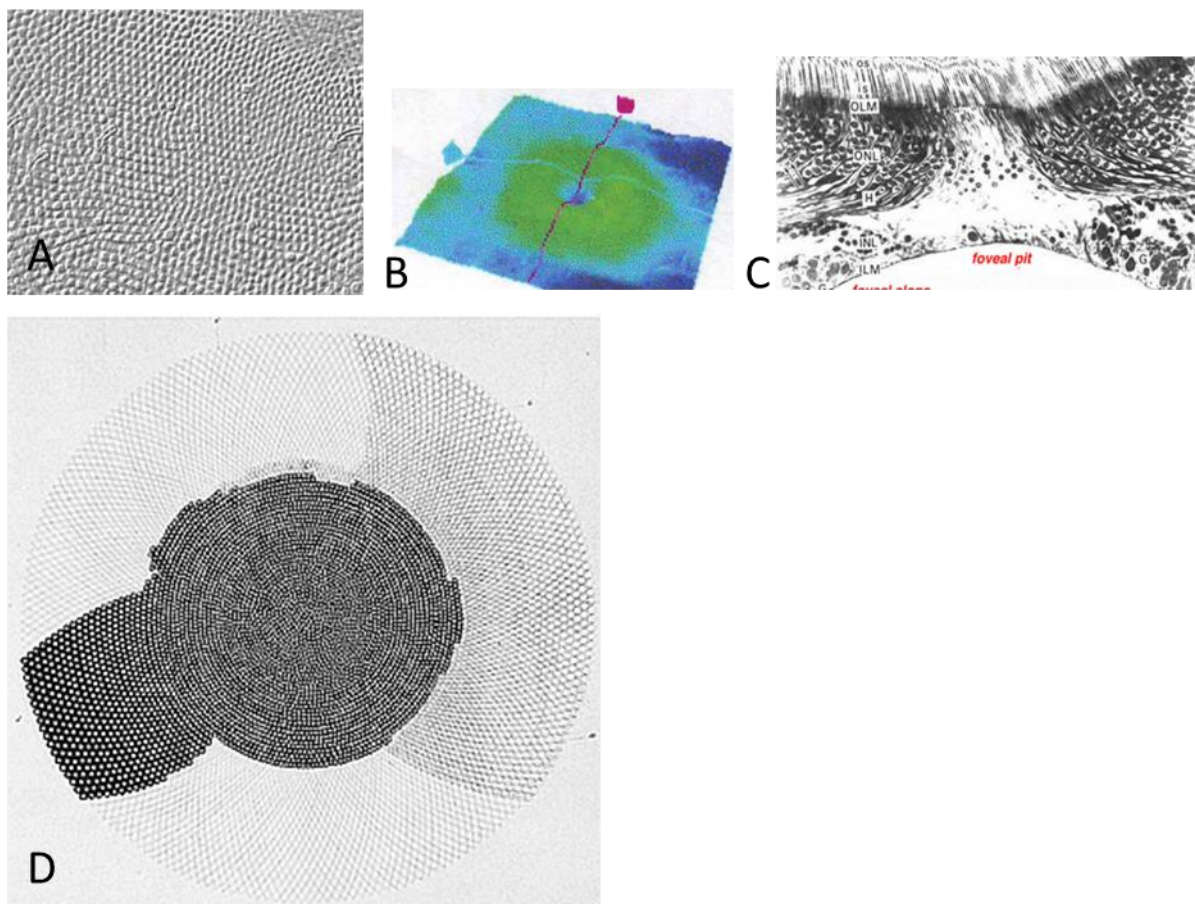


Figure 86 Fovea and fovea centralis of the human eye.

Source: A) Surface view (From Ahnelt et al 1987) B) 3D view (From Snodderly et al 1992) C) Cross-sectional schematic view of rods-cones ganglion receptors in the foveal region (From Yamada 1969)- <http://faculty.washington.edu/chudler/fovea.gif> D) Schematic of the surface showing phyllotactic pattern (from Schultz (1866, *Arch. mikr. Anat*, 2, 175 "The mosaic of the cones in the fovea centralis of human retina").

If model fragments: tessellated> phyllotactic> cellular> rod-like>discoidal 2 surfaces> annular>packing> light transmission are used to search for models of architectures an interesting optical model is identified. This model can be simplified further by eliminating <cellular> and <discoidal 2 surfaces> while retaining the ordering and notion of causality for the end task

<light>The fovea centralis of the human retina has an architecture in which the 3D, equatorial, surficial and XY plane cross-sectional organization of microstructures is strikingly similar to the architecture of the test of *Marginopora sp.* (Figure 86). The surface appears as tiled polyhedral forms packed in hexagonal groups, which are cones of the fovea. The form of the foveal region in 3D is a disc-like structure that is sloped towards the centre. The internal structures (namely the vertically oriented cones and bulbous ganglion) are packed radially. In Figure 86D is shown a schematic of the surface of the fovea centralis in which the high magnification view of fovea centralis and fovea in Figure 86A is made into a large scale mosaic. A mixed (whorled and spiral) phyllotactic pattern maybe discerned in the layout or organization or packing of the cones.

3.10.1.3 Model 3

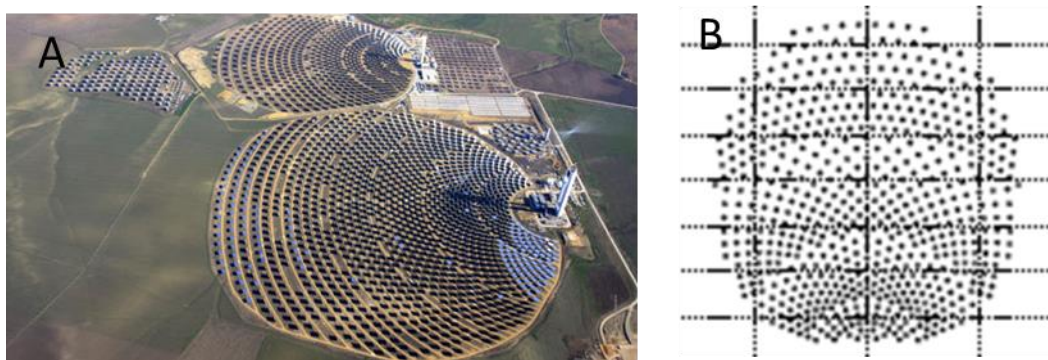


Figure 87 Heliostat layout (A) of polyhedral mirrors and (B) schematic of one type of simulated layout.

Source: <http://scitechdaily.com/natures-sunflower-may-help-increase-solar-efficiency-in-csp-plants/>

If the model fragments Lattice > tessellated> annular> phyllotactic> curvilinear> light are used for a search with a large parts library similar in form to those of *Marginopora sp.* another interesting optical model is identified. In this case, as the fragment <biomineralised> is not included, the model is abiotic or an artefact that has been designed and tested for a particular task-set. A heliostat field consists of highly polished mirrors which may be curved or flat and are usually polyhedral tessellated over a field with the objective of achieving packing efficiency in a disc-like area with a vacant area at the centre of the disc (as shown in Figure 87A). Usually, the central area is occupied by a thermal absorption tower. Various designs are tested and simulations performed for increased efficiencies in packing in a limited area (2D). However heliostats are also designed for sloping fields which adds a third dimension. In this case it has been shown that Fibonacci spiral phyllotactic arrangements provided the optimal efficiency while other spiral and whorled arrangements provide slightly lesser efficiencies (Noone, C.J., Torrilhon, M., & Mitsos, A., 2012) of packing of optical elements in the field and that the efficiencies are greater for a higher number of elements.

3.10.2 Discussion

The application of an adequate models process to the architecture of the test of *Marginopora sp.* resulted in the finding of at least three objects that are closely identifiable with the architecture of the test of *Marginopora sp.* The architectures of two biological structures and an artefact can be associated with the fragments and parts ordered causally towards the end-tasks of growth and

light transmission. The criticality of these end-tasks was presumed based upon a knowledge of the organism. The adequate models process was adopted as a rational effective technique to discover the adaptive value of the architecture of the test. A determination of the optimality of a structure for a function was not the objective. Rather, the aim was to primarily identify, associate function(s) and limit the set of functions best associated with the patterns that dominate the architecture of the test. A robust response to various mechanical loads, particularly bending loads, efficient packing (of structures in a volume or efficient utilisation of surface area and volume) and optical transmission are established functions of the adequate models obtained through the causal ordering of different fragments. The implication is that the bauplan of the test is strongly correlated with the established functions of the causal adequate models described in this section. These results narrow subsequent reasoning; they sharpen the direction in which experimental research should proceed to demonstrate or explicate the physical mechanisms associated with mechanical and optical functions of the test; further quantitative analysis can be guided.

But the adequate models obtained here are not the only possible findings of the application of the adequate model search method to the parts library shown in Table 10. Readers may harvest other models through using the adequate models method and a search of literature; however based on the knowledge of the test, the effort in this research found the three models described here to be the most adequate in parsimony and causality. Also, clearly the method does not provide that models correspond to the test in all the details of their functional aspects. For example, an important difference between the functionality of Model 3 and the test is that the phyllotactic arrangement of mirrored elements focuses light upon a central point in the heliostat whereas light is transmitted through the surface of the crystalline tiles arranged to chamberlets that are arranged as a phyllotactic pattern in the test.

Model 1, the inter-vertebral disc, indicates a correlation between the internal hierarchical chambered-walled discoidal structure and the structure of the test of *Marginopora* sp. But clearly, the test of *Marginopora* sp. does not sustain constant compressive and flexural loads as does the intervertebral disc in its position in the spinal column. However, model 1 suggests that taken as a whole the structural aspects are correlated. It is not clearly known what compressive mechanical loads the test of *Marginopora* sp. may be subjected to in its native state. The test is usually found fixed to rubble or seagrass on one surface by a cytoplasmic glue. Hydrodynamic loading would likely subject the adult test to mechanical flexural or bending stresses. The test of *Marginopora* sp. is mechanically robust; most of the test's structure survives the harsh hydrodynamic, mechanically abrasive sediment loading and high temperatures on tropical beaches. Mechanical properties of the inter-vertebral disc and the shape of the red blood cell, which is the other model derived from a different set of fragments while retaining fragment <discoidal>, relate to effectively counteracting bending loads. Again, a difference of detail is that the red blood cell has a lamellar membrane rather than a biomineralised structure; it is the peculiar shape that offers minimum bending stresses.

Similarly, the structure of the fovea centralis allows for a transmission of light and an efficient packing of optical rods; however the physical detail that incident light is focused upon the surface of the fovea by the eye's lens is not the primary factor under emphasis in the causality or parsimony of the model- the model considers light interaction or incidence upon the surface.

The crystalline lens-like (SWSch) tiles are likely light-scattering rather than light-focusing. The phyllotactic arrangement of efficient packing of optical elements in the discoidal form of the fovea is a structural aspect that is strikingly correlated. Further the structural arrangement of the rods in the fovea, i.e. an annular form, and in cross-sectional view the structural organisation of the rods and sensory microstructures is also strikingly similar to the arrangement observed in the test. Importantly, it is the packing and structural arrangement of optical elements that is revealed as a commonality. This point is emphasised again by the adequate Model 3. Model 3 is an engineered artefact with a desirable specification. That the phyllotactic pattern of organisation of elements allows for an optimal and close to optimal use of the limited space in a circular arrangement is the key aspect of this model. In heliostats the mirrors are optical elements but they differ, as do the rods in the fovea, in their optical function from the crystalline surface and annular walls of the test. Evidently the test walls are not valuable as reflectors focused on a central spot at some distance. Yet, the test walls likely do serve to reflect light; *Marginopora* sp.'s habitat is tropical shallow water.

A device model would be represented by a set of fragments that would describe all the phenomena in the object or system, i.e. the test. This is an intractable problem in the instance of the test of *Marginopora* sp. and probably of most biological objects. This means that any model will not be complete. Another limitation of this method is that it presupposes knowledge of the structure, i.e. it is context dependent. Also, limitations related to the selection of fragments are intrinsic to the modelling process. In other words, deciding what phenomena or end task to model; deciding how to model the chosen phenomena by selection suitable fragments; and satisfying structure or domain constraints. An objective of this method used in AI is to automate the search for models; in this work the search was not automated. Another important limitation is that adequate causal models are usually employed in engineering domains for which several quantitative physical relationships are known through equations e.g. $V=I.R$ (V =voltage, I =current, R =resistance) for a basic electrical device; these are largely unknown for the test of *Marginopora* sp.

However, the causal adequate model is precisely that- an abstraction that is an approximation -it leads to a reasoned rapid simple causal result. The method's limitations are not fatal despite a lack of quantitative causal physical relationships in its application to the finding of an adaptive value of the architecture of the test: the mechanical and optical (lens-like) functions of the tests of large symbiotic foraminifera have been proposed for several decades. However the close-packing functional value and the mechanical value of the phyllotactic pattern has not been related to this architecture. The model fragments do not contradict each other; they refine reasoning and qualitatively articulate in novel ways specific morphologic features or architecture in causal relationships with phenomena of the test.

CHAPTER 4: Conclusions and Outlook

4.1 Summary of Results

The general hypothesis of this research “if the architecture of the test is analysed at multiple scales and dimensions then its structural adaptive value can be inferred through appropriate models” has been tested. The objectives and contributions of this research were:

- to apply a non-invasive method; X-ray microcomputed tomography (X-ray MCT), for characterising in 3D the architecture and the microstructures of the test of an extant, large benthic biomineralised foraminifera – *Marginopora* sp.;

- to complement it with 2D electron microscopy to fully characterise the hierarchy of the architecture at different scales of measurement particularly at the nanoscale;

An analytical approach based upon combining optical, polarizing, and high resolution electron microscopy, and X-ray MCT, to evaluate a well-studied topic has yielded new findings. This research showed that at higher resolutions and magnification of microscopy than have been applied to the test of *Marginopora* sp. the observed constructional sub-units of the calcitic test are nanostructures. These appear to be spherical and colloidal. These were not identified in previous research. Several nano-scale features including inclusions, intra-crystal porosity, varying morphology, 2-10nm sized nanoparticles and organic material were visualized; the dimensions of the crystalline units were quantified in detail for the first time. The nanostructures and crystalline units and their association were introduced as evidence for possible biomineralisation pathways. Importantly, the random-orientation of crystals of the test that has been reported so far has been shown to be an incomplete observation; there are identifiable repeated local arrangements of crystals. This study has demonstrated that the nano-to-macro scale architecture of the test has an overall hierarchical pattern that has not been visualized, identified or analysed in previous research. For the test of *Marginopora* sp., that hierarchical structural pattern and its mechanical adaptive value in the particular architecture of the test was explained in the context of established theory of mechanical structures and other biomineralised structures. A hierarchy of processes was proposed for the organisation and movement of microtubules in the biomineralisation and assembly of the structures of the test. These contributions add significant new knowledge and thought to an understanding of the structural organisation of the test of *Marginopora* sp. A fresh approach using the context of the material sciences has been introduced for the study of the biomineralised tests of foraminifera. Moreover, this context advances linkages with the organisation, material properties and adaptive value of other biomineralised structures.

It was shown that Focused Ion Beam SEM could be effectively used as a technique to precisely observe in very high resolution the desired interior features of biomineralised calcitic tests; and that it could offer an alternative precise and robust technique to prepare specimens for observation with TEM. Further morphological features could be visualized and quantitatively

characterized at micrometre and sub-micrometre resolution in 3D using X-ray MCT in ways not possible with other techniques currently in use. Geometric properties of the lateral chamberlet microstructures were precisely quantified; approximating geometric models which have been historically used as substitutes were not necessary. Indeed, differences in the results obtained by the use of approximating models and the X-ray MCT data based models can be evaluated. This work demonstrated the potential use of X-ray MCT data in future research for biometric evaluations of tests; for evaluating the distribution of density; and its relationship to calcification and to the mechanical properties of the test. X-ray MCT was shown to be a feasible non-destructive method to characterise the porosity of the foraminifera test and shown to be a viable method of evaluating the distribution statistics of the porosity of the tests of foraminifera. Visualizations in 3D, including for the first time, a 3D print-build model of the test were created; these provided an intuitive grasp of the architecture of the complex interior of the test. The practise of sectioning of tests to make thin-sections followed by viewing with electron microscopes and the Hottinger technique which have been used during the past 30 years can be replaced imminently by in-situ sectioning and viewing and by non-invasive 3D viewing and analysis techniques. The highly realistic structural models facilitate meaningful numerical modelling and investigation of the mechanical and hydrodynamic properties of the test. These results contribute towards the adoption of advanced techniques that offer numerous advantages over the existing techniques.

-to analyse the 2D and 3D data sets to create novel holistic visualisations of the structural patterns and architecture of the test through ontogeny;

Networks analysis and visualization techniques were applied for the first time to the test of a foraminifera. It was shown that the internal interconnected tubular and chamber system could be represented and understood in the context of graph theory. An innovative visualization in 3D was used to show as a grid system the complete internal network of the test. Although it is topic that is researched for hundreds of years, a phyllotactic 3D pattern has not previously been identified in an existing biotic, non-plant self-assembled biomineralised structure; in this research it was shown to exist in the test of *Marginopora sp.* through its ontogeny. In studies in the literature the morphogenetic structural patterns visualized in this research have been shown to occur in different self-assembled biological systems and abiotic systems. The observed occurrence of phyllotactic patterns and the hierarchical structural arrangement of the test together persuasively indicate the mechanical adaptive value of the architecture of the test. Through using the adequate model method a net-cast for models yields a specialised optical biological object and an artefact that is so designed only with a specific function and has a computed structural plan that is similar to the 2D structural plan of the test. It indicates a specialized optical adaptive value of the bauplan of the biological system.

-to develop potential applications based upon the patterns and the architecture of the test (See section 4.3)

4.1.1 Role of Visualization

This research has relied considerably upon microscopy-based images, visualization in 2D and 3D and image analysis. Several of these images and visualizations of nanostructures and microstructures are striking. Some offer an unmatched realism and others an abstraction across

several scales of measurement of the 3D object under study. These have a scientific and an aesthetic value. Far more in scientific endeavour than “just pretty pictures”, visualization is basic to the understanding of our world. It has played a dominant role in the historic development of scientific thought and discovery, mathematical elucidation and in artistic effort (Brisson, H.E., 1992). As Henry David Thoreau framed it, “the question is not what you look at, but what you see.”

4.2 Future research

Perhaps the most pressing research related to this thesis is a formal description of the species of *Marginopora* sp. studied here: likely outcomes are a new species or an affinity to a species that is recently being described. In addition to the notes made in earlier sections which pointed out possibilities for future investigations, there are several lines of research that follow from the work in this thesis.

4.2.1 Biomineralisation

The elucidation of the structure of the CCNs identified in this research in the earliest and reproductive stages of the test is of great interest to the study of biomineralisation pathways in different phyla. Research of pristine specimens of other large soritid and large benthic foraminifera through ontogeny that investigates the initiation and morphology of crystals would strengthen the approach towards determining the presence of Amorphous calcium carbonate (ACC) in the pathways of biomineralisation of tests of foraminifera. If the CCNs are not ACC then what is peculiar about the biomineralisation pathways in foraminifera that precludes the formation of ACC either as a precursor or as a constituent of the tests compared to the biomineralisation pathways of structures in other phyla? Do the adaptive requirements of foraminiferal tests forestall the formation of ACC because it would lend undesirable properties to the test, or is ACC a stage that is inefficient in the eukaryotic cell's pathway for the crystallization of tests?

4.2.2 Role of microtubules

Microtubules are likely the most fascinating and critical movers and shakers of the universe of the foraminiferal cell and of the formation of the biomineralised test. The role of microtubules can be likened to that of a primary implementing machine-tool-equipment-assembly in the construction of the test based upon genetic instructions and a cellular response to environmental parameters. Advanced high resolution video microscopy of the microtubule network and 3D images obtained by TEM and electron tomography and by cryo-TEM of the structure of microtubules at different stages of ontogeny could reveal details of the mechanisms of transport of minerals in vesicles and to the mineralisation site, the formation of organic lining templates, the possible templating by microtubules of symmetrical modules of the to-be-biomineralised crystalline test that mimic the nano-crystalline structure of calcite and phylloctactic macro-mineralised architecture of the test and the characteristics of the networks that are the precursor and facilitator frameworks for the self-assembly and self-repair of the test through biomineralisation. Each of these cellular processes may be shared in biomineralised systems.

4.2.3 Role of the proloculus

In the formation of the crystalline structure the role of the proloculus appears to have been given scarce attention. However the prolocular assembly is the initial cellular container and partially calcified test. Its shape changes and it remains the single largest void in the test in which the cytoplasm resides. Its biochemistry has not been described in the research literature; does it differ from that of the organic linings? How does it change through ontogeny and in response to environmental changes? How is linked to the biomineralisation of the test?

4.2.4 *Marginopora sp.* and Homology

The genes associated with signalling and with very early development and organisation of the body are largely the same throughout the animal kingdom and have close relatives in plants. Can the entire DNA sequence of *Marginopora* be made available? If so, is there any knowledge or indication of genes or transcription factors associated with the formation or control of the crystalline architecture? Would it be possible to identify or associate with *Marginopora sp.* a transcription factor similar in function to PAX-6 or Bellringer (BLR) that is associated with light sensing or proteins similar to proteins such as pinformed PIN -the auxin transporter associated with phyllotactic patterns in plants? It's interesting to note that the genes associated with signalling and very early development and organisation of the body are largely the same throughout the animal kingdom and have close relatives in plants. These inquiries may shed light on the development of the phyllotactic pattern in the architecture of the test and its evolutionary links. These links could provide further indications of the adaptive value of the architecture of the tests and the deep homology associated with the evolution of these patterns.

4.2.5 Structure and X-ray MCT

A nano to micrometre scale X-ray computed tomography 3D volume rendering and 3D quantification of the features of the surface of the test would be most interesting. The surface of the test, as it is exposed to the marine environment, to incident light and its transmission to the symbionts, evidently would be under different environmental pressures than the inner walls. Its structure is different. A high resolution 3D evaluation of its structure across the test's dimensions would contribute to a clarification of its adaptive value and specialisation. Similar studies of large benthic symbiotic and a-symbiotic tests of foraminifera of different architectures would allow for a rigorous approach to this topic.

4.2.6 Mechanical Studies

The next step towards a greater understanding of the mechanical value of the architecture of the test would be to investigate using Finite Element Analysis (FEA) the performance of the skeletal structure, i.e. the spiral structure and cellular structure elucidated in this work. Simplified models of structures that are normally used can be replaced by the 3D X-ray MCT derived data that represent the actual architecture of the test. Computing resources that can accommodate the large data sets and enormous operations to manage the analyses using FEA software would be necessary; in this research attempts to conduct FEA of the test using *SolidWorks* software were unsuccessful due to a lack of such resources. The FEA would be quasi-experimental studies that could powerfully demonstrate the mechanical adaptive value of the architectures and be used to test related hypotheses about tests with different architectures.

4.2.7 Microfluidics

How does a spirally arranged grid-like tubular structure interact with linear microtubules and cytoplasmic fluid flow? Is the movement of cytoplasm within the test and the outer surface dependent on the structure and sizes of the outer pores and the diameters of the canals of the test as the cytoplasm has to retract very rapidly? The test could serve as a model of flow in which a large volume of fluid undergoes a rapid intake through multiple intake ports at the periphery of a discoidal structure. Computational fluid dynamics (CFD) studies of this structure-

flow interaction could be interesting and open a portal into comparative studies of different test architectures.

4.2.8 Optical studies

As shown in this work the bauplan of the test of *Marginopora sp.* indicates an optical function, but it is the structure of the test's walls and the morphology of the surface lateral chamberlets that intrigue. The optical properties of scattering and transmission and diffusion of light through the test and its effects on symbionts related to the structure of the test surface and walls is an open topic for research; comparable efforts have been initiated with coralline algae and skeletons (Enriquez, S., Mendez, E.R., & Iglesias-Prieto, R., 2005). An understanding of the optical properties of a single surface tile of the surface chamberlets and the organic lining are essential to understanding the advanced optical performance of the architecture of the test. The nano-scale effects of the crystalline structures and the effects of the arrangements of the crystalline calcite rod-like structures further add complexity to research of the optical properties of the test. The presence or absence of symbionts and effects on absorption of UV-light that could harm shallow-water foraminifera is also a related topic for research; coral skeletons have been investigated in this regard (Levy, O., Dubinsky, Z., & Achituv, Y., 2003).

4.3 Outlook: Biomimetic Applications

The test has a complex architecture in a hierarchical structural arrangement that has several microstructures comprised of basic building units that are organic-inorganic composites self-assembled by biomineralisation from elemental constituents; the test is a host to symbionts and is an interface with the marine environment. This natural self-contained system offers an opportunity to abstract principles and processes that can be used further for engineering and synthesizing object structures and processes. The study of natural systems from a biomimetic perspective and the use of biomimicry and bioinspiration by researchers to create new materials has developed rapidly during the past decade. Biological composite materials, in particular, have been studied with the view to understanding their structure and the processes by which the structures are assembled. A characterization of the natural system leads to an understanding of the principles of construction through the nano-macro scales. This research suggests several potential biomimetic applications of the test of *Marginopora sp.*; a few applications open up areas of science-engineering research while others may be inspiration for design.

4.3.1 Overall architecture

The mechanical and optical adaptive value of the architecture and the phyllotactic pattern can be adapted to the architecture of large structures such as underwater hotels or large museums or of an industrial or university large central building complex. The space structures that are composed of three members without joints such that the geometrical configuration allows a 3D balance of compression-tension can be inspiring for a structural framework; while the distribution of void space and the interconnectivity in 3D present a template of space utilisation within a discoidal structure. The modularity of construction, i.e. seamless annular addition of volume and structure, and numerous entry and exit portals at the periphery with robust

communication-transport networks within the structure presents another important feature for such large architectures. These could be also inspiring or offer biomimicry principles for construction of space habitats and transportation systems. Organic linings in the test and their possible functionalities such as light wavelength transformation, permeable or impermeable barriers, extensions, and mechanical robustness add to the possibilities for combining with the hard structural elements of the large-scale architecture. An inherent simplicity of construction enabled by the use of only a few geometric units of construction to create a vast complex curvilinear structure is another area of abstraction of principle suggested in the architecture of the test.

4.3.2 Arches

The two surfaces of the test are composed of arches which are exaggerated in the reproductive stages of the test. These exaggerated arches are constructed of linear crystalline units. The geometry of these arches often achieves a hyperbolic paraboloid structure such that convex-concave saddle-shaped structures are formed. Felix Candela, a 20th century master architect and builder of Moorish Mexican origin, in some of his buildings, constructed arches with similar geometries. However, in the test of *Marginopora* sp. these arches are seamlessly integrated with each other and with a flatter large discoidal structure.

4.3.3 Assembly and Delivery process

The microtubular processes of framework assembly prior to creating a hard structure that is laid at the site provide possible models for assembly of lightweight scaffolding and removal of scaffolding and replacement at adjacent sites in a complex repeated architectural pattern. Similarly, an elucidation of the entire hierarchical process referred to in this research, in which microtubules transport materials for calcification at site and also transport materials internally and externally of the test through linear extensions in parallel directions in 3D offers an interesting model of transport of materials within a large constructional site. That there is a central possible control site- the prolocular region- within the entire architecture offers another model for a centralised store and distribution of material and processes within a 3D discoidal architecture.

4.3.4 Functional structures

Although the lateral chamberlets' morphologies are aesthetically unremarkable, they are fascinating microstructures of the test. Symbionts packed within the chamberlets and a position at the surface of the test evidently indicate the optical role of the chamberlets. A complete connectivity with the remainder of the chamberlets in the test in which symbionts remain viable, fluids can circulate and an optical path is maintained offers a model for photobioreactors in which algae can be cultivated. The complete discoidal architecture also offers a large surface area and volume. It piques the interest that the *Symbionidium* sp. dinoflagellate, the dominant symbiont in the test, contains one of the highest fatty acid and sterol compositions of five marine dinoflagellates (Mansour, M.P., Volkman, J.K., Jackson, A.E., & Blackburn, S.I., 1999). Detailed comparative design considerations for photobioreactors and the design requirements of the symbiont-foram relationship and materials efficient test construction for high productivity are starting points for such a biomimetic model.

Structural patterns arising from curvilinear arcs in 3D within a disc resulting in a robust structure that survives the dynamic coastal environment in which tests are rolled continuously but are not easily fragmented after diagenesis suggest a mechanical advantage. Wall-less tires are one possible application of this structure which incorporate the phyllotactic structural arrangement using hard rubber arc-elements in a disc of which the periphery is rounded. Mitsubishi Corp has experimented with a similar design for wall-less tires but it is probably not as robust.

Foramina and pores along the marginal chord of the test tend to be circular early in ontogeny but at mature and reproductive stages when the test is large these tend to be elliptical or appear as convoluted ellipses and have elevated lip-like peripheries. Anastomosing crystalline band-like structures occur between pores. These possibly offer stress-dissipating mechanisms in an arrangement of elliptical-stiff-compliant microstructures. Such arrangements may have applications in light-weight structures in which openings or holes exist through which fuel lines, cables etc. are connected e.g. in airplanes, or holes in which some resilience is a desirable property, e.g. in fixtures for rigging.

4.3.5 Ceramic Materials and Shells

The test of *Marginopora sp.* could be categorised as a biocomposite with mechanical properties similar to ceramics and a distribution of macroporosity often desirable in ceramic materials for current applications such as roof tiles, technical ceramics used in medicine and automobile engines or in wastewater filtration. Of several manufacturing processes for ceramics a direct foaming method has parallels to the process of biomineralisation observed in the test of *Marginopora sp.* Both processes result in a macroporous material with dense walls. The test of *Marginopora sp.* in bulk quantities could be used for secondary filtration of wastewater. It could also be used as packed filler ceramic material in instances where packed ceramics particulate filtration e.g. for diesel particulates, which require moderate to high strength in order to resist sustained vibration. The discoidal, thickened, bi-concave shape of the test is also a better stress dissipator when subject to von Mises stresses than a flat uniform discoidal shape (Song, Y. et al., 1994); this implies that load bearing ceramic discs could be redesigned if the applications allow for it. Macroporosity and transport mechanisms of minerals are also key issues in bone-growth research. The test offers biomimetic models for this area of research. Perhaps the largest portal of relevant biomimetic research is the field of encapsulated shells: fabrication strategies for hydrogel matrix shells, sol-gel shells, polymeric shells, and induced mineral shells have seen rapid increase in research for cell implant protection, cell separation, biosensors, cell therapy and tissue engineering. *Marginopora sp.*, a successful eukaryotic foraminifera with one of the largest known tests that encapsulates one of the largest single cells, offers an appropriate model for cell encapsulation.

Lastly, the entire test, remodelled at a scale of several tens of metres could serve as a ceramic sculpture, a hyperfigure, or geometric sculpture in which the network of tubular canals and chamberlets could serve as an internal playground. The upper surface could be of translucent-transparent material. The interior could be illuminated with LEDs affixed along the network of canals. The lower surface of the sculpture could be mirrored. Multiple entries and exits could be assigned to the peripheral pore-like portals. The sculpture could be modelled in 3D and assembled in modules.

Bibliography

- Addadi L., Raz, S., & Weiner, S. (2003). Taking Advantage of Disorder: Amorphous Calcium Carbonate and Its Roles in Biomineralization. *Advanced Materials*, 15(12), 959-970. doi: 10.1002/adma.200300381
- Addadi L., & Weiner, S. (1997). Biomineralization: A pavement of pearl. *Nature*, 389(6654), 912-915.
- Aizenberg J., Sundar, V. C., Yablon, A. D., Weaver, J. C., & Chen, G. (2004). Biological glass fibers: Correlation between optical and structural properties (Vol. 101, pp. 3358-3363).
- Aizenberg J., Tkachenko, A., Weiner, S., Addadi, L., & Hendler, G. (2001). Calcitic microlenses as part of the photoreceptor system in brittlestars (Vol. 412, pp. 819-822): N.
- Aizenberg J., Weaver, J. C., Thanawala, M. S., Sundar, V. C., Morse, D. E., & Fratzl, P. (2005). Skeleton of Euplectella sp.: Structural Hierarchy from the Nanoscale to the Macroscale. *Science*, 309(5732), 275-278. doi: 10.1126/science.1112255
- Alberch P., Gould, S. J., Oster, G. F., & Wake, D. B. (1979). Size and Shape in Ontogeny and Phylogeny. *Paleobiology*, 5(3), 296-317.
- Alberich-Bayarri A., Moratal, D., Escobar Ivirico, J. L., Rodriguez Hernandez, J. C., Valles-Lluch, A., Marti-Bonmati, L., . . . Salmeron-Sanchez, M. (2009). Microcomputed tomography and microfinite element modeling for evaluating polymer scaffolds architecture and their mechanical properties. *Journal of Biomedical Materials Research - Part B Applied Biomaterials*, 91(1), 191-202.
- Alessandro L K. (1990). Hierarchical processes in biological systems. *Mathematical and Computer Modelling*, 14(0), 674-679.
- Amarel S. (1968). On representations of problems of reasoning about actions. *Machine intelligence*, 3(3), 131-171.
- Anderson O., Allan R., Be W.H. (1978). *Recent advances in foraminiferal fine structure research* (Vol. 3). New York: Academic Press.
- Andres M. S., & Pamela Reid, R. (2006). Growth morphologies of modern marine stromatolites: A case study from Highborne Cay, Bahamas. *Sedimentary Geology*, 185(3-4), 319-328.
- Angell R. W. (1980). Test morphogenesis (chamber formation) in the foraminifer Spiroloculina hyalina Schulze. *The Journal of Foraminiferal Research*, 10(2), 89-101. doi: 10.2113/gsjfr.10.2.89
- Arnold Z. M. (1964). Biological observations of the foraminifer Spiroloculina hyalina schulze. *Univ. Cal. Publ. Zoo.*, 72, 1-78.
- Arnold Z. M. (1974). Field and Laboratory Techniques for the Study of Living Foraminifera. In R. H. a. A. Hedley, C.G. (Ed.), *Foraminifera* (Vol. 1, pp. 154-206). London: Academic Press.
- Arwin H. (2000). Ellipsometry on thin organic layers of biological interest: characterization and applications. *Thin Solid Films*, 377-378, 48-56.
- Aurenhammer F. (1991). Voronoi diagrams—a survey of a fundamental geometric data structure. *ACM Computing Surveys (CSUR)*, 23(3), 345-405.
- Bachman R. T. (1984). Intratest porosity in foraminifera. *Journal of Sedimentary Research*, 54(1), 257-262.
- Bar-Cohen Y. (2006). Biomimetics- using nature to inspire human innovation. *Bioinsp. Biomim.* (2006), 1, 1-12.
- Barabasi A.-L., & Oltvai, Z. N. (2004). Network biology: understanding the cell's functional organization. *Nat Rev Genet*, 5(2), 101-113.
- Barabe D. a. J., R. (Ed.). (1998). *Symmetry in Plants*. Singapore: World Scientific Publishing.

- Barna Á., Pécz, B., & Menyhard, M. (1999). TEM sample preparation by ion milling/amorphization. *Micron*, 30(3), 267-276. doi: [http://dx.doi.org/10.1016/S0968-4328\(99\)00011-6](http://dx.doi.org/10.1016/S0968-4328(99)00011-6)
- Bassett G. A., Menter, J. W., & Pashley, D. W. (1958). Moire Patterns on Electron Micrographs, and their Application to the Study of Dislocations in Metals. *Proceedings of the Royal Society of London. Series A. Mathematical and Physical Sciences*, 246(1246), 345-368. doi: 10.1098/rspa.1958.0144
- Bathurst R. G. C. (1974). Marine Diagenesis of Shallow Water Calcium Carbonate Sediments. *Annual Review of Earth and Planetary Sciences*, 2, 257. doi: 10.1146/annurev.ea.02.050174.001353
- Be A. W., Hemleben, C., Anderson, O. R., & Spindler, M. (1979). Chamber formation in planktonic foraminifera. *Micropaleontology*, 25(3), 294-307.
- Bejan A., Lorente, S., & Wang, K. M. (2006). Networks of channels for self-healing composite materials. *Journal of Applied Physics*, 100(3), 033528-033528-033526.
- Bender H., & Hemleben, C. (1988). Constructional aspects in test formation of some agglutinated foraminifera. *Abhandlungen der Geologischen Bundesanstalt*, 41, 13-12.
- Beniash E., Aizenberg J., Addadi, L., Weiner S. (1997). Amorphous calcium carbonate transforms into calcite during sea-urchin larval spicule growth. *Proc. R. Soc. Lond. Ser. B*, 264, 461.
- Beniash E., Metzler R., Lam R., Gilbert P. (2009). Transient amorphous calcium phosphate in forming enamel. *J. Struct. Biol.*, 166, 133.
- Bentov S., Brownlee, C., & Erez, J. (2009). The role of seawater endocytosis in the biomineralization process in calcareous foraminifera. *Proceedings of the National Academy of Sciences*, 106(51), 21500-21504. doi: 10.1073/pnas.0906636106
- Bentov S., & Erez, J. (2005). Novel observations on biomineralization processes in foraminifera and implications for Mg/Ca ratio in the shells. *Geology*, 33(11), 841-844. doi: 10.1130/g21800.1
- Berthold W. U. (1976). Biomineralisation bei milioliden Foraminiferen und die Matritzen-Hypothese. *Naturwissenschaften*, 63(4), 196-197. doi: 10.1007/BF00624226
- Boltovskoy E., Scott, D., & Medioli, F. (1991). Morphological variations of benthic foraminiferal tests in response to changes in ecological parameters: a review. *Journal of Paleontology*, 65(2), 175-185.
- Borah B., Gross, G. J., Dufresne T. E., Smith T. S., Cockman M. D., Chmielewski P.A., Sod E. W. (2001). Three-dimensional microimaging (MR μ l and μ CT), finite element modeling, and rapid prototyping provide unique insights into bone architecture in osteoporosis. *Anatomical Record*, 265(2), 101-110.
- Borkin M. A., Vo, A. A., Bylinskii, Z., Isola, P., Sunkavalli, S., Oliva, A., & Pfister, H. (2013). What Makes a Visualization Memorable? *Visualization and Computer Graphics, IEEE Transactions on*, 19(12), 2306-2315. doi: 10.1109/TVCG.2013.234
- Bostock H. C., Hayward, B. W., Neil, H. L., Currie, K. I., & Dunbar, G. B. (2011). Deep-water carbonate concentrations in the southwest Pacific. *Deep Sea Research Part I: Oceanographic Research Papers*, 58(1), 72-85.
- Bowser S. S., & Travis, J. L. (2000). Methods for Structural Studies of Reticulopodia, the Vital Foraminiferal "Soft Part". *Micropaleontology*, 46, 47-56.
- Braithwaite C. J., Taylor, J. D., Kennedy, W. J. (1973). The Evolution of an Atoll: The Depositional and Erosional History of Aldabra *Philosophical Transactions of the Royal Society of London. Series B, Biological Sciences*, Vol. 266(No. 878).
- Branson O., Redfern, S. A., Tyliszczak, T., Sadekov, A., Langer, G., Kimoto, K., & Elderfield, H. (2013). The coordination of Mg in foraminiferal calcite. *Earth and Planetary Science Letters*, 383(0), 134-141. doi: <http://dx.doi.org/10.1016/j.epsl.2013.09.037>

- Brasier M. (1982). Architecture and evolution of the foraminiferid test-a theoretical approach. *Aspects of Micropalaeontology*, 1-41.
- Brasier M. (1982). Foraminiferid architectural history; a review using the MinLOC and PI methods. *Journal of Micropalaeontology*, 1, 95-105.
- Brasier M. (1986). Why Do Lower Plants and Animals Biomineralize? *Paleobiology*, 12(3), 241-250.
- Briguglio A., & Hohenegger, J. (2011a). How to react to shallow water hydrodynamics: The larger benthic foraminifera solution. *Marine Micropaleontology*, 81(1-2), 63-76.
- Briguglio A., & Hohenegger, J. (2011b). How to react to shallow water hydrodynamics: The larger benthic foraminifera solution. *Marine Micropaleontology*.
- Briguglio A., Hohenegger, J., & Less, G. (2013). Paleobiological Applications of Three-Dimensional Biometry on Larger Benthic Foraminifera: A New Route of Discoveries. *The Journal of Foraminiferal Research*, 43(1), 72-87. doi: 10.2113/gsjfr.43.1.72
- Briguglio A., Metscher, B., & Hohenegger, J. (2011). Growth Rate Biometric Quantification by X-ray Microtomography on Larger Benthic Foraminifera: Three-dimensional Measurements Push Nummulitids into the Fourth Dimension. *Turkish Journal of Earth Sciences (Turkish J. Earth Sci.)*, 20, 683-699.
- Brisson H. E. (1992). Visualization in Art and Science. *Leonardo*, 25(3/4), 257-262. doi: 10.2307/1575847
- Bryan W. H., & Hill, D. (1941). Spherulitic crystallization as a mechanism of skeletal growth in the hexacorals.
- Buzug T. M., Holz, D., Bongartz, J., Kohl-Bareis, M., Hartmann, U., Weber, S., . . . Seitz, H. (2007). Image Based Analysis of Bone Graft Samples made by 3D Printing Using Conventional and Synchrotron-Radiation-Based Micro-Computed Tomography *Advances in Medical Engineering* (Vol. 114, pp. 121-126): Springer Berlin Heidelberg.
- Canham P. B. (1970). The minimum energy of bending as a possible explanation of the biconcave shape of the human red blood cell. *Journal of Theoretical Biology*, 26(1), 61-81.
- Capowiez Y., Pierret, A., & Moran, C. (2003). Characterisation of the three-dimensional structure of earthworm burrow systems using image analysis and mathematical morphology. *Biology and Fertility of Soils*, 38(5), 301-310. doi: 10.1007/s00374-003-0647-9
- Carlson W. D., Rowe, T., Ketcham, R. A., & Colbert, M. W. (2003). Applications of high-resolution X-ray computed tomography in petrology, meteoritics and palaeontology. *Geological Society Special Publications*, 215, 7-22.
- Carpenter A. E., Jones, T. R., Lamprecht, M. R., Clarke, C., Kang, I. H., Friman, O., . . . Sabatini, D. M. (2006). CellProfiler: image analysis software for identifying and quantifying cell phenotypes. *Genome Biology*, 7, R100.
- Cassidy J. J., Hiltner, A., & Baer, E. (1989). Hierarchical structure of the intervertebral disc. *Connect Tissue Res*, 23(1), 75-88.
- Charvolin J. S., Jean-François. (2011). A Phyllotactic Approach to the Structure of Collagen Fibrils. *Soft Condensed Matter*.
- Chen M., Floridi, L. Borgo, R. (2013). What is visualization really for? *ArXiv.org*. <http://arxiv.org/abs/1305.5670>
- Choong K. K., Kim J. Y. (2013). Structural Behaviour of Single Layer Space Frame with Member Arrangement Following Spiral Phyllotaxis. *Advanced Materials Research*, 842, 505-511. doi: 10.4028/www.scientific.net/AMR.842.505
- Chua C., Teh, S., & Gay, R. (1999). Rapid prototyping versus virtual prototyping in product design and manufacturing. *The International Journal of Advanced Manufacturing Technology*, 15(8), 597-603. doi: 10.1007/s001700050107
- Cnudde V., Boone, M., Dewanckele, J., Dierick, M., Van Hoorebeke, L., & Jacobs, P. 3D characterization of sandstone by means of X-ray computed tomography. *Geosphere*, 7(1), 54-61. doi: 10.1130/ges00563.1

- Cnudde V., Masschaele, B., Dierick, M., Vlassenbroeck, J., Hoorebeke, L. V., & Jacobs, P. (2006). Recent progress in X-ray CT as a geosciences tool. *Applied Geochemistry*, 21(5), 826-832.
- Collen J. D., & Garton, D. W. (2004). Larger foraminifera and sedimentation around Fongafale Island, Funafuti Atoll, Tuvalu. *Coral Reefs*, 23(3), 445-454.
- Conger S. D., Green, H. W., & Lipps, J. H. (1977). Test ultrastructure of some calcareous Foraminifera. *The Journal of Foraminiferal Research*, 7(4), 278-296. doi: 10.2113/gsjfr.7.4.278
- Constandache M., Yerly, F., & Spezzaferri, S. (2013). Internal pore measurements on macroperforate planktonic Foraminifera as an alternative morphometric approach. *Swiss Journal of Geosciences*, 106(2), 179-186. doi: 10.1007/s00015-013-0134-8
- Cooke T. J. (2006). Do Fibonacci numbers reveal the involvement of geometrical imperatives or biological interactions in phyllotaxis? *Botanical Journal of the Linnean Society*, 150(1), 3-24.
- Culver S. J. (1991). Early Cambrian Foraminifera from West Africa. *Science*, 254(5032), 689-691. doi: 10.1126/science.254.5032.689
- Currey J. (1999). The design of mineralised hard tissues for their mechanical functions. *J. Exp. Biol.*, 202(23), 3285-3294.
- Currey J. D. (1982). Bone as a mechanical structure. *Journal of Biomechanics*, 15(10), 795-795.
- Currey J. D. (2010). Mechanical properties and adaptations of some less familiar bony tissues. *Journal of the Mechanical Behavior of Biomedical Materials*, In Press, Corrected Proof.
- Currey J. D. (2005). Hierarchies in Biomineral Structures. *Science*, 309(5732), 253-254.
- Currey J. D., Brear, K., & Zioupos, P. (1994). Dependence of mechanical properties on fibre angle in narwhal tusk, a highly oriented biological composite. *Journal of Biomechanics*, 27(7), 885-889, 891-897.
- Cushman J. A. (1959). *Foraminifera: their classification and economic use*. Harvard university press Cambridge, Massachusetts.
- de Nooijer L. J., Toyofuku, T., & Kitazato, H. (2009). Foraminifera promote calcification by elevating their intracellular pH. *Proceedings of the National Academy of Sciences*, 106(36), 15374-15378. doi: 10.1073/pnas.0904306106
- Debenay J. P., Guillou, J. J., Geslin, E., & Lesourd, M. (2000). Crystallization of Calcite in Foraminiferal Tests. *Micropaleontology*, 46, 87-94.
- Debenay J. P., Guillou, J. J., Geslin, E., Lesourd, M., & Redois, F. (1998). Processus de cristallisation de plaquettes rhomboédriques à la surface d'un test porcelané de foraminifère actuel. *Geobios*, 31(3), 295-302.
- Debenay J. P., Guillou, J. J., & Lesourd, M. (1996). Colloidal calcite in foraminiferal tests; crystallization and texture of the test. *The Journal of Foraminiferal Research*, 26(4), 277-288. doi: 10.2113/gsjfr.26.4.277
- Deshpande V. S., Ashby, M. F., & Fleck, N. A. (2001). Foam topology: bending versus stretching dominated architectures. *Acta Materialia*, 49(6), 1035-1040. doi: [http://dx.doi.org/10.1016/S1359-6454\(00\)00379-7](http://dx.doi.org/10.1016/S1359-6454(00)00379-7)
- Deutsch S. J., Green, H. W., & Lipps, J. H. (1973). Transmission electron microscopy studies of the wall structure of some calcareous foraminifera. *Abstracts with Programs - Geological Society of America*, 5(7), 597.
- Dewan R., Marinkovic, M., Noriega, R., Phadke, S., Salleo, A., & Knipp, D. (2009). Light trapping in thin-film silicon solar cells with submicron surface texture. *Opt. Express*, 17(25), 23058-23065.
- Dietrich D., Bäucker, E., & Marx, G. (2003). Preparing Silica Bodies for TEM on the Border of Material and Life Science. *Microscopy and Microanalysis*, 9(SupplementS03), 470-471.
- Douady S., & Couder, Y. (1992). Phyllotaxis as a physical self-organized growth process. *Physical Review Letters*, 68(13), 2098.
- Doube M., Klosowski M., Arganda-Carreras I., Cordelières F., Dougherty R., Jackson J., Schmid B., Hutchinson J., Shefelbine S. (2010). BoneJ: free and extensible bone image analysis in ImageJ. *Bone*, 47, 1076-1079. doi: 10.1016/j.bone.2010.08.023

- Elliott J. C., & Dover, S. D. (1982). X-ray microtomography. *Journal of Microscopy*, 126(2), 211-213. doi: 10.1111/j.1365-2818.1982.tb00376.x
- Enriquez S., Mendez, E. R., & Iglesias-Prieto, R. (2005). Multiple Scattering on Coral Skeletons Enhances Light Absorption by Symbiotic Algae. *Limnology and Oceanography*, 50(4), 1025-1032.
- Erez J. (2003). The Source of Ions for Biomineralization in Foraminifera and Their Implications for Paleoceanographic Proxies. *Reviews in Mineralogy and Geochemistry*, 54(1), 115-149. doi: 10.2113/0540115
- Erickson R. O. (1973). Tubular Packing of Spheres in Biological Fine Structure. *Science*, 181(4101), 705-716. doi: 10.1126/science.181.4101.705
- Fabienke W., Briguglio, A., & Hohenegger, J. (2012). *Volume quantification of Cyclochypus carpenteri by microCT investigation*. Paper presented at the EGU General Assembly Conference Abstracts.
- Feldkamp L., Davis, L., & Kress, J. (1984). Practical cone-beam algorithm. *JOSA A*, 1(6), 612-619.
- Feldkamp L. A., Goldstein, S. A., Parfitt, M. A., Jesion, G., & Kleerekoper, M. (1989). The direct examination of three - dimensional bone architecture in vitro by computed tomography. *Journal of bone and mineral research*, 4(1), 3-11.
- Fisher C. G., Sageman, B. B.,ASURE, S. E., Acker, B., & Mahar, Z. (2003). Planktic Foraminiferal Porosity Analysis as a Tool for Paleoceanographic Reconstruction, Mid-Cretaceous Western Interior Sea. *Palaaios [Palaaios]*, 18(1), 34-46. doi: 10.1043/0883-1351(2003)018
- Folk R. L., & Leo Lynch, F. (2001). Organic matter, putative nannobacteria and the formation of ooids and hardgrounds. *Sedimentology*, 48(2), 215-229. doi: 10.1046/j.1365-3091.2001.00354.x
- Fratzl P., & Weinkamer, R. (2007). Nature's hierarchical materials. *Progress in Materials Science*, 52(8), 1263-1334.
- Frerichs W. E., Heiman, M. E., Borgman, L. E., & Be, A. W. H. (1972). Latitudinal variations in planktonic foraminiferal test porosity; Part 1, Optical studies. *Journal of Foraminiferal Research*, 2(1), 6-13.
- Fu S. S., Tao, C., Prasad, M., Wilkens, R. H., & Frazer, L. N. (2004). Acoustic properties of coral sands, Waikiki, Hawaii. *The Journal of the Acoustical Society of America*, 115(5), 2013-2020.
- Gao H. (2006). Application of Fracture Mechanics Concepts to Hierarchical Biomechanics of Bone and Bone-like Materials. *International Journal of Fracture*, 138(1), 101-137.
- Gershon N., Abarbanel, R., Friedhoff, R. M., Langridge, R., Pearlman, J. D., & Star, J. L. (1993). *Is visualization REALLY necessary?: the role of visualization in science, engineering, and medicine*. Paper presented at the Proceedings of the 4th conference on Visualization '93, San Jose, California.
- Gibbins J. R., Tilney, L. G., & Porter, K. R. (1969). Microtubules in the Formation and Development of the Primary Mesenchyme In *Arbacia Punctulata*: I. The Distribution of Microtubules. *The Journal of Cell Biology*, 41(1), 201-226. doi: 10.1083/jcb.41.1.201
- Gibson L. J. (1989). Modelling the mechanical behavior of cellular materials. *Materials Science and Engineering: A*, 110(0), 1-36. doi: [http://dx.doi.org/10.1016/0921-5093\(89\)90154-8](http://dx.doi.org/10.1016/0921-5093(89)90154-8)
- Gibson L. J. (2005). Biomechanics of cellular solids. *Journal of Biomechanics*, 38(3), 377-399. doi: <http://dx.doi.org/10.1016/j.jbiomech.2004.09.027>
- Gilis M., Grauby, O., Willenz, P., Dubois, P., Heresanu, V., & Baronnet, A. (2013). Biomineralization in living hypercalcified demosponges: Toward a shared mechanism? *Journal of Structural Biology*, 183(3), 441-454. doi: <http://dx.doi.org/10.1016/j.jsb.2013.05.018>
- Glas M. S., Langer, G., & Keul, N. (2012). Calcification acidifies the microenvironment of a benthic foraminifer (*Ammonia* sp.). *Journal of Experimental Marine Biology and Ecology*, 424-425(0), 53-58. doi: <http://dx.doi.org/10.1016/j.jembe.2012.05.006>

- Goldstein S. T., & Richardson, E. A. (2002). Comparison of Test and Cell Body Ultrastructure in Three Modern Allogromiid Foraminifera: Application of High Pressure Freezing and Freeze Substitution. *The Journal of Foraminiferal Research*, 32(4), 375-383. doi: 10.2113/0320375
- Gower L. B. (2008). Biomimetic Model Systems for Investigating the Amorphous Precursor Pathway and Its Role in Biomineralization. *Chemical Reviews*, 108(11), 4551-4627. doi: 10.1021/cr800443h
- H. W. F. (2005). Developmental biology meets materials science: Morphogenesis of biomineralized structures. *Developmental Biology*, 280(1), 15-25.
- Habura A., Wegener, L., Travis, J. L., & Bowser, S. S. (2005). Structural and Functional Implications of an Unusual Foraminiferal β -Tubulin. *Molecular Biology and Evolution*, 22(10), 2000-2009. doi: 10.1093/molbev/msi190
- Hallock P. (1979). Trends in test shape with depth in large, symbiont-bearing foraminifera. *Journal of Foraminiferal Research*, 9(1), 61-69.
- Hallock P. (1985). Why are Larger Foraminifera Large? *Paleobiology*, 11(2), 195-208.
- Hallock P. (2003). Symbiont-bearing Foraminifera *Modern Foraminifera* (pp. 123-139).
- Hallock P. (2005). Global change and modern coral reefs; new opportunities to understand shallow-water carbonate depositional processes. *Sedimentary Geology*, 175(1-4), 19-33.
- Hallock P., & Anonymous. (1986). Musings on functional morphologies in larger foraminifera. *Proceedings - North American Paleontological Convention*, 4, A19.
- Hammel J. U., Filatov, M. V., Herzen, J., Beckmann, F., Kaandorp, J. A., & Nickel, M. (2011). The non-hierarchical, non-uniformly branching topology of a leuconoid sponge aquiferous system revealed by 3D reconstruction and morphometrics using corrosion casting and X-ray microtomography. *Acta Zoologica*, no-no. doi: 10.1111/j.1463-6395.2010.00492.x
- Hansen H. J. (2002). Shell construction in modern calcareous Foraminifera. In B. Sen Gupta (Ed.), *Modern Foraminifera* (pp. 57-102). Dordrecht, Netherlands: Kluwer Academic Publishers.
- Hay W. W., Towe, K. M., & Wright, R. C. (1963). Ultramicrostructure of Some Selected Foraminiferal Tests. *Micropaleontology*, 9(2), 171-195.
- Hayles M. F., Stokes, D. J., Phifer, D., & Findlay, K. C. (2007). A technique for improved focused ion beam milling of cryo-prepared life science specimens. *Journal of Microscopy*, 226(3), 263-269. doi: 10.1111/j.1365-2818.2007.01775.x
- Haynes J. (1965). Symbiosis, wall structure and habitat in Foraminifera. *Contributions from the Cushman Foundation for Foraminiferal Research*, 16, Part 1, 40-43.
- Hedley R. H. (1964). The biology of Foraminifera. *Int Rev Gen Exp Zool*, 1, 1-45.
- Hemleben C. (1990). The evolution and classification of wall structure in planktonic foraminifera. *Abstracts with Programs - Geological Society of America*, 22(7), 106.
- Hemleben C., Anderson, O., Berthold, W., Spindler, M. (1986). Calcification and chamber formation in Foraminifera-a brief overview. In B. R. Leadbeater, R. (Ed.), *Biomineralization in Lower Plants and Animals* (Vol. 30, pp. 237-248). New York: Oxford University Press.
- Hildebrand M. (2008). Diatoms, Biomineralization Processes, and Genomics. *Chemical Reviews*, 108(11), 4855-4874. doi: 10.1021/cr078253z
- Ho S. T., & Hutmacher, D. W. (2006). A comparison of micro CT with other techniques used in the characterization of scaffolds. *Biomaterials*, 27(8), 1362-1376.
- Hohenegger J. (2009). Functional shell geometry of symbiont-bearing benthic Foraminifera. *Galaxea, Journal of Coral Reef Studies*, 11(2), 81-89.
- Hottinger L. (1978). *Comparative anatomy of elementary shell structures in selected larger foraminifera*. London: Acad. Press.
- Hottinger L. (1979). Araldit als helfer der mikropalaontologie. *Aspekte*, 3, 1-11.

- Hottinger L. (1982). Larger foraminifera, giant cells with a historical background. *Naturwissenschaften*, 69(8), 361-371.
- Hottinger L. (1986). Construction, structure and function of foraminiferal shells. In B. R. Leadbeater, R. (Ed.), *Biom mineralization in lower plants and animals* (Vol. 30, pp. 220-235). Oxford: Systematics Association.
- Hottinger L. (2001). Editor's Preface: The Shell Cavity Systems in Elphidiid and Pellatispirine Bilamellar Foraminifera. *Micropaleontology*, 47, 1-4.
- Hottinger L. (2006). The depth-depending ornamentation of some lamellar-perforate foraminifera. *SYMBIOSIS*, 42(3), 11.
- Hottinger L., Leutenegger, S. (1980). The structure of calcarinid foraminifera. *Schweizerische Palaontologische Abhandlungen*, 101, 115-151.
- Hottinger L. C. (2000). Functional Morphology of Benthic Foraminiferal Shells, Envelopes of Cells beyond Measure. *Micropaleontology*, 46, 57-86.
- Hounsfield G. N. (1973). Computerized transverse axial scanning (tomography): Part 1. Description of system. *British Journal of Radiology*, 46(552), 1016-1022.
- Ikoma T., Kobayashi, H., Tanaka, J., Walsh, D., & Mann, S. (2003). Microstructure, mechanical, and biomimetic properties of fish scales from *Pagrus major*. *Journal of Structural Biology*, 142(3), 327-333.
- Jantou V., Turmaine, M., West, G. D., Horton, M. A., & McComb, D. W. (2009). Focused ion beam milling and ultramicrotomy of mineralised ivory dentine for analytical transmission electron microscopy. *Micron*, 40(4), 495-501. doi: <http://dx.doi.org/10.1016/j.micron.2008.12.002>
- Jell J. S., Maxwell, W. H. G., & McKellar, R. G. (1965). The significance of the larger foraminifera in the Heron Island reef sediments. *Journal of Paleontology*, 39(2), 273-279.
- Jones A. C., Arns, C. H., Sheppard, A. P., Hutmacher, D. W., Milthorpe, B. K., & Knackstedt, M. A. (2007). Assessment of bone ingrowth into porous biomaterials using MICRO-CT. *Biomaterials*, 28(15), 2491-2504.
- Joschko M., Graff, O., Müller, P. C., Kotzke, K., Lindner, P., Pretschner, D. P., & Larink, O. (1991). A non-destructive method for the morphological assessment of earthworm burrow systems in three dimensions by X-ray computed tomography. *Biology and Fertility of Soils*, 11(2), 88-92.
- Katsura N. (1991). Nanospace Theory for Biomineralization. In S. Suga & H. Nakahara (Eds.), *Mechanisms and Phylogeny of Mineralization in Biological Systems* (pp. 193-197): Springer Japan.
- Kelly W. J., & Cooke, T. J. (2003). Geometrical relationships specifying the phyllotactic pattern of aquatic plants. *American Journal of Botany*, 90(8), 1131-1143. doi: 10.3732/ajb.90.8.1131
- Kinoshita R. K. (2001). *The evolution of skeletons: What modern foraminifera are telling us*. (Ph.D.), State University of New York at Albany, United States -- New York. Retrieved from <http://proquest.umi.com/pqdweb?did=726322001&Fmt=7&clientId=7511&RQT=309&VName=PQD>
- Knackstedt M. A., Arns, C. H., Senden, T. J., & Gross, K. (2006). Structure and properties of clinical coralline implants measured via 3D imaging and analysis. *Biomaterials*, 27(13), 2776-2786.
- Kohler-Rink S., & Kuhl, M. (2000). Microsensor studies of photosynthesis and respiration in larger symbiotic foraminifera. I - The physico-chemical microenvironment of *Marginopora vertebralis*, *Amphistegina lobifera* and *Amphisorus hemprichii*. *Marine Biology*, 137(3), 473-486.
- Koster A. J., Ziese, U., Verkleij, A. J., Janssen, A. H., & de Jong, K. P. (2000). Three-Dimensional Transmission Electron Microscopy: A Novel Imaging and Characterization Technique with Nanometer Scale Resolution for Materials Science. *The Journal of Physical Chemistry B*, 104(40), 9368-9370. doi: doi:10.1021/jp0015628

- Kudo M., Kameda, J., Saruwatari, K., Ozaki, N., Okano, K., Nagasawa, H., & Kogure, T. (2010). Microtexture of larval shell of oyster, *Crassostrea nippona*: A FIB-TEM study. *Journal of Structural Biology*, 169(1), 1-5. doi: <http://dx.doi.org/10.1016/j.jsb.2009.07.014>
- Kuhlemeier C. (2007). Phyllotaxis. *Trends in Plant Science*, 12(4), 143-150.
- Łabaj P., Topa, P., Tyszk, J., & Alda, W. (2003). 2D and 3D Numerical Models of the Growth of Foraminiferal Shells. *Computational Science — ICCS 2003* (Vol. 2657, pp. 653-653): Springer Berlin / Heidelberg.
- Lai M., Kulak, A. N., Law, D., Zhang, Z., Meldrum, F. C., & Riley, D. J. (2007). Profiting from nature: macroporous copper with superior mechanical properties. *Chemical Communications*(34), 3547-3549. doi: 10.1039/B707469G
- Lakes R. (1993). Materials with structural hierarchy. *Nature*, 361(6412), 511-515.
- Lan S., Wu, Y., Wu, P. C., Sun, C. K., Shieh, D. B., & Lin, R. M. (2014). Advances in Noninvasive Functional Imaging of Bone. *Academic Radiology*, 21(2), 281-301. doi: <http://dx.doi.org/10.1016/j.acra.2013.11.016>
- Langer M. (1992). Biosynthesis of glycosaminoglycans in foraminifera: A review. *Marine Micropaleontology*, 19(3), 245-255.
- Langer M. R., & Gehring, A. U. (1994). Manganese (II) in Tests of Larger Foraminifera from Madang (Papua-New-Guinea). *Journal of Foraminiferal Research*, 24(3), 203-206.
- Langer M. R., Silk, M. T., & Lipps, J. H. (1997). Global ocean carbonate and carbon dioxide production; the role of reef Foraminifera. *Journal of Foraminiferal Research*, 27(4), 271-277. doi: 10.2113/gsjfr.27.4.271
- Lastoskie C., Gubbins, K. E., & Quirke, N. (1994). Pore Size Distribution Analysis and Networking: Studies of Microporous Sorbents *Studies in Surface Science and Catalysis* (Vol. Volume 87, pp. 51-60): Elsevier.
- Lee J. (1974). Towards understanding a niche for foraminifera. In R. H. a. A. Hedley, C.G. (Ed.), *Foraminifera* (Vol. 1, pp. 207-260). London: Academic Press.
- Lee J. (2011). Fueled by Symbiosis, Foraminifera have Evolved to be Giant Complex Protists. In Z. Dubinsky & J. Seckbach (Eds.), *All Flesh Is Grass* (Vol. 16, pp. 427-452): Springer Netherlands.
- Lee J., Hallock, P. (1987). Algal Symbiosis as the Driving Force in the Evolution of Larger Foraminifera. *Annals of the New York Academy of Sciences*, 503(Endocytobiology), 330-347.
- Lee J., McEnery, M. E., Kahn, E. G., & Schuster, F. L. (1979). Symbiosis and the Evolution of Larger Foraminifera. *Micropaleontology*, 25(2), 118-140.
- Lee J., Morales, J., Bacus, S., Diamont, A., Hallock, P., Pawlowski, J., & Thorpe, J. (1997). Progress in characterizing the endosymbiotic dinoflagellates of soritid Foraminifera and related studies on some stages in the life cycle of *Marginopora vertebralis*. *Journal of Foraminiferal Research*, 27(4), 254-263. doi: 10.2113/gsjfr.27.4.254
- Lee M. R., Torney, C., & Owen, A. W. (2012). Biomineralisation in the Palaeozoic oceans: Evidence for simultaneous crystallisation of high and low magnesium calcite by phacopine trilobites. *Chemical Geology*, 314–317(0), 33-44. doi: <http://dx.doi.org/10.1016/j.chemgeo.2012.04.033>
- Lee S. W., Jang, Y. N., Ryu, K. W., Chae, S. C., Lee, Y. H., & Jeon, C. W. (2011). Mechanical characteristics and morphological effect of complex crossed structure in biomaterials: Fracture mechanics and microstructure of chalky layer in oyster shell. *Micron*, 42(1), 60-70. doi: <http://dx.doi.org/10.1016/j.micron.2010.08.001>
- Lenat D. B., & Feigenbaum, E. A. (1991). On the thresholds of knowledge. *Artificial Intelligence*, 47(1–3), 185-250. doi: [http://dx.doi.org/10.1016/0004-3702\(91\)90055-O](http://dx.doi.org/10.1016/0004-3702(91)90055-O)
- Levi-Kalishman Y., Falini, G., Addadi, L., & Weiner, S. (2001). Structure of the Nacreous Organic Matrix of a Bivalve Mollusk Shell Examined in the Hydrated State Using Cryo-TEM. *Journal of Structural Biology*, 135(1), 8-17.

- Levy O., Dubinsky, Z., & Achituv, Y. (2003). Photobehavior of stony corals: responses to light spectra and intensity. *J. Exp. Biol.*, 206(22), 4041-4049. doi: 10.1242/jeb.00622
- Li H., Xu, Z. H., & Li, X. (2013). Multiscale Hierarchical Assembly Strategy and Mechanical Prowess in Conch Shells (*Busycon carica*). *Journal of Structural Biology*(0). doi: <http://dx.doi.org/10.1016/j.jsb.2013.10.011>
- Liang Y., Zhao, J., Wang, L., & Li, F. (2008). The relationship between mechanical properties and crossed-lamellar structure of mollusk shells. *Materials Science and Engineering: A*, 483-484, 309-312.
- Lima-de-Faria A. (1997). The atomic basis of biological symmetry and periodicity. *Biosystems*, 43(2), 115-135. doi: [http://dx.doi.org/10.1016/S0303-2647\(97\)01694-8](http://dx.doi.org/10.1016/S0303-2647(97)01694-8)
- Limaye A. (2006). *Drishti - Volume Exploration and Presentation Tool*. Paper presented at the Vis 2006, Baltimore. Poster presentation retrieved from
- Lipps J. H. (1973). Test Structure in Foraminifera. *Annual Review of Microbiology*, 27(1), 471-486. doi: 10.1146/annurev.mi.27.100173.002351
- Lipps J. H. (1982). Biology/paleobiology of foraminifera. *Studies in Geology*, 6, 1-21.
- Lipps J. H. (1983). Biotic interactions in benthic foraminifera. *Information Systems Division, National Agriculture Library*.
- Lipşa D. R., Laramée, R. S., Cox, S. J., Roberts, J. C., Walker, R., Borkin, M. A., & Pfister, H. (2012). Visualization for the Physical Sciences. *Computer Graphics Forum*, 31(8), 2317-2347. doi: 10.1111/j.1467-8659.2012.03184.x
- Loeblich A. R., & Tappan, H. (1984). Suprageneric Classification of the Foraminiferida (Protozoa). *Micropaleontology*, 30(1), 1-70.
- Loeblich A. R., Tappan H. (1974). Recent advances in the classification of the Foraminiferida. In R. H. Hedley, and Adams, C.G. (Ed.), *Foraminifera* (Vol. 1, pp. 1-54). London: Academic Press.
- Loncaric S. (1998). A survey of shape analysis techniques. *Pattern Recognition*, 31(8), 983-1001.
- Louveaux M., & Hamant, O. (2013). The mechanics behind cell division. *Current Opinion in Plant Biology*(0). doi: <http://dx.doi.org/10.1016/j.pbi.2013.10.011>
- Lowenstam H. A., & Weiner, S. (1989). On Biomineralization.
- Lucitti J. L., Jones E.A., Huang C., Chen J., Fraser S. E., Dickinson M. E. (2007). Vascular remodeling of the mouse yolk sac requires hemodynamic force. *Development*, 134, 3317.
- Lynts G., Pfister, R. (1967). Surface Ultrastructure of Some Tests of Recent Foraminiferida from the Dry Tortugas, Florida. *Journal of Eukaryotic Microbiology*, 14(3), 387-399.
- Macintyre I., Reid, P. (1998). Recrystallization in Living Porcelaneous Foraminifera (*Archaias Angulatis*): Textural Changes Without Mineralogic Alteration *Journal of Sedimentary Research*, 68. doi: 10.1306/D42686EE-2B26-11D7
- Maiklem W. R. (1968). Some hydraulic properties of bioclastic carbonate grains. *Sedimentology*, 10(2), 101-109.
- Mann S., & Ozin, G. A. (1996). Synthesis of inorganic materials with complex form. *Nature*, 382, 313-318.
- Mansour M. P., Volkman, J. K., Jackson, A. E., & Blackburn, S. I. (1999). The fatty acid and sterol composition of five marine dinoflagellates. *Journal of Phycology*, 35(4), 710-720. doi: 10.1046/j.1529-8817.1999.3540710.x
- Marko M., Hsieh, C., Schalek, R., Frank, J., & Mannella, C. (2007). Focused-ion-beam thinning of frozen-hydrated biological specimens for cryo-electron microscopy. *Nat Meth*, 4(3), 215-217. doi: http://www.nature.com/nmeth/journal/v4/n3/supinfo/nmeth1014_S1.html
- Marszalek D. S., Wright, R. C., & Hay, W. W. (1969a). Foraminiferal test as an environmental buffer. *The American Association of Petroleum Geologists Bulletin*, 53(3), 730.
- Marszalek D. S., Wright, R. C., & Hay, W. W. (1969b). Function of the test in Foraminifera. *Transactions - Gulf Coast Association of Geological Societies*, 19, 341-352.

- Martin R. E. (Ed.). (2000). *Environmental Micropaleontology: the application of microfossils to environmental geology*. New York: Kluwer Academic.
- Matejíček J., Kolman, B., Dubský, J., Neufuss, K., Hopkins, N., & Zwick, J. (2006). Alternative methods for determination of composition and porosity in abradable materials. *Materials Characterization*, 57(1), 17-29.
- Mayer G. (2005). Rigid Biological Systems as Models for Synthetic Composites. *Science*, 310(5751), 1144-1147. doi: 10.1126/science.1116994
- Mayer G., & Sarikaya, M. (2002). Rigid biological composite materials: Structural examples for biomimetic design. *Experimental Mechanics*, 42(4), 395-403.
- McGrath K. M. (2001). Probing Material Formation in the Presence of Organic and Biological Molecules. *Advanced Materials*, 13(12-13), 989-992.
- Meicenheimer R. (1998). Decussate to spiral transitions in phyllotaxis *Symmetry in Plants*. Singapore: World Scientific Publishing.
- Meldrum F. C., & Colfen, H. (2008). Controlling Mineral Morphologies and Structures in Biological and Synthetic Systems. *Chemical Reviews*, 108(11), 4332-4432. doi: 10.1021/cr8002856
- Meyers M., Chen, P. Y., Lin, A. Y. M., & Seki, Y. (2008). Biological materials: Structure and mechanical properties. *Progress in Materials Science*, 53(1), 1-206.
- Meyers M., Hodge, A., & Roeder, R. (2008). Biological materials science and engineering: Biological materials, biomaterials, and biomimetics. *JOM Journal of the Minerals, Metals and Materials Society*, 60(6), 21-22.
- Meyers M., Lin, A., Seki, Y., Chen, P. Y., Kad, B., & Bodde, S. (2006). Structural biological composites: An overview. *JOM Journal of the Minerals, Metals and Materials Society*, 58(7), 35-41.
- Mikhalevich V. I. (2009). Comparison between the Test and Wall Structure of the Miliolata and Fusulinoida (Foraminifera), Based on New Data from Antarctic Miliolids. *Micropaleontology*, 55(1), 1-21. doi: 10.2307/20627969
- Mizutani R., Saiga, R., Takeuchi, A., Uesugi, K., & Suzuki, Y. (2013). Three-dimensional network of Drosophila brain hemisphere. *Journal of Structural Biology*, 184(2), 271-279. doi: <http://dx.doi.org/10.1016/j.jsb.2013.08.012>
- Mukai H., Saruwatari, K., Nagasawa, H., & Kogure, T. (2010). Aragonite twinning in gastropod nacre. *Journal of Crystal Growth*, 312(20), 3014-3019. doi: <http://dx.doi.org/10.1016/j.jcrysgro.2010.07.002>
- Murray J. W. (1991). *Ecology and palaeoecology of benthic foraminifera* New York: Longman Scientific & Technical.
- Murray S. J., Renard, A. F., & Gibson, J. (1891). *Report on deep-sea deposits based on the specimens collected during the voyage of HMS Challenger in the years 1872 to 1876*: Printed for HM Stationery off., by Neill and company.
- Nayak P. P., & Joskowicz, L. (1996). Efficient compositional modeling for generating causal explanations. *Artificial Intelligence*, 83(2), 193-227. doi: [http://dx.doi.org/10.1016/0004-3702\(95\)00024-0](http://dx.doi.org/10.1016/0004-3702(95)00024-0)
- Newell A. C., Shipman, P. D., & Sun, Z. (2008). Phyllotaxis as an example of the symbiosis of mechanical forces and biochemical processes in living tissue. *Plant signaling & behavior*, 3(8), 586-589.
- Nikiforova V. J., & Willmitzer, L. (2007). Network visualization and network analysis. *Plant Systems Biology*. In S. Baginsky & A. R. Fernie (Eds.), (Vol. 97, pp. 245-275): Birkhäuser Basel.
- Nisoli C., Gabor, N. M., Lammert, P. E., Maynard, J. D., & Crespi, V. H. (2009). Static and Dynamical Phyllotaxis in a Magnetic Cactus. *Physical Review Letters*, 102(18), 186103.
- Nisoli C., Gabor, N. M., Lammert, P. E., Maynard, J. D., & Crespi, V. H. (2010). Annealing a magnetic cactus into phyllotaxis. *Physical Review E*, 81(4), 046107.

- Noone C. J., Torrilhon, M., & Mitsos, A. (2012). Heliostat field optimization: A new computationally efficient model and biomimetic layout. *Solar Energy*, 86(2), 792-803.
- Nürnberg D., Bijma, J., & Hemleben, C. (1996). Assessing the reliability of magnesium in foraminiferal calcite as a proxy for water mass temperatures. *Geochimica et Cosmochimica Acta*, 60(5), 803-814. doi: [http://dx.doi.org/10.1016/0016-7037\(95\)00446-7](http://dx.doi.org/10.1016/0016-7037(95)00446-7)
- Oberdorfer J. A., & Buddemeier, R. W. (1985). Coral reef hydrogeology. *Proceedings - International Coral Reef Symposium*, 5(3), 307.
- Oehmig R. (1993). Entrainment of planktonic foraminifera: effect of bulk density. *Sedimentology*, 40(5), 869-877.
- Okabe T. (2012). Geometric interpretation of phyllotaxis transition. *arXiv preprint arXiv:1212.3112*.
- Oshima M. (2001). Importance of Visualization in Science and Technology. *Journal of Visualization*, 4(4), 305-305. doi: 10.1007/BF03183886
- Palmer L. C., Newcomb, C. J., Kaltz, S. R., Spoerke, E. D., & Stupp, S. I. (2008). Biomimetic Systems for Hydroxyapatite Mineralization Inspired By Bone and Enamel. *Chemical Reviews*, 108(11), 4754-4783. doi: 10.1021/cr8004422
- Pecheux M. J. (1995). Ecomorphology of a recent largeforaminifer, *Operculina ammonoides*. *Geobios*, 28(5), 529-566.
- Penney M. D. (1962). Small Junks built in Hong Kong. *Transactions of the Royal Institution of Naval Architects*, 104, 99.
- Phaneuf M. W. (1999). Applications of focused ion beam microscopy to materials science specimens. *Micron*, 30(3), 277-288. doi: [http://dx.doi.org/10.1016/S0968-4328\(99\)00012-8](http://dx.doi.org/10.1016/S0968-4328(99)00012-8)
- Pochon X., Pawlowski, J., Zaninetti, L., & Rowan, R. (2001). High genetic diversity and relative specificity among Symbiodinium-like endosymbiotic dinoflagellates in soritid foraminiferans. *Marine Biology*, 139(6), 1069-1078.
- Raabe D., Romano, P., Sachs, C., Fabritius, H., Al-Sawalmih, A., Yi, S. B., . . . Hartwig, H. G. (2006). Microstructure and crystallographic texture of the chitin-protein network in the biological composite material of the exoskeleton of the lobster *Homarus americanus*. *Materials Science and Engineering: A*, 421(1-2), 143-153. doi: <http://dx.doi.org/10.1016/j.msea.2005.09.115>
- Raja R., & Saraswati, P. K. (2007). A field-based study on variation in Mg/Ca and Sr/Ca in larger benthic foraminifera. *Geochemistry Geophysics Geosystems*, 8. doi: 10.1029/2006gc001478
- Raja R., Saraswati, P. K., Rogers, K., & Iwao, K. (2005). Magnesium and strontium compositions of recent symbiont-bearing benthic foraminifera. *Marine Micropaleontology*, 58(1), 31-44.
- Rao P. (2003). Biomimetics. *Sadhana*, 28(3), 657-676.
- Raven J. A., Knoll, A. (2010). Non-skeletal biomineralization by eukaryotes: matters of moment and gravity. *Geomicrobiology Journal*, 27(6&7), 572-584.
- Raz S., Weiner, S., & Addadi, L. (2000). Formation of High-Magnesian Calcites via an Amorphous Precursor Phase: Possible Biological Implications. *Advanced Materials*, 12(1), 38-42.
- Reem D. (2011). The geometric stability of Voronoi diagrams with respect to small changes of the sites. *Proceedings of the 27th annual ACM symposium on Computational Geometry*, 254-263. doi: arXiv:1103.4125
- Reiss Z. (1958). Classification of Lamellar Foraminifera. *Micropaleontology*, 4(1), 51-70.
- Richardson S. L. (2001). Endosymbiont change as a key innovation in the adaptive radiation of Soritida (Foraminifera). *Paleobiology*, 27(2), 262-289. doi: 10.1666/0094-8373(2001)
- Rivier N., Occelli, R., Pantaloni, J., & Lissowski, A. (1984). Structure of Bénard convection cells, phyllotaxis and crystallography in cylindrical symmetry. *Journal de Physique*, 45(1), 49-63.
- Robb R. A. (1982). X-ray computed tomography: an engineering synthesis of multidisciplinary principles. *Crit Rev Biomed Eng*, 7(4), 265-333.

- Ross C. A. (1972). Biology and Ecology of Marginopora-Vertebralis (Foraminiferida), Great Barrier Reef. *Journal of Protozoology*, 19(1), 181-&.
- Ross C. A. (1976). Shell ultrastructure of Marginopora vertebralis (Foraminiferida). *Abstracts with Programs Geological Society of America*, 8(6), 1076-1077.
- Ross C. A., & Ross, J. R. (1978). Adaptive evolution in the soritids Marginopora and Amphisorus (Foraminiferida). *Scanning Electron Microscopy*, 2, 53-60.
- Röttger R., Irwan, A., Schmaljohann, R., & Franzisket, L. (1980). Growth of the symbiont-bearing foraminifera Amphistegina lessonii D'Orbigny and Heterostegina depressa D'Orbigny (Protozoa). *Endosymbiosis and Cell Biology. Walter de Gruyter, Berlin*, 125-132.
- Röttger R., Spindler, M., Schmaljohann, R., Richwien, M., & Fladung, M. (1984). Functions of the canal system in the rotaliid foraminifer, Heterostegina depressa. *Nature*, 309(5971), 789-791.
- Sakellariou A., Sawkins, T., Senden, T., & Limaye, A. (2004). X-ray tomography for mesoscale physics applications. *Physica A: Statistical Mechanics and its Applications*, 339(1), 152-158.
- Sakellariou A., Senden, T. J., Sawkins, T. J., Knackstedt, M. A., Turner, M. L., Jones, A. C., . . . Arns, C. H. (2004). *An x-ray tomography facility for quantitative prediction of mechanical and transport properties in geological, biological, and synthetic systems*. Paper presented at the Optical Science and Technology, the SPIE 49th Annual Meeting.
- Sánchez-Illescas P. J., Carpena, P., Bernaola-Galván, P., Sidrach-de-Cardona, M., Coronado, A. V., & Álvarez, J. L. (2008). An analysis of geometrical shapes for PV module glass encapsulation. *Solar Energy Materials and Solar Cells*, 92(3), 323-331.
- Sandino C., Planell, J. A., & Lacroix, D. (2008). A finite element study of mechanical stimuli in scaffolds for bone tissue engineering. *Journal of Biomechanics*, 41(5), 1005-1014.
- Saraswati P. K. (2002). Growth and habitat of some recent miliolid foraminifera: Palaeoecological implications. *Current Science*, 82(1).
- Saraswati P. K., Seto, K., & Nomura, R. (2004). Oxygen and carbon isotopic variation in co-existing larger foraminifera from a reef flat at Akajima, Okinawa, Japan. *Marine Micropaleontology*, 50(3-4), 339-349.
- Sarikaya M. (1992). Hierarchical structures of biological hard tissues. *Materials & Design*, 13(2), 101-102.
- Schiffbauer J. D., & Xiao, S. (2009). Novel application of focused ion beam electron microscopy (FIB-EM) in preparation and analysis of microfossil ultrastructures: A new view of complexity in early Eukaryotic organisms. *Palaios*, 24(9), 616-626. doi: 10.2110/palo.2009.p09-003r
- Schmahl W. W., Griesshaber, E., Merkel, C., Kelm, K., Deuschle, J., Neuser, R. D., . . . Mader, W. (2008). Hierarchical fibre composite structure and micromechanical properties of phosphatic and calcitic brachiopod shell biomaterials - an overview. *Mineral Mag*, 72(2), 541-562. doi: 10.1180/minmag.2008.072.2.541
- Sen Gupta B. (2003). Introduction to modern Foraminifera *Modern Foraminifera* (pp. 3-6).
- Severin K. P. (1987). *Functional morphology of benthic foraminifera*. (Ph.D.), University of California, Davis, United States -- California. Retrieved from <http://proquest.umi.com/pqdweb?did=749621691&Fmt=7&clientId=7511&RQT=309&VName=PQD>
- Severin K. P., & Lipps, J. H. (1989). The weight-volume relationship of the test of Alveolinella quoyi: Implications for the taphonomy of large fusiform foraminifera. *Lethaia*, 22(1), 1-12. doi: 10.1111/j.1502-3931.1989.tb01163.x
- Sheppard A. P., Arns, C. H., Sakellariou, A., Senden, T. J., Sok, R. M., Averdunk, H., . . . Knackstedt, M. A. (2006). *Quantitative properties of complex porous materials calculated from X-ray CT images*.
- Shipman P. D., & Newell, A. C. (2005). Polygonal planforms and phyllotaxis on plants. *Journal of Theoretical Biology*, 236(2), 154-197. doi: <http://dx.doi.org/10.1016/j.jtbi.2005.03.007>

- Smith D. A., & Cheung, K. F. (2002). Empirical Relationships for Grain Size Parameters of Calcareous Sand on Oahu, Hawaii. *Journal of Coastal Research*, 18(1), 82-93.
- Smith R. (1968). An intertidal Marginopora colony in Suva Harbor, Fiji. *Contributions from the Cushman Foundation for Foraminiferal Research*, 29, 12-17.
- Sondi I., & Skapin, S. D. (2010). A Biomimetic Nano-Scale Aggregation Route for the Formation of Submicron-Size Colloidal Calcite Particles. In A. Mukherjee (Ed.), *Biomimetics Learning from Nature*. InTech.
- Song J., Reichert, S., Kallai, I., Gazit, D., Wund, M., Boyce, M. C., & Ortiz, C. (2010). Quantitative microstructural studies of the armor of the marine threespine stickleback (*Gasterosteus aculeatus*). *Journal of Structural Biology*, 171(3), 318-331.
- Song Y., Black, R. G., & Lipps, J. H. (1994). Morphological Optimization in The Largest Living Foraminifera - Implications from Finite-Element Analysis. *Paleobiology*, 20(1), 14-26.
- Speijer R. P., Van Loo, D., Masschaele, B., Vlassenbroeck, J., Cnudde, V., & Jacobs, P. (2008). Quantifying foraminiferal growth with high-resolution X-ray computed tomography: New opportunities in foraminiferal ontogeny, phylogeny, and paleoceanographic applications. *Geosphere*, 4(4), 760-763. doi: 10.1130/ges00176.1
- Stapleton R. P. (1970). *Ultrastructure of Tests of Some Recent Benthic Hyaline Foraminifera*. (Ph.D.), University of Southern California, United States -- California. Retrieved from <http://proquest.umi.com/pqdweb?did=760663791&Fmt=7&clientId=7511&RQT=309&VName=PQD>
- Stock S. R. (2008). Recent advances in X-ray microtomography applied to materials. *International Materials Reviews*, 53, 129-181. doi: DOI: 10.1179/174328008X277803
- Stock S. R. (2009). *Introduction MicroComputed Tomography* (Vol. null, pp. 1-8). Boca Raton: CRC Press.
- Stolarski J., Meibom, A., Przeniosło, R., & Mazur, M. (2007). A Cretaceous Scleractinian Coral with a Calcitic Skeleton. *Science*, 318(5847), 92-94. doi: 10.1126/science.1149237
- Su X., Belcher, A. M., Zaremba, C. M., Morse, D. E., Stucky, G. D., & Heuer, A. H. (2002). Structural and Microstructural Characterization of the Growth Lines and Prismatic Microarchitecture in Red Abalone Shell and the Microstructures of Abalone "Flat Pearls". *Chemistry of Materials*, 14(7), 3106-3117. doi: 10.1021/cm011739q
- Sumper M., & Brunner, E. (2006). Learning from diatoms: nature's tools for the production of nanostructured silica. *Adv. Funct. Mat.*, 16, 17.
- Tajima K., Chen, K. K., Takahashi, N., Noda, N., Nagamatsu, Y., & Kakigawa, H. (2009). Three-dimensional finite element modeling from CT images of tooth and its validation. *Dental Materials Journal*, 28(2), 219-226.
- Tappan H. N., & Lipps, J. H. (1966). Wall structures, classification, and evolution in planktonic Foraminifera. *Bulletin of the American Association of Petroleum Geologists*, 50(3, Part 1), 637.
- Tarsitano S. F., Lavalli, K. L., Horne, F., & Spanier, E. (2006). The constructional properties of the exoskeleton of homarid, palinurid, and scyllarid lobsters *Issues of Decapod Crustacean Biology* (pp. 9-20).
- Taud H., Martinez-Angeles, R., Parrot, J. F., & Hernandez-Escobedo, L. (2005). Porosity estimation method by X-ray computed tomography. *Journal of Petroleum Science and Engineering*, 47(3-4), 209-217.
- Thompson D. W. (1942). On growth and form. *On growth and form*.
- Towe K. M., & Cifelli, R. (1967). Wall Ultrastructure in the Calcareous Foraminifera: Crystallographic Aspects and a Model for Calcification. *Journal of Paleontology*, 41(3), 742-762.
- Traas J. (2013). Phyllotaxis. *Development at a Glance*, 140(2), 249-253. doi: 10.1242/dev.074740
- Ulrich D., Hildebrand, T., Van Rietbergen, B., Muller, R., & Ruegsegger, P. (1997). The quality of trabecular bone evaluated with micro-computed tomography, FEA and mechanical testing. *Studies in health technology and informatics*, 40, 97-112.

- van Lenthe G. H., Hagenmüller, H., Bohner, M., Hollister, S. J., Meinel, L., & Müller, R. (2007). Nondestructive micro-computed tomography for biological imaging and quantification of scaffold-bone interaction in vivo. *Biomaterials*, 28(15), 2479-2490.
- van Wijk J. J. (2006). Views on Visualization. *Visualization and Computer Graphics, IEEE Transactions on*, 12(4), 421-432. doi: 10.1109/TVCG.2006.80
- Veis A., & Dorvee, J. (2013). Biomineralization Mechanisms: A New Paradigm for Crystal Nucleation in Organic Matrices. *Calcified Tissue International*, 93(4), 307-315. doi: 10.1007/s00223-012-9678-2
- Wallbridge S. (1998). *Laboratory determination of the settling, threshold and transport velocities of unusually shaped grains (Foraminifera): The effect of shape on grain hydrodynamics*. (Ph.D.), University of Southampton (United Kingdom), England. Retrieved from <http://proquest.umi.com/pqdweb?did=736525221&Fmt=7&clientId=7511&RQT=309&VName=PQD>
- Wegst U. G., & Ashby, M. F. (2004). The mechanical efficiency of natural materials. *Philosophical Magazine*, 84(21), 2167-2186. doi: 10.1080/14786430410001680935
- Weiner S. (1984). Organization of the organic matrix components in mineralized tissues. *American Zoologist*, 24(4), 945-951.
- Weiner S., & Addadi, L. (2011). Crystallization Pathways in Biomineralization. *Annual Review of Materials Research*, 41(1), 21-40. doi: 10.1146/annurev-matsci-062910-095803
- Weiner S., & Erez, J. (1984). Organic matrix of the shell of the foraminifer, *Heterostegina depressa*. *The Journal of Foraminiferal Research*, 14(3), 206-212. doi: 10.2113/gsjfr.14.3.206
- Weiner S., & Lowenstam, H. (1986). Organization of Extracellularly Mineralized Tissues: A Comparative Study of Biological Crystal Growth. *Critical Reviews in Biochemistry and Molecular Biology*, 20(4), 365-408. doi: 10.3109/10409238609081998
- Weiner S. A. L. (1997). Design strategies in mineralized biological materials. *J. Mater. Chem.*, 7, 689-702. doi: 10.1039/a604512j
- Wetmore K. L. (1987). Correlations between test strength, morphology and habitat in some benthic foraminifera from the coast of Washington. *Journal of Foraminiferal Research*, 17(1), 1-13.
- Wetmore K. L. (1999). Chamber formation in *Archaias angulatus*. *Journal of Foraminiferal Research*, 29(1), 69-74.
- Wetmore K. L., Plotnick, R. E., & Wetmore, K. L. (1992). Correlations between test morphology, crushing strength, and habitat in *Amphistegina gibbosa*, *Archaias angulatus*, and *Laevipeneroplis proteus* from Bermuda. *Journal of Foraminiferal Research*, 22(1), 1-12.
- Wimsatt W. C. (1990). Taming the Dimensions-Visualizations in Science. *PSA: Proceedings of the Biennial Meeting of the Philosophy of Science Association*, 1990, 111-135. doi: 10.2307/193062
- Wolf S. E., Lieberwirth, I., Natalio, F., Bardeau, J.-F., Delorme, N., Emmerling, F., . . . Marin, F. (2012). Merging models of biomineralisation with concepts of nonclassical crystallisation: is a liquid amorphous precursor involved in the formation of the prismatic layer of the Mediterranean Fan Mussel *Pinna nobilis*? *Faraday Discussions*, 159(0), 433-448. doi: 10.1039/C2FD20045G
- Wood A. (1949). The structure of the wall of the test in the Foraminifera; its value in classification. *Quarterly Journal of the Geological Society of London*, 104, Part 2(414), 229-255.
- Wood A. (1963). Wall structure of foraminifera in polarized light. *Micropaleontology*, 9(4).
- Wood R., Curtis Andrew, Kayser Andreas. (2009). United States Patent No.
- Wray C. G., Langer, M. R., DeSalle, R., Lee, J. J., & Lipps, J. H. (1995). Origin of the foraminifera. *Proceedings of the National Academy of Sciences*, 92(1), 141-145.
- Xie Z., Kilpatrick, N., Swain, M., Munroe, P., & Hoffman, M. (2008). Transmission electron microscope characterisation of molar-incisor-hypomineralisation. *Journal of Materials Science: Materials in Medicine*, 19(10), 3187-3192. doi: 10.1007/s10856-008-3441-2

- Yao H.-B., Fang, H.-Y., Wang, X.-H., & Yu, S.-H. (2011). Hierarchical assembly of micro-/nano-building blocks: bio-inspired rigid structural functional materials. *Chemical Society Reviews*, 40(7), 3764-3785.
- Yokoo N., Suzuki, M., Saruwatari, K., Aoki, H., Watanabe, K., Nagasawa, H., & Kogure, T. (2011). Microstructures of the larval shell of a pearl oyster, *Pinctada fucata*, investigated by FIB-TEM technique. *American Mineralogist*, 96(7), 1020-1027. doi: 10.2138/am.2011.3657
- Young I. T., Walker, J. E., & Bowie, J. E. (1974). An analysis technique for biological shape. I. *Information and Control*, 25(4), 357-370.
- Zhang D., & Lu, G. (2004). Review of shape representation and description techniques. *Pattern Recognition*, 37(1), 1-19. doi: <http://dx.doi.org/10.1016/j.patcog.2003.07.008>
- Zhang Z., Zhang, Y. W., & Gao, H. (2011). On optimal hierarchy of load-bearing biological materials. *Proceedings of the Royal Society B: Biological Sciences*, 278(1705), 519-525. doi: 10.1098/rspb.2010.1093

Appendix A

X-ray MCT – Thresholding procedure and parameters used

ImageJ-BoneJ procedure for calculation of volumes; Data sets are included electronic format.

When each image is loaded do the following.

Load images: file-import-image sequence. Choose the first .tif file of the stack in number order. Default takes first file selected as bottom of stack and goes through files one by one. Used on the .tif files

Set image properties: Image-properties set to um for micrometres and set voxel size to that listed from data for that dataset

For volume: adjust red threshold (image-adjust-threshold) to a low lower threshold (but above 0) and max high threshold, the values need not be exact. This will not be used for data collection but to give wand tool a better outline to follow (in these datasets the background is black and doesn't appear on thresholds above 0). Use the wand tool (defaults to legacy mode, tolerance 0) to outline the sample and add it to the ROI manager (ctrl-t to bring up, t to add ROI, or edit-selection-add to manager. Multiple selections made by holding shift if the slice has multiple pieces.) Particularly in large samples the wand finds a gap in a pore and instead of selecting an outline follows internal features. To stop this, with the pencil tool (one pixel wide, if need be pixel width can be set by double clicking the pencil icon) draw a white line (image-colour-colour picker to select colour, this selection stays when you close ImageJ) to close off the hole at the external edge of the sample. This will make sure the wand tool keeps an outline. Add each selection from each slice to ROI manager (the slices can be cycled through by clicking the left and right arrow keys). The slices in ROI manager are listed as number sequences, the first four digits is the slice number that region is from so you can identify missing or doubled up slices. These can then be saved in ROI manager in more-save (saves as a .zip file, make sure no individual ROI's are selected when saving or it will only save one). Use pugins-bonej-volume fraction this will bring up an options menu. Use surface (makes an isosurface of the selected voxels), use roi manager, show 3d surface. (why surface?) This brings up the threshold menu.

Use over under threshold: set upper and lower threshold. Any coloured parts (blue low and green high) are ignored, grey uncoloured data is used. (Could use red threshold too, any red parts between the upper and lower threshold values are taken as data other parts are ignored) Once threshold is set there are outputs: a 3d surface which is checked to see if it shows an accurate representation and a values table with BV, (bone volume) TV (total volume) and BV/TV. BV is the volume of the thresholded area, in this case the solid volume. TV is the volume of the whole selected area. BV/TV is the ratio of selected area over total area. Void volume calculated as TV-BV.

Data set for Figure 65 Porosity of tests of growth stages. (Volumes in μm^3 diameter in μm)

Sample	solid volume	total volume	void volume	Thresh. low	Thresh. hi	Porosity	average dia.
m111	15719017	37834279	22115262	7565	56735	0.584	490.66
m331	58103806	99644379	41540573	459	58559	0.416	807.33
m332	74284065	130269654	55985588	771	65535	0.429	955.82
m441	78337023	136860557	58523534	744	63199	0.427	929.29
m551	2.55E+09	3.56E+09	1.01E+09	9227	54719	0.283	3173.29
m smallest	391708383	621361977	229653594	6478	61183	0.369	1586.70
m smaller	700031942	1.03E+09	329090692	8270	60225	0.319	1877.21
m small	2.65E+09	4.34E+09	1.69E+09	15218	62591	0.388	3361.76
m middle	8.78E+10	1.08E+11	2.00E+10	10285	41631	0.185	10572.74
m large	1.45E+11	1.74E+11	2.85E+10	907	46271	0.163	15157.12
m largest	2.40E+11	2.95E+11	5.51E+10	1861	36511	0.186	16681.23
m young	863292884	1.09E+09	227566874	76	255	0.208	2154.19

Appendix B- Supplementary SEM images

In the supplementary electronic material see PDF document entitled:

Series of SEM images- supplement to Chapter 3.